MICRO- AND MACROMECHANICAL MODELING OF GRANULAR MATERIAL UNDER CONSTANT VOLUME CYCLIC SHEARING

by

Ming Yang

B. Sc, Tsinghua University, 2013
M. Sc, Tsinghua University, 2015

A THESIS SUBMITTED IN PARTIAL FULFILLMENT OF
THE REQUIREMENTS FOR THE DEGREE OF

DOCTOR OF PHILOSOPHY

in

THE FACULTY OF GRADUATE AND POSTDOCTORAL STUDIES
(Civil Engineering)

The University of British Columbia
(Vancouver)

October 2020

The following individuals certify that they have read, and recommend to the Faculty of Graduate and Postdoctoral Studies for acceptance, the thesis entitled:

Micro- and macromechanical modeling of granular material under constant volume cyclic shearing

submitted by Ming Yang in partial fulfillment of the requirements for

the degree of Doctor of Philosophy

in Civil Engineering

Examining Committee:

Dr. Mahdi Taiebat, Civil Engineering at The University of British Columbia
Supervisor

Dr. Gioacchino Viggiani, Civil Engineering and Geomechanics at Université Grenoble Alpes
External Examiner

Dr. Gregory A. Lawrence, Civil Engineering at The University of British Columbia
University Examiner

Dr. Mauricio Ponga, Mechanical Engineering at The University of British Columbia
University Examiner

Dr. Farhang Radjaï, CNRS at University of Montpellier
Supervisory Committee Member

Dr. Arcesio Lizcano, Industry Expert (SRK Consulting)
Supervisory Committee Member

Additional Supervisory Committee Members:

Dr. Reza Vaziri, Civil Engineering at University of British Columbia
Supervisory Committee Member

Abstract

Cyclic liquefaction of granular soils during earthquakes often results in catastrophic damages to civil infrastructure. Understanding and modeling of this complex phenomenon are of crucial importance in geotechnical engineering. Motivated by its practical importance, this study focuses on modeling the granular materials response under constant volume cyclic shearing from both micromechanics and continuum mechanics.

At the micromechanical level, discrete element method was used to carry out an extensive set of uni- and multidirectional cyclic shear simulations on idealized granular assemblies. Unidirectional simulations were analyzed to explore the microstructural evolution concerning particle connectivity, force transmission, and anisotropies. Liquefaction state was marked by a significant drop in coordination number, where the granular system became fluid-like, and deformed significantly to rebuild the contact network. Stress-force-fabric relationship was verified, revealing increasing and decreasing patterns, respectively, for the proportions of fabric and force anisotropies. The multidirectional analysis explored the effects of shear paths on the cyclic response of granular assembly. Multidirectional simulations presented lower cyclic liquefaction resistance than unidirectional ones. Microscopically, particle connectivity, particle-void fabric, and anisotropies were investigated to shed light on the stability, deformation, and load-bearing network of the granular assembly, respectively.

At the continuum level, the study focused on constitutive modeling of sand response in both pre- and post-liquefaction stages. A new constitutive model is formulated by incorporating two new constitutive ingredients into the platform of a reference critical state compatible bounding surface plasticity model with kinematic hardening. The first ingredient is a memory surface for more precisely controlling stiffness affecting the plastic deviatoric and volumetric strains and ensuing pore pressure development in the pre-liquefaction stage. The second ingredient is the concept of semifluidized state and the related formulation of stiffness and dilatancy degradation, aiming at modeling large shear strain development in the post-liquefaction stage. The new model successfully simulates undrained cyclic torsional and triaxial tests with different CSRs, separately for the pre- and post-liquefaction stages, as well as liquefaction strength curves. The new model was also assessed in the simulation of several multidirectional cyclic shear tests. The development of this constitutive model contributes to future applications in seismic site response analysis.

Lay Summary

Saturated granular deposits under dynamic shaking such as earthquakes, wave or wind forces, can develop large deformation, which may cause serious damage to people and infrastructure in the vicinity of such deposits. To avoid such damage, it is necessary to explore the nature of sand response when subjected to cyclic shearing as well as develop numerical tools that can adequately reproduce the observed response. The first half of the dissertation resorts to micromechanical modeling approach to characterize micro- and macroscopic response of the granular system under cyclic shearing, broadening the knowledge of microstructural evolutions. The second half of the dissertation adopts continuum modeling approach to develop an advanced constitutive model that can reproduce undrained cyclic response of sand, enhancing the predictability and reliability of future applications in geotechnical earthquake engineering.

Preface

This study was initialized by my research supervisor Prof. Mahdi Taiebat in terms of a research project on *multidirectional constitutive and numerical modeling in geotechnical seismic analysis and design* in 2015. During his sabbatical year in 2015-2016 at Massachusetts Institute of Technology (MIT), Prof. Taiebat established the micromechanical framework for multidirectional cyclic shear test based on the numerical tool of discrete element method developed by Prof. Farhang Radjaï and Dr. Patrick Mutabaruka. Then with the help of Prof. Taiebat and Dr. Mutabaruka, I was able to use and continue improving this numerical tool, laying the foundation for the micromechanical investigation conducted in this study. The exploration of continuum mechanics started with a MATLAB constitutive driver developed by Prof. Taiebat, leading me to get familiar with implementation of constitutive models. Later Prof. Taiebat arranged me involved in an international collaborative project named Liquefaction Experiments and Analysis Projects (LEAP), which allowed me to realize shortcomings of the adopted constitutive model. In late 2018, the early trials of improving the model performance in simulating undrained cyclic shear tests were carried out and certain success was attained. With tremendous theoretical creativity and guidance from Profs. Taiebat and Yannis F. Dafalias, the new model was able to be well shaped and finalized. Evaluation of the model in multidirectional cyclic shear test was based on an earlier study conducted under the guidance of Prof. Taiebat for a keynote presentation that he delivered in the third International Conference on Performance-based Design in Earthquake Geotechnical Engineering (PBD-III).

I, Ming Yang, am the principal contributor to all seven chapters of this thesis. I was responsible for all major areas of code development, simulation realization, model formulation, verification and validation, data collection and analysis, and writing the chapters. Some parts of the findings of this thesis have been published in two journals and four conferences so far and some parts are being prepared for submission to journals.

Published, submitted or preparing material to journals:

- Yang, M., Seidalinov, G., and Taiebat, M. (2019). Multidirectional cyclic shearing of clays and sands: Evaluation of two bounding surface plasticity models. *Soil Dynamics and Earthquake Engineering*, 124:230–258

  This paper constitutes most parts of Chapter 6. The modification is replacing the original

sand constitutive model with the latest one developed in Chapter 5, along with updating the corresponding simulation results. In this paper I was responsible for collection of laboratory experimental database, simulation and evaluation of the results for the earlier version of SANISAND model. The paper explores the SANISAND model performance in simulating multidirectional cyclic shear tests against laboratory experimental data. I, Dr. Gaziz Seidalinov, and Prof. Taiebat planned the paper together. The first draft of the paper was prepared by Dr. Seidalinov and me. Prof. Taiebat provided technical assistance in revising the manuscript.

- Yang, M., Taiebat, M., and Dafalias, Y. F. (2020a). SANISAND-MSf: a memory surface enhanced sand plasticity model with semifluidized state for undrained cyclic shearing. *Géotechnique*. Doi: 10.1680/jgeot.19.P.363
  This paper comprises Chapter 5. The idea was initialized by an early trial of adding another type of "memory surface" to the reference model, which achieved certain success in simulation of pore pressure generation in pre-liquefaction stage. Profs. Taiebat and Dafalias proposed a new version of "memory surface" more compatible with the reference model, and based on my implementation, we improved formulations together. The paper demonstrates development of the model and validation against available laboratory experimental data. I, Profs. Taiebat and Dafalias planned the paper together. I conducted all the analyses and prepared the first draft. Profs. Taiebat and Dafalias provided technical assistance in revising the manuscript.

- Yang, M., Taiebat, M., Mutabaruka, P., and Radjaï, F. (2020b). Evolution of granular materials under isochoric cyclic simple shearing. Submitted
  This paper comprises Chapter 3, where a number of isochoric cyclic simple shear simulations were carried out to explore microstructural evolution of the granular assembly along cyclic shearing. I and Prof. Taiebat planned the paper together. Under the guidance of Prof. Taiebat, I conducted the simulations and data analysis, and prepared the first draft. Prof. Taiebat, Dr. Mutabaruka and Prof. Radjaï provided technical assistance in revising the manuscript.

- Yang, M., Taiebat, M., Mutabaruka, P., and Radjaï, F. (2020c). Macro response and micro structure of 3D granular media subjected to multidirectional cyclic shearing. In preparation
  This paper comprises Chapter 4, where a number of multidirectional cyclic shear simulations were carried out to explore effects of shear paths on micro- and macroscopic response of granular system. I and Prof. Taiebat planned the paper together. Under the guidance of Prof. Taiebat, I conducted the simulations and data analysis, and prepared the first draft.

Prof. Taiebat, Dr. Mutabaruka and Prof. Radjaï provided technical assistance in revising the manuscript.

Published material in conferences:

- Yang, M., Taiebat, M., and Vaid, Y. P. (2016). Bidirectional monotonic and cyclic shear testing of soils: state of knowledge. In *69th Canadian Geotechnical Conference*, Vancouver, BC, Canada. Paper ID: 4198, 8 pages
  This paper comprises parts of Chapters 2 and 6, referring to collection of laboratory experimental database of multidirectional cyclic shear tests. I conducted data collection and prepared the first draft. Profs. Taiebat and Yogi P. Vaid provided technical assistance in revising the manuscript.

- Seidalinov, G., Yang, M., and Taiebat, M. (2017). Multidirectional cyclic shearing of clays and sands: evaluation of two advanced plasticity models. In *3rd International Conference on Performance-based Design in Earthquake Geotechnical Engineering*, pages 1–21
  This paper comprises part of Chapter 6. I, Dr. Seidalinov and Prof. Taiebat planned the paper together. I conducted data collection and simulations of the SANISAND model. The first draft of the paper was prepared by me and Dr. Seidalinov. Prof. Taiebat provided technical assistance in revising the manuscript.

- Yang, M., Taiebat, M., Mutabaruka, P., and Radjaï, F. (2018). Multidirectional cyclic shearing of granular media using discrete element simulations. In *IS-Atlanta 2018: Geo-Mechanics from Micro to Macro*, pages 1–6. Atlanta, Georgia, US
  This paper comprises part of Chapter 4. I and Prof. Taiebat planned the paper together. I conducted the simulations and data analysis, and prepared the first draft. Prof. Taiebat, Dr. Mutabaruka and Prof. Radjaï provided technical assistance in revising the manuscript.

- Yang, M., Taiebat, M., and Dafalias, Y. F. (2021). A new sand constitutive model for pre- and post-liquefaction stages. In *16th International Conference of IACMAG*, pages 1–8. Torino, Italy
  This paper comes from Chapter 5. I, Profs. Taiebat and Dafalias planned the paper together. I conducted the simulations and data analysis, and prepared the first draft. Profs. Taiebat and Dafalias provided technical assistance in revising the manuscript.

Table of Contents

List of Tables

List of Figures

List of Symbols

$\otimes$	Dyadic product
$\cdot$	Single contraction product
$:$	Double contraction product
$\lvert\cdot\rvert$	Absolute value or norm of a vector
$\lVert\cdot\rVert$	Norm of a tensor
$\langle\cdot\rangle$	Macauley brackets or arithmetic mean
$\mathrm{tr}(\cdot)$	Trace operator
a_c	Fabric anisotropy
a_n	Normal force anisotropy
a_t	Tangential force anisotropy
a_i	Radius of particle i
$\boldsymbol{a}_c$	Fabric anisotropy tensor
$\boldsymbol{a}_n$	Normal force anisotropy tensor
$\boldsymbol{a}_t$	Tangential force anisotropy tensor
A_0	Dilatancy model variable
A_0'	Dilatancy model constant
AR	Aspect ratio
b_0	Plastic modulus model variable
b^{M}	Projection distance between $\boldsymbol{\alpha}_\theta^{\mathrm{M}}$ and $\boldsymbol{\alpha}$ along $\mathbf{n}$

b_{ref}	Bounding surface length along **n**
B	Model variable
c	Contact ID or Lode angle interpolation constant
c_{c}	Memory surface model constant with a default value of 1.0
c_h	Plastic modulus model constant
c_ℓ	Semifluidized state model constant
c_{r}	Semifluidized state model constant
c_z	Fabric dilatancy model constant
c_n	Spring normal viscosity
c_t	Spring tangential viscosity
c_r	Spring rolling viscosity
c_o	Spring torsion viscosity
C	Model variable
$\boldsymbol{C}^{\mathrm{e}}$	Fourth-order elastic stiffness tensor
$\boldsymbol{C}^{\mathrm{ep}}$	Fourth-order elastoplastic stiffness tensor
CSR	Cyclic stress ratio
CSR_x	Cyclic stress ratio along x axis
CSR_y	Cyclic stress ratio along y axis
CSR_y	Cyclic resistance ratio along y axis
d	Particle diameter
d_{max}	Maximum particle diameter
d_{min}	Minimum particle diameter
$\mathrm{d}X$	Loading variable
D	Dilatancy

D_c	Centroid distance
$\boldsymbol{D}_c^i$	Vector connecting $\boldsymbol{O}^i$ and $\boldsymbol{P}^i$ normalized by R_{50}
D_r	Relative density
e	Void ratio
e_0	Initial void ratio
e_c	Critical void ratio
$e_\mathrm{c}^\mathrm{ref}$	Critical state line model constant
$\mathbf{e}$	Deviatoric strain tensor
$\mathbf{e}^\mathrm{e}$	Elastic deviatoric strain tensor
$\mathbf{e}^\mathrm{p}$	Plastic deviatoric strain tensor
$\boldsymbol{E}$	Strain constraints matrix
f	Yield surface
f^M	Memory surface
f_ℓ	Semifluidized state model constant with a default value of 0.01
f_x	Frequency along x axis
f_y	Frequency along y axis
f_n	Normal contact force
f_t	Tangential contact force
f_NR	Non-rattler fraction
$\boldsymbol{f}, \boldsymbol{f}^\mathrm{c}, \boldsymbol{f}^\mathrm{k}$	Contact force vector
$\boldsymbol{f}_t$	Tangential contact force vector
$\boldsymbol{f}^{c,p}$	Contact force vector applied on particle p
$\hat{f}_{[\,]}$	Candidate contact force
$g(\theta, c)$	Lode angle dependent interpolation function

G	Hypoelasticity shear modulus
G_0	Hypoelasticity model constant
h	Sample height or hardening coefficient for kinematic hardening
h_0	Model variable
h_0'	Plastic modulus model constant
h^{M}	Hardening coefficient for kinematic hardening of memory surface
h^*	User-defined constant for determination of h^{M}
I	Inertial number
$I(x_\alpha)$	Interpolation function
I_m	Mobilized friction index
$\boldsymbol{I}$	Second-order identity matrix
k_n	Spring normal stiffness
k_t	Spring tangential stiffness
k_r	Spring rolling stiffness
k_o	Spring torsion stiffness
K	Hypoelasticity bulk modulus
K_{p}	Plastic modulus
K_0	Earth pressure coefficient at rest
ℓ	Strain liquefaction factor
L	Plastic multiplier
$\boldsymbol{l}^c$	Branch vector
m	Yield surface size model constant
m^{M}	Memory surface size model variable
M	Critical state stress ratio in p-q space

M_f	Slope of failure surface
n	Current step number
n_{f}	Total number of steps
n_{his}	Frequency number
n^{b}	Bounding surface model constant
n_ℓ	Semifluidized state model constant with a default value of 8.0
n_g	Model constant
n^{d}	Dilatancy model constant
$\boldsymbol{n}$	Unit vector perpendicular to contact plane
$\mathbf{n}$	Unit norm second-order tensor normal to yield surface
$\mathbf{n}_\alpha$	Unit norm second-order tensor along $\boldsymbol{\alpha}$
N	Number of loading cycles
N_{ini},N_{IL}	Number of loading cycles to initial liquefaction
N_c	Total number of contacts
N_p	Total number of particles
N_p^0	Number of particles without contacts
N_p^1	Number of particles with one contact
$\boldsymbol{O}^i$	Center of Voronoi cell i
p	Particle ID or Mean effective stress
p_{at}	Atmospheric pressure
p_0	Initial mean effective stress
p_{r}	Threshold pressure ratio
p_{th}	Threshold pressure with a default value of 10 kPa
$\boldsymbol{P}^i$	Center of particle i

q	Deviatoric stress
r_u	Pore pressure ratio
$r_{u,\mathrm{lim}}$	Limiting pore pressure ratio
$\mathbf{r}$	Deviatoric stress ratio tensor
$\boldsymbol{r}^c$	Position of contact c
$\boldsymbol{r}^p$	Center position of particle p
$\boldsymbol{r}^{c,p}$	Vector connecting $\boldsymbol{r}^c$ and $\boldsymbol{r}^p$
R_{50}	Mean radius of particles
$\mathbf{R}'$	Deviatoric flow rule tensor of DM04 model
$\mathbf{R}^*$	Deviatoric flow rule tensor of SANISAND-MSf model
$S_{[\,]}$	First joint invariant between two tensors
SSR	Static stress ratio
SSR_x	Static stress ratio along x axis
SSR_y	Static stress ratio along y axis
$\mathbf{s}$	Deviatoric stress tensor
$\boldsymbol{S}$	Stress constraints matrix
$\boldsymbol{t}$	Unit vector in contact plane along $\boldsymbol{f}_t$
u	Memory surface model constant
v_x	Moving rate of top wall
V	Computing domain
V_p	Particle p volume
$V_{p,V}$	Volume of particle p in V
w	Memory surface model constant with a default value of 2.0
x	Semifluidized state model constant

x_α	Relative distance between $\boldsymbol{\alpha}^{\mathrm{b}}_{\theta_\alpha}$ and $\boldsymbol{\alpha}$
x_w	Cumulative horizontal displacement of top wall along x axis
y_w	Cumulative horizontal displacement of top wall along y axis
z_{g}	Geometrical coordination number
$z_{\max}$	Fabric dilatancy model constant
$\mathbf{z}$	Fabric dilatancy tensor
$\alpha^{\mathrm{b}}_{\theta_\alpha}$	Length of $\boldsymbol{\alpha}^{\mathrm{b}}_{\theta_\alpha}$
$\boldsymbol{\alpha}$	Yield surface center tensor
$\boldsymbol{\alpha}_{\mathrm{in}}$	Value of $\boldsymbol{\alpha}$ at initiation of new loading
$\boldsymbol{\alpha}^{\mathrm{M}}$	Memory surface center tensor
$\boldsymbol{\alpha}^{\mathrm{b}}_{\theta}$	Projection of $\boldsymbol{\alpha}$ on bounding surface along $\mathbf{n}$
$\boldsymbol{\alpha}^{\mathrm{b}}_{\theta+\pi}$	Projection of $\boldsymbol{\alpha}$ on bounding surface along $-\mathbf{n}$
$\boldsymbol{\alpha}^{\mathrm{b}}_{\theta_\alpha}$	Projection of $\boldsymbol{\alpha}$ on bounding surface along $\mathbf{n}_\alpha$
$\boldsymbol{\alpha}^{\mathrm{d}}_{\theta}$	Projection of $\boldsymbol{\alpha}$ on dilatancy surface along $\mathbf{n}$
$\boldsymbol{\alpha}^{\mathrm{M}}_{\theta}$	Projection of $\boldsymbol{\alpha}$ on memory surface along $\mathbf{n}$
γ	Shear strain
γ_x	Shear strain along x axis
γ_y	Shear strain along y axis
$\delta_{[\,]}$	Overlap between two particles
δ_n	Normal overlap between two particles
Δu	Pore pressure
ε	Memory surface model constant with a default value of 0.01
$\boldsymbol{\varepsilon}$	Strain tensor
ε_{a}	Axial strain

ε_{v}	Volumetric strain
$\varepsilon_{\mathrm{v}}^{\mathrm{e}}$	Elastic volumetric strain
$\varepsilon_{\mathrm{v}}^{\mathrm{p}}$	Plastic volumetric strain
θ	Angle of $\boldsymbol{n}$ projected on shear plane or Lode angle along $\mathbf{n}$
θ_α	Lode angle along $\mathbf{n}_\alpha$
Θ	Angle between $\mathbf{n}$ and $\dot{\mathbf{r}}$
κ	Stiffness parameter defined by $k_n/(pd)$
$\lambda_{\mathbf{c}}$	Critical state line model constant
μ_0	Memory surface model constant
μ_t	Tangential friction coefficient
μ_r	Rolling friction coefficient
μ_o	Torsion friction coefficient
ν	Hypoelasticity Poission's ratio
ξ	Critical state line model constant
ρ	Particle density
σ_{c}	Consolidation stress
σ_{11},σ_{xx}	xx-component of stress tensor
σ_{22},σ_{yy}	yy-component of stress tensor
σ_{33},σ_{zz}	zz-component of stress tensor
σ_{23},σ_{yz}	yz-component of stress tensor
σ_{13},σ_{xz}	xz-component of stress tensor
σ_{12},σ_{xy}	xy-component of stress tensor
σ'_{vc}	Effective vertical consolidation stress
ς	Memory surface shrinkage model constant with a default value of 0.00001

$\boldsymbol{\sigma}$	Stress tensor
τ	Shear stress
τ_x	Horizontal shear stress along x axis
τ_y	Horizontal shear stress along y axis
τ^{amp}	Amplitude of shear stress
$\tau_{u,\mathrm{lim}}$	Shear stress corresponding to $r_{u,\mathrm{lim}}$
ϕ	Phase angle
φ	Azimuthal angle
$\boldsymbol{\phi}_c$	Fabric tensor
$\boldsymbol{\phi}_n$	Normal force fabric tensor
$\boldsymbol{\phi}_t$	Tangential force fabric tensor
ψ	State parameter

Acknowledgements

I deliver my deepest thanks to my wife SU Miaomiao for her devotion, consideration, accompanying, support and encouragement in the past decade. She has always been so supportive and optimistic that my life has been lightened, even in my struggling period. My two sons Maple and Mango also add extensive happiness to this special journey.

I would like to express my sincerest gratitude to my research supervisor, Professor Mahdi Taiebat, for his kind offering of this research opportunity, and continuously significant guidance and encouragement in the past few years. His characters of pursing details, perfection, clarity and conciseness have always challenged and motivated me to become a better researcher.

I also want to thank Professor Yannis F. Dafalias for the help of formulating memory surface and the insistence of developing a generic model. His energetic, knowledgeable, creative and open mind has benefited me remarkably. I am always grateful to Professor Yogi P. Vaid for the numerous consultations happening on Tuesday afternoon. His kindness, curiosity and erudition have impressed me significantly. The numerical tool of discrete element modeling developed by Dr. Patrick Mutabaruka has improved my coding capability extensively, let alone the meaningful discussions and suggestions from him. My supervisory committee members also contributed a lot to completion of this dissertation. I am really grateful to Dr. Arcesio Lizcano for his valuable encouragement and comments as a close friend and an admirable scholar. Professor Reza Vaziri has been a great teacher leading me to the field of computational mechanics and also a respectful researcher for providing such constructive advice to shape this work generally. I really enjoy the discussions with Professor Farhang Radjaï, and deal with his gentle and insightful suggestions like a breath of fresh air.

I have been so lucky to work with diverse and exceptional colleagues, the past and present members of the Theoretical & Applied Geomechanics (TAG) research group. Fruitful discussions, insightful suggestions, close cooperations and mutual encouragement have push my research so far. I'm greatly thankful to Dr. Andrés R. Barrero picking me from YVR airport the first time I came to Vancouver, Mr. Boris Kolev always promising to see me in the office, Dr. Gaziz Seidalinov coauthoring my first journal, Mr. James Adinata, Ms. Francesca Palmieri, Mr. Sounik Banerjee, Mr. Andrés Reyes, Mr. Erick Lino and Ms. Keith Pérez.

I also want to thank the basketball friends. Playing with them always makes me feel how time

flies, adding so much ease and pure delight to this journey.

My deepest thanks are given to my parents, Hongdang Yang and Rongsi Qin, who always love and encourage me without any reason. Without their sacrifice and support, I could not have traveled across the Pacific Ocean and accomplished this dissertation.

Financial support provided by the Natural Sciences and Engineering Research Council of Canada (NSERC) is gratefully acknowledged.

Chapter 1: Introduction

1.1 Motivation of research

In geotechnical engineering, dynamic properties of soils are always of great interest and significance because they are closely applicable to the analyses related to engineering requirements including operation of heavy machinery, blasts, or natural hazards such as earthquakes, wave or wind forces. Among them, earthquakes have caused catastrophic damage on people and constructed facilities, which accelerated advancement of soil dynamics. Figure 1.1

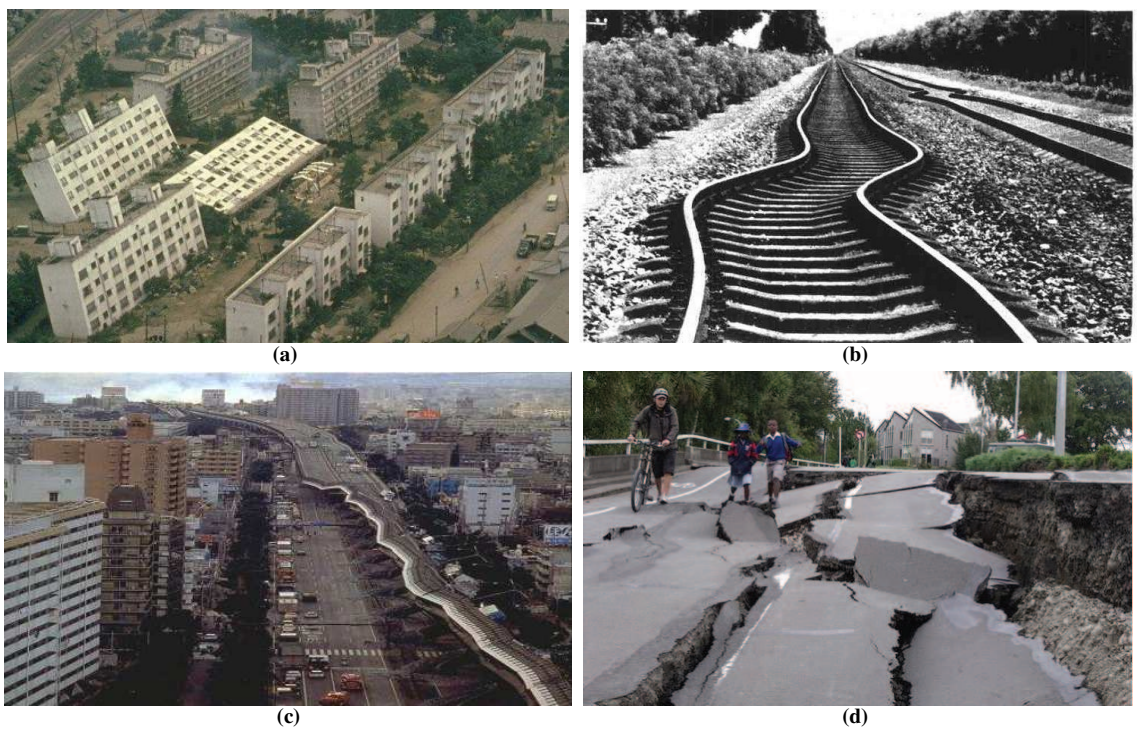

Figure 1.1: Illustration of seismic hazards caused by (a) 1964 Niigata Earthquake M7.5, (b) 1976 Tangshan Earthquake M7.6, (c) 1995 Kobe Earthquake M7.2 and (d) 2011 Christchurch Earthquake M6.2.

presents four well-known earthquakes to illustrate the destructive nature and the consequences, including load-bearing capacity failure, structure collapsing, lateral spreading, which all are

related to soil response under dynamic loading. Specifically, most of these earthquake damaging is encompassed by soil liquefaction.

Soil liquefaction refers to soil deposits losing strength and appearing to flow as fluids, and the strength of the soil is reduced, often drastically, to the point where it is unable to support structures or remain stable (Kramer, 1996). While the phenomenon of liquefaction has been long recognized, its devastating effects started to draw substantial attention of engineers after the 1964 Alaska earthquake and 1964 Niigata earthquake (shown in Figure 1.1(a)). Since then, liquefaction has been studied extensively by researchers around the world, such as Seed and Idriss (1967), Castro (1975), Ishihara et al. (1975), Vaid and Chern (1983), Been and Jefferies (1985), Ishihara (1993), Idriss and Boulanger (2008), Jefferies and Been (2015), to name a few. Despite liquefaction being used for description of many different but related phenomena, this thesis will specially focus on cyclic liquefaction of granular materials such as sand, indicating liquefaction is caused by dynamic or cyclic loading. It occurs with accumulation of large shear strains in the soil. Under unidirectional cyclic shearing, it may come along with zero effective stress where large shear strain develops, as observed in conventional undrained cyclic triaxial or simple shear tests. This type of liquefaction is also rephrased as semifluidized state following Barrero et al. (2018) and Barrero et al. (2020). However, pore pressure may not need to fully develop to induce large deformation and exceptional scenarios have been revealed in multidirectional cyclic shear test by, for example, Ishihara and Yamazaki (1980) and Boulanger and Seed (1995). Hence, generally cyclic liquefaction is an extreme manifestation of progressive accumulation of noticeable shear strains due to breaking or collapsing of internal structure.

In consideration of the discrete nature of granular material, discrete element method (DEM) (Cundall and Strack, 1979) has been widely used for simulation of cyclic liquefaction in recent decades, which allows easy extraction of microscopic information such as fabric, force distributions, thereby providing another view of investigating cyclic liquefaction. DEM study of cyclic liquefaction due to unidirectional cyclic shearing dates back to Ng and Dobry (1994) and is quickly expanded by Sitharam (2003), Soroush and Ferdowsi (2011), Wang and Wei (2016), Wang et al. (2016), Huang et al. (2018), Huang et al. (2019b), Evans and Zhang (2019), Martin et al. (2020) to different aspects such as contact network in semifluidized state, microstructures governing macroscopic deformation, mechanisms for effects of initial and loading conditions on liquefaction resistance.

Continuum-based numerical modeling of the cyclic liquefaction of granular materials is achievable using cyclic nonlinear models to describe the stress-strain behaviors properly. This type of material model is also called constitutive model usually built on plasticity theory, meant for capturing the actual stress-strain path of laboratory experiments, which also serves as the core for the numerical platforms such as finite element, finite difference or material point method.

Developing such constitutive models is quite challenging as one needs to consider small strain behaviors, loading-unloading-reloading, stiffness degradation, coupling between volumetric and deviatoric response, and others. Even so, a number of constitutive models presenting quite promising simulation results for certain aspects related to cyclic liquefaction of unidirectional cyclic shear tests, have been proposed in recent decades, including but not limited to Papadimitriou and Bouckovalas (2002), Elgamal et al. (2003), Dafalias and Manzari (2004), Zhang and Wang (2012), Iai et al. (2011), Boulanger and Ziotopoulou (2013), Poblete et al. (2016).

In dynamic analysis of geo-structures, like the simple site response analysis all the way to more complex soil-structure interactions, the analysis is usually performed using only one horizontal component of ground motion. However, in real earthquakes, soil layers are subjected to multidirectional cyclic shearing, with different amplitudes and frequencies. Even if the vertical component of seismic loading is neglected, there still exist two horizontal shear components as depicted in Figure 1.2, where the acceleration history and acceleration orbit based on the records of the 1995 Kobe Earthquake are presented. Apparently, one can expect that the shaking history at

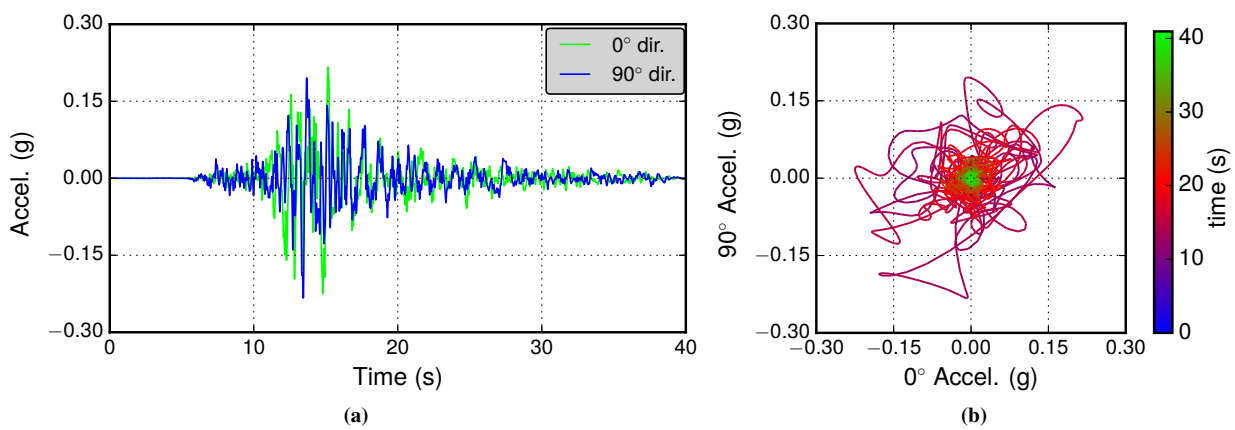

Figure 1.2: Two horizontal shaking components at of Kobe Earthquake in 1995: (a) acceleration histories and (b) acceleration orbit.

the site condition of horizontal ground during Kobe Earthquake cyclic shearing only in one horizontal direction is not enough to simulate the real stress-strain response of soil in such conditions. Meanwhile, in view of soil's nonlinear mechanical properties, the principle of superposition does not apply. Even with the assumption that soil is transversely isotropic, it is not accurate to obtain the realistic stress state under multidirectional cyclic shearing only based on the results of unidirectional shear tests. Another interesting case is accounting for the initial offset shear stress exerted on soil elements beneath the slope and then evaluating the response when soil is sheared in a different direction. In the corresponding laboratory element test, the specimen should be consolidated with a static shear stress applied to account for the slope. Then another

shear stress not in line with the first one is to be applied. This is something that conventional unidirectional simple shear devices cannot handle. Overall, it is necessary to simultaneously account for both horizontal components of the motion into the analysis, which can be seen as a closer approximation to the seismic loading case.

Numerically, to achieve that, an advanced constitutive model should be developed and evaluated to properly reproduce the stress-strain response. Before that, it is also necessary to understand and explore cyclic response of granular material at element level. According to its discrete and continuum nature, this dissertation focuses on numerical modeling of the response of granular material when subjected to constant volume uni- and multidirectional cyclic shearing, with the aim to explore the physics of the granular system and develop a constitutive model used for liquefaction-related problems.

1.2 Objective and methodology

Figure 1.3 illustrates connections between laboratory element testing, discrete element modeling and constitutive modeling. As physical experiments were obtained from literature other than carried out here, the objective of this dissertation is two fold: (1) exploring the physics of granular system mainly when approaching liquefaction under constant volume uni- and multidirectional cyclic shearing from both micro and macro views; (2) developing an advanced plasticity model to adequately capture undrained cyclic response of sands under unidirectional cyclic shearing, especially in terms of pre-liquefaction pore pressure generation and post-liquefaction shear strain development, and then evaluating the model in simulation of multidirectional cyclic shear tests. These two sub-objectives are further expanded into two parts, respectively, as follows:

(1) The first part of the first sub-objective was achieved by adopting discrete element method (DEM) to conduct "virtual experiments" of constant volume cyclic simple shear test, which provided the access to exploiting particle-level information. Here a bi-periodic system was built to constrain lateral normal strains and also minimize the boundary effects that posted limitation to the use of the physical test results. The granular assembly was comprised of spherical particles interacting based on soft-particle laws. During the simulation, evolution of microstructure of the granular system approaching and exiting liquefaction(or semifluidized state) was recorded, allowing one to investigate micromechanics.

(2) Different shear paths of multidirectional cyclic shear tests were applied to the same granular assembly for investigation of their effects on the response of granular system, which accomplished the second part of the first sub-objective. Here a stress-controlled scheme was configured to guarantee the applied stress path was what the granular assembly experienced.

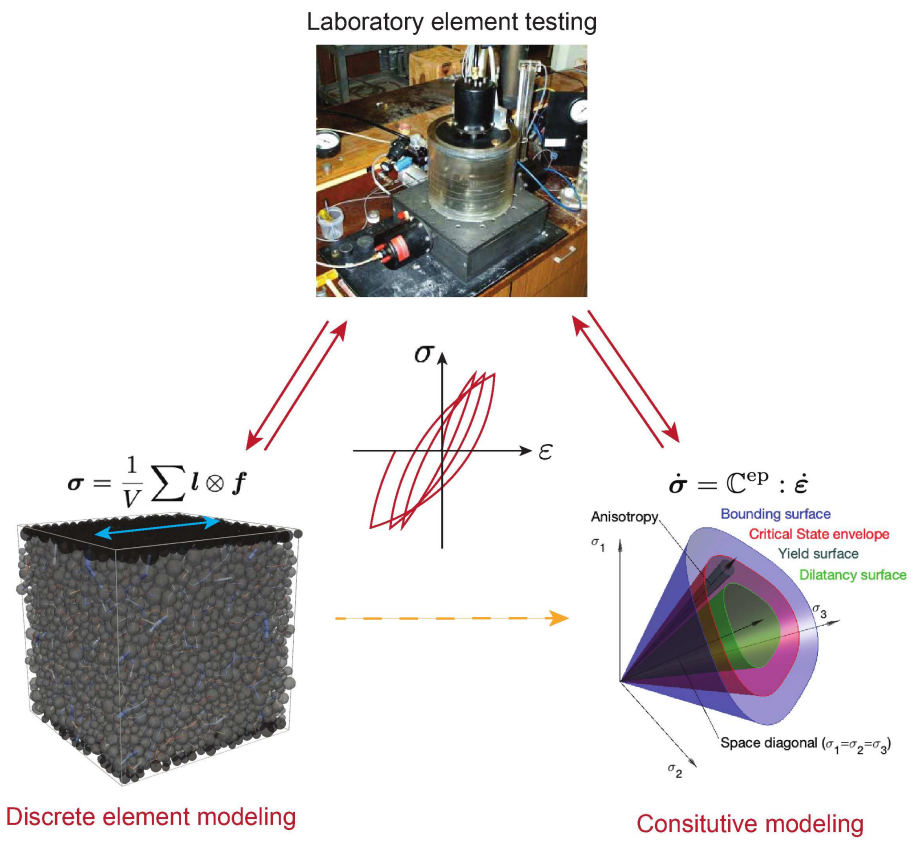

Figure 1.3: Triangle for illustration of connections between laboratory element testing, discrete element modeling and constitutive modeling: the photo of laboratory element testing is from Kammerer et al. (2002) and the highlighted red parts are related to the research objective.

Using the exact same sample under different types of shear paths also ensured accuracy of the simulation results. Over fifty simulations were carried out to macroscopically reveal the volumetric and deviatoric response due to difference in the shear path. Several microscopic indicators were also presented to shed light on the stability, deformation and fabric anisotropy of the granular system.

(3) The first part of the second sub-objective was realized by developing a sand constitutive model used for undrained unidirectional cyclic shearing. This model was built on a notable Simple Anisotropic SANID (SANISAND) plasticity model. The flow rule of the reference model was modified for better description of non-proportional monotonic and cyclic shearing. A novel ingredient of memory surface (MS) was formulated and incorporated into the reference model to better balance the coupling of volumetric and deviatoric response in pre-liquefaction period, which lead to adequate simulation of pore pressure generation. The existence of MS also allowed simplification of an existing constitutive ingredient of semifluidized state, used for capturing post-liquefaction shear strain development. This new

model, denoted as SANISAND-MSf, was well suited for simulating the whole process of sands under undrained unidirectional cyclic shearing.

(4) Applying the developed constitutive model SANISAND-MSf to simulate a series of multidirectional cyclic shear tests concluded the second part of the second sub-objective. This evaluation was conducted on the established laboratory experimental database of Monterey No. 0/30 sand, where simulations of different shear paths were performed. Discussion of the performance of this new model in the so called neutral loading paths was also carried out.

One can build the link between discrete element modeling and constitutive modeling, and capability of DEM in easy generation of versatile virtual experiments does provide guidance for revising certain formulations of the constitutive model, as shown in Figure 1.3. Modification of the flow rule of the reference model was an example. However, given the very distinct frameworks of these two numerical approaches, this dissertation deals with the sub-objectives (1)(2) and (3)(4) independently, i.e., the link between them was not deeply pursued here.

1.3 Outline

This dissertation consists of seven chapters. These chapters are organized in the sequential order starting from description of numerical platforms supporting the subsequent explorations, followed by adoption of DEM to investigate the response of granular system subjected to uni- and multidirectional cyclic shearing, respectively, and then moving to development of an advanced constitutive model of sand for undrained unidirectional cyclic shearing, and finally evaluation of this new model in simulating multidirectional cyclic shear tests from the laboratory experiments.

Chapter 2 starts with the brief state of knowledge summarizing the previous research from the view of laboratory element testing and numerical modeling, given a more detailed literature review to be conducted at the beginning of each subsequent chapter. The laboratory element tests covered the available undrained uni- and multidirectional cyclic shear tests, with more focus on the knowledge gained from them. By reviewing the previous studies of numerical modeling on granular materials, research gaps were revealed, some of which would be filled by this dissertation. Then it comes to introduction and description of two numerical platforms, namely a DEM program GRFlow3D (Mutabaruka, 2013) and a standalone constitutive driver ConModel. The general frameworks of GRFlow3D and ConModel were expounded and more attention was put on modifications and explorations of the two platforms, which provided the basis for expansion of the research in the subsequent main chapters.

In Chapter 3 GRFlow3D was applied to study the microstructural evolution of granular assembly under isochoric cyclic simple shearing. Following a proper sample preparation

procedure, the cyclically sheared assemblies presented a promising macro-mechanical response, much like the physical experiments. At the grain scale, the evolution of the particle connectivity, force transmission, and anisotropies of contact and force networks was analyzed. It was observed that entering the liquefaction state is characterized by a variety of microscopic indicators. After a considerable shear deformation in liquefaction state, contact network was first reconstructed, providing the geometrical basis for rebuilding the force network, thereby exiting liquefaction state. The relationship between deviatoric stress ratio and anisotropies, known to hold in the triaxial setting, was also valid with reasonable accuracy in the cyclic simple test. Interestingly, fabric and force anisotropies at the peak shear stress appeared to level off after several cycles in the post-liquefaction period. Their respective contributions to the shear stress were not affected by changing initial and loading conditions.

Chapter 4 expanded the DEM study to multidirectional cyclic shear tests. A comprehensive series of simulations covering 1-D linear, 2-D linear, circular/oval and figure-8 shear paths were generated. The macroscopic stress path and stress-strain response agreed well with laboratory experiments. At system level, effects of shear paths on pore pressure generation and shear strain development were explored, revealing a lower liquefaction resistance for the sample under multidirectional loading although the sample did not go through transient zero mean effective stress under certain shear paths. At the grain scale, evolution of particle connectivity indicated the system became unstable instantaneously for the selected 1-D and figure-8 paths, and stayed stable for 2-D and circular paths. A paricle-void descriptor named centroid distance was monitored to shed light on the shear strain development, from which a general decreasing trend with shear strain accumulation was evidenced. Finally, evolution of fabric and force anisotropies at specified states of each loading cycle revealed that the former needed more time to follow the external shearing compared with the latter. All these anisotropies tended to level off in post-liquefaction period and their proportions contributing to the deviatoric stress ratio were not affected by shear paths.

Chapter 5 formulated a new sand constitutive model by incorporating two constitutive ingredients into the platform of a reference critical state compatible bounding surface plasticity model with kinematic hardening, in order to address primarily the undrained cyclic response. The first ingredient was a memory surface for more precisely controlling stiffness affecting the plastic volumetric strain and ensuing excess pore pressure development in pre-liquefaction stage. The second ingredient was the concept of semifluidized state and the related formulation of stiffness and dilatancy degradation, aiming at modeling large shear strain development in post-liquefaction stage. In parallel, a modified flow rule aiming at better description of non-proportional monotonic and cyclic loading was introduced. With a single set of constants, for which a detailed calibration procedure was provided, this new model successfully simulated undrained cyclic torsional and

triaxial tests with different CSRs, separately for the pre- and post-liquefaction stages, as well as liquefaction strength curves based on pore pressure ratio and shear strain criteria for initial liquefaction. The successful reproduction of sand element response under undrained cyclic shearing contributed to future applications in realistic and thorough seismic site response analysis.

Chapter 6 focused on evaluation of the constitutive model developed in Chapter 5 for simulating the response of sand under multidirectional cyclic shearing. First an overall experimental database of multidirectional cyclic shear tests available in the literature was summarized, followed by details of the selected experiments to be simulated in this chapter. The new model was calibrated against laboratory experiments of undrained monotonic triaxial and cyclic simple shear tests and then was applied to simulate multidirectional cyclic shear tests with respect to 1-D linear, 2-D linear, circular/oval and figure-8 paths. Comparisons between experiments and simulations revealed the model performed well in simulating the pore pressure generation and needed further improvement to develop large shear strain oscillations. Proximity of the model to neutral loading when simulating these tests was also evaluated.

Chapter 7 concluded this dissertation with summary, conclusions and recommendations for future work.

1.4 Notations

Within this dissertation, scalar variables are denoted by characters with normal letters (e.g., p for mean effective stress), vectors and second-order tensors are formatted by bold face characters (e.g. $\boldsymbol{f}$ for contact force, $\boldsymbol{\sigma}$ for stress tensor). The dyadic product between two tensors is denoted by $\boldsymbol{a} \otimes \boldsymbol{b}$, i.e., $a_{ij}b_{kl}$ in the index notation. The symbol : between two tensors denotes summations over the adjacent pairs of indices in reverse order of the tensors, which in the case of second-order tensors implies the trace, namely $\mathrm{tr}(\mathbf{AB}) = \mathbf{A} : \mathbf{B} = A_{ij}B_{ji}$. The norm of a tensor $\boldsymbol{a}$ is defined by $\|\boldsymbol{a}\| = \sqrt{\boldsymbol{a} : \boldsymbol{a}}$. In multiaxial space, the stress tensor $\boldsymbol{\sigma}$ is usually decomposed into its volumetric part $p = \mathrm{tr}(\boldsymbol{\sigma})/3$ and deviatoric part $\mathbf{s} = \boldsymbol{\sigma} - p\mathbf{I}$ where $\mathbf{I}$ is the identity tensor; the strain tensor $\boldsymbol{\varepsilon}$ follows the similar way, where the volumetric strain $\varepsilon_{\mathrm{v}} = \mathrm{tr}(\boldsymbol{\varepsilon})$ and the deviatoric strain tensor $\mathbf{e} = \boldsymbol{\varepsilon} - (\varepsilon_{\mathrm{v}}/3)\mathbf{I}$. In triaxial test, the deviatoric stress $q = \sqrt{(3/2)\mathbf{s} : \mathbf{s}}$ can be simplified as $\sigma_{33} - \sigma_{11}$ where 1 and 3 refers to the radial and axial direction, and the axial strain ε_{a} is equivalent to ε_{33}. In simple shear test, shear stress τ refers to σ_{13} and shear strain γ is equal to $2\varepsilon_{13}$.

Chapter 2: Literature Review and Numerical Platforms

2.1 Introduction

This chapter consists of three main sections: literature review, DEM program and Constitutive driver. Literature review is focused on summarizing the existing knowledge on the response of granular materials under constant volume or undrained cyclic shearing according to laboratory element testing and numerical modeling. Research gaps of numerical modeling are pointed out and some of them will be resolved in the next chapters. Two numerical platforms are adopted in this study, including a DEM program GRFlow3D for discrete element modeling and a standalone constitutive driver ConModel developed by the author for incremental integration of a constitutive model under various loading conditions. Introduction of GRFlow3D starts with illustration of the general framework, expands with the modifications conducted by the author and ends with exploring two basic questions related to sample preparation and representative volume element (RVE), respectively. In the section of Constitutive driver, the numerical approach and configurations for some complex element tests are explained, providing the basis for the simulations carried out in later chapters.

2.2 Literature review

This section summarizes previous research work on granular material at element level subjected to constant volume cyclic shearing from two main aspects: laboratory testing and numerical modeling. In laboratory element tests, irregular seismic loading with random manners in magnitude and frequency is simplified as regular harmonic loading. Representative volume element (RVE) is prepared and placed on the laboratory apparatus which provides the physical way to study the mechanical response of granular material under the modes of uni- and multidirectional cyclic shearing. Equivalently, in numerical modeling, given the particulate nature of granular materials, discrete element method (DEM), by computing the motion and effect of a number of particles, can be used to approximate the preparation and shearing of RVE as carried out in the laboratory, allowing extraction of microscopic information as well. By treating RVE as

a continuum medium, one can also develop a constitutive model for adequately capturing its stress and strain response, serving as the core for successful continuum modeling with great potential of applications in boundary value problem simulations.

2.2.1 Laboratory experiments of undrained cyclic shear test

To generate the ideal unidirectional cyclic shear mode, i.e., regular harmonic loading, two types of laboratory devices are usually adopted: direct simple shear apparatus (Bjerrum and Landva, 1966) and hollow cylinder torsional device (Tatsuoka et al., 1982). The corresponding tests are named as simple shear test and torsional test. Hereafter simple shear test will be used to refer to both types of experiments as they share the same deformation mode, as depicted in Figure 2.1(a). The representative cubic sample is deformed in plane strain condition so that $\dot{\varepsilon}_{yy} = 0$. In the xz plane, its shape changes from a rectangle to a parallelogram. There is no normal strain along x direction, and because of the constant volume setting, there is no vertical strain either. The only non-zero component of strain is the shear strain γ_{xz}:

$$\dot{\varepsilon}_{xx} = \dot{\varepsilon}_{yy} = \dot{\varepsilon}_{zz} = \dot{\gamma}_{xy} = \dot{\gamma}_{yz} = 0; \;\; \dot{\gamma}_{xz} \neq 0 \tag{2.1}$$

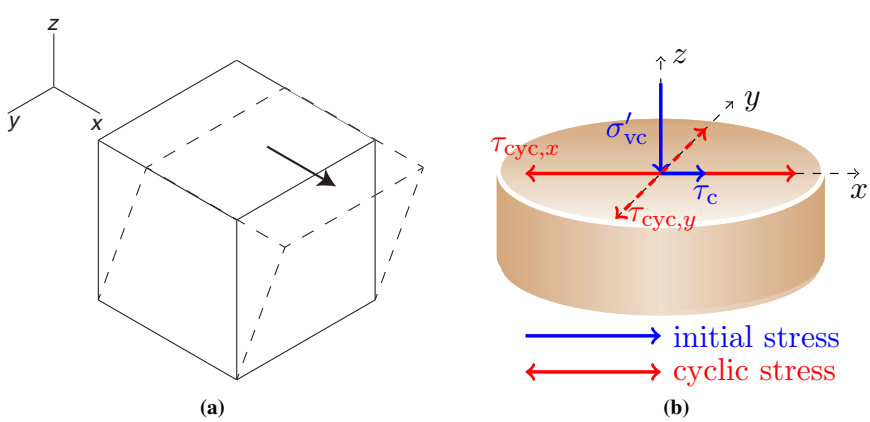

Figure 2.1: Schematic illustration of one soil element in: (a) simple shear test (modified from Wood (1990)); (b) multidirectional cyclic shear test.

The deformation mode described by Equation (2.1) can be achieved in the laboratory test on saturated soil samples with pore water present in the system and the drainage valve turned off while shearing; this is called truly undrained simple shear test. As the bulk modulus of water is much larger than that of the soil skeleton, it may be considered incompressible; hence, constant volume and truly undrained simple shear tests are expected to show almost the same response as

shown experimentally in Dyvik et al. (1987). In the current study, the numerical simulations in both discrete and continuum levels have been carried out in constant volume, and the results are considered comparable to the experiments carried out either constant volume or truly undrained.

One of the typical constant volume cyclic simple shear tests is conducted in the way that the shear direction will be reversed if the monitored shear stress τ_{xz} reaches the shear stress amplitude τ^{amp}, and it is denoted as stress-limit cyclic shear simple test. This type of test has been adopted by the laboratory researchers to investigate the response of soil under cyclic shearing (Towhata and Ishihara, 1985; Kiyota et al., 2008; Chiaro et al., 2013) and effects of different factors on the liquefaction resistance, including but not limited to cyclic stress ratio (CSR) (Tatsuoka et al., 1982; Wijewickreme et al., 2005), relative density D_{r} (Tatsuoka et al., 1982; Georgiannou and Konstadinou, 2014), initial confinement p_0 (Vaid and Chern, 1985; Vaid and Sivathayalan, 1996; Wijewickreme et al., 2005; Koseki et al., 2005), anisotropic consolidation (Tatsuoka et al., 1982; Ishihara et al., 1985; Konstadinou and Georgiannou, 2013; Georgiannou and Konstadinou, 2014), static shear stress (Vaid and Liam Finn, 1979; Tatsuoka et al., 1982; Sivathayalan and Ha, 2011; Chiaro et al., 2012), sample preparation method (Tatsuoka et al., 1982). Here CSR refers to the ratio of cyclic shear stress amplitude τ^{amp} and the initial mean stress p_0. Static stress ratio (SSR) is used to quantify the ratio of static shear stress τ_{c} and the initial mean stress p_0. Liquefaction resistance refers to the number of loading cycles required to reach zero mean effective stress or certain levels of shear strain. As the laboratory results indicate, increasing CSR decreases the number of cycles for liquefaction, increasing initial confinement decreases the liquefaction resistance (this decreasing is more pronounced in dense sample than loose sample), increasing relative density increases the liquefaction resistance, and the effect of SSR on liquefaction resistance depends on the sample state such as relative density (Boulanger and Seed, 1995).

Considering the multidirectional nature of earthquakes, the unidirectional shear mode has been extended to multidirectional cyclic shearing where two horizontal shear components are exerted simultaneously on the top of the specimen (Ishihara and Yamazaki, 1980; Boulanger and Seed, 1995; Kammerer et al., 2002; Matsuda et al., 2011). This type of test is illustrated in Figure 2.1(b) where the blue arrows indicate the sample stress state at the end of sample preparation and the red ones are the two cyclic shear components applied during the shear stage. The two cyclic shear components can have different magnitudes, frequencies, and phase angles, which constitutes a list of shearing paths. Generally in constant volume multidirectional cyclic shear test, plane strain does not apply any more and the deformation mode is indicated by the following constraints:

$$\dot{\varepsilon}_{xx} = \dot{\varepsilon}_{xy} = \dot{\varepsilon}_{zz} = \dot{\gamma}_{xy} = 0; \;\; \dot{\gamma}_{yz} \neq 0, \dot{\gamma}_{xz} \neq 0 \tag{2.2}$$

State of knowledge with respect to multidirectional cyclic shear test on soil element has been conducted and summarized in Yang et al. (2016) and Yang et al. (2019), including its history, laboratory test procedures, adopted shear paths and available experimental database. Chapter 6 will summarize the experimental database available from the previous laboratory research. Basically, research interest on multidirectional cyclic shear test lies in: (a) mechanical response of sand under this shearing mode (Boulanger and Seed, 1995; Kammerer et al., 2005) such as deformation type, excess pore pressure generation pattern; (b) comparisons in liquefaction resistance between uni- and multidirectional cyclic shear tests (Ishihara and Yamazaki, 1980; Boulanger and Seed, 1995; Kammerer et al., 2005); (c) effects of SSR, CSR and shearing direction on the dynamic properties of granular materials such as excess pore pressure generation, post-shake settlement (Kammerer et al., 2005; Matsuda et al., 2011).

2.2.2 Micro and macro-mechanical modeling

Numerical modeling of uni- and multidirectional cyclic shear tests on granular material can be carried out via discrete and continuum approaches. One of the most widely used numerical methods in discrete modeling is discrete element method (DEM) where the motion and effect of particles in the granular system are simulated, and it consists of molecular dynamics (MD), contact dynamics (CD), event driven (ED) to name a few. Finite element (FE), finite difference (FD), and material point method (MPM) are some examples of continuum modeling where the stress and strain response at material level plays the key role, also known as constitutive model. As this dissertation focuses on modeling of granular material at element level, the following literature review only covers related previous numerical research, excluding modeling of large scale boundary value problems.

DEM simulations of unidirectional cyclic shear test have been conducted by a few researchers in recent three decades. The research topics that they were trying to tackle include: (a) qualitative and quantitative validation of DEM simulation results against laboratory experiments (Ng and Dobry, 1994; Dabeet, 2014; Kuhn et al., 2014); (b) exploration of disadvantages of simple shear device like the stress or strain non-uniformity (Dabeet, 2014; Asadzadeh and Soroush, 2017); (c) investigating boundary effects on the model response (Asadzadeh and Soroush, 2018; Zhang and Evans, 2018); (d) revealing evolution of microstructure along the cyclic shearing (Wang and Wei, 2016; Sufian et al., 2017). With expanding the unidirectional cyclic simple shear mode to consider other loading types such as triaxial tests, many other DEM studies can provide instruction and guidance to the work of modeling unidirectional cyclic simple shear test. These extra works include Guo and Zhao (2013), Bernhardt et al. (2016), Wang et al. (2016), Huang et al. (2018), Huang et al.

(2019a), Huang et al. (2019b), Sufian et al. (2019), Evans and Zhang (2019), Martin et al. (2020). There are few DEM studies on the multidirectional cyclic shear test except Wei (2017) and Wei et al. (2020) where circular/oval and figure-8 shearing paths are applied on isotropically consolidated samples and evolutions of some microstructures are presented.

Constitutive modeling of sands under undrained cyclic simple shearing has been attracting extensive attention from numerical modelers, considering its widespread applications in seismic site response analysis. Over the decades, a number of constitutive models have been developed with the aim for capturing different aspects of the response of sands under undrained cyclic shearing. These aspects include: (a) pre-liquefaction pore pressure generation (Wang et al., 1990; Papadimitriou and Bouckovalas, 2002; Dafalias and Manzari, 2004; Poblete et al., 2016; Fuentes et al., 2019); (b) post-liquefaction shear strain development (Elgamal et al., 2003; Zhang and Wang, 2012; Wang et al., 2014; Barrero et al., 2020); (c) effect of CSR on stress and strain response (Khosravifar et al., 2018); (d) effect of initial conditions such as D_{r}, p_0 and SSR on stress and strain response (Khosravifar et al., 2018; Wang and Ma, 2019). Given the difficulty of developing a constitutive model to properly simulate the aforementioned aspects under unidirectional cyclic shear mode, there is little research on proposing a constitutive model meant for multidirectional cyclic shear test, which is more demanding. Despite the great potential of applications, the loading type complexity and limited experimental database hold numerical modelers back. Still, one can evaluate the performance of the existing good constitutive models in simulating this type of test and seek for possible improvement. This gap was filled by the author using one of the constitutive models developed by Dafalias and Manzari (2004).

2.2.3 Summary

The literature review of laboratory research on unidirectional cyclic shear tests suggests a large number of laboratory element tests of sands, which is very helpful for understanding the response of sand under undrained cyclic shearing and validating the results of numerical modeling. However, a comprehensive laboratory experimental database of analyzing effects of different factors on the stress and strain response of the same sand is still missing (or maybe not public), which to some extent, holds back development of a versatile constitutive model. When it comes to multidirectional cyclic shear tests, only the work of Kammerer et al. (2002) allows a rather complete evaluation of numerical simulation results. But the limited laboratory experiments for each loading path still constrains establishment of basic knowledge of the response of sands under multidirectional cyclic shearing. More laboratory study on multidirectional cyclic shear test is needed.

There are a few publications that used DEM to explore the response of granular material

under constant volume simple shear test but few DEM studies related to multidirectional cyclic shear test. Some of them adopted certain microscopic indicators to reveal the evolution of microstructure along the shearing process. But the adopted indicators were pretty narrow and only reflected limited information, not enough for providing the panorama. Thus, it is necessary to generalize the choices of microscopic descriptors to achieve an overall understanding of what happens inside the granular assembly, which may help explore the link between the microstructure and macro response. In addition, given the capability and versatility of DEM in simulating "virtual experiments", it is worth applying DEM to conduct a series of multidirectional cyclic shear tests, revisiting and extending the gained knowledge of the material response from laboratory test results, such as effects of loading types on the stress and strain response. Meanwhile, exploring the underlying microstructure linked to macro behaviors is also rewardable.

Most of the advanced constitutive models are focused on simulation of post-liquefaction shear strain development and do not pay much attention to pore pressure generation in pre-liquefaction period which leads to initial liquefaction (i.e., zero mean effective stress). Usually they are able to present satisfying simulation results for the tests with high CSRs but can not properly predict the number of loading cycles to initial liquefaction for the tests with low CSRs. According to the author's knowledge, modeling the behaviors of sands in pre-liquefaction period can be carried out independently from the post-liquefaction shear strain development, which implies other constitutive ingredients should be pursed to improve simulation of the pre-liquefaction response. With this target being achieved, one can explore the capabilities of the constitutive model in capturing effects of relative density D_{r}, initial confinement p_0 and static shear ratio SSR on the stress and strain response, evaluate the model performance in simulating multidirectional cyclic shear tests, or apply the model to simulate boundary value problems.

2.3 DEM program - GRFlow3D

There are a number of DEM programs that can be used for simulation of cyclic shearing. These include the commercial ones, including Particle Flow Code (PFC) (Itasca, 2018) and EDEM (EDEM, 2016), and open-source ones including LIGGGHTS (Kloss et al., 2012) and YADE (Šmilauer et al., 2010), to name a few. In this study, a three-dimensional particle dynamic DEM numerical platform GRFlow3D developed by Mutabaruka (2013) is adopted. Some reasons behind the choice of this program are advantages in the aspects of the programming language (C++), installation (no library dependence), platform (macOS and Linux), and, most importantly, the ease of use and further developments because of an ongoing collaboration with the main developers of the program. GRFlow3D has a simple and clean structure with a limited number of header and source files, making it relatively straightforward for the user/developer to get familiar

with the whole architecture and modify it for the desired research purposes.

Here GRFlow3D is used to study the mechanics of response of granular materials under isochoric cyclic shearing according to their discrete nature. The samples are simulated using poly-disperse spheres interacting based on soft-particle laws. The contact laws of the spheres based on the linear spring dashpot, are well explained in Luding (2008) and Mutabaruka (2013), and will be covered in Chapter 3. This section is focused on introducing the general framework of GRFlow3D, modifications and improvements conducted by the author, and some preparatory work for expanding the explorations as conducted in Chapters 3 and 4.

2.3.1 Framework

The overall framework of GRFlow3D is described by the flowchart of Figure 2.2, revealing adoption of stationary scheme (Tu and Andrade, 2008). This stationary scheme is suitable for running purely strain-controlled tests such as undrained simple shear test but needs to be updated with the iterative scheme for stress-controlled ones such as multidirectional cyclic shear test, where the iteration process can guarantee the system deforms by following the applied shear stress paths. While one can refer to Wei (2017) and Wei et al. (2020) for details of the implementation, Chapter 4 dealing with DEM simulation of multidirectional cyclic shear test will elaborate a bit more on that. Here the focus is on the core of the DEM program, as presented in Figure 2.2.

To conduct a DEM simulation using GRFlow3D, an input file needs to be prepared, including settings of running time, contact model constants, simulated test, parameters for Verlet's method, along with four state files consisting of sample file, boundary file, contact file and force file. During the routine *Initialization*, all the information is read by the corresponding object created by GRFlow3D, thus setting up the initial condition and loading configuration. While the current step number n is smaller than the total number of steps n_{f}, GRFlow3D first checks whether the neighbor list needs to be updated or not according to the frequency number freq, which is an input parameter. In the routine *Build neightbor list*, two lists are updated, namely SupVerlet and Verlet. The former one looks for all pairs of particles within a large cutoff for potential contacts in the next hundred of steps, which requires two loops over all particles. Verlet list is built by looping over SupVerlet for the pairs of particles within a smaller cutoff, used for the routine *Detect contacts* executed at every time step. Apparently, Verlet list is updated at a higher frequency than SupVerlet. The routine *Predict states* solves the kinematic equations over all particles and boundaries by updating their positions and velocities. GRFlow3D combines the routines *Detect contacts* and *Calculate forces* in one function, where by conducting one loop over all particles and one loop over the Verlet list, the interparticle force and moment are calculated, along with

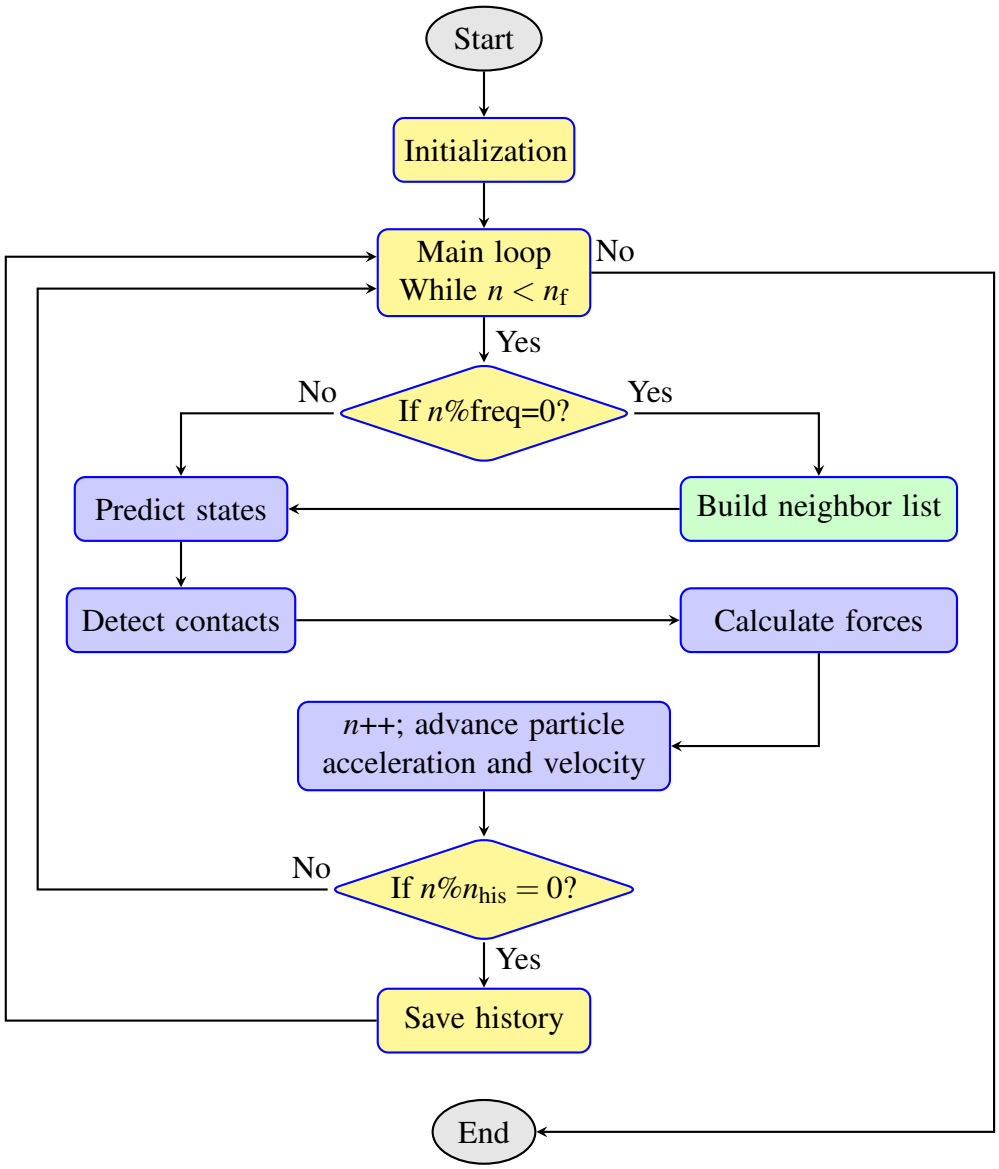

Figure 2.2: Flowchart of GRFlow3D. Yellow operations can't be parallelized and blue operations can be parallelized using OpenMP. Green operation is the function that may consume most time and can be improved by Verlet's method or further parallelizing (modified from Martins and Atman (2017) and Gopalakrishnan and Tafti (2013)). n is the current step number, n_f is the total number of steps, freq is the frequency number quantifying how often neighbor list is updated, and n_{his} refers to the frequency number quantifying how often history files are saved. The symbol % is modulo operator and $n++$ refers to $n = n + 1$.

other types of forces such as gravity if needed. Thus the total force and moment of each particle can be determined, followed by updating the acceleration and velocity in the routine *advance particle acceleration and velocity*. Then the frequency number n_{his} is used to judge whether the current state should be saved as history files or not. These saved history files can be used for extra post-processing or relaunching simulations without starting from the very beginning.

2.3.2 Modifications

Several modifications have been made to GRFlow3D, including adoption of iterative scheme, update of stress tensor calculation, optimization of the code, introduction of servo-controlled algorithm, to name a few. While one can refer to these publications (Wei et al., 2020; O'Sullivan, 2011; Martins and Atman, 2017; Thornton, 2000) for the ideas, it is necessary to expand two of them here, namely stress tensor calculation and optimizing the code.

The widely used formula to determine the stress tensor of the granular system is proposed by Christoffersen et al. (1981)

$$\boldsymbol{\sigma} = \frac{1}{V} \sum_{c \in N_c} \boldsymbol{l}^c \otimes \boldsymbol{f}^c \tag{2.3}$$

which is linked to the interparticle interactions over a selected computing domain V. Here $\boldsymbol{l}^c$ is the branch vector connecting the centers of two particles for interior contact or connecting the particle center and the contact point for exterior contacts, $\boldsymbol{f}^c$ is the contact force, $\otimes$ denotes the tensor dyadic product and the summation runs over all the contacts N_c in the selected volume V. One can go to O'Sullivan (2011) and Kuhn (2017) for the derivation. Calculating system-level stress tensor using Equation (2.3) is appropriate if the selected volume is carefully designed to fully encompass the particles (Kuhn, 2017). But it may lose certain accuracy when the volume is crafted to pass through some peripheral particles. For example, the selected volume in this study shares the same center and horizontal cross-section but cuts 80% height of the whole sample, where there must be some particles located on the top and bottom boundaries. The key lies in how to deal with the peripheral particles. The alternative approach modified from Equation (2.3) is

$$\boldsymbol{\sigma} = \frac{1}{V} \sum_{p \in V} \frac{V_{p,V}}{V_p} \sum_{c \in C^p} \boldsymbol{r}^{c,p} \otimes \boldsymbol{f}^{c,p} \tag{2.4}$$

where $p \in V$ is defined by particle p having intersection with the selected volume V; the particle volume and the intersection volume are denoted as V_p and $V_{p,V}$, respectively; C^p represents the set of contacts belonging to particle p, $\boldsymbol{r}^{c,p} = \boldsymbol{r}^c - \boldsymbol{r}^p$ connecting the contact point and the center of particle p and $\boldsymbol{f}^{c,p}$ is the contact force applied on particle p at the contact point c. One can see

that $(1/V_p)\sum_{c\in C^p} \boldsymbol{r}^{c,p} \otimes \boldsymbol{f}^{c,p}$ is the stress tensor for particle p, thus Equation (2.4) implies the average stress tensor weighted by the volumes of particles within the selected volume V (Potyondy and Cundall, 2004; Li et al., 2009; O'Sullivan, 2011).

To verify the effectiveness of Equation (2.4) compared with Equation (2.3), a chain of N_p particles comprises a column with a vertical stress of 100 kPa being applied on the top. Figure 2.3(a) displays a column of 10 spheres for an example and Figure 2.3(b) compares calculated vertical stresses using Equations (2.3) and (2.4) with the target of 100 kPa. Apparently, while the accuracy of Equation (2.3) is increased with increasing N_p, Equation (2.4) matches the target precisely, irrespective of the number of layers, which is required by the current study.

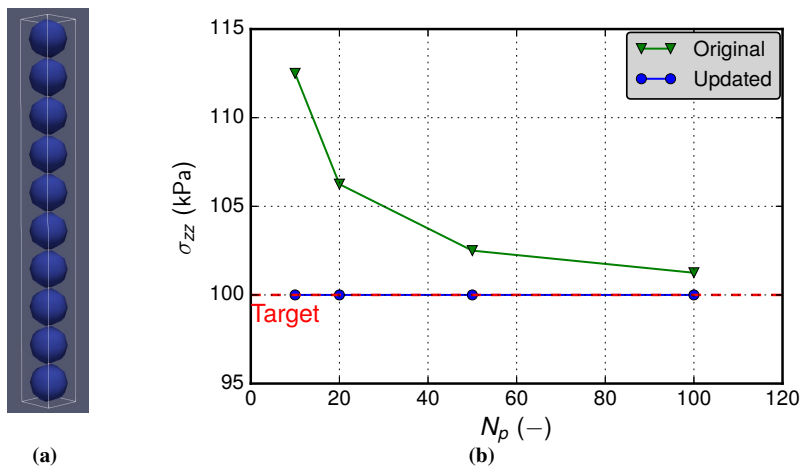

Figure 2.3: Internal stress determined from compressing a column of spheres: (a) a chain of 10 spheres and (b) calculated vertical stresses using Equations (2.3) and (2.4).

Another modification is to optimize the DEM program GRFlow3D with the aim of speeding up the simulations. Generally there are two directions, the first being optimization of the serial code by rewriting certain functions and the second being parallelization of the serial code. No matter which one is adopted, the very first step is to analyze the time profiler of running a GRFlow3D simulation, which points out which functions needs to be optimized. Instruments belonging to the software Xcode of mac OS allows calculation of running time for each function based on clang compiled executable file. Figure 2.4(a) presents the percentage of total time spent by each GRFlow3D routine on a single core according to running a constant volume cyclic simple shear test on the sample of 4096 spheres within 50000 steps. The total running time is around 20.95 min. One can notice that the most time consuming routine is linterRetrieve, mapping the old contact list to new established one, which is necessary for retrieving history dependent quantities related to the contact such as the tangential overlap. It belongs to *Build neighbor list* in Figure 2.2 and can be parallelized. The next two routines exist and getParameter are executed at every time step to check whether the contact laws exist or not and get the contact model constants if they

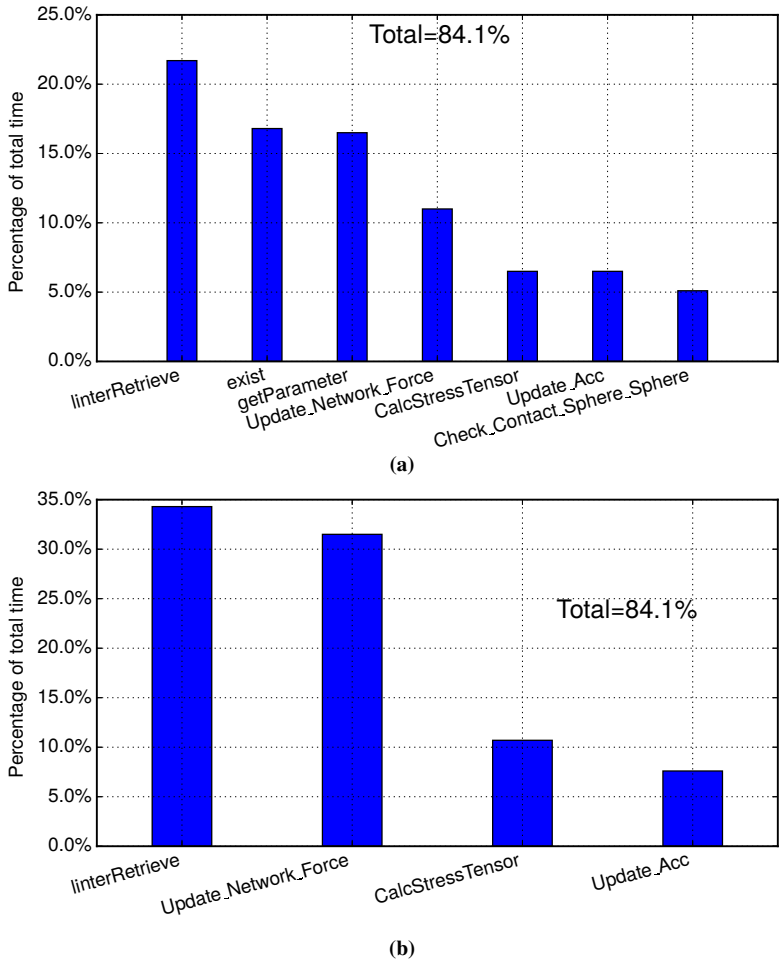

Figure 2.4: Percentage of total time spent by GRFlow3D routines on a single core based on simulation of constant volume cyclic simple shearing of 4096 **spheres in** 50000 **steps: (a) prior to optimizing the serial code and (b) after optimizing the serial code.**

exist, respectively, which are searched from the dictionary container, slowing down the simulation. The routine exit can be improved by using bool type and the routine getParameter is replaced by getParameterQuickly adopting the sequential container. While the following routines can be parallelized later, Figure 2.4(b) updates the percentage of total time spent by optimizing exist and getParameter of GRFlow3D and the total running time drops to 12.91 min.

To parallelize the serial code, an implicit parallelism model called OpenMP is adopted given its simplicity and good comparability with GRFlow3D. One can go to the online course *Introduction to OpenMP* by Mattson (2013) or Chapman et al. (2008) for details of OpenMP. Guided by Figure 2.2, the four routines listed in Figure 2.4(b) are parallelized by incorporating compiler directives into the for loops, meanwhile being careful of avoiding race condition and false sharing (Chapman et al., 2008). Figure 2.5 shows the comparisons of simulation results of constant volume cyclic simple shear tests using serial and parallel GRFlow3D in terms of stress

path and stress-strain response. Their complete overlap verifies the correctness of this parallelized

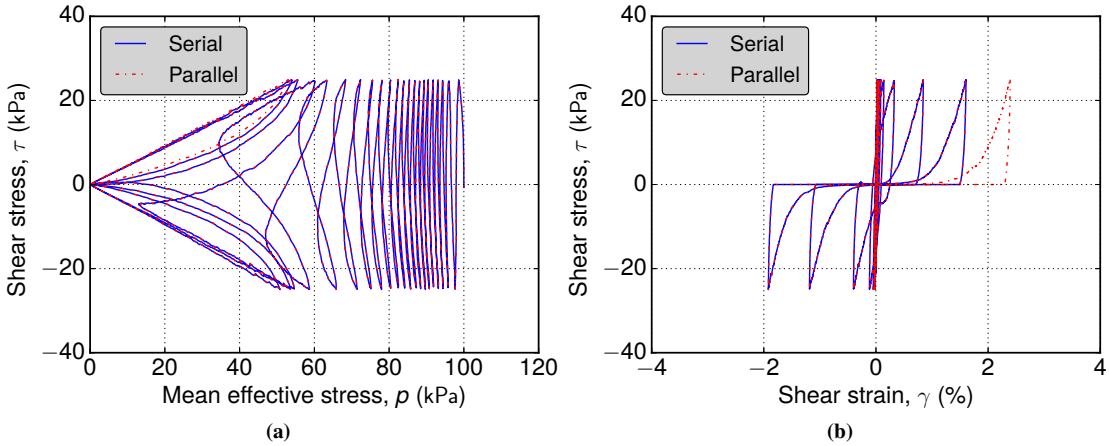

Figure 2.5: Comparisons of simulation results of constant volume cyclic simple shear test using serial and parallel GRFlow3D with respect to (a) stress path and (b) stress-strain response.

GRFlow3D. Figure 2.6 presents the performance of the updated system using two metrics. The speedup is the ratio between the execution clock time in serial and the execution time in parallel of the same example. Figure 2.6(a) indicates a speedup of three times when running the program with at least 6 threads. The speedup trend getting far away from the ideal case with further

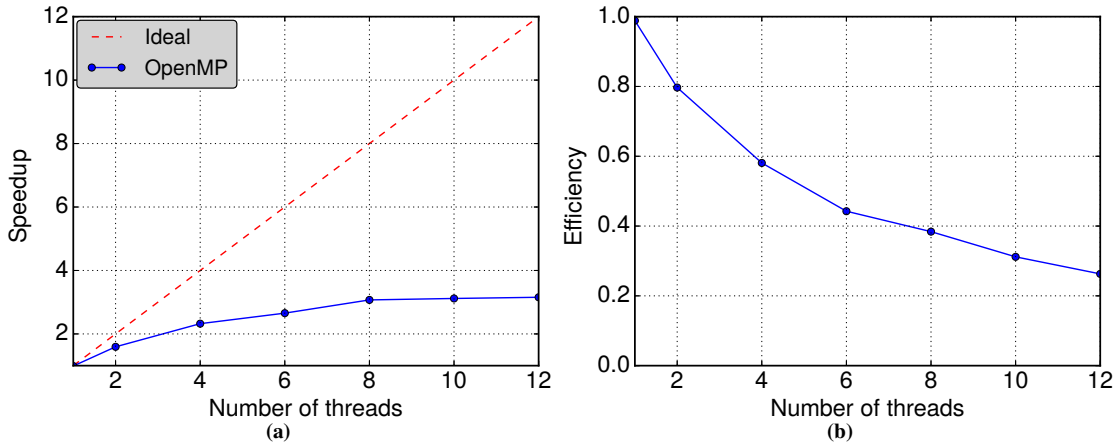

Figure 2.6: Scalability of the parallelized GRFlow3D simulation of constant volume cyclic shear test on the granular assembly of 4096 **spheres within** 50000 **steps: (a) speedup and (b) efficiency.**

increase of the thread number may be attributed to the inherent Verlet method, which compared with domain decomposition method (Amritkar et al., 2014), can't be fully parallelized. Or it may be attributed to combination of GRFlow3D and OpenMP following the fork/join model, where certain routines cost more time in the join process. Figure 2.6(b) shows that the efficiency defined by the ratio of speedup and the number of threads which gives the average utilization of each thread in the running, decreases with increasing the number of threads. It reveals that each thread

is not fully used. While one can explore other ways to improve the program such as replacing OpenMP with MPI, given the problem size in this study, it is better to stop here. At least compared with the initial version of GRFlow3D, this optimization process brings about a total speedup of around five times ($20.95/12.91 \times 3.07 \approx 4.97$).

2.3.3 Some concerns of DEM simulations

Given the well established tool GRFlow3D, this subsection focuses on exploring two basic questions related to the subsequent constant volume cyclic shearing of the granular assembly, i.e., how to prepare a sample and how to guarantee the sample is Representative Volume Element (RVE).

In this study the sample is prepared by isotropically compressing the particle assembly inside a cube. The particles are generated by following certain particle size distribution and then are placed randomly on a three-dimensional lattice. This lattice is contained in a box whose top and bottom sides are rigid walls and the four lateral sides are periodic boundaries. During the compression stage by moving six sides of the box, tangential friction coefficient μ_t is tuned to achieve a sample with certain packing density. Totally there are four steps in the compression process to approximate what happen in the laboratory experiments, which is elucidated by taking an example of constructing a medium dense sample with the target mean stress $p_0 = 100$ kPa:

(1) with $\mu_t = 0.20$, densifying the sparse sample by moving the six sides at a constant velocity until void ratio e reaches 1.0;

(2) setting velocities of particles and the six sides as zero, and using servo-control algorithm to compress the sample isotropically with the target $p = 10$ kPa where μ_t remains 0.2;

(3) increasing the target p to half of p_0, i.e., 50 kPa, and continuing compression of the sample with $\mu_t = 0.20$;

(4) modifying μ_t to 0.5 used for further compressing the sample with the target $p = p_0 = 100$ kPa and subsequent cyclic shearing.

Readers can refer to Thornton (2000) and O'Sullivan (2011) for the detail of servo-control algorithm.

Tuning tangential friction coefficient μ_t to prepare certain sample packing states is one of the common methods, which can be analogous to lubricating the contacts (Agnolin and Roux, 2007). Nevertheless, one may expect to flush the lubricant before the quasi-static shearing stage so that the sample state at the end of sample preparation is physically more reasonable, which motivates the step (4) in the assembling stage of putting μ_t as 0.5 used for cyclic shearing and increasing

confinement to the target one. Figure 2.7 shows the distributions of the normal force f_n, the tangential force $\boldsymbol{f}_t$ and the ratio of tangential to normal force for two isotropically compressed systems with the difference of putting μ_t as 0.2 or 0.5 in step (4). Figure 2.7(a) indicates these

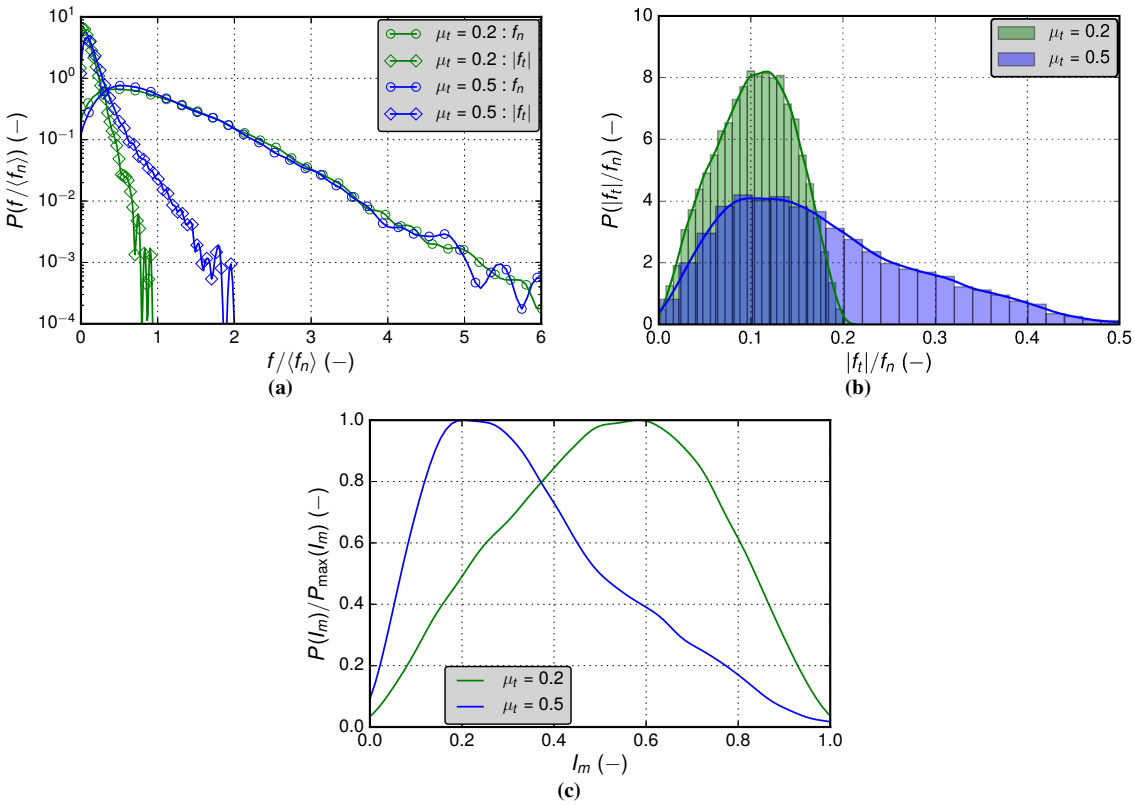

Figure 2.7: Probability distributions of (a) normal (f_n) and tangential ($|\boldsymbol{f}_t|$) forces normalized by the mean normal force $\langle f_n\rangle$, (b) $|\boldsymbol{f}_t|/f_n$, (c) the mobilized friction $I_m = |\boldsymbol{f}_t|/(\mu_t f_n)$ for two isotropically compressed systems.

two systems have very similar normal force distributions but the tangential force distributions are a bit different: the one with $\mu_t = 0.5$ has a lower proportion of small tangential forces and a higher proportion of large tangential forces due to increased μ_t. To investigate the role of friction in the system, the distributions of two similar variables $|\boldsymbol{f}_t|/f_n$ and $I_m = |\boldsymbol{f}_t|/(\mu_t f_n)$ are presented in Figures 2.7(b) and (c), respectively. The former one varies in the range of 0 and μ_t, and the latter one I_m, with the former one being normalized by μ_t, varies between 0 and 1, also named as mobilized friction index. Both can be used to describe how far a contact is from the sliding. In Figure 2.7(b), as μ_t is put as 0.5 in step (4), one can see a smooth distribution when $|\boldsymbol{f}_t|/f_n$ ranges between 0.2 and 0.5, compared with the vanishing one in the case of $\mu_t = 0.2$. This initial difference in terms of force distributions may significantly influence the corresponding cyclic response as shown in Figure 2.8 where a constant shear stress with the same CSR $= 0.25$ is applied to both samples where μ_t is set as the same 0.5. One can see that the system with $\mu_t = 0.2$

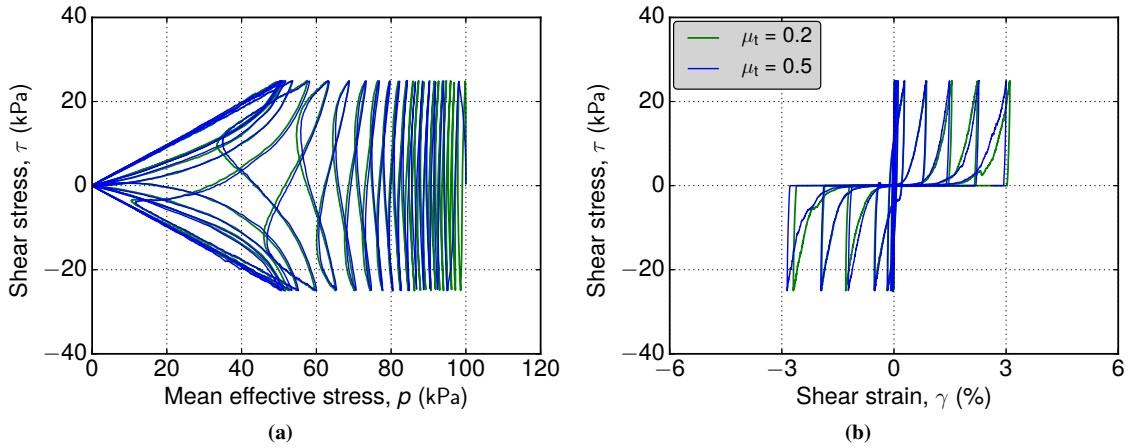

Figure 2.8: Comparisons of macroscopic response in constant volume cyclic shear tests of two samples: (a) stress path; (b) stress-strain response.

needs more loading cycles to degrade the mean effective stress, which can be attributed to the contacts at the end of sample preparation in Figure 2.7(b) taking more time to develop into the sliding regime. In addition, this influence mainly happens in the early loading stage as subsequently the stress path and stress-strain response are quite similar for both systems. Figure 2.7(c) shows the distributions of I_m for both systems and both present that most of the contacts are below the Coulomb failure condition. The latter one indicates a higher proportion of low I_m values, more similar to the one reported by Majmudar and Behringer (2005), which confirms the sample preparation procedures adopted in this study.

The concept of Representative volume element (RVE) is introduced to represent a scale that is significantly larger than the particles themselves and statistically representative of the material under consideration. To explore the proper number of particles in RVE, five types of samples with the same particle size distribution but different number of particles were prepared and cyclically sheared following the same sample preparation protocol as described above. Each type of samples consists of three packings and the results are summarized in Figure 2.9. Figure 2.9(a) indicates that larger samples tend to have a lower void ratio and higher geometrical coordination number. When these samples were cyclically sheared in the constant volume condition, the liquefaction resistance, defined by the number of loading cycles to initial liquefaction (zero mean effective stress), is not that different, as illustrated in Figure 2.9(b). One may expect to see a narrower error bar of liquefaction resistance with increasing the number of particles but Figure 2.9(b) does not present that. This is because of the obvious influence of inherent fabric on the pre-liquefaction response induced by the random placement of spheres on the lattice and the subsequent compression. Again given the fact that N_{ini} is discrete unlike e_0 and z_{g}, the fairly wide error bar of N_{ini} does not imply big oscillations. In addition to the overall quantities, Figure 2.10 compares the cyclic response of two types of samples with different number of spheres but very similar number of cycles to

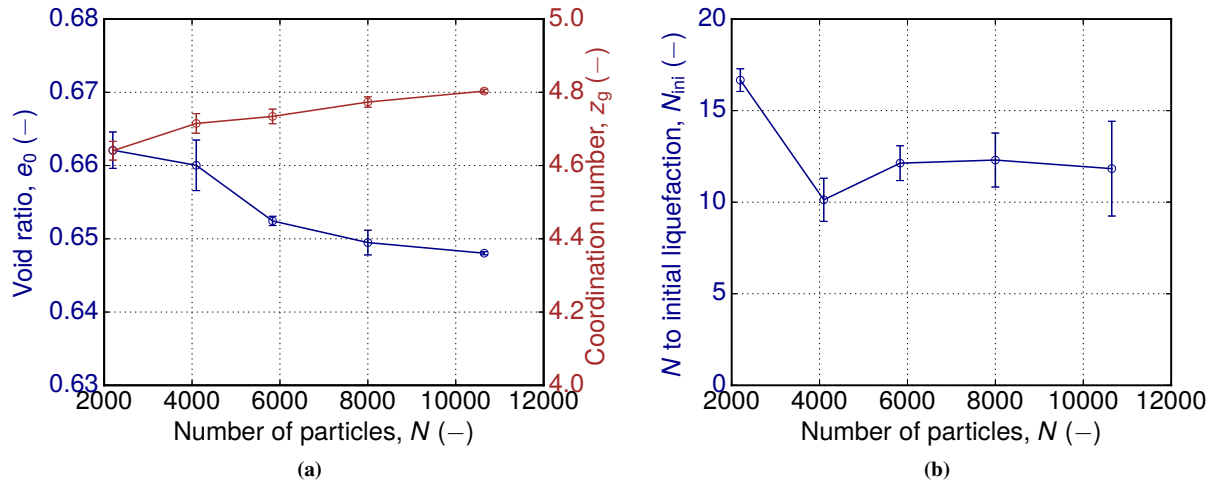

Figure 2.9: Variation in measured parameters with sample size: (a) void ratio e_0 and geometrical coordination number z_g at the end of sample preparation; (b) number of cycles N_{ini} to initial liquefaction and the corresponding geometrical coordination number z_g.

initial liquefaction. Clearly, the cyclic response is reasonably similar and at least it is difficult to

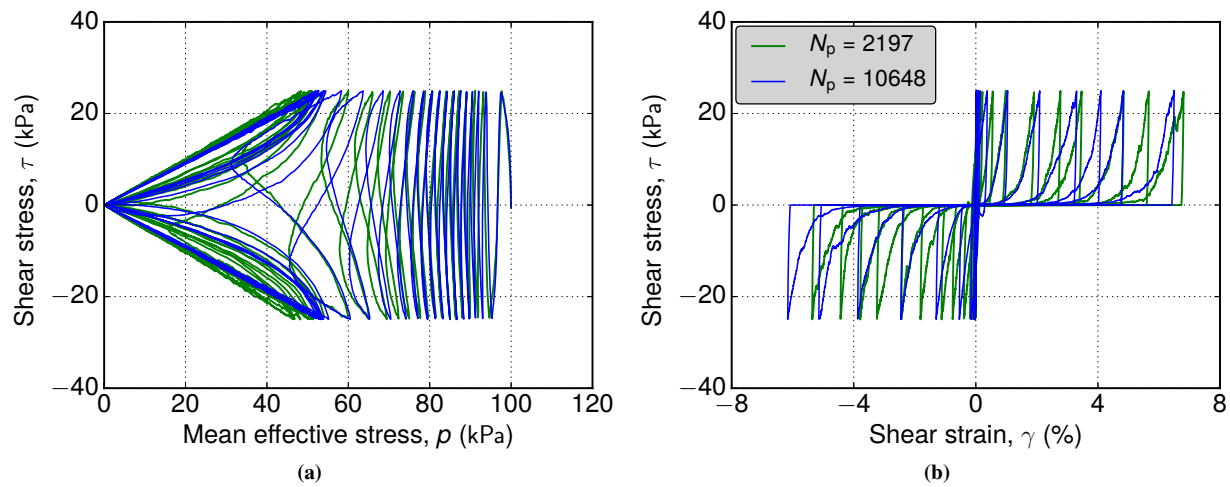

Figure 2.10: Comparisons of macroscopic response in constant volume cyclic shear tests of two samples: (a) stress path; (b) stress-strain response.

distinguish the small sample from the large one. In view of this exploration, this study focuses on the sample with 8000 particles, as shown in Chapters 3 and 4.

2.4 Constitutive driver - ConModel

This section describes the platform used for incremental integration of a constitutive model, ConModel, representing Constitutive Model. It adopts the explicit Euler scheme for solving the corresponding ordinary differential equations, simplifying the implementation of advanced

constitutive models and incorporation of new loading types. ConModel is realized by C++ Object-Oriented Programming, allowing for fast simulation of laboratory element tests. For example, it usually takes less than one minute to complete simulation of an element test. One can refer to Bardet and Choucair (1991) for details of the theory and implementation procedures on some simple constitutive models and Taiebat (2008) for the architecture of programming using MATLAB.

2.4.1 Linearized constraints

The goal of constitutive driver is to determine the unknown components of strain $\boldsymbol{\varepsilon}$ and stress $\boldsymbol{\sigma}$ from the well-established relationship between $\boldsymbol{\varepsilon}$ and $\boldsymbol{\sigma}$. Generally, this relationship is expressed by a combination of strain and stress components, referred to as mixed control (Alawaji et al., 1992), such as drained triaxial test, undrained simple shear test. Purely stress or strain controlled tests are only special cases of the general mixed control. To acquire the relationship between $\boldsymbol{\varepsilon}$ and $\boldsymbol{\sigma}$ of a laboratory element test, one can come up with five equations for the constraints and the sixth one is expressed with respect to the loading variable denoted by $\mathrm{d}X$. For example, in a triaxial test, $\mathrm{d}X$ can be referred to the axial strain increment $\mathrm{d}\varepsilon_{\mathrm{a}}$ or the axial stress increment $\mathrm{d}\sigma_{\mathrm{a}}$. However, it should be noted that these constraints are usually nonlinear equations. Linearizing these constraints is necessary to obtain the constitutive model response according to the prescribed $\mathrm{d}X$. Before that, such second-order symmetric tensors as stress and strain are represented by a vector of six components, for example, $\boldsymbol{\sigma} = [\sigma_{11}, \sigma_{22}, \sigma_{33}, \sigma_{23}, \sigma_{13}, \sigma_{12}]^{\mathsf{T}}$, where the subscripts 1, 2 and 3 refer to x, y and z, respectively. Mathematically speaking, given the loading variable $\mathrm{d}X$, one needs to determine twelve quantities of strain increment $\mathrm{d}\boldsymbol{\varepsilon}$ and stress increment $\mathrm{d}\boldsymbol{\sigma}$.

By linearizing the first five constraints from the laboratory element test, one can derive the following five relations (Bardet and Choucair, 1991):

$$\sum_{j=1}^{6} \left(S_{ij}\,\mathrm{d}\sigma_j + E_{ij}\,\mathrm{d}\varepsilon_j \right) = 0,\ i = 1, \ldots, 5 \tag{2.5}$$

The sixty coefficients S_{ij} and E_{ij} are assumed to be constant during a loading increment, although they may keep being updated from one loading increment to the next one due to describing the nonlinear constraints (Bardet and Choucair, 1991). The sixth relationship, related to the loading variable $\mathrm{d}X$ that controls the loading process, can be determined in a similar way to Equation (2.5) as follows:

$$\sum_{j=1}^{6} \left(S_{6j}\,\mathrm{d}\sigma_j + E_{6j}\,\mathrm{d}\varepsilon_j \right) = \mathrm{d}X \tag{2.6}$$

Again, the twelve coefficients S_{6j} and E_{6j} are constant during a loading increment. Equations (2.5) and (2.6) can be combined in the abbreviated notation:

$$\boldsymbol{S}\,\mathrm{d}\boldsymbol{\sigma} + \boldsymbol{E}\,\mathrm{d}\boldsymbol{\varepsilon} = \mathrm{d}\boldsymbol{Y} \tag{2.7}$$

where $\mathrm{d}\boldsymbol{Y} = [0,0,0,0,0,\mathrm{d}X]^{\intercal}$. Apparently, each laboratory element test is characterized by the choice of $\boldsymbol{S}$, $\boldsymbol{E}$ and $\mathrm{d}\boldsymbol{Y}$.

While six linear constraints can be derived from a laboratory element test in Equation (2.7), the other six equations are necessary to determine the updated stress and strain, which can resort to the constitutive relationship between $\mathrm{d}\boldsymbol{\sigma}$ and $\mathrm{d}\boldsymbol{\varepsilon}$, i.e.,

$$\mathrm{d}\boldsymbol{\sigma} = \boldsymbol{C}^{*} : \mathrm{d}\boldsymbol{\varepsilon} \tag{2.8}$$

Here the fourth-order tensor $\boldsymbol{C}^{*}$ is replaced by the six-by-six matrix; for elastic loading, $\boldsymbol{C}^{*} = \boldsymbol{C}^{\mathrm{e}}$, i.e., the elastic tangent stiffness tensor, while for elastoplastic loading, $\boldsymbol{C}^{*} = \boldsymbol{C}^{\mathrm{ep}}$, i.e., the elastoplastic tangent stiffness tensor.

By combining Equations (2.7) and (2.8), a strain-based solution technique is devised, which consists of solving $\mathrm{d}\boldsymbol{\varepsilon}$ first and updating $\mathrm{d}\boldsymbol{\sigma}$ subsequently, according to

$$\left(\boldsymbol{S}\cdot\boldsymbol{C}^{*} + \boldsymbol{E}\right)\mathrm{d}\boldsymbol{\varepsilon} = \mathrm{d}\boldsymbol{Y} \tag{2.9}$$

$$\mathrm{d}\boldsymbol{\sigma} = \boldsymbol{C}^{*}\,\mathrm{d}\boldsymbol{\varepsilon} \tag{2.10}$$

Clearly, to guarantee the solution uniqueness, the matrix $\boldsymbol{S}\cdot\boldsymbol{C}^{*} + \boldsymbol{E}$ is required to be non-singular which is generally true for proper choices of $\boldsymbol{S}$ and $\boldsymbol{E}$, despite the fact that $\boldsymbol{C}^{*}$ may be singular occasionally happening for strain softening materials.

Details of how to implement Equations (2.9) and (2.10) compatible with a constitutive model are referred to Bardet and Choucair (1991). One can also refer to Janda and Mašín (2017) for generalization to an arbitrary number of controlling and controlled variables.

2.4.2 Application to element tests

Bardet and Choucair (1991), Taiebat (2008), Janda and Mašín (2017) and Seidalinov (2018) provide configurations of a number of laboratory element tests via determination of $\boldsymbol{S}$, $\boldsymbol{E}$ and $\mathrm{d}\boldsymbol{Y}$, including drained and undrained triaxial tests, drained and undrained simple shear tests, isotropic compression test, constant mean stress test, to name a few. It is still necessary to list some other configurations related to this thesis or other challenging tests, including torsion test with rotation of principal stress direction, circular loading in principal stress space and multidirectional cyclic

shear tests.

Torsion test with rotation of principal stress direction is widely used to investigate effects of principal stress axes rotation on the model response. Bardet and Choucair (1991) described the first two phases of this test, namely, isotropic compression and drained triaxial test but the configuration for phase three, i.e., rotating principal stress axes, may induce singularity of $\boldsymbol{S}\cdot\boldsymbol{C}^{*}+\boldsymbol{E}$, where the loading variable dX is chosen as dσ_{33} (axial stress increment). A better approach is to introduce α_{σ} to describe the angle between the rotated σ_{33} and the vertical direction, initialized by zero. Basically, the five constraints of principal stress rotation test are listed as follows:

$$\sigma_{22}=\sigma_{22}^{0},\ \sigma_{12}=0,\ \sigma_{23}=0 \tag{2.11a}$$

$$\frac{1}{4}(\sigma_{33}-\sigma_{11})^{2}+\sigma_{13}^{2}=R^{2} \tag{2.11b}$$

$$\sigma_{11}+\sigma_{33}=\sigma_{11}^{0}+\sigma_{33}^{0} \tag{2.11c}$$

where the superscript 0 refers to the sample state prior to phase three and R is the radius of shear stress orbit, quantified by $(\sigma_{33}^{0}-\sigma_{11}^{0})/2$. Equation (2.11b) can be reformulated with respect to α_{σ}

$$\sigma_{33}-\sigma_{11}=2R\cos(2\alpha_{\sigma}) \tag{2.12a}$$

$$\sigma_{13}=R\sin(2\alpha_{\sigma}) \tag{2.12b}$$

Through linearization, combination and simplification, one can come up with

$$-\frac{\cos(2\alpha_{\sigma})}{4R}\mathrm{d}\sigma_{11}+\frac{\cos(2\alpha_{\sigma})}{4R}\mathrm{d}\sigma_{33}+\frac{\sin(2\alpha_{\sigma})}{2R}\mathrm{d}\sigma_{13}=0 \tag{2.13a}$$

$$\frac{\sin(2\alpha_{\sigma})}{4R}\mathrm{d}\sigma_{11}-\frac{\sin(2\alpha_{\sigma})}{4R}\mathrm{d}\sigma_{33}+\frac{\cos(2\alpha_{\sigma})}{2R}\mathrm{d}\sigma_{13}=\mathrm{d}\alpha_{\sigma} \tag{2.13b}$$

In conjunction with linearized Equations (2.11a) and (2.11c), $\boldsymbol{S}$ and $\boldsymbol{E}$ can be finalized as follows:

$$\boldsymbol{S}=\begin{bmatrix} 0 & 1 & 0 & 0 & 0 & 0 \\ 0 & 0 & 0 & 1 & 0 & 0 \\ 0 & 0 & 0 & 0 & 0 & 1 \\ -1 & 0 & 1 & 0 & 0 & 0 \\ -\frac{\cos(2\alpha_{\sigma})}{4R} & 0 & \frac{\cos(2\alpha_{\sigma})}{4R} & 0 & \frac{\sin(2\alpha_{\sigma})}{2R} & 0 \\ \frac{\sin(2\alpha_{\sigma})}{4R} & 0 & -\frac{\sin(2\alpha_{\sigma})}{4R} & 0 & \frac{\cos(2\alpha_{\sigma})}{2R} & 0 \end{bmatrix},\ \boldsymbol{E}=\boldsymbol{0},\ \mathrm{d}\boldsymbol{Y}=\begin{bmatrix} 0 \\ 0 \\ 0 \\ 0 \\ 0 \\ \mathrm{d}\alpha_{\sigma} \end{bmatrix} \tag{2.14}$$

Circular loading in principal stress space is conducted using the true triaxial device to induce a circular stress orbit in the space of principal stresses. It consists of three loading phases: phase

one is isotropic compression to increase the confinement to a certain value σ_c, phase two is drained triaxial test where σ_{33} is increased to σ_{33}^0 while keeping σ_{11} and σ_{22} equal to σ_c and phase three is to vary the three principal stresses to follow a circular path. As phase one and phase two are straightforward to realize, phase three needs extra attention about choosing the loading variable dX as the improper choice can induce singularity of $\boldsymbol{S}\cdot\boldsymbol{C}^*+\boldsymbol{E}$, appearing in Bardet and Choucair (1991). First the five constraints of drained circular loading are listed as follows:

$$(\sigma_{11}-\sigma_{22})^2+(\sigma_{22}-\sigma_{33})^2+(\sigma_{11}-\sigma_{33})^2=2(\sigma_{33}^0-\sigma_c)^2 \tag{2.15a}$$

$$\sigma_{11}+\sigma_{22}+\sigma_{33}=2\sigma_c+\sigma_{33}^0 \tag{2.15b}$$

$$\sigma_{23}=0,\ \sigma_{13}=0,\ \sigma_{12}=0 \tag{2.15c}$$

Linearizing them is pretty trivial and the key part lies in the sixth constraint, requiring the introduction of Lode angle θ given by the following equation:

$$\tan(\theta)=\frac{\sqrt{3}(\sigma_{11}-\sigma_{22})}{2\sigma_{33}-\sigma_{11}-\sigma_{22}} \tag{2.16}$$

Here $\theta=0$ refers to triaxial compression test and increasing θ implies a counterclockwise rotation. Recall that $(\sigma_{33}^0-\sigma_c)=\sqrt{3}(\sigma_{11}-\sigma_{22})/[2\sin(\theta)]=(2\sigma_{33}-\sigma_{11}-\sigma_{22})/[2\cos(\theta)]$, then one can manage to derive the standard equation related to the loading variable dθ from differentiating Equation (2.16):

$$\mathrm{d}\theta=\frac{\sin(\theta+\pi/3)}{\sigma_{33}^0-\sigma_c}\mathrm{d}\sigma_{11}+\frac{\sin(\theta-\pi/3)}{\sigma_{33}^0-\sigma_c}\mathrm{d}\sigma_{22}-\frac{\sin(\theta)}{\sigma_{33}^0-\sigma_c}\mathrm{d}\sigma_{33} \tag{2.17}$$

By linearizing Equations (2.15a), (2.15b) and (2.15c), this type of circular loading can be configured as

$$\boldsymbol{S}=\begin{bmatrix} 2\sigma_{11}-\sigma_{22}-\sigma_{33} & 2\sigma_{22}-\sigma_{33}-\sigma_{11} & 2\sigma_{33}-\sigma_{11}-\sigma_{22} & 0 & 0 & 0 \\ 1 & 1 & 1 & 0 & 0 & 0 \\ 0 & 0 & 0 & 1 & 0 & 0 \\ 0 & 0 & 0 & 0 & 1 & 0 \\ 0 & 0 & 0 & 0 & 0 & 1 \\ \frac{\sin(\theta+\pi/3)}{\sigma_{33}^0-\sigma_c} & \frac{\sin(\theta-\pi/3)}{\sigma_{33}^0-\sigma_c} & -\frac{\sin(\theta)}{\sigma_{33}^0-\sigma_c} & 0 & 0 & 0 \end{bmatrix},\ \boldsymbol{E}=\boldsymbol{0},\ \mathrm{d}\boldsymbol{Y}=\begin{bmatrix} 0 \\ 0 \\ 0 \\ 0 \\ 0 \\ \mathrm{d}\theta \end{bmatrix} \tag{2.18}$$

In undrained condition, Equation (2.15b) is replaced by $\varepsilon_{11}+\varepsilon_{22}+\varepsilon_{22}=\varepsilon_v^0$ where ε_v^0 is the volumetric strain prior to phase three.

Multidirectional cyclic shear test consists of several types depending on the applied shear stress path including 1-D linear, 2-D linear, circular/oval and figure-8. It is pretty trivial to configure 1-D linear and 2-D linear paths and needs extra attention for circular/oval and figure-8 ones. One can refer to Seidalinov (2018) for one way of configuration. Here the explicit framework is still obeyed to maintain the simplicity without introducing iterations. Basically the applied shear stress path of multidirectional cyclic shear test can be expressed by

$$\sigma_{23} = \tau_{\text{off},y} + \tau_{\text{amp},y} \sin(2\pi f_y t + \phi) \tag{2.19a}$$

$$\sigma_{13} = \tau_{\text{off},x} + \tau_{\text{amp},x} \sin(2\pi f_x t) \tag{2.19b}$$

Circular/oval path is obtained by setting $f_x = f_y$ and $\phi = \pi/2$ and one can linearize the corresponding Equation (2.19) to derive the following equations:

$$\frac{\cos(2\pi f_y t)}{\tau_{\text{amp},y}} \mathrm{d}\sigma_{23} - \frac{\sin(2\pi f_x t)}{\tau_{\text{amp},x}} \mathrm{d}\sigma_{13} = 0 \tag{2.20a}$$

$$\frac{\sin(2\pi f_y t)}{\tau_{\text{amp},y}} \mathrm{d}\sigma_{23} + \frac{\cos(2\pi f_x t)}{\tau_{\text{amp},x}} \mathrm{d}\sigma_{13} = 2\pi f_x \mathrm{d}t \tag{2.20b}$$

For figure-8 path referring to the case of $\phi = 0$ with either $f_x = 2f_y$ or $f_y = 2f_x$, for the scenario of $f_x = 2f_y$ (the other is similar), Equation (2.19) can be reformulated as

$$-\frac{4\sin(2\pi f_y t)\cos(2\pi f_x t)}{\tau_{\text{amp},y}} \mathrm{d}\sigma_{23} + \frac{\sin(2\pi f_x t)}{\tau_{\text{amp},x}} \mathrm{d}\sigma_{13} = 0 \tag{2.21a}$$

$$\frac{4\sin(2\pi f_y t)\sin(2\pi f_x t)}{\tau_{\text{amp},y}} \mathrm{d}\sigma_{23} + \frac{\cos(2\pi f_x t)}{\tau_{\text{amp},x}} \mathrm{d}\sigma_{13} = 2\pi f_x \mathrm{d}t \tag{2.21b}$$

Along with the other constraints listed as the following:

$$\varepsilon_{11} = \varepsilon_{11}^0,\ \varepsilon_{22} = \varepsilon_{22}^0,\ \varepsilon_{33} = \varepsilon_{33}^0 \tag{2.22a}$$

$$\sigma_{12} = 0 \tag{2.22b}$$

the configuration for circular/oval path of multidirectional cyclic shear test is

$$\boldsymbol{S} = \begin{bmatrix} 0 & 0 & 0 & 0 & 0 & 0 \\ 0 & 0 & 0 & 0 & 0 & 0 \\ 0 & 0 & 0 & 0 & 0 & 0 \\ 0 & 0 & 0 & 0 & 0 & 1 \\ 0 & 0 & 0 & \frac{\cos(2\pi f_y t)}{\tau_{\text{amp},y}} & -\frac{\sin(2\pi f_x t)}{\tau_{\text{amp},x}} & 0 \\ 0 & 0 & 0 & \frac{\sin(2\pi f_y t)}{\tau_{\text{amp},y}} & \frac{\cos(2\pi f_x t)}{\tau_{\text{amp},x}} & 0 \end{bmatrix}, \boldsymbol{E} = \begin{bmatrix} 1 & 0 & 0 & 0 & 0 & 0 \\ 0 & 1 & 0 & 0 & 0 & 0 \\ 0 & 0 & 1 & 0 & 0 & 0 \\ 0 & 0 & 0 & 0 & 0 & 0 \\ 0 & 0 & 0 & 0 & 0 & 0 \\ 0 & 0 & 0 & 0 & 0 & 0 \end{bmatrix} \mathrm{d}\boldsymbol{Y} = \begin{bmatrix} 0 \\ 0 \\ 0 \\ 0 \\ 0 \\ 2\pi f_x \mathrm{d}t \end{bmatrix} \tag{2.23}$$

while for figure-8 path of $f_x = 2f_y$, $\boldsymbol{S}$ needs to be changed as

$$\boldsymbol{S} = \begin{bmatrix} 0 & 0 & 0 & 0 & 0 & 0 \\ 0 & 0 & 0 & 0 & 0 & 0 \\ 0 & 0 & 0 & 0 & 0 & 0 \\ 0 & 0 & 0 & 0 & 0 & 1 \\ 0 & 0 & 0 & -\frac{4\sin(2\pi f_y t)\cos(2\pi f_x t)}{\tau_{\text{amp},y}} & \frac{\sin(2\pi f_x t)}{\tau_{\text{amp},x}} & 0 \\ 0 & 0 & 0 & \frac{4\sin(2\pi f_y t)\sin(2\pi f_x t)}{\tau_{\text{amp},y}} & \frac{\cos(2\pi f_x t)}{\tau_{\text{amp},x}} & 0 \end{bmatrix} \tag{2.24}$$

It should be noted that $\boldsymbol{S} \cdot \boldsymbol{C}^* + \boldsymbol{E}$ of figure-8 becomes singular when $\sin(2\pi f_y t) = 0$. A numerical trick to bypass it is replace t appearing in $\boldsymbol{S}$ with $t + 0.1\,\mathrm{d}t$, avoiding vanishing of $\sin(2\pi f_y t)$.

2.5 Summary

The brief literature review presented in the chapter reveals that the existing laboratory experimental work is pretty rich for understanding the macroscopic response of sands under unidirectional cyclic shearing but more research should be carried out in terms of multidirectional cyclic shear tests. There is some DEM work trying to reveal the microscopic behaviors related to sand liquefaction, but most of them were focused on cyclic triaxial tests. Extra study should be conducted with respect to cyclic simple shearing and even multidirectional cyclic shearing from both macro- and microscopic levels, which will probably shed some light on the distinct macro-mechanical response. Some existing constitutive models present promising results for sands under undrained cyclic simple shearing, but a constitutive model that can give precise predictions in both pre- and post-liquefaction periods for a series of tests with different CSRs is still rare. The author once evaluated the performance of an advanced constitutive model (Dafalias and Manzari, 2004) in simulating multidirectional cyclic shear tests while this model needs extra improvement in simulating unidirectional cyclic shear test. Applying a

constitutive model that attains noticeable success in modeling unidirectional cyclic shear test to multidirectional ones may help gain more insight into the development orientation of constitutive models.

A flowchart of the DEM program GRFlow3D is provided for illustrating its general framework, from which one can extract routines that need to be improved or optimized. The stress calculation routine was improved by properly dealing with peripheral particles. To speed up the program in running simulations, two troublesome routines including exit and getParameter were improved in the serial code and OpenMP directives were incorporated into GRFlow3D with the goal of modifying the program minimally, enabling the feature of parallel computing. The two types of optimization advanced GRFlow3D by a total speedup of five times. Then the sample preparation protocol and the required number of particles for a RVE sample were investigated, which support the final determination of 8000 spheres used for preparing a sample.

A standalone constitutive driver called ConModel was established according to the theoretical basis of Bardet and Choucair (1991), which allows fast simulation of element tests. By linearizing the six constraints extracted from the laboratory element test, plus the incremental stress-strain relationship, one can adopt explicit Euler scheme to solve these ordinary differential equations. Execution of an element test requires non-singularity of the matrix $\boldsymbol{S} \cdot \boldsymbol{C}^* + \boldsymbol{E}$, which needs careful configurations of $\boldsymbol{S}$ and $\boldsymbol{E}$. While configurations of conventional element tests can be found in Bardet and Choucair (1991), Taiebat (2008), Janda and Mašín (2017) and Seidalinov (2018), the challenging ones including *torsion test with rotation of principal stress direction*, *circular loading in principal stress space* and *multidirectional cyclic shear test* with respect to circular/oval and figure-8 paths, were clarified in detail.

Chapter 3: Evolution of Granular Materials under Isochoric Cyclic Simple Shearing

In this chapter, discrete element method (DEM) is used to carry out a list of isochoric cyclic simple shear tests, revealing signatures of the granular system approaching liquefaction state. This chapter is reproduced from the paper co-authored with Mahdi Taiebat, Patrick Mutabaruka and Farhang Radjaï, which is submitted to a journal for publication.

3.1 Introduction

The macroscopic behavior of fluid-saturated cohesionless granular materials under dynamic loading has been explored and modeled for a long time in the realm of soil mechanics in recent decades (Seed and Idriss, 1967; Castro, 1975; Been and Jefferies, 1985; Ishihara, 1993; Elgamal et al., 2003; Zhang and Wang, 2012; Radjai et al., 2017; Barrero et al., 2020; Yang et al., 2020a). For a compact assembly confined under a given pressure, the stable solid skeleton can be gradually disturbed by external excitations. In particular, at constant volume, the initial solid-like assembly may instantaneously tend towards a fluid-like state under cyclic shearing, characterized by the vanishing of mean stress, denoted as *cyclic liquefaction* in the community of soil mechanics. Motivated by macroscopic observations from laboratory experiments, continuum-based elastoplasticity models have been developed and applied to liquefaction-related applications (Taiebat et al., 2010; Wang et al., 2014; Fuentes et al., 2019; Reyes et al., 2020). In addition, investigating the mechanics of granular material deep into its microscopic structural and rheological features helps develop physics-based constitutive models (He et al., 2019; Zhang et al., 2020).

Discrete element method (DEM) has been adopted widely to explore the micro-mechanics of granular material under isochoric (at constant volume) cyclic shearing numerically. Applying DEM to carry out isochoric tests leading to liquefaction phenomenon dates back to Ng and Dobry (1994), where the capability of modeling cyclic liquefaction was verified from cyclic simple shear simulations. Later, Sitharam (2003) conducted two-dimensional (2D) DEM simulations of cyclic biaxial tests and observed the drop of coordination number when a loose sample reached

liquefaction. In a subsequent series of three-dimensional (3D) DEM simulations of cyclic triaxial tests, Soroush and Ferdowsi (2011) found the degree of structural or contact network anisotropy increased dramatically in liquefaction state, which was confirmed by Huang et al. (2018) who also observed that near liquefaction the granular system became unstable. They characterized the destabilization by means of Hill's condition of instability (Hill, 1958). Later, the study was extended to explore the evolution of mechanical stability and reversibility of the force transmission network (Huang et al., 2019b). In addition to investigating the mechanical stability, Martin et al. (2020) pointed out that the onset of liquefaction occurred with a significant increase of particle clusters. Some research work has also been devoted to the microscopic mechanisms governing shear strain development after initial liquefaction (Wang and Wei, 2016; Wang et al., 2016), and the effects of initial and loading conditions on the number of loading cycles approaching initial liquefaction (Evans and Zhang, 2019), known as *liquefaction resistance* (Kramer, 1996).

Most of the aforementioned fruitful studies focus on isochoric cyclic triaxial tests where the principal stress directions are imposed. The shear mode of a cyclic simple shear test is, however, closer to what sand experiences in the field (Zhang and Evans, 2018). For studies related to cyclic simple shearing, the exploration of microscopic features has been limited to the coordination number, and there is presently no panorama of the evolution of microstructures during the liquefaction process. It is well known that the load-bearing network disappears at the onset of liquefaction, but the details of how the initially stable system gradually disintegrates under cyclic shearing and how the fragile system reconstructs the contact network, are still worth exploring. In addition, given the partition of shear strength into fabric and force anisotropies in monotonic tests (Rothenburg and Bathurst, 1989; Radjai et al., 1998; Radjai and Roux, 2004; Radjai and Richefeu, 2009; Radjai et al., 2017; Cantor et al., 2018), it is essential to understand how these anisotropies evolve and how they correlate with other microstructural descriptors in cyclic loading leading to liquefaction.

This paper analyzes the contact and force network evolution of 3D packings composed of spherical particles when subjected to isochoric cyclic simple shearing. A number of 3D simulations with different initial and loading conditions were carried out, with a large number of time steps for adequately covering the whole process before and after the initial liquefaction. We focus on both the temporal behavior in terms of various microstructural descriptors of the packing and their statistical distributions at characteristic states during the transition to the liquefaction state. In Section 3.2, the DEM contact model, sample preparation, and simulation procedures are described. In Section 3.3, the macroscopic response is presented in terms of stress path and stress-strain loop from a representative simulation. The evolution of granular microstructure in this simulation is explored in terms of particle connectivity, force transmission, and fabric and force anisotropies

in Section 3.4. In Section 3.5, effects of the initial and loading conditions on the evolution of particle connectivity and anisotropies are investigated. Finally, we summarize the findings and sketch potential perspectives for this work.

3.2 Numerical procedure

3.2.1 Contact model

A 3D particle dynamics DEM numerical platform, named GRFlow3D (Mutabaruka, 2013), was used in this work. The granular assembly was simulated using spheres interacting via soft-particle laws. The contact interactions between spheres consist of normal collision, tangential sliding, rolling and torsion, and the key quantity is the elastic deflection between particles, $\delta_{[\,]}$, from which the corresponding force $\hat{f}_{[\,]}$ can be calculated using a linear spring-dashpot model:

$$\hat{f}_{[\,]} = -k_{[\,]}\delta_{[\,]} - c_{[\,]}\dot{\delta}_{[\,]} \tag{3.1}$$

where $k_{[\,]}$ is the spring stiffness, and $c_{[\,]}$ is the viscous dashpot coefficient. The subscript placeholders can be for n (normal contact), t (tangential sliding), r (rolling), or o (torsion). Given the radii of two particles, a_i, a_j and their positions, $\boldsymbol{r}_i$, $\boldsymbol{r}_j$, the normal contact deflection δ_n along the normal direction is the overlap between the two particles, given by

$$\delta_n = \left\|\boldsymbol{r}_i - \boldsymbol{r}_j\right\| - a_i - a_j \tag{3.2}$$

The inter-particle forces and torques exist only when $\delta_n < 0$. To exclude the non-realistic attractive force due to viscous damping at incipient separation between two particles, the normal force f_n is represented by a ramp function $R(\hat{f}_n)$ where $R(x) = x$ if $x > 0$ and $R(x) = 0$ if $x \leq 0$. The tangential force f_t is equal to $\hat{f}_t$ if $|\hat{f}_t| < \mu_t f_n$ and as $\mathrm{sgn}(\hat{f}_t)\mu_t f_n$ if $|\hat{f}_t| > \mu_t f_n$. Calculating the rolling and torsional forces (torques) is analogous to the tangential force. Unlike the normal deflection δ_n, the other three elastic deflections cannot be directly calculated, but should be cumulated by integration over time from the moment two particles come to contact, as explained in detail in Luding (2008) and Radjaï and Dubois (2011).

Once all the forces and torques on a particle are obtained, the translational and rotational accelerations can be calculated using Newton's second law of motion. These accelerations, together with the particle velocities at the beginning of each time step are then used to update the velocities and positions of all particles. We used a velocity-Verlet time-stepping scheme in our simulations.

3.2.2 Sample preparation and shearing protocols

The simulations of isochoric simple shearing involve two steps: preparing particle assemblies via isotropic compression condition, and applying cyclic simple shear mode to these assemblies under isochoric condition.

The constructed samples consist of spheres with low polydispersity, i.e. $d_{\max}/d_{\min} = 2$ where $d_{\min} = 1.0$ mm and $d_{\max}$ refer to the minimum and maximum particle diameters, respectively. Between $d_{\min}$ and $d_{\max}$, the particle size follows a uniform distribution of particle volumes, so that the number of particles belonging to a class of diameter d is proportional to d^{-3}. One can refer to Voivret et al. (2007) and Mutabaruka et al. (2019) for details of generating the particle size distribution. Once the particles are generated, they are placed randomly on a 3D sparse lattice to avoid the overlap. This 3D lattice is contained in a rectangular cell whose top and bottom sides are rigid walls, and the four lateral sides are periodic boundaries. This setting is denoted as a bi-periodic simulation cell.

The samples are compressed isotropically by moving the six sides of the cell. During the compression process, the gravity is set to zero. The six sides of the cell follow a translational move. The tangential friction coefficient μ_t is tuned to achieve a given value of void ratio e, defined as the ratio of the total pore volume to the solid volume. One has $e = 1/\Phi + 1$, where Φ is the packing fraction. Many of the laboratory procedures for sample preparation at different densities can not be precisely simulated; therefore, we adopted a simple computational procedure, modified from Kuhn et al. (2014) and Thornton (2015), to prepare samples comparable with the laboratory ones. The procedure consists of four substeps, which we describe here by taking the case of constructing a medium dense sample with the target mean stress $p_0 = 100$ kPa: (1) with $\mu_t = 0.20$, densifying the sparse sample by moving the six sides at a constant velocity until the void ratio e reaches 1.0; (2) setting velocities of particles and the six sides to zero, and using a servo-control algorithm to compress the sample isotropically with the target $p = 10$ kPa where μ_t remains 0.2; (3) increasing the target p to half of p_0, i.e. 50 kPa, and continuing compression of the sample with $\mu_t = 0.20$; (4) modifying μ_t to 0.5 used for further compressing the sample with the target $p = p_0 = 100$ kPa and subsequent cyclic shearing. Readers can refer to Thornton (2000) and O'Sullivan (2011) for the detail of servo-control algorithm. The first three substeps generate an initially dense packing via controlling the tangential friction coefficient and increasing the confinement. The last step is necessary to obtain a smooth distribution of $f_t/(\mu_t f_n)$ between 0 and 1, as usually a different value of μ_t is used in the step of cyclic shearing. We conducted other simulations on samples with different numbers of spheres ranging between 2197 and 10648. We did not see much difference in the macroscopic response under isochoric cyclic shearing. Hence, samples with 8000 spheres were used in this study, falling into a similar range presented in Kuhn et al. (2014) and Martin et al. (2020). Figure 3.1(a) displays one of the samples prepared by the above procedure.

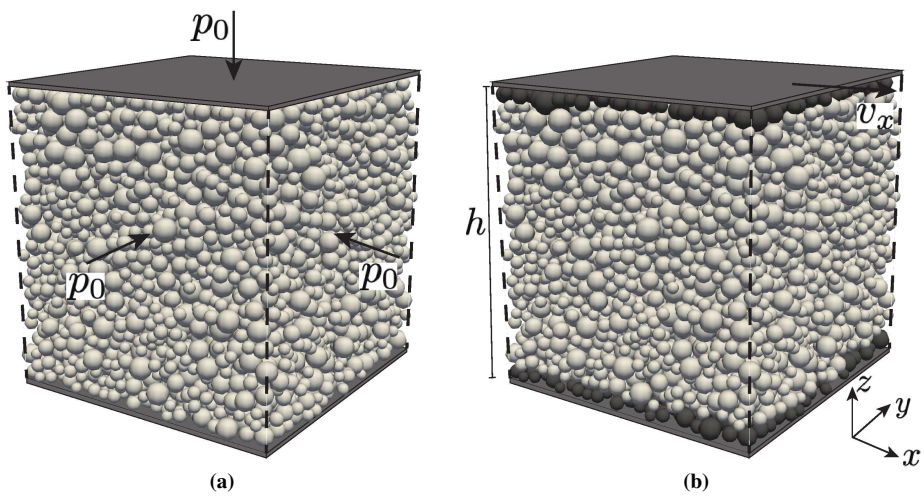

Figure 3.1: Illustration of particle arrangements and boundary conditions for a sample composed of 8000 **particles: (a) at the end of sample preparation; (b) during constant height cyclic shearing. The gray particles are glued to the top and bottom walls of the simulation cell.**

In the step of isochoric cyclic simple shearing, the sample volume is maintained by fixing four lateral sides and the bottom wall and keeping the sample height constant. Cyclic simple shearing is undertaken by moving the top wall horizontally at a constant velocity v_x. To reduce possible slippage between the walls and the sample, one layer of particles is glued to the top and bottom walls, respectively, as indicated by gray spheres in Figure 3.1(b). The shear direction is reversed each time the shear stress τ extracted from the calculated stress tensor, as explained below, reaches a target amplitude τ^{amp}. This corresponds to the so called "uniform amplitude cyclic simple shear test" (Kuhn et al., 2014). In soil mechanics, a dimensionless quantity named *cyclic stress ratio* (CSR) is used to quantify the cyclic shearing intensity, defined by the ratio

$$\text{CSR} = \frac{\tau^{\text{amp}}}{p_0}, \tag{3.3}$$

where p_0 is the initial mean stress. Table 3.1 summarizes the simulated isochoric cyclic simple shear tests. T1, T2, and T3 are configured by varying the initial void ratio e of samples, T2, T4, and T5 are different in the initial mean stress p_0, while T2, T6, and T7 are conducted for different values of CSR. In this study, we did not consider simulations of samples with a void ratio below 0.629 or above 0.670 because very dense systems get jammed under shearing at constant volume, and very loose samples can easily become fluid-like even without the shear stress reaching the targeted value of CSR.

To maintain a quasistatic shear regime, we consider the inertial number $I = \dot{\gamma} d \sqrt{\rho / p}$, where $\dot{\gamma} = |v_x|/h$ is the shear strain rate with h the sample height, ρ the density of particles, and d the mean particle diameter. The shear is nearly quasistatic if $I \ll 1$ (MiDi, 2004), and typically the

Table 3.1: Simulated cyclic simple shear tests

ID	$e(-)$	p_0 (kPa)	CSR $(-)$
T1	0.629	100	0.25
T2	0.647	100	0.25
T3	0.670	100	0.25
T4	0.647	200	0.25
T5	0.647	600	0.25
T6	0.647	100	0.20
T7	0.647	100	0.30

threshold is chosen as 1×10^{-3}, which can be strictly obeyed before p drops to almost zero. The deformation process can not be quasistatic in this limit of vanishing p even by decreasing v_x since the granular material undergoes a phase transition from a solid-like to a liquid-like state. The sensitivity analysis on the moving rate of top wall indicates that $v_x = 0.01$ m/s or shear strain rate $\dot{\gamma} \approx 0.38$ s^{-1} is a good option, consistent with Martin et al. (2020), which guarantees $I < 0.001$ before p gets too small.

The simulation parameters are given in Table 4.1. One can introduce the stiffness number κ such that the average normal deflection δ_n satisfies $\delta_n/d \propto \kappa^{-1}$ (Radjaï and Dubois, 2011). For the linear contact law in the normal direction, $\kappa = k_n/(pd)$. In this study k_n is chosen as 10^6 N/m to guarantee $\delta_n \sim 10^{-3}d$ in each contact, i.e., the particles can be considered as nearly undeformable (Mutabaruka et al., 2019). Then, c_n is determined to attain a value of 0.15 for the normal coefficient of restitution based on Schwager and Pöschel (2007). $\mu_t = 0.5$ is a common value of the friction coefficient (Guo and Zhao, 2013; Huang et al., 2018; Jiang et al., 2019). The values for other microscopic material parameters can be obtained from their relations to k_n, c_n or μ_t suggested by Luding (2008) and listed in Table 4.1. The rolling and torsion stiffnesses and friction coefficients were set to a small nonzero value in order to make rotations slightly dissipative as a simple way to account for the effects due to aspherical particle shape (Radjaï and Dubois, 2011).

3.3 Macroscopic response

At the sample scale, stresses and strains in the cyclic shearing phase are analyzed to monitor pore pressure generation and shear strain development. The stress tensor $\boldsymbol{\sigma}$ of the granular assembly can be expressed as a function of the microscopic interactions between particles over a selected

Table 3.2: DEM parameters

Description	Value
Density, ρ	$2650\ \mathrm{kg/m^3}$
Normal stiffness, k_n	$10^6\ \mathrm{N/m}$
Normal viscosity, c_n	$1.15\ \mathrm{kg/s}$
Tangential stiffness, k_t	$0.8k_n$
Tangential viscosity, c_t	$0.2c_n$
Tangential friction coefficient, μ_t	0.5^1
Rolling stiffness, k_r	$0.1k_n$
Rolling viscosity, c_r	$0.05c_n$
Rolling friction coefficient, μ_r	0.1
Torsion stiffness, k_o	$0.1k_n$
Torsion viscosity, c_o	$0.05c_n$
Torsion friction coefficient, μ_o	0.1

volume V:

$$\boldsymbol{\sigma} = \frac{1}{V} \sum_{c \in N_c} \boldsymbol{l}^c \otimes \boldsymbol{f}^c \tag{3.4}$$

where $\boldsymbol{l}^c$ is the branch vector connecting the centers of two particles for interior contact or connecting the particle center and the contact point for exterior contacts, $\boldsymbol{f}^c$ is the contact force, $\otimes$ denotes the dyadic tensor product, and the summation runs over all the contacts N_c in the selected volume V. The superscript c in $\boldsymbol{l}^c$ and $\boldsymbol{f}^c$ will be dropped in the sequel for simplicity. In simple shear test, the shear stress τ and mean stress p can be obtained from stress tensor, i.e. $\tau = \tau_{zx}$ and $p = (\sigma_{xx} + \sigma_{yy} + \sigma_{zz})/3$. The constant volume condition in cyclic shearing mimics the deformation of a porous solid matrix filled with an incompressible pore fluid without the drainage of the latter, i.e. a "truly undrained test". Both laboratory experiments and DEM studies have confirmed similarity in the results of these two systems (Dyvik et al., 1987; Bonilla, 2004). In constant volume shearing, the variation of the average pressure in the the solid skeleton pores is compensated by the *excess pore pressure* deduced as

$$\Delta u = p_0 - p. \tag{3.5}$$

It is common to use the dimensionless pore pressure ratio defined by

$$r_u = \frac{\Delta u}{p_0} = 1 - \frac{p}{p_0}. \tag{3.6}$$

Vanishing pressure p corresponds to $r_u = 1$, where the whole mean stress is supported by the suspending fluid. The cumulative shear strain γ is defined by

$$\gamma = \frac{x_w}{h}, \tag{3.7}$$

where x_w is the cumulative horizontal displacement of the top wall:

$$x_w(t) = \int_0^t v_x \, \mathrm{d}t \tag{3.8}$$

Note that the shear rate $\dot{\gamma}$ is constant and changes its sign only when the shear stress τ reaches the target amplitude τ^{amp}. For this reason, the time interval $T/2$ between two successive shear reversals varies in different cycles of shearing. Let $T(N)$ be the period of cycle N and t_N its initial time. Since the shear rate is constant, we define a "fractional cycle number" by interpolation between two successive cycles:

$$N' = N + \frac{t - t_N}{T(N)}, \tag{3.9}$$

where t is the current time. The value of N' coincides with N at $t = t_N$, and increases by one unit at $t = t_N + T$. To avoid confusion, we continue below to use N but in the sense of fractional cycles as defined by N'.

Figure 3.2 presents the typical macroscopic behavior for simulation T2 in Table 3.1, described in terms of stress path and stress-strain curve, as well as the pore pressure ratio evolution and shear strain development as functions of the number of cycles. The simulation starts from $\tau = 0$, $p = 100$ kPa and $\gamma = 0$, corresponding to point A_0 of Figure 3.2(a) and the origin of the coordinate system in Figure 3.2(b). As cyclic shearing continues, the stress path of (p, τ) oscillates up and down and moves leftwards as shown in Figure 3.2(a), indicating a decreasing p (increasing r_u) that is result of the contraction tendency of the system. The first time r_u in Figure 3.2(c) reaches 0.99 is termed *initial liquefaction*, and its corresponding number of cycles is denoted as N_{IL} shown in Figure 3.2. Thus, the cyclic shearing process is divided into two periods, before and after initial liquefaction, namely pre- and post-liquefaction periods, as colored in gray and red in Figure 3.2, respectively. In the pre-liquefaction period, the development of shear strain is negligibly small, as shown in Figure 3.2(b) and (d). In the post-liquefaction period, the stress path gets trapped and oscillates along with a butterfly shape and a transient vanishing of the mean stress. Shear strain develops significantly, especially when shear stress approaches zero and r_u gets very close to 1, and its amplitude increases cycle by cycle as shown in Figure 3.2(d). The deduced pore pressures throughout each loading cycle show a repetition of the behavior. Hereafter, we assume that the system gets into liquefaction state when r_u exceeds 0.99 and it exits liquefaction state when r_u drops below 0.99.

Three loading cycles, including cycle A and cycle B in the pre-liquefaction period, and cycle C in the post-liquefaction period, are also highlighted in Figure 3.2. These cycles are selected to zoom into the detailed evolution of microstructures that will be explored below. In each cycle, at least four characteristic states are pointed out, where subscript 0 refers to the first time $\tau \geq 0$ distinguishing loading from unloading, 1 refers to τ reaching τ^{amp}, 2 refers to the first time $\tau < 0$ when sample is sheared reversely, and 3 refers to τ reaching $-\tau^{\text{amp}}$. In cycle C, two more states are selected, i.e., $C_{0'}$ and $C_{2'}$, referring to the exit from the liquefaction state. In the post-liquefaction cycle, indistinctive oscillations of τ around 0 may confuse loading and unloading. Near C_0 or C_2, one can search for the state with the highest number of particles without contacts (i.e. floaters), which can be used to further distinguish C_0 or C_2.

Figure 3.3 presents several snapshots of normal contact force chains at different states of simulation T2 given in Figure 3.2. The forces are represented by bars along the branch vectors joining particle centers, and their thickness is proportional to the intensity of the normal contact

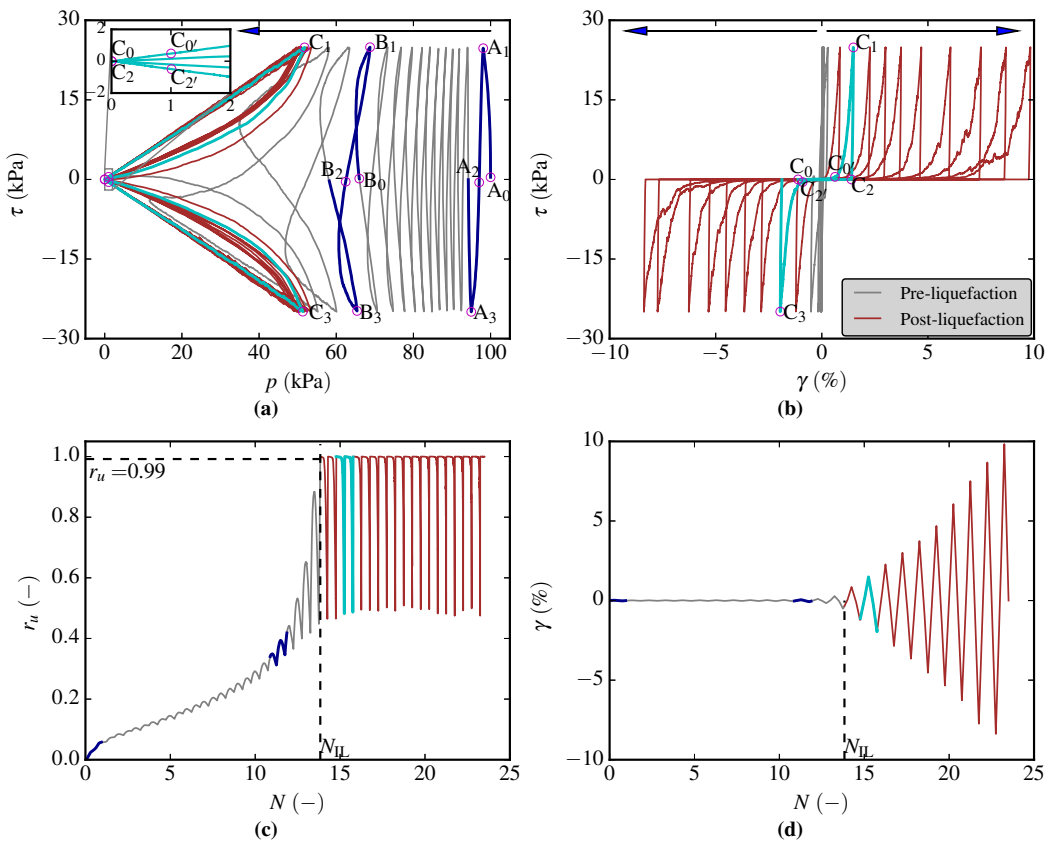

Figure 3.2: Macroscopic response of isochoric cyclic simple shear test T2 in Table 3.1: (a) stress path; (b) stress-strain curve; (c) pore pressure evolution; (d) shear strain development.

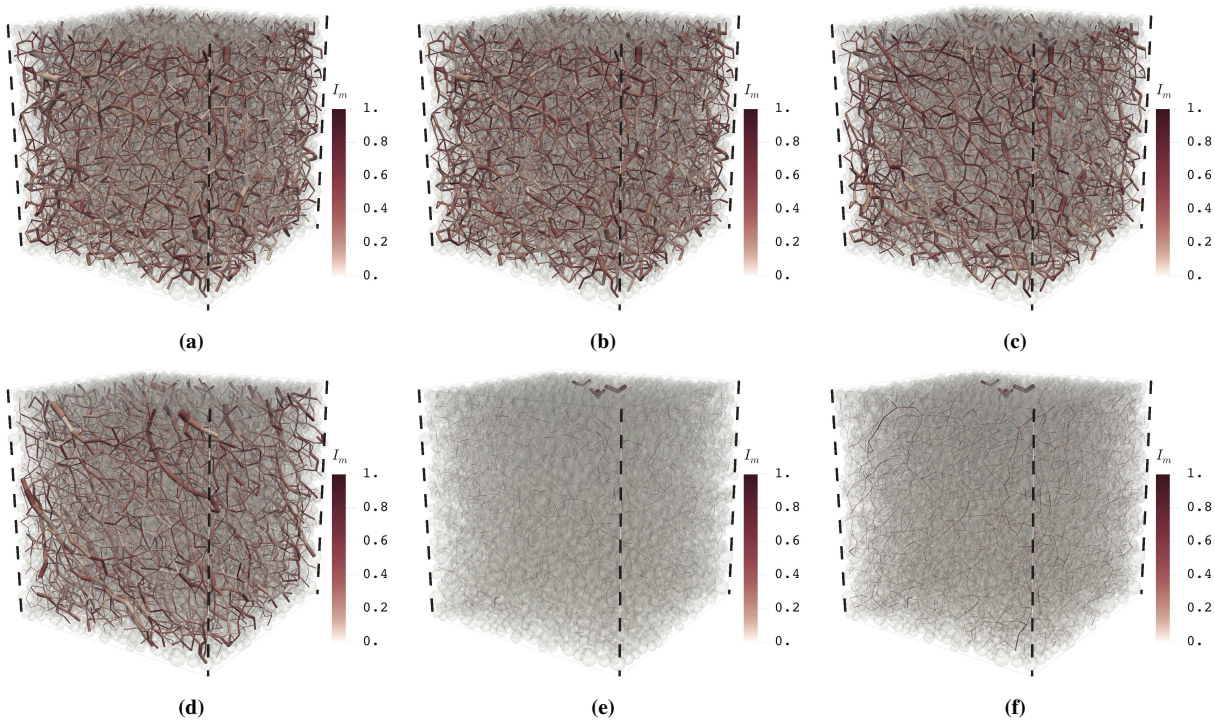

Figure 3.3: Snapshot of normal forces in the sheared sample for characteristic state: (a) A_0; (b) A_1; (c) B_1; (d) C_1; (e) C_2; (f) $C_{2'}$. Line thickness is proportional to the normal force at each contact. Color code represents the mobilized friction index I_m (see text) in the range between 0 and 1. The same camera view as Figure 3.1 is used here.

force. The same figure also shows the friction mobilization index I_m at each contact defined by

$$I_m = \frac{|f_t|}{\mu_t f_n}. \tag{3.10}$$

It varies between 0 and 1 and is displayed in color code. The value $I_m = 1$ implies sliding or fully mobilized friction. Visual inspection reveals several features. First, the initially isotropic force network (A_0) becomes slightly anisotropic at shear stress reaching its maximum amplitude (A_1) and even more anisotropic along loading cycles (B_1 and C_1). Well-connected strong force chains tend to span the system along the direction of the first principal stress (i.e., compressive direction). Then, upon unloading to liquefaction state (C_2), large force transmission networks are replaced by fragile scattered small force chains (Huang et al., 2019a; Martin et al., 2020), where normal contact forces drop to much smaller values, and the friction is prone to be mobilized at a large number of contacts, corresponding to an unjammed state (Bi et al., 2011; Huang et al., 2019a). Whether the current system is isotropic cannot be inferred from Figure 4.13(e). While the sample evolves in liquefaction state until the exit ($C_{2'}$), large deformation accumulates and the collapsed force transmission network is rebuilt. In Figure 4.13(f), one can notice the network

nearly percolates along the diagonal from bottom left corner to top right corner (contrary to C_1) in the xz shear plane (see Figure 3.1(b)) although the intensity of normal forces is still small.

3.4 Granular microstructure

In this section, we investigate the evolution of the granular microstructure for the simulation T2 in Table 3.1 in terms of particle connectivity, force transmission, and fabric and force anisotropies.

3.4.1 Particle connectivity

The lowest-order scalar quantity describing the contact network is the coordination number z_{g}, defined the average number of contacts per particle (Radjai et al., 2004). The coordination number can also approximate the level of static redundancy in the system, i.e., the difference between the total number of constraints and the total number of degrees of freedom. Each contact provides six constraints in an ideal system with infinite tangential, rolling, and torsion friction coefficients. Given six degrees of freedom (dynamic variables) per particle, the critical coordination number, defining the isostatic state with equal numbers of degrees of freedom and constraints, is $z_{\mathrm{iso}} = 2$. This is an extreme value for our system. It will increase if the rolling and twisting interactions are removed. In general, positive and large values of static redundancy $z_{\mathrm{g}} - z_{\mathrm{iso}}$ reflect a stable quasistatic behavior, whereas negative values mean unstable and dynamic states. In all cases, there is always a subset of particles with no contacts (floaters) and a subset of contacts bearing no force. Hence, for the definition of the coordination number we consider only the non-floaters and force-bearing contacts:

$$z_{\mathrm{g}} = \frac{2N_{\mathrm{c}}}{N_p - N_p^0}, \tag{3.11}$$

where N_p is the total number of particles, N_p^0 is the number of floaters, and N_{c} is the number of force-bearing contacts.

Figure 3.4(a) displays the evolution of z_{g} with the number of cycles N, where the time histories are colored according to the value of r_u. The initial liquefaction (IL) corresponding to $r_u = 0.99$ is marked by a black circle. We see that z_{g} decreases from its initial value $z_{\mathrm{g}} \simeq 4.76$ with small oscillations in pre-liquefaction period and drops below 4.0 while the system tends to its initial liquefaction state. In the post-liquefaction period, z_{g} stays below 4.0 and fluctuates significantly down to values as low as 1.5 with a negative static redundancy, implying there are not enough constraints to hold the system stable. The observed oscillations suggest that z_{g} can be used to approximately distinguish the pre- from post-liquefaction periods. One can also notice that z_{g}

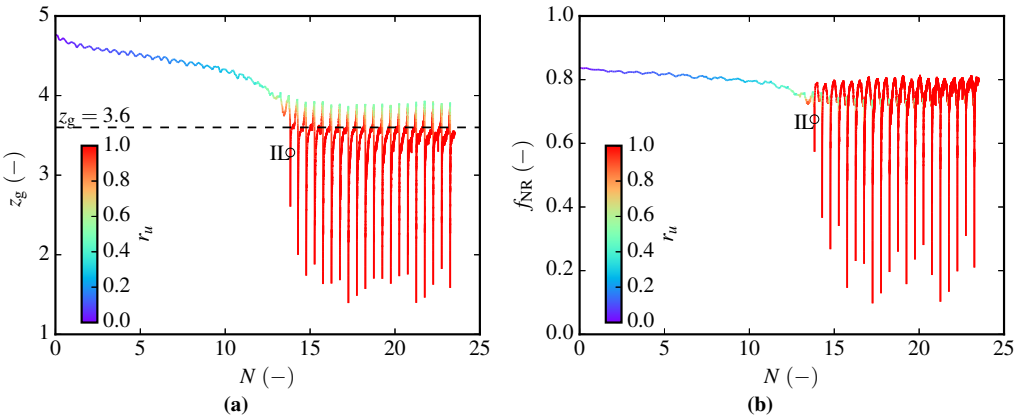

Figure 3.4: Evolution of (a) coordination number z_g and (b) non-rattler fraction f_{NR} for simulation T2.

increases with a decreased r_u (or an increased p), implying a monotonic relationship between z_g and p (Shundyak et al., 2007; Huang et al., 2019b). The horizontal dashed line for $z_g = 3.6$ corresponds to the inflection point of z_g as a function of N, above which z_g and p increase rapidly. This value of z_g may be considered as the percolation threshold of the particles allowing for force transmission across the system through the contact network.

Another statistical descriptor complementing the coordination number is *non-rattler fraction* defined by Bi et al. (2011)

$$f_{NR} = \frac{N_p - N_p^0 - N_p^1}{N_p}, \tag{3.12}$$

which represents the proportion of particles with at least two contacts, i.e., excluding particles with zero contact (N_p^0) or one contact (N_p^1). Figure 3.4(b) shows the evolution of f_{NR}. According to this figure, around 15% of these particles at the initial state do not contribute to the sample's contact network; this should be because of the granular assembly's polydispersity. During the pre-liquefaction period, f_{NR} declines and drops to 70% at initial liquefaction. In the post-liquefaction period, f_{NR} oscillates significantly and drops below 40% transiently when r_u approaches 1.0. It should be noted that the local maxima of f_{NR} are not attained when r_u drops to the local minima, implying that f_{NR} and p do not follow a monotonic relationship.

Figure 3.5 displays detailed evolution of z_g and f_{NR} in cycles A, B and C as previously shown in Figure 3.2. It is remarkable that in cycle A z_g and f_{NR} do not follow the trend of r_u whereas in cycle B they follow the variations of r_u. Then in cycle C of the post-liquefaction period, the variations of z_g and f_{NR} are inversely related to r_u except in the liquefaction state ($r_u \geq 0.99$); z_g achieves its local maximum when $\tau = \pm\tau^{amp}$ while the peak of f_{NR} occurs in the liquefaction state. The horizontal dashed line in the subplot of z_g and N shows that the value $z_g = 3.6$ prompts the packing to exit from the liquefaction state.

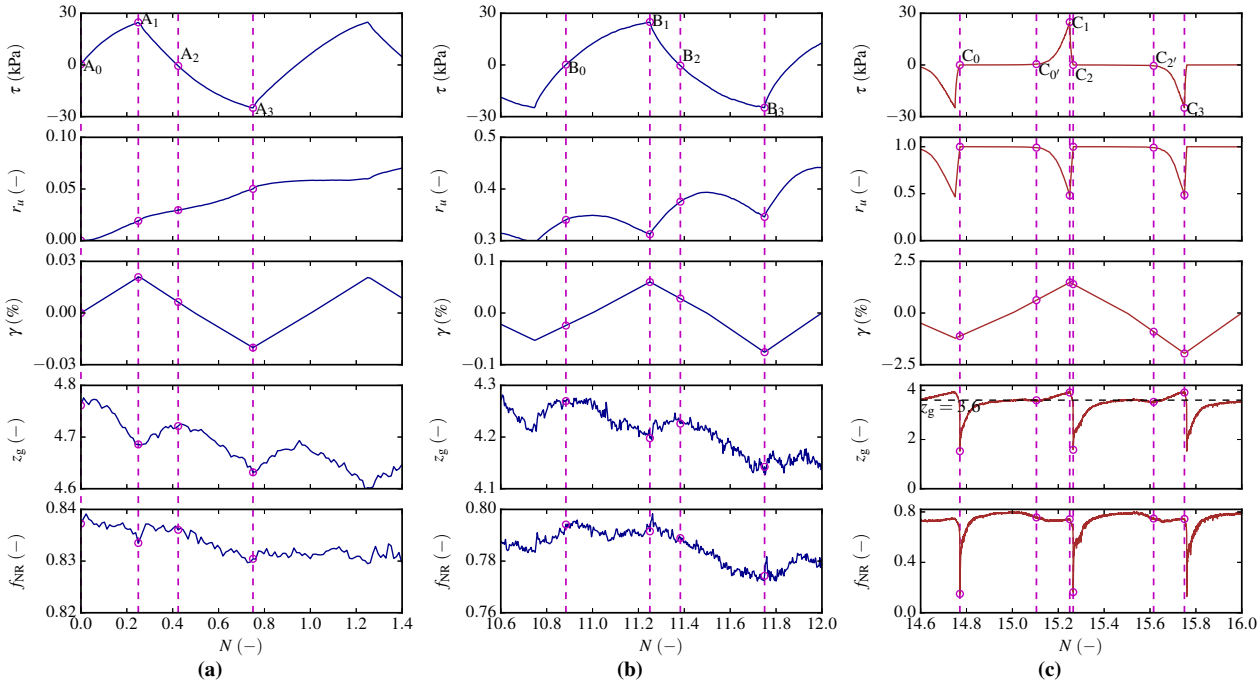

Figure 3.5: Detailed evolutions of z_g and f_{NR} for simulation T2 during three selected cycles:(a) cycle A; (b) cycle B; (c) cycle C.

To understand the relationship between p and z_g, let us consider the following relation derived from Eq. (3.4):

$$p \propto z_g \frac{N_p - N_p^0}{N_p} \langle \boldsymbol{l} \cdot \boldsymbol{f} \rangle = z_g \frac{N_p - N_p^0}{N_p} \langle l f_n \rangle \tag{3.13}$$

where $\langle \boldsymbol{l} \cdot \boldsymbol{f} \rangle$ refers to the average over all contacts. For the spherical particles used in this study, $\boldsymbol{l} = l\boldsymbol{n}$ with l being branch vector length, and thus $\boldsymbol{l} \cdot \boldsymbol{f} = l f_n$ with f_n being the contact normal force. In the pre-liquefaction cycle, the non-floater fraction $(N_p - N_p^0)/N_p$ can be regarded as constant given Figure 3.6(a) and (b) such that the variation of r_u (or p) is controlled by z_g and $\langle l f_n \rangle$. Hence, the initial out-sync between r_u and z_g is compensated by $\langle l f_n \rangle$, which can be easily affected by cyclic shearing. This compensation becomes less and less significant as the system approaches the initial liquefaction. In post-liquefaction period, f_n becomes negligible when the system falls into a liquefaction state, which explains why the significant changes of z_g do not affect p noticeably. Outside the liquefaction state, z_g increases mildly, and the increase of p should be mainly attributed to the evolution of $\langle l f_n \rangle$.

The connectivity of particles P_c is defined as the proportion of particles with exactly c contacts. Its distribution at the characteristic states of the three selected cycles shown in Figure 3.6 provides more detailed information about the microscopic state of the granular material than z_g and f_{NR}.

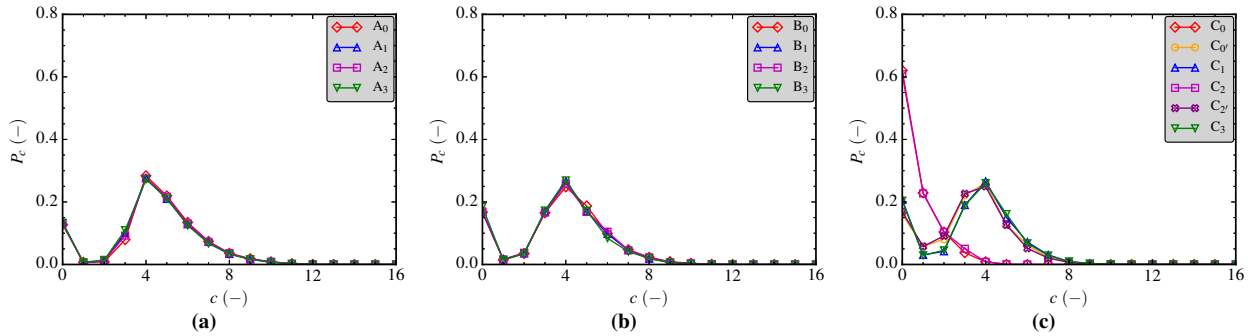

Figure 3.6: Connectivity diagram expressing the fractions P_c of particles with exactly c contacts for simulation T2 at the characteristic states of: (a) cycle A; (b) cycle B; (c) cycle C.

P_0 represents the proportion of floating particles. In the pre-liquefaction cycles, the distribution $\{P_c\}$ is nearly unchanged during shear cycle with very small values of P_1 and P_2, a peak at $c = 4$, and long tail for $c > 4$. In cycle C of post-liquefaction period, the states C_0 and C_2 exhibit a high proportion of particles with $c < 4$, implying a fragile contact network. This fragile network disappears only when the system exits the liquefaction state as shown by $\{P_c\}$ at $C_{0'}$ and $C_{2'}$. Given large shear strain development between C_0 and $C_{0'}$ or C_2 and $C_{2'}$, one can infer that sample deformation rebuilds the fragile network resulting from unloading (compare C_1 and C_2) although p does not increase markedly. The system stays stable at C_1 or C_3 while C_0 or C_2 represents the state with the weakest contact network in the post-liquefaction cycle.

To get insight into the temporal evolution of P_c, we plot in Figure 3.7 P_c for $c = 0, 1 \ldots 9$ at $\tau = \tau^{\text{amp}}$ and $\tau \simeq 0$ (transitioning from unloading to loading) as a function of the number of cycles N. $\tau \simeq 0$ refers to C_2 in post-liquefaction period. At $\tau = \tau^{\text{amp}}$, we observe that the proportion of floaters (P_0) takes the place of P_5 to become the second most dominant after a few cycles while P_4 does not change noticeably. At $\tau \simeq 0$, near initial liquefaction ($N \simeq 14$), a significant change occurs in the connectivity diagram: the system tends to have more proportions of particles with contacts fewer than 3. In the post-liquefaction period, the values of P_0, P_1 and P_2 increase first, implying that the system gets weaker and explaining the increasing shear strain amplitude, and then tends to a steady state. Furthermore, in the post-liquefaction period, the distribution $\{P_c\}$ is continuous between floaters (P_0) and the non-floaters, and the peak at $c = 4$ has disappeared. This means that $\{P_c\}$ does not anymore reflect a balanced contact network but a dynamic one in which dynamic events such as binary collisions (P_1) and unstable chains (P_2) of particles occur frequently.

3.4.2 Force transmission and friction mobilization

The force network of a granular system is defined by the spatial distribution of contact forces $\boldsymbol{f}$. A local coordinate system $(\boldsymbol{n}, \boldsymbol{t})$ is attached to each contact point, where $\boldsymbol{n}$ is the unit vector

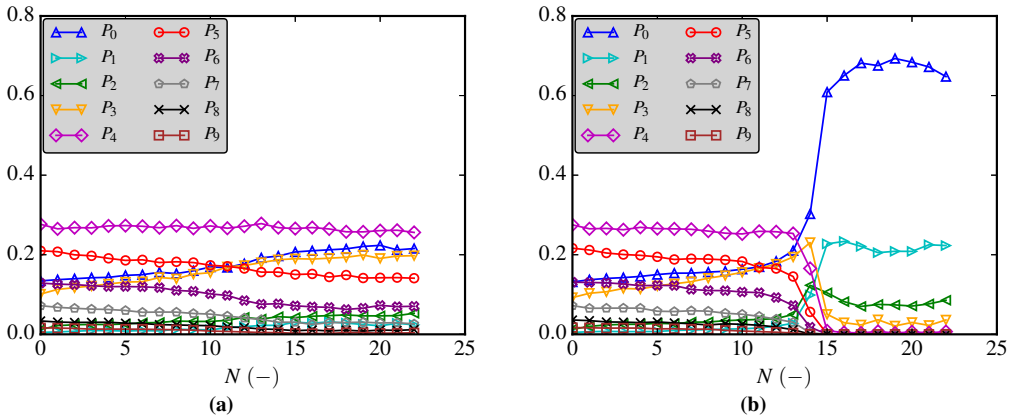

Figure 3.7: Evolution of proportion P_c of particles with c contacts at characteristic states of (a) $\tau = \tau^{\text{amp}}$ and (b) $\tau \simeq 0$ transitioning from unloading to loading (or C_2 in post-liquefaction period) for simulation T2.

perpendicular to the contact plane and $\boldsymbol{t}$ is an orthonormal unit vector in the contact plane oriented along the tangential contact force. Thus, we have $\boldsymbol{f} = f_n\boldsymbol{n} + f_t\boldsymbol{t}$, with f_n and f_t representing the magnitudes of normal and tangental contact forces, respectively. The inhomogeneity of contact forces in granular media can be characterized by the probability density function (PDF) of normal contact forces P_n (Radjaï et al., 1996; Majmudar and Behringer, 2005) presenting two major features: (1) the PDF is roughly a decreasing exponential function for forces above the mean, and (2) in the range of weak forces below the mean the PDF does not decline to zero with force. These two features have been observed in confined packings (Radjaï et al., 1996; Radjai, 2015) or sheared granular media reaching steady flow regime (Azéma et al., 2007; Richefeu et al., 2009; Cantor et al., 2018) where the system preserves a statistically stable force distribution. For the granular assembly under isochoric cyclic shearing, the network goes through collapsing and rebuilding stages, and variations of P_n are expected.

Figure 3.8 displays the PDF of normal contact forces in log-linear and log-log scales at the characteristic states depicted in Figure 3.2. In the pre-liquefaction cycles, the forces are normalized by the mean normal contact force $\langle f_n \rangle$ at each state given the tiny variations of $\langle f_n \rangle$ in a cycle. In the post-liquefaction cycles, $\langle f_n \rangle$ changes significantly. For example, $\langle f_n \rangle \simeq 0.16$ N at C_1 and 0.03 N at $C_{2'}$, as shown by the vertical dashed lines in Figures 3.8(c) and (f). Thus, to see the variations of force PDF, it is more suitable not to normalize f_n any more. We see that P_n is well fitted by a decreasing exponential function $ke^{\beta(1-f_n/\langle f_n \rangle)}$ for $f_n \geq \langle f_n \rangle$ where k and β are two parameters (Radjaï et al., 1999) representing the value of P_n at $f_n = \langle f_n \rangle$ and the slope of the log-linear plots in Figure 3.8, respectively. We find $\beta \simeq 1.55$ in cycle A, 1.25 in cycle B, and 1.00 in cycle C at C_1 and C_3. This means that the force network is increasingly more inhomogeneous as it evolves from cycle A to B and then C. Upon entering the liquefaction state (C_0 or C_2), the system has a slightly larger proportion of large forces than C_1 or C_3 as shown in Figures 3.8(c) and (f).

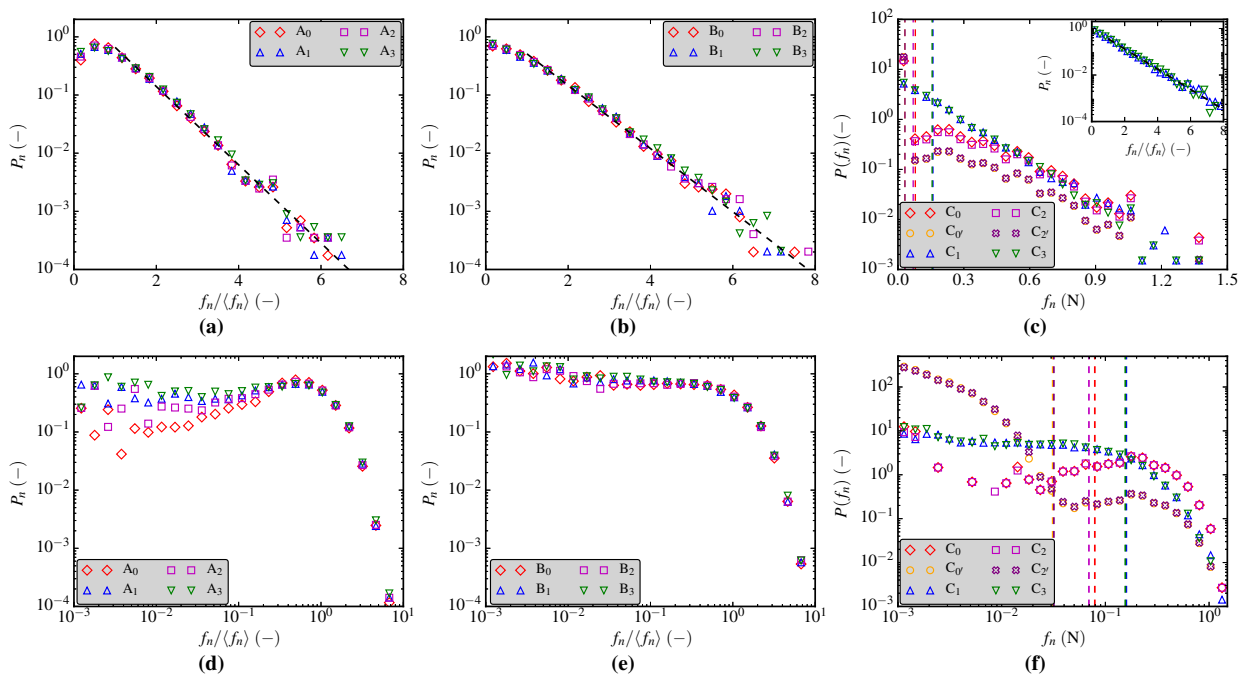

Figure 3.8: Probability density functions P_n of normal forces f_n normalized by the mean normal force in log-linear (a)(b)(c) and log-log scales (d)(e)(f) for simulation T2 at characteristic states of: (a)(d) cycle A; (b)(e) cycle B; (c)(f) cycle C (the vertical dashed lines refer to $\langle f_n \rangle$ at each state).

However, the proportion of large forces becomes smaller than C_1 or C_3 when the system leaves the liquefaction state ($C_{0'}$ and $C_{2'}$).

The distribution of tangential contact forces in the system can be analyzed in a similar way (Radjaï et al., 1996; Majmudar and Behringer, 2005). In addition, one can also link each tangential contact force to the friction mobilization, as given by the friction mobilization index $I_m = |f_t|/(\mu_t f_n)$ (Azéma and Radjaï, 2012; Majmudar and Behringer, 2005; Cantor et al., 2018). This index ranges between 0 and 1, the latter indicating sliding or mobilized contact. Generally, the proportion of mobilized contacts is expected to increase with shear stress (Guo and Zhao, 2013). This is confirmed in Figure 3.9 by comparing states of subscript 0 or 2 with those with subscripts 1 or 3 in pre-liquefaction cycles.

We also observe the I_m distribution's right shift, indicating a larger proportion of contacts getting close to sliding. In the post-liquefaction period, a large proportion of mobilized contacts is generated at C_0 and C_2: the probability density near $I_m = 1.0$ increases from 0.6 to 14.7. With shear strain developing in the liquefaction state from C_0 to $C_{0'}$ or C_2 to $C_{2'}$, the proportion of mobilized contacts drops to around 0.3, and the system regains larger number of contacts far from sliding. It should be noted that the distribution of I_m at $\tau = \pm\tau^{\text{amp}}$ is nearly the same for the cycles A, B, and C, implying a close relation between friction mobilization and the stress state τ^{amp}.

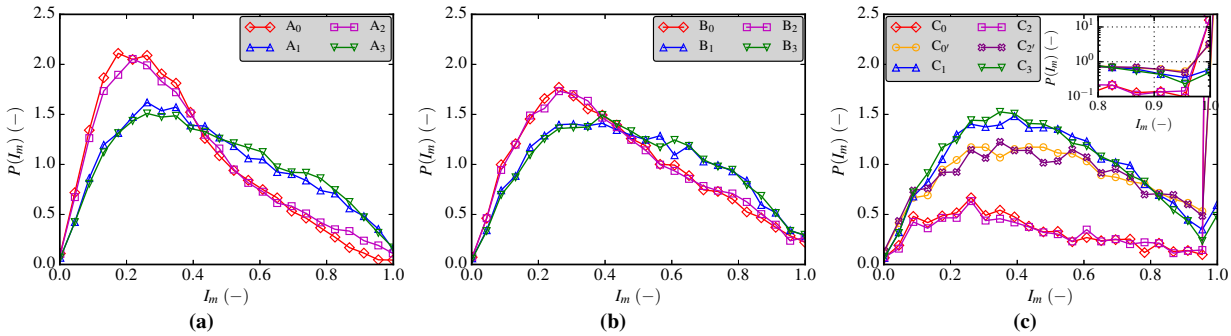

Figure 3.9: Probability density functions of friction mobilization index for simulation T2 at characteristic states of (a) cycle A; (b) cycle B; (c) cycle C.

3.4.3 Fabric and force anisotropies

By analyzing the distribution of directional data in the system, a list of higher-order quantities such as fabric and force tensors can be introduced (Kanatani, 1984). These directional data include contact normals $\boldsymbol{n}$, mean branch vectors $\langle l \rangle(\boldsymbol{n})$, mean normal and tangential forces denoted by $\langle f_n \rangle(\boldsymbol{n})$ and $\langle \boldsymbol{f}_t \rangle(\boldsymbol{n})$, to name a few. Given the low polydispersity of samples in this study, fabric anisotropy due to $\langle l \rangle(\boldsymbol{n})$ is nearly negligible and will not be presented here. Let us consider $S(\boldsymbol{n})$, the set of contact normal vectors pointing in the direction $\boldsymbol{n} = (\theta, \varphi)$ as shown in Figure 3.10, where θ is the angle of contact normal vector projected on the shear plane, i.e. xz plane in Figure 3.10, and φ the azimuthal angle.

The PDF of contact normals, and the average normal and tangential forces are expressed as

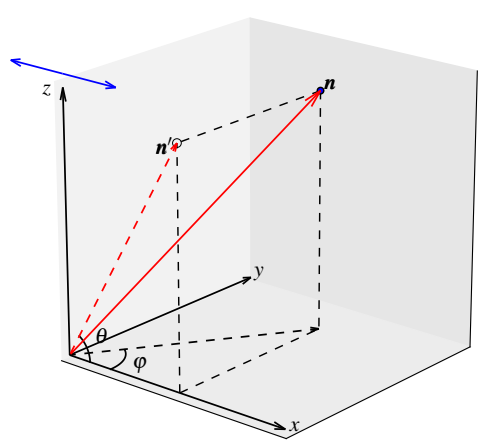

Figure 3.10: Normal contact orientation given the azimuthal angle φ and the angle θ defined by the projection of the contact direction on the shear plane of xz. The blue arrow represents the shear direction.

functions of the orientation $\boldsymbol{n}$ (Azéma et al., 2013; Cantor et al., 2018):

$$P(\boldsymbol{n}) = \frac{N_c(\boldsymbol{n})}{N_c}, \tag{3.14}$$

$$\langle f_n \rangle(\boldsymbol{n}) = \frac{1}{N_c(\boldsymbol{n})} \sum_{c \in \mathscr{S}(\boldsymbol{n})} f_n, \tag{3.15}$$

$$\langle \boldsymbol{f}_t \rangle(\boldsymbol{n}) = \frac{1}{N_c(\boldsymbol{n})} \sum_{c \in \mathscr{S}(\boldsymbol{n})} \boldsymbol{f}_t, \tag{3.16}$$

where $N_c(\boldsymbol{n})$ is the number of contacts pointing in the direction $\boldsymbol{n}$ within a small solid angle $\delta\Omega$ around $\boldsymbol{n}$.

Given the invariance of simple shear loading along the y axis, we expect that the distributions do not depend on the azimuthal angle, and hence we consider only the projections of contact orientations on the shear plane. Thus, contact normal $\boldsymbol{n}$ is replaced by the vector $\boldsymbol{n}'$ on the shear plane with orientation angle θ as shown in Figure 3.10 and the unit vector $\boldsymbol{t}$ representing the direction of corresponding tangential force is replaced by the vector $\boldsymbol{t}'$ on the shear plane with orientation angle $\theta + 90°$, perpendicular to $\boldsymbol{n}'$.

Figure 3.11 displays a polar representation of the functions $P(\boldsymbol{n})$, $\langle f_n \rangle(\boldsymbol{n})$ and $\langle \boldsymbol{f}_t \rangle(\boldsymbol{n})$ in shear plane as a function of θ at the characteristic states. We observe an obviously anisotropic behavior when the shear stress reaches the peak: for $P_n(\theta)$ and $\langle f_n \rangle(\theta)$, the major principal components occur in the direction $\theta \simeq 135°$; for $\langle f_t \rangle(\theta)$ it occurs at $\theta \simeq 90°$, and the other peak at $\theta \simeq 45°$ corresponds to the minor principal component where $\langle f_t \rangle(\theta) < 0$. The directions for the peaks of $\langle f_n \rangle(\theta)$ and $\langle f_t \rangle(\theta)$ can be approximated by the directions of planes with major principal stress and maximum shear stress, respectively. By drawing a Mohr circle, one can see that the angle between these two directions is 45°, which verifies Figures 3.11(b) and (c). Comparing the anisotropies of A_1, B_1, and C_1, one can notice an increasing trend for $P_n(\theta)$, a shrinking trend for $\langle f_n \rangle(\theta)$ due to the decrease of p, and a decreasing trend for $\langle f_t \rangle(\theta)$, which will be elucidated quantitatively below. When the shear stress vanishes (A_0, C_2 and $C_{2'}$) in the pre-liquefaction period, the system tends to be isotropic, but it becomes anisotropic in the post-liquefaction period except for $\langle f_t \rangle(\theta)$. From C_2 to $C_{2'}$, one observes that the fabric anisotropy is first regained prior to the force anisotropies, as generally observed during shear reversal (Radjai and Richefeu, 2009).

To account for the lowest-order anisotropy of $P(\boldsymbol{n})$ a second-order fabric tensor can be defined as (Oda, 1982; Satake, 1982):

$$\boldsymbol{\phi}_c = \frac{1}{N_c} \sum_{c \in N_c} \boldsymbol{n}^c \otimes \boldsymbol{n}^c, \tag{3.17}$$

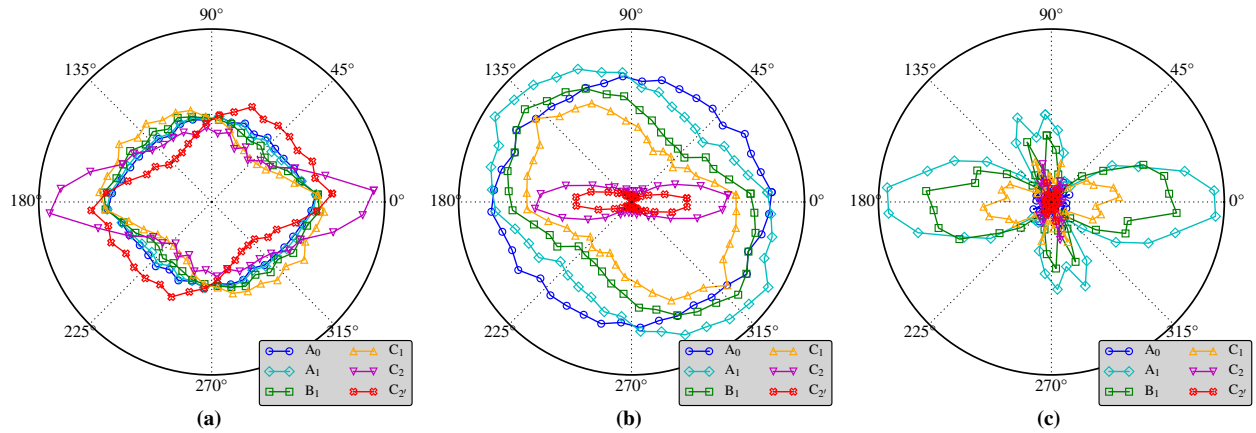

Figure 3.11: Polar representation of the functions (a) $P_n(\theta)$, (b) $\langle f_n \rangle(\theta)$ and (c) $\langle f_t \rangle(\theta)$ at selected characteristic states for simulation T2.

from which the fabric anisotropy tensor $\boldsymbol{a}_c$ can be defined by

$$\boldsymbol{a}_c = \frac{15}{2}\left(\boldsymbol{\phi}_c - \frac{1}{3}\boldsymbol{I}\right), \tag{3.18}$$

where $\boldsymbol{I}$ is the second-order identity tensor. In the same way, force tensors characterizing the second-order anisotropy of $\langle f_n \rangle(\boldsymbol{n})$ and $\langle \boldsymbol{f}_t \rangle(\boldsymbol{n})$ are defined by the following weighted fabric tensors:

$$\boldsymbol{\phi}_n = \frac{1}{N_c}\sum_{k \in N_c} \frac{f_n^k \boldsymbol{n}^k \otimes \boldsymbol{n}^k}{1 + \boldsymbol{a}_c : (\boldsymbol{n}^k \otimes \boldsymbol{n}^k)}, \tag{3.19}$$

$$\boldsymbol{\phi}_t = \frac{1}{N_c}\sum_{k \in N_c} \frac{\boldsymbol{f}_t^k \otimes \boldsymbol{n}^k}{1 + \boldsymbol{a}_c : (\boldsymbol{n}^k \otimes \boldsymbol{n}^k)}. \tag{3.20}$$

Hence, the force anisotropy tensors are given by (Ouadfel and Rothenburg, 2001; Sitharam et al., 2009)

$$\boldsymbol{a}_n = \frac{15}{2}\left[\frac{\boldsymbol{\phi}_n}{\mathrm{tr}(\boldsymbol{\phi}_n)} - \frac{1}{3}\boldsymbol{I}\right], \tag{3.21}$$

$$\boldsymbol{a}_t = \frac{15}{3}\frac{\boldsymbol{\phi}_t}{\mathrm{tr}(\boldsymbol{\phi}_n)}, \tag{3.22}$$

where $\mathrm{tr}(\cdot)$ is the trace operator. Eq. (4.12) implies that $\mathrm{tr}(\boldsymbol{\phi}_t) = 0$ given the normality of $\boldsymbol{n}$ and $\boldsymbol{t}$.

We use the deviatoric invariants of the anisotropy tensors to quantify the anisotropies of the

contact network, normal forces and tangential forces (Guo and Zhao, 2013):

$$a_{[\,]} = \mathrm{sign}(S_{[\,]})\sqrt{\frac{3}{2}\boldsymbol{a}_{[\,]} : \boldsymbol{a}_{[\,]}} \tag{3.23}$$

where the subscript [ ] stands from c, n or t, corresponding to the three aforementioned anisotropies, respectively.$S_{[\,]}$ is the normalized first joint invariant between two tensors defined by:

$$S_{[\,]} = \frac{\boldsymbol{a}_{[\,]} : \mathbf{s}}{\sqrt{\boldsymbol{a}_{[\,]} : \boldsymbol{a}_{[\,]}}\sqrt{\mathbf{s} : \mathbf{s}}} \tag{3.24}$$

where $\mathbf{s} = \boldsymbol{\sigma} - p\boldsymbol{I}$ and the deviatoric stress $q = \sqrt{(3/2)\mathbf{s} : \mathbf{s}}$. Generally $S_{[\,]}$ quantifies the level of proportionality between two tensors, with $S_{[\,]} = 1.0$ corresponding to the proportionality of two tensors. As these anisotropy tensors are affected by $\mathbf{s}$, $S_{[\,]}$ can be approximately regarded as characterizing the relative orientation of the principal axes (PA) of $\boldsymbol{a}_{[\,]}$ with respect to that of $\mathbf{s}$, i.e. the level of coaxiality.

The fabric and force anisotropies are the origins of shear strength in granular materials (Rothenburg and Bathurst, 1989; Ouadfel and Rothenburg, 2001) as $\mathbf{s}/p$ can be well approximated as a linear combination of the anisotropy tensors:

$$\frac{\boldsymbol{\sigma}'}{p} \simeq \frac{2}{5}\left(\boldsymbol{a}_c + \boldsymbol{a}_n + \frac{3}{2}\boldsymbol{a}_t\right) \tag{3.25}$$

At $\tau = \pm\tau^{\mathrm{amp}}$, these anisotropy tensors become nearly proportional to $\mathbf{s}$. Thus Eq. (3.25) can be further simplified to

$$\frac{q}{p} \simeq \frac{2}{5}\left(a_c + a_n + \frac{3}{2}a_t\right) \tag{3.26}$$

This Eq. (3.26) holds quite well for our data in Figure 3.12 in which the evolutions of fabric and force anisotropies at $\tau = \pm\tau^{\mathrm{amp}}$ are shown along with the contributing weight of each anisotropy to q/p. It should be noted that these anisotropies are normalized by $(2/5)a_c + (2/5)a_n + (3/5)a_t$. We see that a_c and a_n present an increasing trend while a_t decreases slowly in the pre-liquefaction period, and all of them tend to level off after several cycles in the post-liquefaction period. The contribution of a_c to q/p increases, compensating the decreasing contribution of a_t, and the contribution of a_n does not change markedly.

The contact network anisotropy a_c provides the geometrical support of the stress anisotropy. Its contribution reflects the larger number of contacts oriented along the compression direction (principal direction of the strain-rate tensor) compared with that along the extension direction. This means that there are more contacts to support the forces along the major principal stress

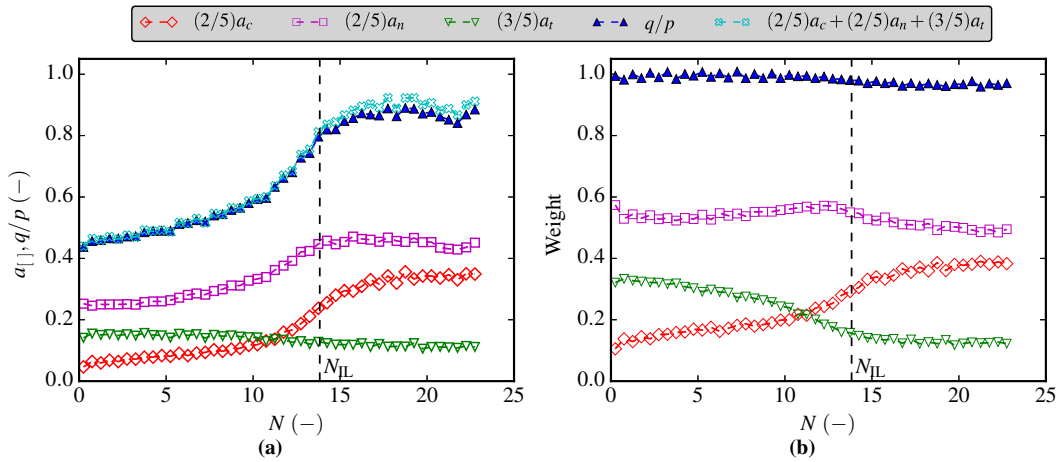

Figure 3.12: (a) Evolutions of the contact and force anisotropies at $\tau = \pm\tau^{\text{amp}}$ for simulation T2 and deviatoric stress ratio q/p both measured from the simulation data and expressed as a function of the anisotropies as in Eq. (3.26). (b) Contributing weights of fabric and force anisotropies to the deviatoric stress ratio q/p: all normalized by $(2/5)a_c + (2/5)a_n + (3/5)a_t$.

direction than the minor principal stress direction. In a dense system, the contact anisotropy's buildup implies the loss of contacts along the extension direction. This is consistent with the increase in the number of particles with fewer than 4 contacts, as observed in Figure 3.6. The normal force anisotropy a_n means that stronger force chains are formed along the major principal stress direction as compared to the minor principal direction. This, in turn, implies an increase in the number of weak forces, as observed in the PDF of normal forces in Figure 3.8. The tangential force anisotropy a_t represents the largest friction mobilization occurring in the shear plane. Indeed, the polar diagram of the average tangential force in Figure 3.11(c) can be approximated by a truncated Fourier expansion $\langle f_t \rangle(\theta) = a_t \langle f_n \rangle \sin 2(\theta - \pi/4)$. Hence, the friction mobilization index $I_m = \langle f_t \rangle / (\mu_t \langle f_n \rangle) = a_t/\mu_t$ is proportional to the tangential force anisotropy $\theta = 0$ or $\pi/2$. In the post-liquefaction period, not only the anisotropies but also the force distributions, friction mobilization distribution, and connectivity function are nearly stable, as shown in Figure 3.13 at $\tau = \pm\tau^{\text{amp}}$ in the last few cycles of the simulation.

Figure 3.14 presents the evolutions of $S_{[\,]}$ and anisotropies in the selected three cycles, along with comparisons between the measured values of q/p and τ/p according to Eq. (3.4) and predicted values suggested by Eqs. (3.26) and (3.25), respectively. From the quick adjustment of S_n and S_t, one can realize that the force anisotropies are easily affected by cyclic shearing, while the fabric anisotropy needs more time for the gain of new contacts along a new direction when the shear direction is revered. In the liquefaction state of Figure 3.14(c) (C_0 to $C_{0'}$ or C_2 to $C_{2'}$), all the anisotropies present noisy oscillations, implying a chaotic state with local instabilities. Then, a_c starts to build up and grows into a force-bearing network. In the pre-liquefaction period, the predicted quantities from Eqs. (3.26) and (3.25) agree well with the measured ones, despite a

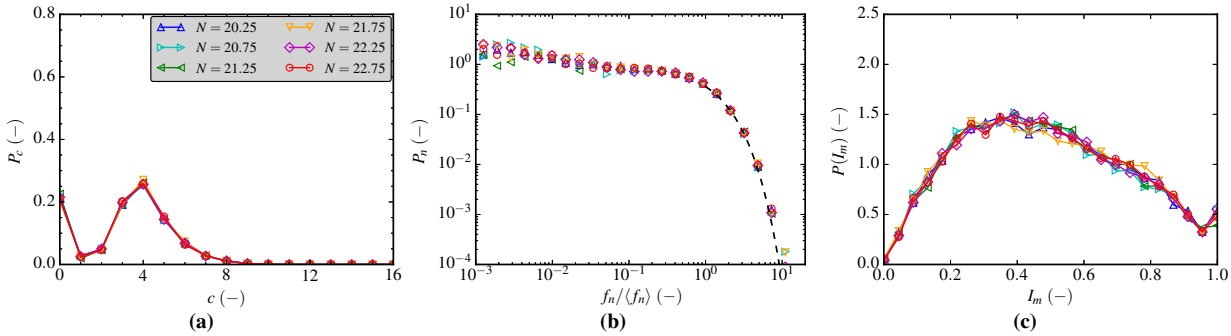

Figure 3.13: Snapshots of (a) particle connectivity diagram, probability density functions of (b) normal forces and (c) mobilized friction index when shear stress reaches its maximum amplitude in the last three cycles of simulation T2.

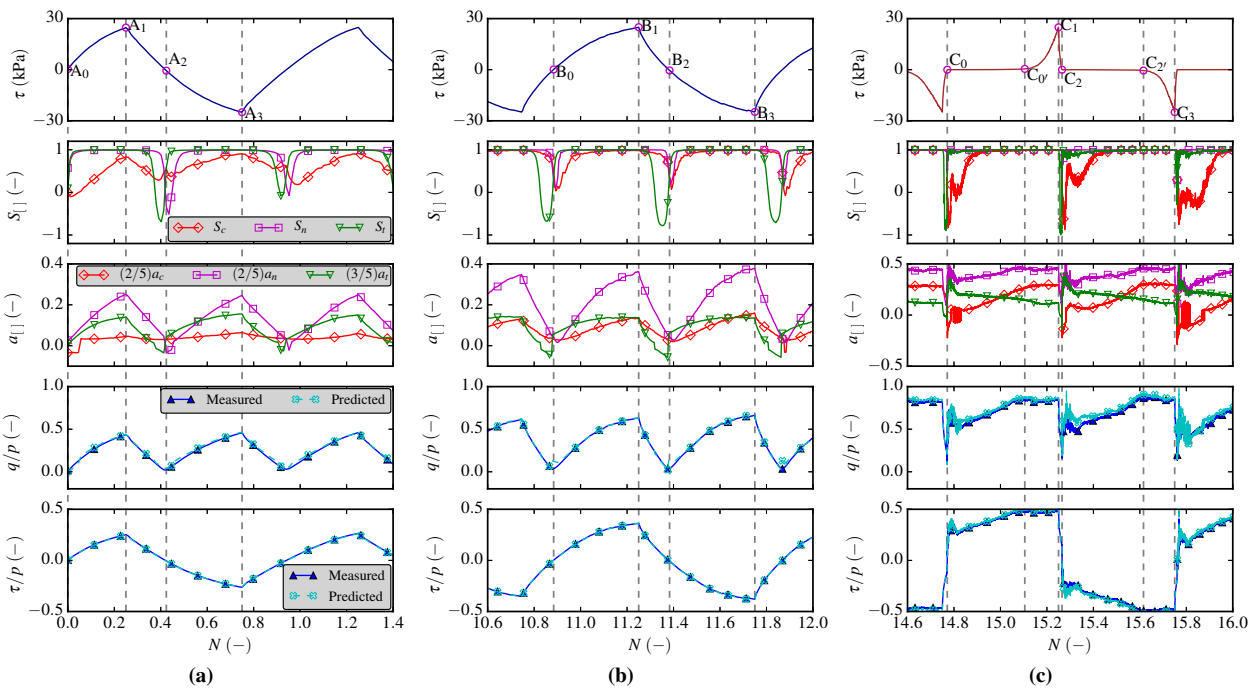

Figure 3.14: Evolutions of $S_{[\,]}$ and anisotropies, along with comparisons between calculated q/p and τ/p and their predicted values by Eqs. (3.26) and (3.25) for simulation T2: (a) cycle A; (b) cycle B; (c) cycle C.

slight loss of accuracy upon unloading for the predicted q/p due to noncoaxiality between the stress tensor and anisotropy tensors during transient reversal. This inaccuracy spreads into liquefaction state in the post-liquefaction period where q, p and τ have quite small values (Radjai and Richefeu, 2009).

Figure 3.15 presents the fabric anisotropy a_c versus the coordination number z_g during the cyclic shearing process. The evolution of the system in the fabric diagram (z_g, a_c) provides a picture of the reorganizations of the contact network in response to external loading (Radjai et al., 2012). The negative values of a_c correspond to the states where S_c is negative, i.e., the principal

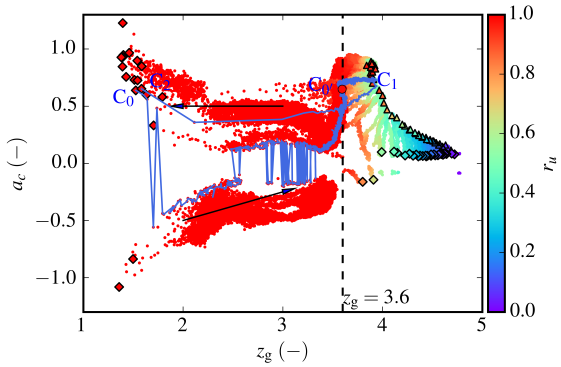

Figure 3.15: Fabric anisotropy a_c versus coordination number z_g during the cyclic shearing for simulation T2.

directions of the stress tensor and fabric anisotropy tensor make an angle larger than $\pi/2$. The instances of shear stress sign change, i.e., the states with subscripts 0 and 2 in each cycle, are marked by the diamond symbols. The instances of peak shear stress, i.e., the states with subscripts 1 and 3 in each cycle, are marked by the triangle. The states from C_0 to C_2 of cycle C are connected to reveal the fabric evolution path in the post-liquefaction period, with characteristic states highlighted.

On the right side of the fabric diagram above $z_g > 3.6$ in the pre-liquefaction period, the evolution of the system starts from $a_c \simeq 0$ and high value of z_g (where $\tau \simeq 0$), and follows a path towards the left (lower values of z_g) via oscillations between $a_c = 0$ and a maximum value of a_c that increases gradually with the number of cycles. The upper limit of a_c defines a decreasing function of z_g, which was termed "gain saturation line" in Radjai et al. (2012) since for large values of z_g no more contacts can be gained along the direction of contraction. The steric exclusions restrict the number of contacts that can be gained and, thus, the fabric anisotropy's value. A simple model predicts that the maximum value of fabric anisotropy varies as $1/z_g$ in agreement with our data points in Figure 3.15. Interestingly, the largest value of fabric anisotropy occurs at $z_g \simeq 4$ with $a_c \simeq 0.9$, where the initial liquefaction occurs.

In the post-liquefaction period, both z_g and a_c vary significantly and follow long paths exemplified by that from C_0 to $C_{0'}$. In particular, we observe a plateau along which a_c is nearly constant while z_g either increases or declines. This means that along this plateau, the contacts are lost or gained isotropically. We see that after the system gets out of liquefaction state, a_c does not change noticeably from $C_{0'}$ to C_1 despite the increase of the applied shear stress τ. z_g increases consistently with p. Upon unloading from C_1 to C_2, z_g drops significantly while a_c does not change noticeably. At low values of z_g, a larger anisotropy is reached by loss of contacts along the direction of extension. But the anisotropy is limited by "loss saturation". Indeed, the particles' relative stability impedes the loss of all contacts along the direction of extension. However, due to

the shear deformation of the sample, the contact network is rebuilt by first isotropic and then anisotropic gain of contacts with steady increase of both z_g and a_c.

3.5 Effects of initial and loading conditions

This section extends our study to the other simulations listed in Table 3.1 to explore the effects of initial and loading conditions on the evolution of microstructure. Simulations T1, T2, and T3 are used to analyze the effect of the initial void ratio e_0. Simulations T2, T4, and T5 are used to analyze the effect of the initial mean stress p_0. Simulations T6, T2 and T7 are used to analyze the effect of CSR defined by Eq. (3.3). Figure 3.16 displays the evolution of z_g for all the simulations listed in Table 3.1. We normalize the number of cycles N by N_{IL}, thus the vertical line $N/N_{IL} = 1$ distinguishes the pre-liquefaction period from the post-liquefaction period. In the inset window of each figure, the x-axis is replaced by $(N - N_{IL})$ to zoom into the details near the initial liquefaction.

We see that the evolution of the coordination number in all simulations is quite similar to that of T2. Recall that, as observed in Figure 3.4(a), z_g stays below 4.0 in the post-liquefaction period, but this is not the case for simulation T5 in Figure 3.16(b) where the mean stress corresponding to $\tau = \pm\tau^{amp}$ in the post-liquefaction period is expected to be around six times that of simulation T2. Given the monotonic relationship between z_g and p (Agnolin and Roux, 2007; Huang et al., 2019b) indicated by Eq. (3.13), it is reasonable that z_g evolves beyond 4.0 in the post-liquefaction period for a simulation inducing a high post-liquefaction mean stress. Given the sudden drop of z_g upon unloading in each post-liquefaction cycle, it is difficult to find the value corresponding to transition to the liquefaction state. As indicated by Figure 3.16, z_g stays above 3.6 in the pre-liquefaction period. Hence, the value $z_g = 3.6$ seems to control transition to the liquefaction state independently of e_0, p_0, and CSR.

Figure 3.17 shows the evolution of the respective contributions of the fabric and force anisotropies to the deviatoric stress ratio q/p at $\tau = \pm\tau^{amp}$ for the simulations of Table 3.1 except

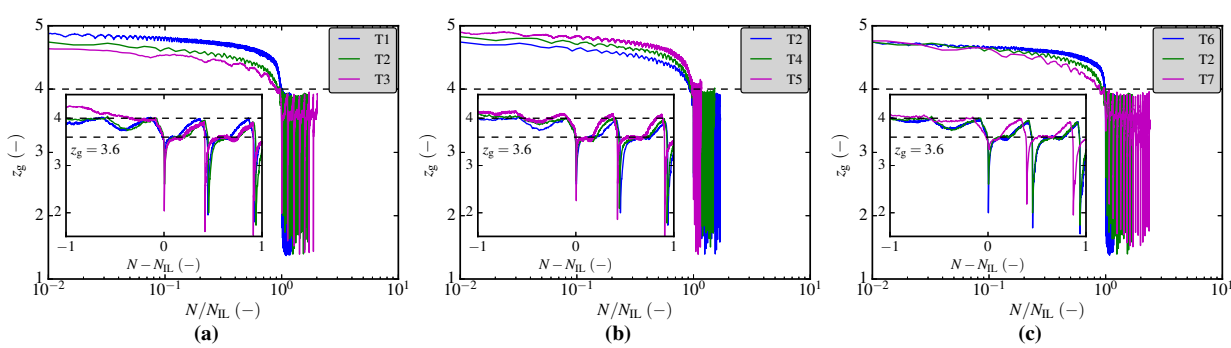

Figure 3.16: Effects of (a) initial void ratio e, (b) initial mean stress p_0 and (c) cyclic stress ratio (CSR) on the evolution of coordination number z_g.

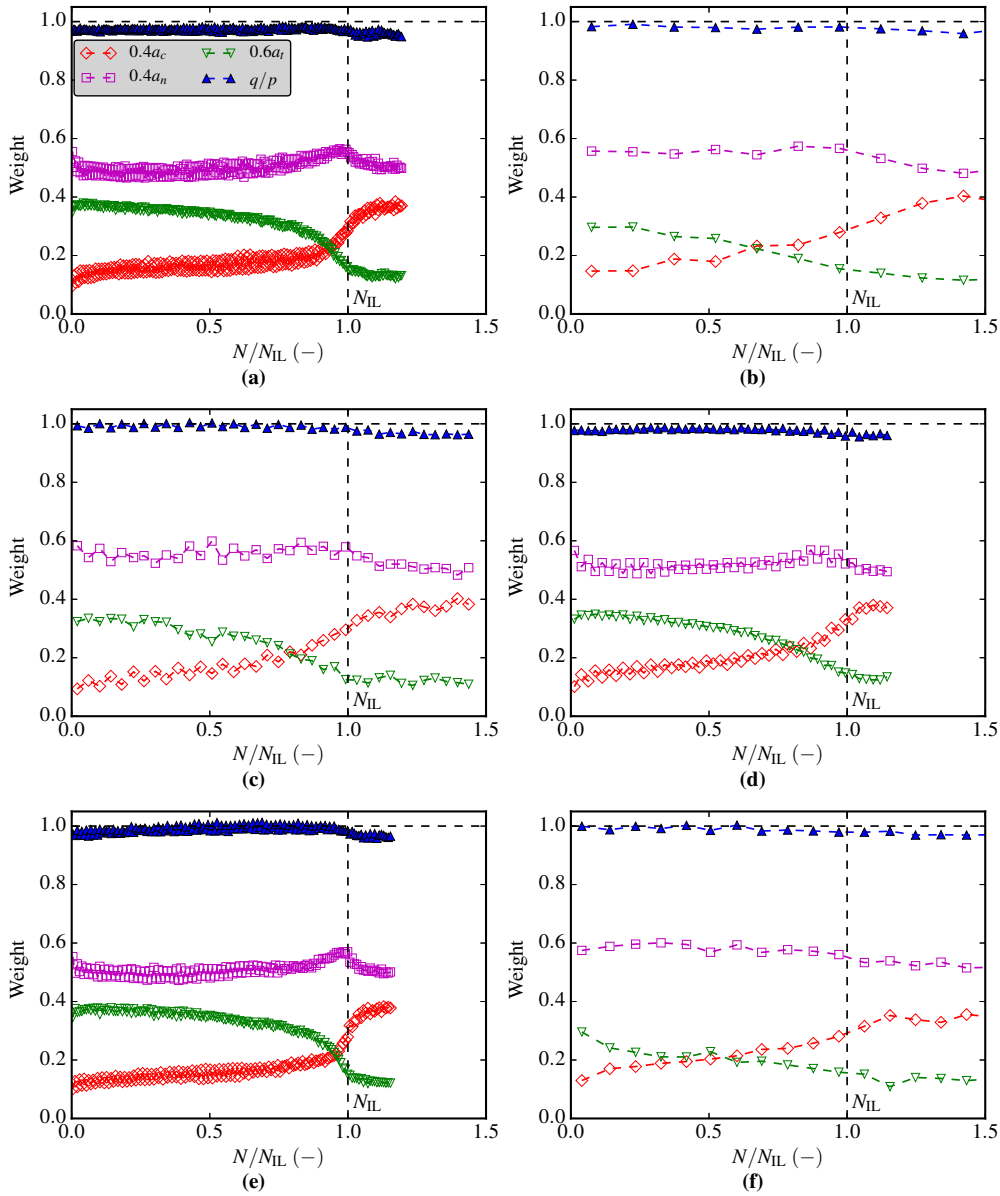

Figure 3.17: Evolution of the respective contributions of anisotropies to the stress ratio q/p at $\tau = \pm\tau^{\mathrm{amp}}$ and the theoretical value of q/p according to Eq. (3.26) for (a) T1, (b) T3, (c) T4, (d) T5, (e) T6 and (f) T7.

T2. The theoretical value of q/p calculated from the anisotropies by Eq. (3.26) is shown, too. We see that effect of the initial and loading conditions on the evolution patterns is negligible. In all cases, the contribution of a_t is larger than that of a_c in the pre-liquefaction period, but their roles interchange slightly before and during the post-liquefaction period. The larger contribution of a_c in the post-liquefaction period reflects the higher mobility and lower coordination number of the particles allowing larger fabric anisotropy. The higher mobility also involves a lower degree of frustration of particle rotations and thus lower friction mobilization, which is at the origin of tangential anisotropy.

Despite their similarity, one can observe some differences in the first few loading cycles, but cyclic shearing reduces these initial differences in the subsequent cycles. After a sufficient number of cycles in the post-liquefaction period, the contribution of $(2/5)a_c$ statures at around 0.4, that of $(2/5)a_n$ saturates at around 0.5, and the rest is attributed to $(3/5)a_t$. In the post-liquefaction period, the stress path falls into the butterfly shape, implying a constant deviatoric stress ratio q/p during loading outside the liquefaction state (refer to the period between $C_{0'}$ and C_1 in Figure 3.14(c)). The system can quickly adjust itself to support the shear stress amplitude by properly allocating each anisotropy weight. Figure 3.18 displays the particle connectivity diagram, probability density functions of normal forces and mobilized friction index at the last time when the shear stress reaches the maximum amplitude in each simulation. The effects of the initial and loading conditions on these distributions are not significant.

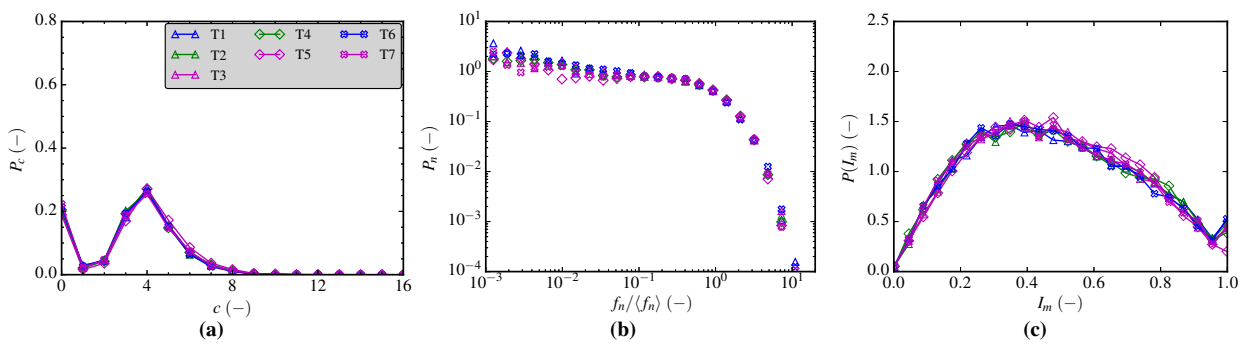

Figure 3.18: (a) Particle connectivity diagram, probability density functions of (b) normal forces and (c) mobilized friction index when the shear stress reaches its maximum amplitude in the last simulated cycle.

3.6 Summary and perspectives

In this paper, we investigated the highly nonlinear evolution of granular microstructure during isochoric cyclic simple shearing using discrete-element numerical simulations and for different values of the initial mean stress, initial void ratio, and cyclic stress ratio. The macroscopic behavior is characterized by typical oscillations of shear stress and gradual buildup of excess pore pressure until the system enters a liquefaction state. In the transition to the liquefaction state, where the mean stress approaches zero, the coordination number and the non-rattler fraction drop significantly, and the force-bearing network collapses. Unconventional distributions of normal contact forces occur in this state as compared to a stable packing, and a considerable number of mobilized contacts are generated.

In the liquefied state, large shear deformation is required to rebuild the contact network and exit the liquefaction state, as characterized by the particle connectivity diagram and polar representation of contact normals, providing the geometrical support for the subsequent shear.

The relationship between deviatoric stress ratio and the force and fabric anisotropies was also verified, revealing a nearly constant contribution of the normal force anisotropy, an increasing contribution of the fabric anisotropy, and a decreasing contribution of the tangential force anisotropy or friction mobilization to the deviatoric stress ratio as cyclic shearing proceeds. We also explored the effects of the initial and loading conditions on the microstructural evolutions. It was found that in all cases, the transition to the liquefaction state is characterized by a specific value of the coordination number ($\simeq 3.6$). We also observed a similar evolution of the fabric and force anisotropies and their saturation values in simulations with different initial and loading conditions.

This work can be expanded and completed in several directions. Since the liquefaction transition value of the coordination number is quite robust with respect to the initial and loading conditions, an issue is how it depends on the sample's inherent properties, such as particle size distribution, particle shape (Nguyen et al., 2015), or inter-particle interaction parameters. The contributions of each anisotropy to the stress ratio may also vary due to the change in these inherent properties, for example, the contribution from branch vector anisotropy will become pronounced when a large band of particle size distribution or particle shape is introduced. The microstructural analysis can also be enriched by a more detailed analysis of the evolution of force correlations and force fluctuations at the transition to the liquefaction state (Peters et al., 2005; Amirrahmat et al., 2020). The evolution of the pore space (Wang and Wei, 2016; Sufian et al., 2015, 2019) may also be analyzed in this regard. Finally, more detailed analysis is underway to characterize the evolution of anisotropy from particle scale processes during cyclic shearing.

Chapter 4: Macro Response and Microstructure of 3D Granular Media Subjected to Multidirectional Cyclic Shearing

In this chapter, discrete element method (DEM) is adopted to simulate a comprehensive series of multidirectional cyclic shear tests under constant volume condition, with the goal of exploring effects of shear paths on the macro and micro response of the granular system. This chapter is reproduced from the paper co-authored with Mahdi Taiebat, Patrick Mutabaruka and Farhang Radjaï, which is planned for submission to a journal for publication.

4.1 Introduction

In dynamic analysis of geo-structures, like simple site response analysis all the way to more complex soil-structure interaction, we usually perform the analysis using only one horizontal component of the ground motion. In real earthquakes, however, soil layers are subjected to multidirectional cyclic shearing, and each component has varied amplitudes and a plethora of frequencies. Even if the vertical component of the seismic loading is neglected, there exist two horizontal shear components, and neglecting one of them can potentially lead to underestimation of seismic risk.

Pyke et al. (1975) was the first to study sand response under multidirectional shaking where through shaking table tests on dry Monterey No. 0 sand, they found that the settlement caused by shaking in two horizontal directions was about the sum of the settlements caused by each individual component alone. Su and Li (2008) conducted a pair of centrifuge tests on loose Toyoura sand under uni- and biaxial shaking, and comparison of the results indicated that the latter could develop 20% greater peak pore pressure near the sample bottom and 12% more permanent settlement. Recently, El Shafee et al. (2017) presented a series of centrifuge tests on a level site consisting of loose saturated Nevada 120 sand subjected to uni- and multidirectional base excitations, and they concluded that the common practice method of increasing the unidirectional shaking component by 10% underestimated the soil response under multidirectional shaking. In the same way, Cerna-Diaz et al. (2017) performed dynamic centrifuge tests on saturated dense Ottawa sand under uni- and multidirectional shaking and they

found that multidirectional shaking caused increases in pore pressure and volumetric strain of approximately 200% compared to unidirectional shaking, considerably larger than other experimental findings on loose sands.

To mimic the response of soil element under level or sloping grounds when subjected to multidirectional cyclic shearing under undrained conditions, extensive laboratory experimental work has been conducted over the decades (Ishihara and Yamazaki, 1980; Boulanger and Seed, 1995; Kammerer et al., 2002; Matsuda et al., 2011; Sun, 2019), generating a comprehensive experimental database for understanding the physics of the sheared system. Generally, it was found that multidirectional cyclic shearing induced more significant reduction in the liquefaction resistance than unidirectional shearing. Kammerer et al. (2005) proposed two conflicting effects of the applied shear stress to understand the reason for development of large deformation, the first being zero mean effective stress occurring with shear stress release and the second the existence of large driving shear stress. However, these laboratory findings are still restricted to overall macroscopic behaviors given the very limited applications of special experimental techniques in cyclic shearing, such as X-ray computed tomography (Hall et al., 2010) and photoelasticity technique (Majmudar and Behringer, 2005). In addition to experiments, continuum modeling of soil deposits under multidirectional shaking has been developed by Ghaboussi and Dikmen (1981), Su and Li (2008), Carlton and Kaynia (2016), Zeghal et al. (2018), Yang et al. (2019) and Reyes et al. (2019), to name a few. However, all these continuum models are not based on the grain-scale evolution of the granular microstructure under complex multi-directional loading, which, to our best knowledge, remains essentially unexplored.

Discrete element method (DEM) (Cundall and Strack, 1979) provides a suitable framework to study the mechanical response of the granular assembly from both macro- and microlevel perspectives when subjected to multidirectional cyclic shearing. It also guarantees perfect reproducibility of each "numerical experiment" as the same sample can be reused, thereby getting rid of random noise and natural uncertainty due to variability usually occurring in laboratory tests. Applying DEM to reproduce liquefaction phenomenon induced by conventional unidirectional cyclic shearing such as triaxial or simple shear tests dates back to Ng and Dobry (1994). Later Sitharam (2003) explored the micromechanics to a certain level such as the drop of coordination number for loose sample approaching liquefaction. Other topics with respect to undrained cyclic shearing include but are not limited to stability analysis (Huang et al., 2018, 2019b), fabric anisotropy (Soroush and Ferdowsi, 2011; Wei et al., 2018), post-liquefaction deformation mechanism (Wang and Wei, 2016; Wang et al., 2016), effects of initial and loading conditions on liquefaction resistance (Evans and Zhang, 2019; Wei and Wang, 2017; Zhang and Evans, 2020). Recently Wei (2017) and Wei et al. (2020) conducted DEM simulations of granular packing subjected to uni- and multidirectional cyclic shearing, and they found that the

same "stable fabric" was reached after sufficient number of loading cycles regardless of multidirectional loading paths.

This study extends the previous work from two aspects. First, a series of multidirectional cyclic shear tests on a medium dense sample are carried out to explore the effect of shear paths on the macroscopic response, including pore pressure generation and shear strain development. Then, four representative simulations are selected for micromechanical investigation from three directions: (1) adopting contact-based indicators to reveal the stability of the system along with cyclic shearing; (2) using void-based fabric to shed light on the post-liquefaction deformation; (3) applying stress-force-fabric relationship to illustrate how contact and force anisotropies are contributing to the load-bearing network.

4.2 DEM simulation set up

4.2.1 Multidirectional cyclic shear test

Cyclic simple shear or torsional tests are usually carried out in the laboratory using harmonic shearing, which is also followed by multidirectional cyclic shear test. Multidirectional cyclic shear test is quite similar to simple shear test with the difference that two horizontal shear components can be applied simultaneously on the soil specimen. The resultant shear stresses can change in both magnitude and orientation. Generally, there are two stages in this test: a consolidation stage by applying confinement with or without static shear stress to bring the sample to the initial state, and an undrained cyclic shear stage by applying the cyclic shear stresses. Thus the two components of shear stress, τ_x and τ_y, can be decomposed as follows:

$$\frac{\tau_x}{p_0} = \mathrm{SSR}_x + \mathrm{CSR}_x \sin(2\pi f_x t) \tag{4.1}$$

$$\frac{\tau_y}{p_0} = \mathrm{SSR}_y + \mathrm{CSR}_y \sin(2\pi f_y t + \phi) \tag{4.2}$$

Here p_0 is the initial mean stress used for normalizing the shear stress, usually adopted for isotropically consolidated samples. For K_0 consolidated samples (samples are prepared by unidirectional compression with lateral normal strains being constrained), the initial vertical stress substitutes. The same terminology as in simple shear test is adopted here for multidirectional cyclic shear test, i.e., static stress ratio (SSR) representing the ratio of static shear stress and initial confinement stress, and cyclic stress ratio (CSR) corresponding to the ratio of cyclic shear stress amplitude and initial confinement stress. Non-zero SSR mimics the initial stress state of soil element under sloping ground. One may expect two SSRs for two static shear stresses and two

CSRs for two cyclic shear stresses in multidirectional cyclic shear test, but by properly establishing the coordinate system, the number of SSRs can degrade to one, either SSR_x or SSR_y. f_x and f_y are frequencies of the two harmonic cyclic shear stresses along the x and y directions, respectively, and ϕ is the initial phase difference between them.

Given the fact that the two cyclic stresses can have different amplitudes, frequencies and phase angles, these will generate a wide range of shear paths. In this chapter, we consider four types of shear paths including 1-D linear, 2-D linear, circular/oval, and figure-8, as depicted in Figure 4.1 where applied shear stress in consolidation stage and undrained cyclic shear stage are colored in blue and red, respectively.

The 1-D linear path in Figure 4.1(a), is the traditional cyclic simple shear test, which may also include a static shear stress in the same direction as the subsequent undrained cyclic shearing. It can be attained by setting $SSR_x = 0$, $CSR_x = 0$ in Equation (4.1) and $\phi = 0$ in Equation (4.2). 1-D linear path indicates plane strain condition, mimicking unidirectional shaking of level ($SSR_x = 0$) or

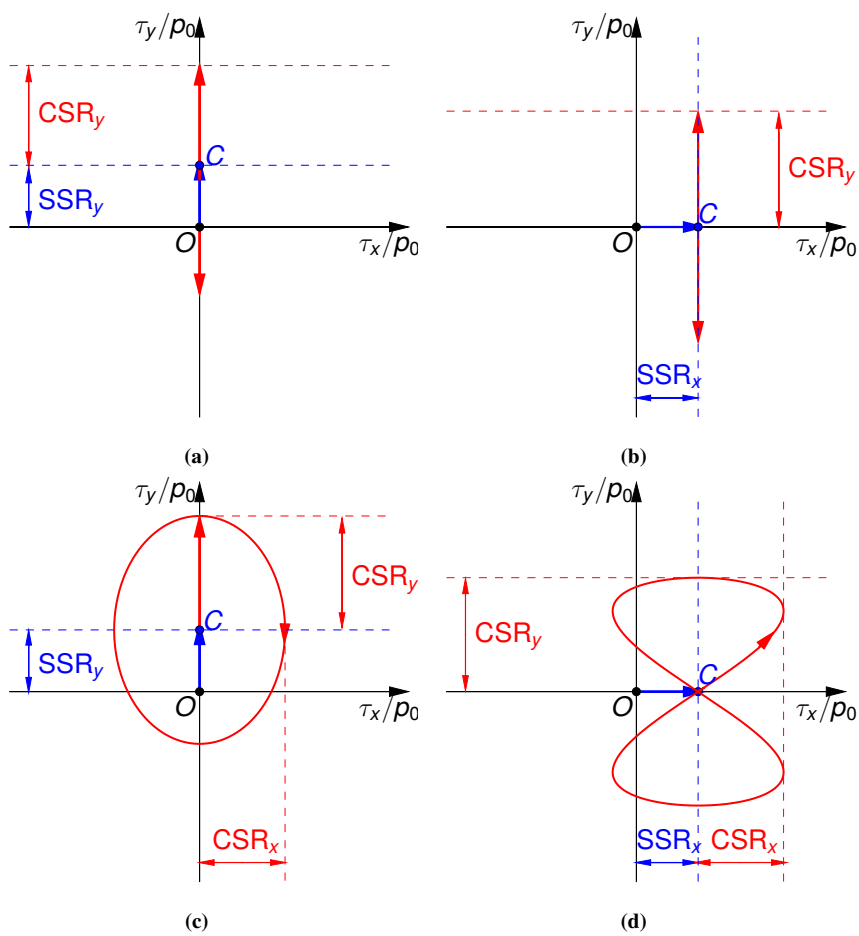

Figure 4.1: Shear paths simulated in this study (modified from Yang et al. (2016)): (a) 1-D linear shear path; (b) 2-D linear shear path; (c) circular/oval shear path; (d) figure-8 shear path.

sloping ground ($SSR_x \neq 0$) where shaking is parallel to the slope direction. When the unidirectional cyclic shearing is applied perpendicular to the direction of static shear stress, the shear path is denoted by 2-D linear path, as shown in Figure 4.1(b). It can be achieved by setting $CSR_x = 0$ in Equation (4.1) and $SSR_y = 0$, $\phi = 0$ in Equation (4.2). Clearly 2-D linear shear path breaks the symmetry of the system due to the presence of SSR_x. Circular/oval path in Figure 4.1(c) is obtained by setting $SSR_x = 0$, $f_x = f_y$ and $\phi = \pi/2$. When $CSR_x = CSR_y$, it refers to a circular path. Otherwise, it is an oval path. Figure-8 path in Figure 4.1(d) is configured by setting $SSR_y = 0$, $\phi = 0$, and $f_x = 2f_y$.

4.2.2 Simulation procedure

A three-dimensional (3D) particle dynamic DEM numerical platform, named GRFlow3D (Mutabaruka, 2013), was used in this study. The granular assembly was simulated using polydisperse spheres interacting based on soft-particle laws. The contact interactions of spheres consist of normal collision, tangential sliding, rolling and torsion, and the key quantity is the overlap between particles, from which the corresponding force can be calculated using linear spring and dashpots. Details are explained in Luding (2008) and Mutabaruka (2013), not repeated here for brevity.

The simulations involve two steps: preparing a particle assembly via isotropic compression, and applying specified shear path to the assembly under constant volume condition. The constructed sample consists of spheres with low plolydispersity, i.e., $d_{\max}/d_{\min} = 2$ where $d_{\max}$ and $d_{\min}$ refer to the maximum and minimum particle diameters, respectively. Between $d_{\min}$ and $d_{\max}$, the particles follow a uniform distribution of particle volumes. One can refer to Voivret et al. (2007) and Mutabaruka et al. (2019) for details of generating the particle size distribution. Once the particles with their sizes were generated, they were placed randomly on a 3D sparse lattice to avoid the overlap. This 3D lattice was contained in a rectangular cell whose top and bottom sides are rigid walls and four lateral sides are periodic boundaries, denoted as bi-periodic cell.

The sample was compressed isotropically by moving the six sides of the cell. During the compression process, the gravity was set to zero. The six sides followed a translational move and the contact tangential friction coefficient μ_t was tuned to achieve a certain void ratio e, defined as the ratio of the total pore volume to the solid volume. As many of laboratory procedures for sample preparation can not be simulated, a simpler computational procedure was adopted, modified from Kuhn et al. (2014) and Thornton (2015), in order to prepare samples comparable with the laboratory ones. The procedure consists of four substeps, which is explained by constructing a medium dense sample with the target mean stress $p_0 = 100$ kPa: (1) with

$\mu_t = 0.20$, densifying the sparse sample by moving the six sides at a constant speed until void ratio e reaches 1.0; (2) setting velocities of particles and the six sides as zero, and using servo-control algorithm to compress the sample isotropically with the target $p = 10$ kPa where μ_t remains 0.2; (3) increasing the target p to half of p_0, i.e., 50 kPa, and continuing compression of the sample with $\mu_t = 0.20$; (4) modifying μ_t to 0.5 used for further compressing the sample with the target $p = p_0 = 100$ kPa and subsequent cyclic shearing. One can refer to Thornton (2000) and O'Sullivan (2011) for the detail of servo-control algorithm. The first three substeps are used to generate an initially dense packing via controlling the tangential friction coefficient and increasing the confinement. The last step is necessary to obtain a smooth distribution of $f_t/(\mu_t f_n)$ between 0 and 1 as usually a different μ_t is used in the step of cyclic shearing. Other simulations on samples with different number of spheres ranging between 2197 and 10648 were conducted and the macroscopic response was not very different. So the sample with 8000 spheres was used in this study, falling into the similar range of Martin et al. (2020) and Kuhn et al. (2014). Figure 4.2(a) displays the prepared sample.

In the step of cyclic shearing, the sample volume was kept constant to mimic undrained condition. It was attained by fixing four lateral sides and the bottom wall as well as moving the top wall horizontally, i.e., keeping the sample height h constant as in Figure 4.2(b). The specified stress paths were exerted on the top wall via a servo-controlled approach proposed by Wei et al. (2020). To reduce possible slippage between the walls and the sample, one layer of particles was glued to the top and bottom walls, respectively, as indicated by dark spheres in Figure 4.2(b).

The inertial number $I = \dot{\gamma} d \sqrt{\rho/p}$ was adopted to maintain a quasistatic shear regime, where

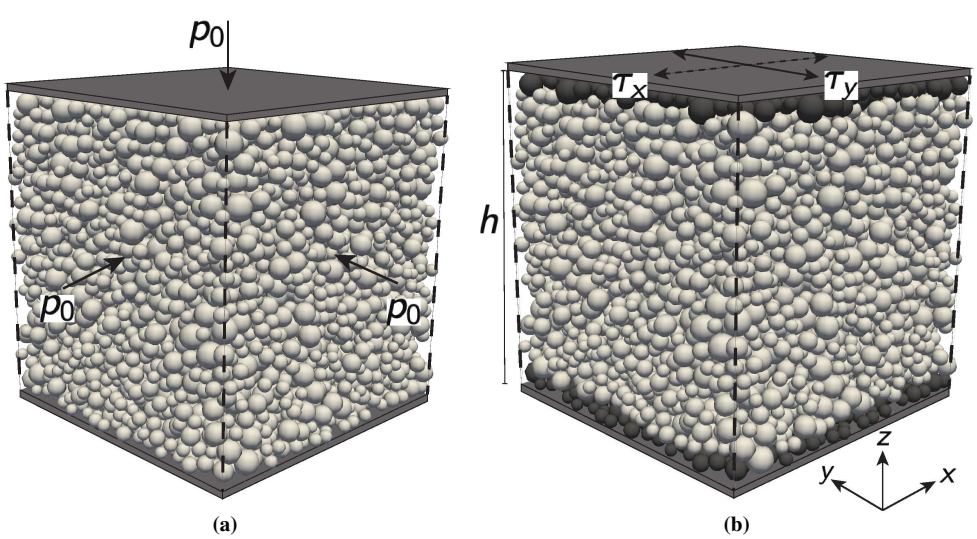

Figure 4.2: Illustration of particle arrangements and boundary conditions for a sample composed of 8000 **particles: (a) at the end of sample preparation; (b) during constant height cyclic shearing.**

$\dot{\gamma} = v/h$ is the shear strain rate with v the moving rate of top wall, ρ the density of particle, d the mean diameter of particles, and p the mean stress. The shear is considered quasistatic if $I \ll 1$ (MiDi, 2004) and typically the threshold is chosen as 0.001. This condition can be strictly obeyed before p drops to almost zero. The deformation process can not be quasistatic in this limit of p approaching zero even by decreasing v since the granular material undergoes a phase transition from solid-like to liquid-like state. The sensitivity analysis on the moving rate of top wall indicates that $v = 0.01$ m/s or shear strain rate $\dot{\gamma} \simeq 0.38\ s^{-1}$ is a good option, consistent with Martin et al. (2020), which guarantees $I < 0.001$ before p gets very tiny.

We checked the velocity profile of the sample during the cyclic shearing step. Outside the region of p getting very small, the velocity profile is almost linear along the height of the sample, i.e., the whole sample is sheared by the motion of the top wall. When p becomes very tiny, the linear velocity profile vanishes and the whole system gets into the collisional regime.

The simulation parameters are given in Table 4.1. According to Radjaï and Dubois (2011), the stiffness number κ is introduced such as the average normal deflection δ_n satisfies $\delta_n/d \propto \kappa^{-1}$. For the linear contact law in the normal direction, $\kappa = k_n/(pd)$ with k_n being the normal stiffness. In this study k_n is chosen as 10^6 N/m to guarantee $\delta_n \sim 10^{-3}d$ in each contact, i.e., the particles can be considered as nearly undeformable (Mutabaruka et al., 2019). Then c_n is determined to attain a value of 0.15 for the normal coefficient of restitution based on Schwager and Pöschel (2007). $\mu_t = 0.5$ is a common choice for shearing the sample (Guo and Zhao, 2013; Huang et al., 2018; Jiang et al., 2019). The values for other microscopic material parameters can be obtained from their relations to k_n, c_n or μ_t suggested by Luding (2008) and listed in Table 4.1. The rolling and

Table 4.1: DEM parameters

Description	Value
Density, ρ	2650 kg/m^3
Normal stiffness, k_n	10^6 N/m
Normal viscosity, c_n	1.15 kg/s
Tangential stiffness, k_t	$0.8k_n$
Tangential viscosity, c_t	$0.2c_n$
Tangential friction coefficient, μ_t	0.2^+ & 0.5^*
Rolling stiffness, k_r	$0.1k_n$
Rolling viscosity, c_r	$0.05c_n$
Rolling friction coefficient, μ_r	0.1
Torsion stiffness, k_o	$0.1k_n$
Torsion viscosity, c_o	$0.05c_n$
Torsion friction coefficient, μ_o	0.1

$^+$Isotropic compression step *cyclic shearing step

torsion laws adopted in this study provide some resistance to the particle rotation, a simple way to model certain effects due to the particle shape (Radjaï and Dubois, 2011).

It should be noted that for simulations of $\mathrm{SSR}_{[\,]} \neq 0$ with the subscript [ ] being x or y, the static shear stress was applied in the constant volume cyclic shearing phase prior to adding the cyclic shear stress other than in the isotropic compression stage. As the current study focuses on investigating the effect of shear paths on the cyclic response of the granular assembly, it becomes natural to use the same sample. One may wonder a noticeable difference between these two scenarios. However, given that the sample prepared in this study is medium dense, the initial condition is not expected to change significantly if $\mathrm{SSR}_{[\,]}$ is applied in the isotropic compression stage. The obvious impact of $\mathrm{SSR}_{[\,]}$ on the sample response lies in its presence in the cyclic shearing stage, which shifts the cyclic shear paths along a certain direction.

Table 4.2 lists 57 multidirectional cyclic shear tests simulated in this study, including the conditions implied by the second, third, fourth, fifth and sixth columns. The last three columns of Table 4.2 refer to the outcomes, which will be explained in the sequel.

Table 4.2: Conditions and outcomes of multidirectional cyclic shear tests on a medium dense sample[†]

Test	Shear path	SSR_x	SSR_y	CSR_x	CSR_y	N_{IL}	$r_{u,\mathrm{lim}}$	$\tau_{u,\mathrm{lim}}/p_0$
1	1-D linear				0.20	65.3	1.00	0.00
2			0.05		0.20	53.3	1.00	0.00
3			0.10		0.20	35.2	1.00	0.00
4			0.15		0.20	24.2	1.00	0.00
5			0.20		0.20	37.2	1.00	0.00
6			0.25		0.20	70.2	0.64	0.05
7			0.30		0.20	117.2	0.42	0.11
8					0.25	17.3	1.00	0.00
9			0.05		0.25	15.8	1.00	0.00
10			0.10		0.25	12.2	1.00	0.00
11			0.20		0.25	11.2	1.00	0.00
12			0.30		0.25	39.2	0.61	0.05
13					0.30	8.7	1.00	0.00
14			0.10		0.30	7.2	1.00	0.00
15			0.20		0.30	7.2	1.00	0.00
16			0.30		0.30	18.2	1.00	0.00
17			0.30		0.35	6.2	1.00	0.00

continued on next page

Table 4.2 – continued from previous page

Test	Shear path	SSR_x	SSR_y	CSR_x	CSR_y	N_{IL}	$r_{u,\lim}$	$\tau_{u,\lim}/p_0$
18	2-D linear	0.05			0.20	60.6	0.91	0.05
19		0.10			0.20	42.0	0.80	0.10
20		0.15			0.20	26.6	0.69	0.15
21		0.20			0.20	21.7	0.56	0.20
22		0.30			0.20	54.7	0.22	0.30
23		0.05			0.25	15.1	0.91	0.05
24		0.10			0.25	12.1	0.80	0.10
25		0.20			0.25	9.2	0.55	0.20
26		0.30			0.25	15.1	0.26	0.31
27		0.05			0.30	6.5	0.91	0.05
28		0.10			0.30	6.0	0.79	0.10
29		0.20			0.30	5.5	0.57	0.20
30		0.30			0.30	7.1	0.27	0.31
31	Circular/oval			0.15	0.15	48.9	0.71	0.15
32			0.10	0.15	0.15	29.6	0.91	0.05
33			0.20	0.15	0.15	23.6	0.89	0.05
34				0.05	0.20	56.8	0.91	0.05
35				0.10	0.20	34.3	0.80	0.10
36				0.15	0.20	16.9	0.70	0.15
37				0.20	0.20	9.2	0.61	0.20
38			0.05	0.20	0.20	8.5	0.70	0.15
39			0.10	0.20	0.20	6.7	0.80	0.10
40			0.15	0.20	0.20	5.6	0.91	0.05
41			0.20	0.20	0.20	5.9	1.00	0.00
42			0.25	0.20	0.20	8.7	0.90	0.05
43			0.30	0.20	0.20	17.8	0.65	0.12
44				0.25	0.25	3.7	0.50	0.25
45			0.30	0.25	0.25	4.8	0.90	0.05
46	Figure-8			0.15	0.15	21.1	1.00	0.00
47		0.10		0.15	0.15	12.0	0.92	0.04
48		0.20		0.15	0.15	16.0	0.76	0.11
49				0.05	0.20	44.5	1.00	0.00

continued on next page

Table 4.2 – continued from previous page

Test	Shear path	SSR_x	SSR_y	CSR_x	CSR_y	N_{IL}	$r_{u,\lim}$	$\tau_{u,\lim}/p_0$
50				0.10	0.20	20.1	1.00	0.00
51				0.15	0.20	9.8	1.00	0.00
52				0.20	0.20	5.5	1.00	0.00
53		0.10		0.20	0.20	4.0	0.92	0.04
54		0.20		0.20	0.20	4.8	0.81	0.09
55		0.30		0.20	0.20	12.6	0.62	0.17
56				0.25	0.25	2.3	1.00	0.00
57		0.30		0.25	0.25	4.5	0.67	0.15

†Void ratio $e = 0.647$ and $p_0 = 100$ kPa measured at the end of isotropic compression

Empty space in the third, fourth and fifth columns implies zero value

4.3 Macroscopic response

At the system level, stresses and strains in the cyclic shear phase were analyzed to reveal degradation of mean effective stress and shear strain development. The stress tensor $\boldsymbol{\sigma}$ is linked to inter-particle interactions over a selected volume V by

$$\boldsymbol{\sigma} = \frac{1}{V} \sum_{c \in N_c} \boldsymbol{l}^c \otimes \boldsymbol{f}^c \tag{4.3}$$

where $\boldsymbol{l}^c$ is the branch vector connecting the centers of two particles for interior contact or connecting the particle center and the contact point for exterior contacts, $\boldsymbol{f}^c$ is the contact force, $\otimes$ denotes the tensor dyadic product and the summation runs over all the contacts N_c in the selected volume V. The superscript c in $\boldsymbol{l}^c$ and $\boldsymbol{f}^c$ will be dropped in the sequel for simplicity. The two shear stresses τ_x and τ_y in Equations (4.1) and (4.2) refer to the components σ_{zx} and σ_{zy}, respectively. The mean effective stress p is calculated by $(\sigma_{xx} + \sigma_{yy} + \sigma_{zz})/3$. Although water was not simulated explicitly in this study, one can still extract a notional pore pressure according to the reduction of mean effective stress, i.e., $\Delta u = p_0 - p$, and the pore pressure ratio $r_u = \Delta u / p_0$. The cumulative shear strain pair (γ_x, γ_y) are measured as $(x_w/h, y_w/h)$, where x_w and y_w refer to the cumulative horizontal displacements of the top wall along x and y directions, respectively, calculated by the difference of the new and original (x, y) coordinates of the top wall.

4.3.1 4-way plot

The typical macroscopic behaviors of granular material under the shear paths of 1-D linear, 2-D linear, circular and figure-8 are presented in Figures 4.3, 4.4, 4.5 and 4.6, respectively, in the form of 4-way plot (Kammerer et al., 2002). These figures refer to the tests 1, 19, 37 and 52, respectively, where the same CSR of 0.20 was applied. The 4-way plot for 1-D linear path consists of stress path, stress-strain loop, pore pressure ratio evolution and shear strain development. The 4-way plots for the other three paths consist of the applied shear stress path, obtained shear strain path, pore pressure ratio evolution and development of the resultant shear strain $\gamma \equiv \sqrt{\gamma_x^2 + \gamma_y^2}$. In the four selected DEM simulations, a static shear bias of 0.10 was applied for the 2-D linear path and there was no static shear stress for the other three paths. For each simulation, "initial liquefaction" is defined as when the resultant shear strain reaches 3.0% for the first time (Kammerer et al., 2002), i.e., $\gamma_{\mathrm{IL}} = 3.0\%$, and the corresponding number of cycles is denoted as N_{IL}, as shown in Figures 4.3, 4.4, 4.5 and 4.6. This state divides the cyclic shear phase into two parts, pre-liquefaction and post-liquefaction for the period prior to and after initial liquefaction, colored in grey and dark red in these figures, respectively. Besides, the limiting pore pressure ratio $r_{u,\mathrm{lim}}$ is defined by the achieved maximum pore pressure ratio, and the corresponding resultant shear stress and number of cycles are denoted as $\tau_{u,\mathrm{lim}}$ and $N_{u,\mathrm{lim}}$, respectively.

In the four simulations, one can see the notional pore pressure develops along with the

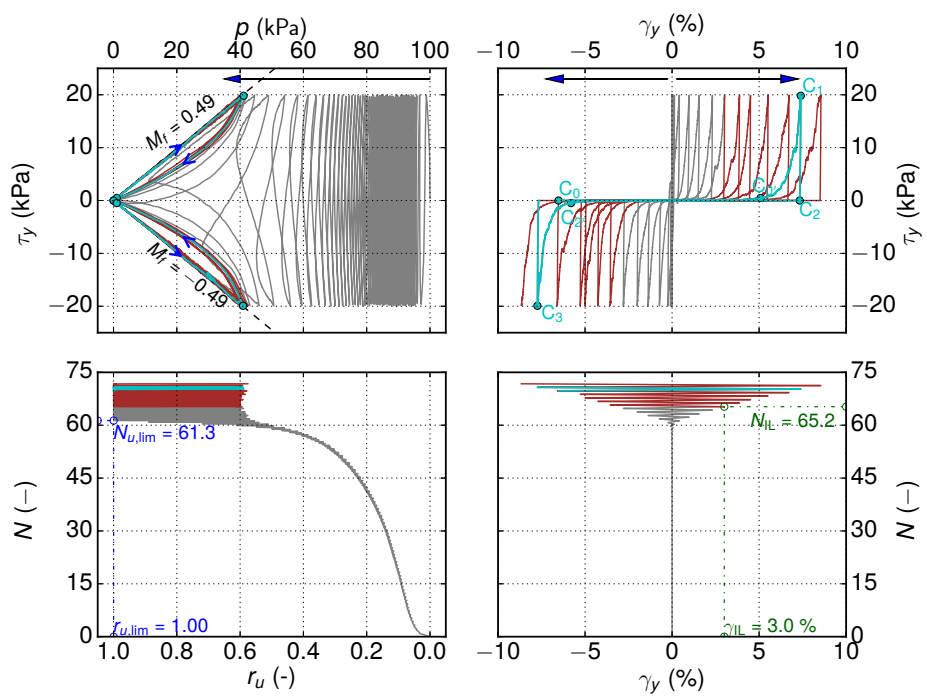

Figure 4.3: Macroscopic response of constant-volume simple shear test with CSR $= 0.20$.

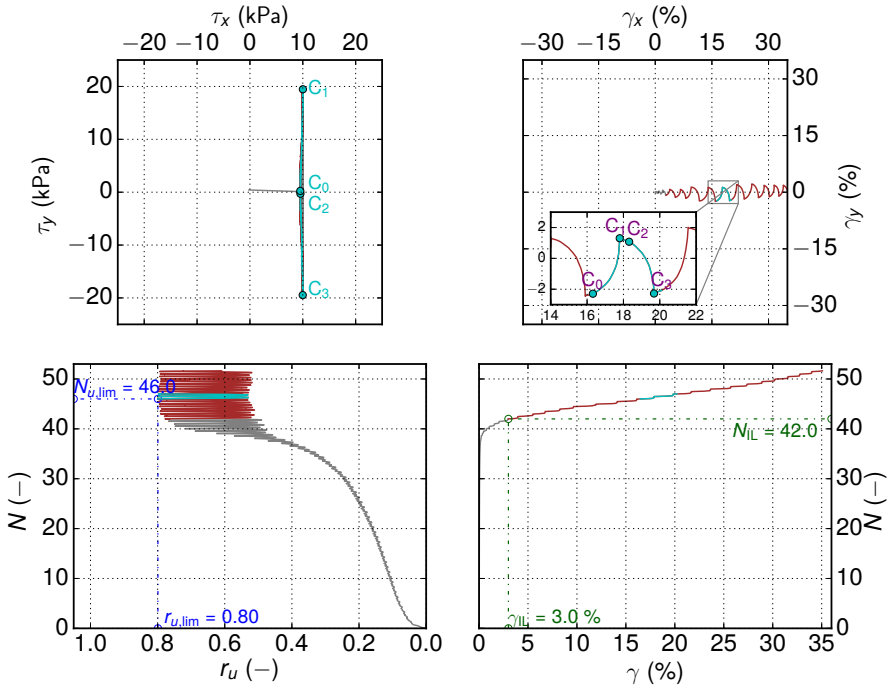

Figure 4.4: Macroscopic response of constant-volume multidirectional cyclic shear test with CSR $= 0.20$: 2-D linear shear path.

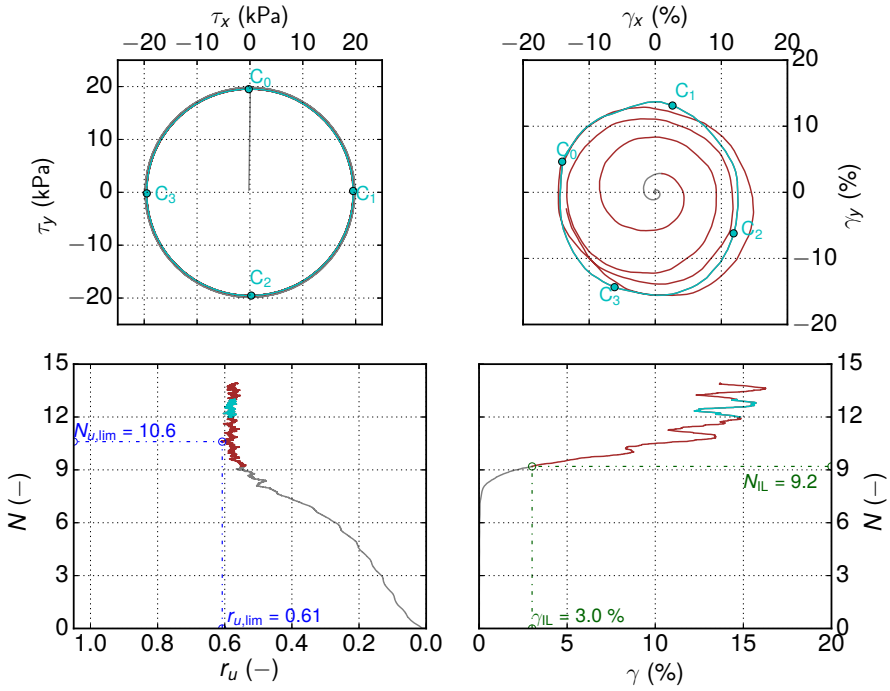

Figure 4.5: Macroscopic response of constant-volume multidirectional cyclic shear test with $\mathrm{CSR}_x = \mathrm{CSR}_y = 0.20$: circular shear path.

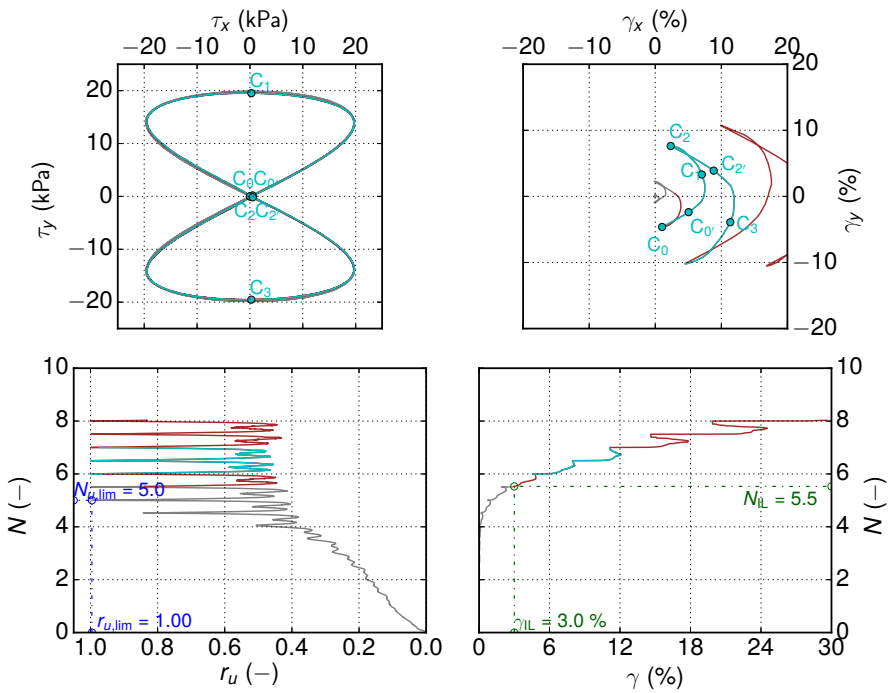

Figure 4.6: Macroscopic response of constant-volume multidirectional cyclic shear test with $\mathbf{CSR}_x = \mathbf{CSR}_y = 0.20$: figure-8 shear path.

constant volume cyclic shearing, where $r_{u,\mathrm{lim}}$ of 1-D linear and figure-8 paths attains 1.0 transiently, indicating vanishing of p while $r_{u,\mathrm{lim}}$ of 2-D linear and circular paths is far from 1.0. All the simulations generate large shear strains, and these suggest that zero mean effective stress is not a requirement for large shear strain development, although it is valid for cyclic simple shear test in Figure 4.3. Given SSR indicating the slope dip direction, Figure 4.4 suggests that large shear strain develops mainly along the slope direction although the cyclic loading is perpendicular to that direction. In addition, the four simulations imply that N_{IL} and $N_{u,\mathrm{lim}}$ are pretty close, suggesting that initial liquefaction occurs almost simultaneously with p dropping to its minimum. All these observations are consistent with the laboratory findings (Ishihara and Yamazaki, 1980; Boulanger and Seed, 1995; Kammerer et al., 2002, 2005).

One loading cycle in the post-liquefaction period of each simulation was selected to zoom into details of the evolution of microscopic descriptors to be revealed later, as highlighted in cyan in Figures 4.3, 4.4, 4.5 and 4.6. In the loading cycle of 1-D linear and figure-8 paths, six characteristic states were adopted where C_0 refers to the instance with the largest number of floaters (particles without any contact) when τ transitions from negative to positive (1-D linear) or from quadrant III to quadrant I in the space of applied shear stresses (figure-8), $C_{0'}$ refers to when $r_u < 0.99$ for the first time after C_0, the subsequent C_1 refers to τ_y reaching the amplitude and C_2, $C_{2'}$ and C_3 are similar to C_0, $C_{0'}$ and C_3, respectively, but in the remaining loading cycle. $C_{0'}$ and $C_{2'}$ are missing

in the shear paths of 2-D linear and circular but the others apply to 2-D linear and one can infer the meanings of these instances for circular path in Figure 4.5.

4.3.2 Post-liquefaction pore pressure behavior

Evolution of pore pressure ratio in Figures 4.3, 4.4, 4.5 and 4.6 indicates that once the limiting pore pressure ratio is achieved, the measured pore pressures throughout each loading cycle show repetition of behavior (Kammerer et al., 2005). Thus one can extract the limiting pore pressure ratio $r_{u,\mathrm{lim}}$ for each simulated test in Table 4.2 and the corresponding shear stress $\tau_{u,\mathrm{lim}}$. One type of "shear stress ratio" is defined as the ratio of $\tau_{u,\mathrm{lim}}$ and the initial mean stress p_0, as shown in the last column of Table 4.2. Figure 4.7 shows $r_{u,\mathrm{lim}}$ against $\tau_{u,\mathrm{lim}}/p_0$ for each simulation. One can observe a roughly inverse relationship between $r_{u,\mathrm{lim}}$ and $\tau_{u,\mathrm{lim}}/p_0$. Most of the data points can be fitted by a linear function of $y = -2.08x + 1.00$, and the slope is very close to $-1/M_f = -2.04$, with M_f being the slope of stress path at butterfly shape as shown in Figure 4.3, indicating that these data points fall on the failure surface of cyclic simple shear test.

It should be noted that $\tau_{u,\mathrm{lim}}$ is very similar to the minimum shear stress, i.e., $\min\sqrt{\tau_x^2+\tau_y^2}$, thereby allowing for good prediction of $r_{u,\mathrm{lim}}$ only based on the shear stress path. The fit function gives a y-intercept of 1.0 suggesting that $r_{u,\mathrm{lim}} = 1.00$ occurs simultaneously with $\tau_{u,\mathrm{lim}} = 0$. They are necessary and sufficient for each other.

The few outliers noticeably below the fit function consist of three from 1-D linear path, three from 2-D linear path and one from circular path. The cases of 1-D linear path occur where SSR_x exceeds CSR_y, thus there is no shear stress reversal, i.e., the minimum value of τ_y stays positive. For these tests, when $r_{u,\mathrm{lim}}$ is attained, the corresponding stress state (τ_y, p) is still a bit far from

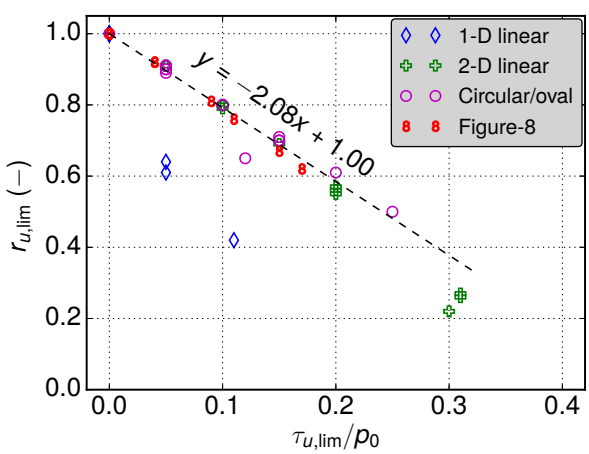

Figure 4.7: Relationship between limiting pore pressure ratio $r_{u,\mathrm{lim}}$ and the corresponding shear stress ratio $\tau_{u,\mathrm{lim}}/p_0$.

the failure surface of Figure 4.3, which is consistent with the laboratory experiments (Boulanger et al., 1991; Hyodo et al., 1991; Vaid et al., 2001; Chiaro et al., 2012; Wichtmann and Triantafyllidis, 2016). The three outliers of 2-D linear path are attributed to cases with a large SSR_y. For the outlier of circular path, its stress path does not contain the origin of the applied shear stress space (τ_x, τ_y) representing zero shear stress state. Kammerer et al. (2005) also pointed out certain similar cases where the imposed shear stress remained so large that the soil could not soften. Hence, contraction due to decreasing of the applied shear stress is not large enough to bring the granular system close to the failure surface.

4.3.3 Cyclic liquefaction resistance

As shown in Figure 4.1, to configure the 1-D linear and 2-D linear shear paths, CSR_y needs to be specified while one has to specify both CSR_x and CSR_y for the circular/oval and figure-8 shear paths. To facilitate the subsequent analysis, CSR_y is selected as the control variable and meanwhile only simulations with $\mathrm{CSR}_x = \mathrm{CSR}_y$, i.e., aspect ratio (AR) of 1, for circular and figure-8 shear paths, are adopted. Recall that Figures 4.3, 4.4, 4.5 and 4.6 are simulations with $\mathrm{CSR}_y = 0.20$, thus one needs other simulations with a list of CSR_y to make the cyclic liquefaction strength curve. It should be noted that static stress stress is not considered for the 1-D linear, circular and figure-8 shear paths except the 2-D linear case where $\mathrm{SSR}_x = 0.10$.

Figure 4.8 displays the liquefaction strength curves for the four types of shear paths where initial liquefaction is defined as the first time of the total shear strain $\gamma = \sqrt{\gamma_x^2 + \gamma_y^2}$ reaching 3%. For each shear path, three simulations are adopted and these data points can be fitted by the dashed line representing the power-law function (Idriss and Boulanger, 2006; Huang et al., 2018)

$$\mathrm{CSR}_y = aN_{\mathrm{IL}}^{-b} \tag{4.4}$$

where a and b are fitting parameters. These dashed lines indicate a general decrease in liquefaction resistance with increasing CSR_y, as expected. Furthermore, we observe a decrease of liquefaction resistance following the order of 1-D linear, 2-D linear, circular and figure-8 shear paths, in good agreement with laboratory findings (Kammerer et al., 2002).

A series of another four simulations of different CSR_x and fixed $\mathrm{CSR}_y = 0.20$ for circular/oval and figure-8 shear paths are also added to Figure 4.8, symbolized by the thinner ellipse and figure-8, to explore the effect of $\mathrm{AR}(= \mathrm{CSR}_x/\mathrm{CSR}_y)$ on the cyclic liquefaction resistance. The data points from both paths indicate an increase in liquefaction resistance with a decreasing AR as they approach the 1-D linear case, in agreement with the experiments (Ishihara and Yamazaki, 1980; Kammerer et al., 2002), and one can expect they coincide with the 1-D linear case when AR

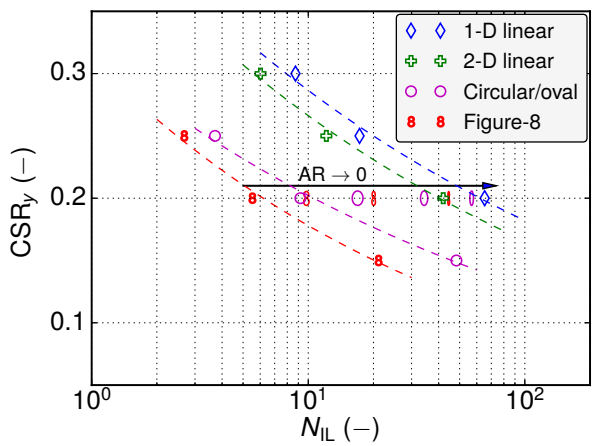

Figure 4.8: Cyclic liquefaction strength curve for different shear stress paths.

reaches zero.

To explore the effect of static shear stress on cyclic liquefaction resistance, Figure 4.8 can be extended by incorporating liquefaction strength curves with various values of $\mathrm{SSR}_{[\,]}$'s. Here the bracket subscript [ ] represents y for 1-D linear and circular shear paths or x for 2-D linear and figure-8 shear paths, as illustrated in Figure 4.1. In doing so, one would see lots of curves with different shear paths and different $\mathrm{SSR}_{[\,]}$'s, from which the CSR_y required to cause initial liquefaction at 10 loading cycles (denoted hereafter as CRR_y) can be extracted to characterize the cyclic liquefaction resistance of the sample (Vaid and Chern, 1983; Hyodo et al., 1991; Boulanger and Seed, 1995; Yang and Sze, 2011). It should be noted that for circular and figure-8 paths only simulations with $\mathrm{AR} = 1$ are adopted, excluding the effect of AR.

Figure 4.9 presents the values of CRR_y against $\mathrm{SSR}_{[\,]}$ for the four shear paths. The diagonal black dashed line refers to $\mathrm{CRR}_y = \mathrm{SSR}_{[\,]}$, which divides the parameter space into two regions. For 1-D linear shear path, they represent regions of shear stress experiencing reversal or not; for circular shear path, they refer to regions of applied shear stress path containing the origin or not; for figure-8 shear path, they describe regions of τ_x staying positive or not; but they are not indicative for 2-D linear shear path.

A marked feature in Figure 4.9 is that $\mathrm{SSR}_{[\,]}$ affects the cyclic resistance differently for these shear paths. For 1-D linear shear path, CRR_y presents an increasing trend with increasing SSR_y and the curve stays in the reversal region with shear stress reversal, matching the laboratory experiments (Hyodo et al., 1991; Yang and Sze, 2011). The curve of 2-D linear shear path stays below the 1-D linear one and it does not change significantly, consistent with the laboratory results on medium dense sample (Boulanger and Seed, 1995). The curves of circular and figure-8 shear paths are located even below the 2-D linear one and both cross the dashed line of $\mathrm{CRR}_y = \mathrm{SSR}_{[\,]}$. We can not find any corresponding laboratory study revealing the effect of static

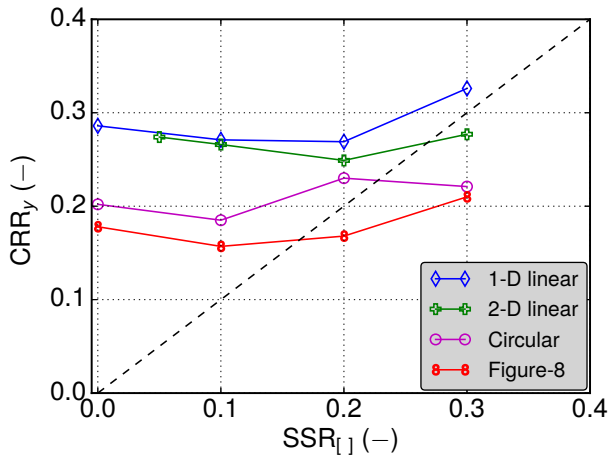

Figure 4.9: Cyclic liquefaction resistance as a function of the level of static stress ratio.

shear stress on cyclic liquefaction resistance in terms of circular and figure-8 shear paths in such a systematic way. Interestingly, near $\mathrm{SSR}_x = 0.20$, the CRR_y values of 2-D linear and circular shear paths get close, and near $\mathrm{SSR}_x = 0.30$, the difference between circular and figure-8 shear paths becomes negligible, both indicating the significant impact of static shear stress.

We can introduce the two conflicting effects of imposed shear stress (Kammerer et al., 2005) to better understand Figures 4.8 and 4.9. As previously shown, for min $\sqrt{\tau_x^2 + \tau_y^2}/p_0$ approaching 0 transiently, the expected value of $r_{u,\mathrm{lim}} = 1$ provides the state where large shear strain can develop due to negligible resistance of the granular system, also known as cyclic mobility for the 1-D linear test with shear stress reversal. For tests with min $\sqrt{\tau_x^2 + \tau_y^2}/p_0$ clearly larger than 0, $r_{u,\mathrm{lim}}$ will stay away from 1.0 but the imposed shear stress can still drive the system to deform progressively, also named as the mode of development of residual deformation for 1-D linear test without shear stress reversal (Hyodo et al., 1991; Chiaro et al., 2012). Apparently, the initial liquefaction in 1-D linear cases of Figure 4.8 is caused by the first effect, the second effect induces large deformation for 2-D linear and circular cases, and these two effects are combined in figure-8 cases (one can compare the strain path from C_0 to $\mathrm{C}_{0'}$ with the one from $\mathrm{C}_{0'}$ to C_1 in Figure 4.6). It should be noted that noticeable stress rotation also occurs in circular and figure-8 cases of Figure 4.8, which may cause extra degradation of the granular system load-bearing structure. Figure 4.9 indicates that the lowest value of CRR_y is attained along with a certain amount of static shear stress, consistent with the claim that the balance between these two competing aspects results in high shear strain potential (Kammerer et al., 2005).

4.4 Granular microstructure

In this section, first we analyze the particle connectivity and friction mobilization, which are linked to the system stability. Then, a particle-void fabric is adopted to shed some light on the macro deformation. In the end, fabric and force anisotropies are used to partition the load-bearing network, which reveals the micro origins of shear resistance.

4.4.1 Particle connectivity and friction mobilization

The coordination number z_{g}, namely the average number of contacts per particle excluding floaters (particles without contacts), is adopted to characterize the overall stability of the granular system. It is defined as

$$z_{\mathrm{g}} = \frac{2N_c}{N_p - N_p^0} \tag{4.5}$$

Here, N_p is the total number of particles and N_p^0 is the number of floaters. Figure 4.10 shows evolution of z_{g} along with the cyclic shearing process for the four simulations in Figures 4.3, 4.4, 4.5 and 4.6, respectively. The time histories are colored by r_u ranging between 0 and 1. A zoomed-up window for each test is added to reveal how z_{g} varies in several loading cycles of post-liquefaction period and the highlighted dots represents selected characteristic states. Generally, one can notice a decreasing trend of z_{g} along the cyclic shearing for all the four shear paths. After the state of $\min(N_{u,\mathrm{lim}}, N_{\mathrm{IL}})$, for 1-D linear and figure-8 shear paths, z_{g} tends to oscillate significantly and drops below 3.6 when r_u is bigger than 0.99; for 2-D linear and circular shear paths, z_{g} oscillates mildly and stays above 3.6.

One can also view z_{g} as an approximate measurement of the level of redundancy in the system, i.e., the total number of constraints compared to the total number of degrees of freedom. For the 3D-DEM with contact laws consisting of normal collision, tangential sliding, rolling and torsion, each contact involves three forces and three torques (constraints) to be determined whereas the number of equations equals six force/torque balance equations (degrees of freedom) for each particle. Hence, removing the floating particles and equaling the number of degrees of freedom with the number of forces/torques. we come up with $6N_c = 6(N_p - N_p^0)$ for the isostatic system. Thus, the critical value of z_{g} for isostaticity is $z_{\mathrm{iso}} = 2$ (Martin et al., 2020).

For the granular system in this study, theoretically we can determine $z_{\mathrm{iso}} \geq 2$. According to Martin et al. (2020), it is rational to assume that $z_{\mathrm{iso}} \leq 3$. According to Figure 4.10(a), one can assert that the system of 1-D linear shear path becomes transiently under-constrained. For the 2-D linear and circular shear paths, the system stays over-constrained as z_{g} is bigger than 3

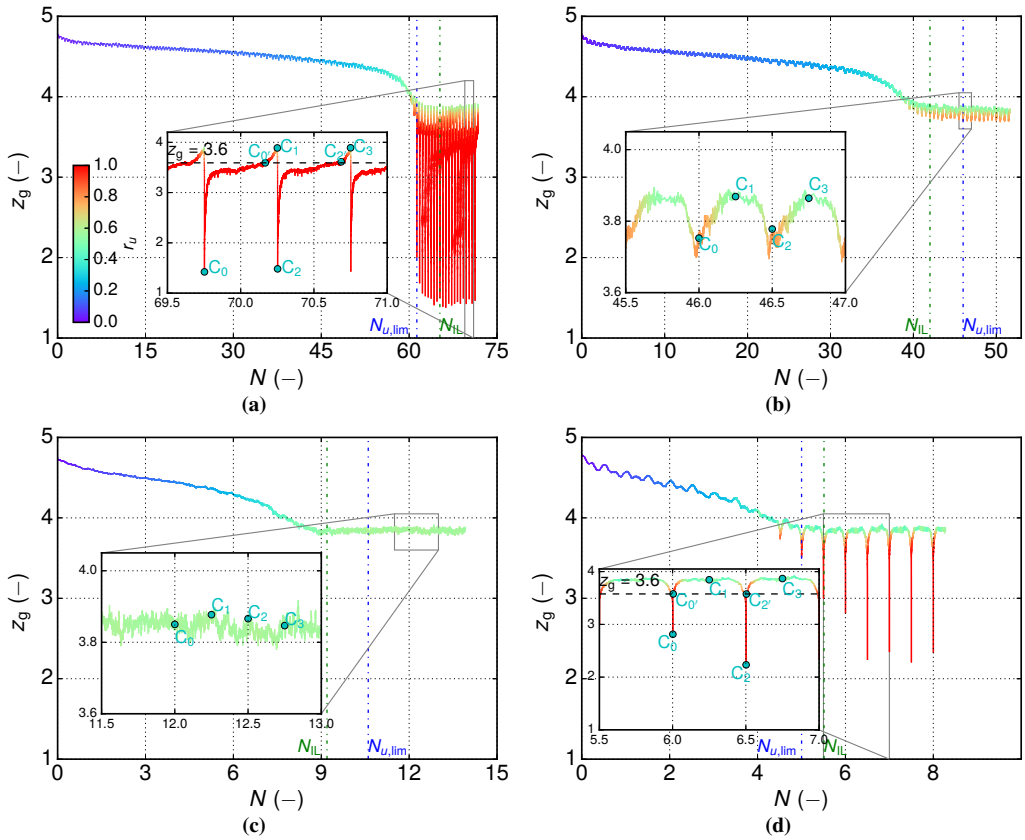

Figure 4.10: Evolution of coordination number z_g under shear path of: (a) 1-D linear; (b) 2-D linear; (c) circular; (d) figure-8.

noticeably. The system of the figure-8 shear path may become under-constrained temporally given the recorded minimum value of z_g being so close to 2. One can refer to Kruyt (2010), Gong et al. (2012), Pouragha and Wan (2016), Zhou et al. (2017), Huang et al. (2018) and Martin et al. (2020) for the direct measurement of redundancy index.

Let us go back to the characteristic states given in Figures 4.3, 4.4, 4.5 and 4.6. Figure 4.11 presents the corresponding connectivity $P(c)$ of the particles, defined as the proportion of particles with exactly c contacts. In 1-D linear and figure-8 shear paths, an irregular distribution with a higher proportion of floaters at C_0 and C_2 is observed. These are the states corresponding to the lowest z_g, revealing the collapse of contact network. For the other selected states, the contact network is well formed. One should notice the surprising difference of $P(c)$ between C_0 and $C_{0'}$, or C_2 and $C_{2'}$, given the proximity of their mean stresses. In fact, during that period of $r_u \geq 0.99$, the sample deforms significantly, helping rebuild the disappearing contact network without changing p obviously. For 2-D linear and circular paths, the distribution does not vary noticeably, consistent with the over-constrained state of the system.

To each contact a local coordinate system $(\boldsymbol{n}, \boldsymbol{t})$ can be attached, with $\boldsymbol{n}$ being the unit vector

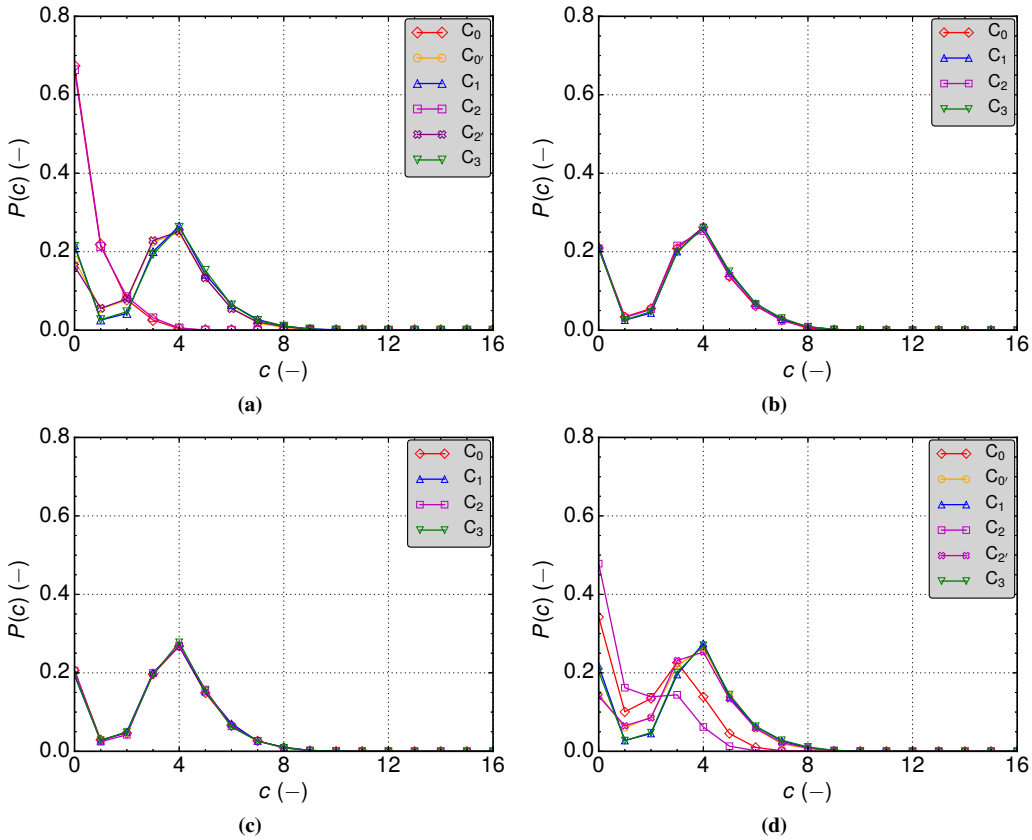

Figure 4.11: Connectivity diagram expressing the fraction $P(c)$ of particles with exactly c contacts at characteristic states in shear path of: (a) 1-D linear; (b) 2-D linear; (c) circular; (d) figure-8.

perpendicular to the contact plane and $\boldsymbol{t}$ an orthonormal unit vector in the contact plane oriented along the tangential contact force. Thus, the contact force $\boldsymbol{f} = f_n\boldsymbol{n} + f_t\boldsymbol{t}$, with f_n and f_t representing the magnitudes of normal and tangential contact forces, respectively. To quantify the proximity of a contact to sliding which is associated with soil plasticity (Alonso-Marroquin et al., 2005), one can introduce the friction mobilization index (Majmudar and Behringer, 2005; Azéma and Radjaï, 2012) defined by

$$I_m = \frac{|f_t|}{\mu_t f_n} \tag{4.6}$$

where μ_t refers to the tangential friction coefficient. This index varies between 0 and 1, with 1 indicating sliding or fully mobilized contact. Figure 4.12 presents the snapshots of the probability density function of I_m at selected states for the four shear paths. At C_0 and C_2 where shear stress vanishes for 1-D and figure-8 shear paths, one can expect a large proportion of mobilized contacts as shown in the inset window. The proportion of mobilized contacts decreases with increasing shear stress (Guo and Zhao, 2013), verified by C_1 and C_3. By Comparing C_0 with $C_{0'}$ or C_2 with $C_{2'}$, one can conclude that the force network is still not fully established despite the resilience of

geometrical contact network in Figures 4.10(a) and (d). Given the stability of the system for 2-D linear and circular shear paths, it is expected that $P(I_m)$ does not vary significantly, as shown in Figure 4.12(b) and (c) although Figure 4.12(b) exhibits a slight increase in the number of mobilized contacts at τ reaching its minimum (C_0 or C_2).

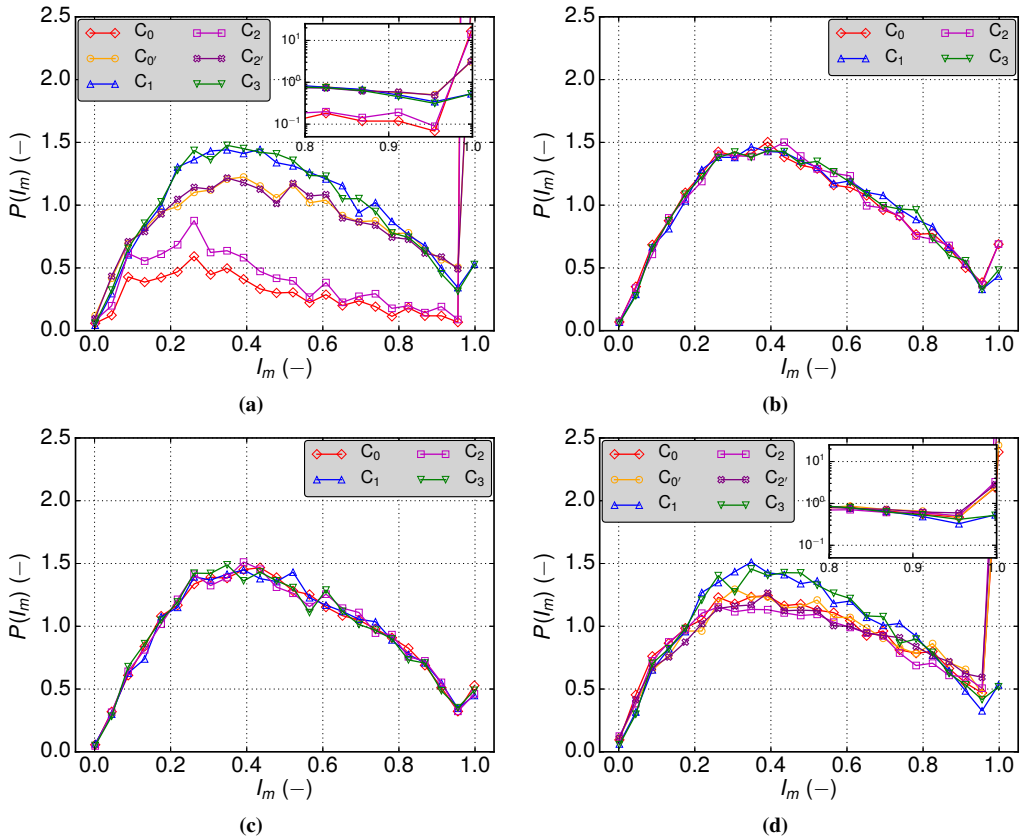

Figure 4.12: Probability density function of friction mobilization index at characteristic states in the shear path of: (a) 1-D linear; (b) 2-D linear; (c) circular; (d) figure-8.

Figure 4.13 shows snapshots of normal forces in sheared sample at C_2 for each shear path, i.e., the weakest state of the system in a post-liquefaction loading cycle. Forces are represented with bars joining particle centers with bar thickness proportional to the intensity of the normal force. The bar is colored according to the value of I_m at the contact. One can observe a scattering of weak and short force chains with a large proportion of mobilized contacts for 1-D linear and figure-8 shear paths, known as unjammed state (Bi et al., 2011; Huang et al., 2019a), and a span of strong and long force chains connecting top and bottom walls for 2-D linear and circular shear paths, confirming the static equilibrium.

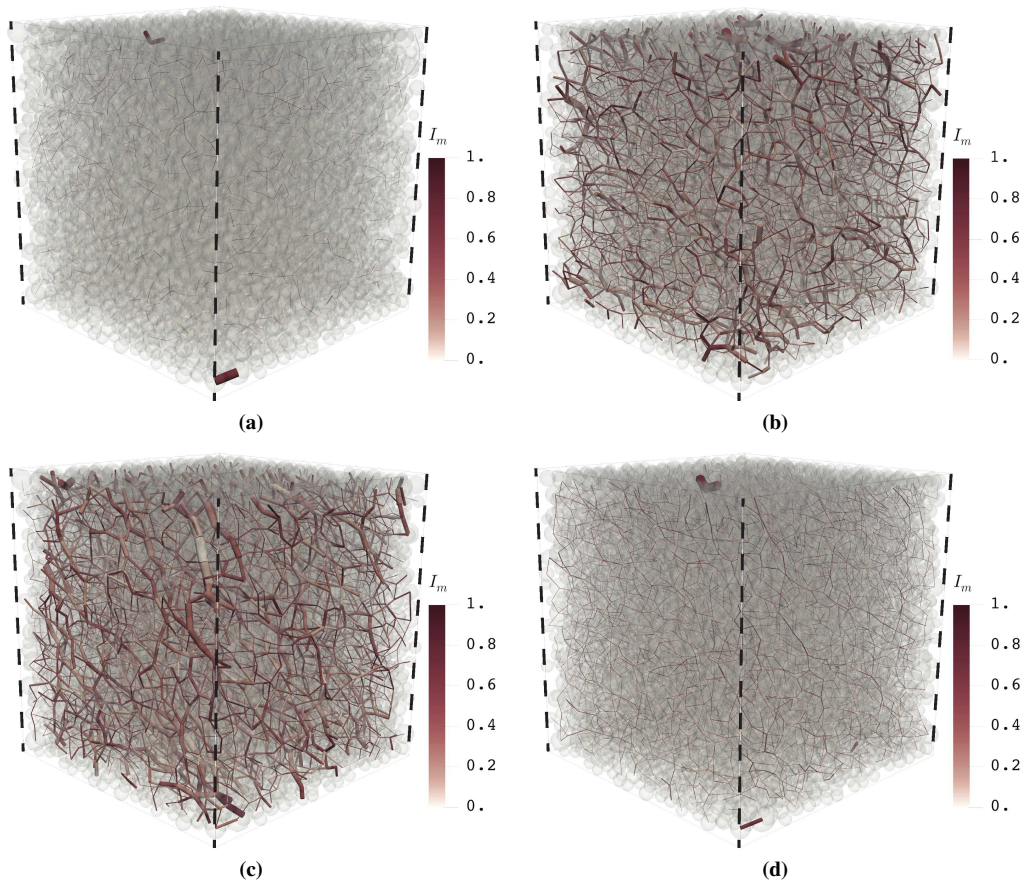

Figure 4.13: Snapshot of normal forces in the sheared sample at C_2 in the shear path of (a) 1-D linear; (b) 2-D linear; (c) circular; (d) figure-8. Line thickness is proportional to the normal force intensity. Color code represents the mobilized friction index I_m in the range between 0 and 1.

4.4.2 Particle-void fabric

The previous analysis concludes that the system falls into under-constrained state occasionally for 1-D linear and figure-8 shear paths and remains over-constrained for 2-D linear and circular paths. A subsequent natural question is why large shear strain still develops in the 2-D linear and circular tests as shown in Figures 4.4 and 4.5. The analysis of stress fluctuations during monotonic loading (Kuhn and Daouadji, 2019) may shed light on this question as local failure probably due to a multi-slip mechanism occurs very frequently despite the overall stability of the system. This local failure decreases the shear resistance gradually, inducing a mild increase of shear strain. For cyclic loading, an abrupt reduction in the number of sliding contacts is observed at the transition from loading to unloading (Alonso-Marroquin and Herrmann, 2004), producing a higher resistance. The distinct resistance between loading and unloading causes the accumulation of shear strain along one direction, i.e., the mode of development of residual deformation. In addition to these, one can resort to void-related fabrics in the particle system to search for some hints, given the consensus

that voids have been seen more directly related to the strain (Kuhn, 2017).

A particle-void indicator called centroid distance D_c is borrowed from Wang and Wei (2016) and Wei et al. (2020) to explain the shear strain development. For each particle i, one can obtain its circumscribed Voronoi cell, and thus the vector connecting the cell center $\boldsymbol{O}^i$ and particle center $\boldsymbol{P}^i$, also normalized by the mean radii of particles R_{50}, expressed as

$$\boldsymbol{D}_c^i = \frac{\boldsymbol{P}^i - \boldsymbol{O}^i}{R_{50}} \tag{4.7}$$

As a particle i surrounded by a large Voronoi cell tends to give a large value of $\left\|\boldsymbol{D}_c^i\right\|$, $\left\|\boldsymbol{D}_c^i\right\|$ can be used to reflect the distribution of voids surrounding the particles (Wei et al., 2020). Thus a centroid distance D_c averaging $\left\|\boldsymbol{D}_c^i\right\|$ over all the particles in the system is defined by

$$D_c = \frac{1}{N_p} \sum_{i \in N_p} \left\|\boldsymbol{D}_c^i\right\| \tag{4.8}$$

indicating the adjustment of the packing structure and redistribution of relatively large voids (Wang and Wei, 2016; Wei et al., 2020).

Figure 4.14 presents the evolutions of D_c for the four shear paths, along with the inset window for zooming up the selected loading cycle. The time history in each subplot is colored by the developed shear strain, as shown in the colorbar. Generally, for the four shear paths, at the beginning of cyclic loading prior to initial liquefaction, D_c does not change noticeably, then drops significantly near initial liquefaction, and follows a decreasing trend in post-liquefaction period. The values of D_c at initial liquefaction are very close (around 0.0704) for 1-D linear, circular and figure-8 paths, smaller than that of 2-D linear (around 0.0720), which may indicate that there still exists large voids in the test of 2-D linear compared with the others. This may be because in the 2-D linear test, the packing network is not fully destroyed according to Figure 4.10(b), constraining redistribution of voids due to cyclic shearing. One may notice the coincidence of D_c's significant drop and large shear strain accumulation, confirming the direct link between void redistribution and large shear strain development. From that view, the pre-liquefaction period can be seen as a duration of gradually propagating disturbance of cyclic loading (such as generating more connected but smaller voids) to the whole sample. The 2-D linear and circular tests imply the trend of D_c's saturation in the last few loading cycles, however, it is not reflected by 1-D linear and figure-8 paths (maybe more loading cycles are needed). In the zoomed-up windows of 1-D linear and figure-8 tests, the significant change mainly occurs between C_0 and $C_{0'}$, or C_2 and $C_{2'}$, corresponding to the deformation mode of cyclic mobility. In the zoomed-up windows of 2-D linear and circular tests, the change tends to happen randomly in the loading cycle, which may be

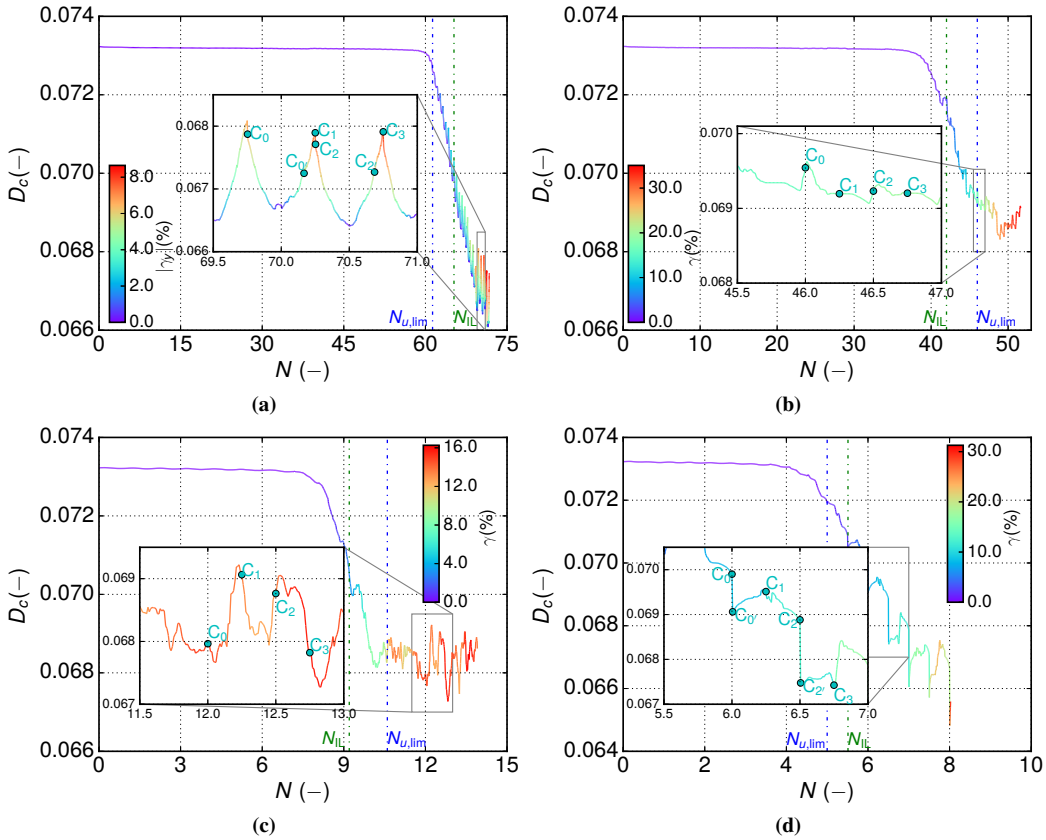

Figure 4.14: Evolution of centroid distance D_c for shear path of (a) 1-D linear; (b) 2-D linear; (c) circular; (d) figure-8.

linked to the mode of residual deformation development. Interestingly, in the zoomed-up window of 1-D linear test, D_c attains the local minima at nearly zero shear strain as indicated by the colorbar.

4.4.3 Fabric and force anisotropies

To quantify the anisotropies in the granular system statistically, the fabric tensor $\boldsymbol{\phi}_c$ describing the distribution of contact normals $\boldsymbol{n}$ (Oda, 1982; Satake, 1982) is adopted. It is defined as

$$\boldsymbol{\phi}_c = \frac{1}{N_c} \sum_{c \in N_c} \boldsymbol{n} \otimes \boldsymbol{n} \tag{4.9}$$

from which the fabric anisotropy tensor is computed as

$$\boldsymbol{a}_c = \frac{15}{2} \left(\boldsymbol{\phi}_c - \frac{1}{3} \boldsymbol{I} \right) \tag{4.10}$$

Here $\boldsymbol{I}$ is the second-order identity tensor.

In the same way, the force tensors describing the distribution of normal and tangential contact forces (Kanatani, 1984; Ouadfel and Rothenburg, 2001; Sitharam et al., 2009) are given by

$$\boldsymbol{\phi}_n = \frac{1}{N_c} \sum_{c \in N_c} \frac{f_n \boldsymbol{n} \otimes \boldsymbol{n}}{1 + \boldsymbol{a}_c : (\boldsymbol{n} \otimes \boldsymbol{n})} \tag{4.11}$$

$$\boldsymbol{\phi}_t = \frac{1}{N_c} \sum_{c \in N_c} \frac{\boldsymbol{f}_t \otimes \boldsymbol{n}}{1 + \boldsymbol{a}_c : (\boldsymbol{n} \otimes \boldsymbol{n})} \tag{4.12}$$

and thus the force anisotropy tensors can be obtained as

$$\boldsymbol{a}_n = \frac{15}{2} \left(\frac{\boldsymbol{\phi}_n}{\mathrm{tr}(\boldsymbol{\phi}_n)} - \frac{1}{3} \boldsymbol{I} \right) \tag{4.13}$$

$$\boldsymbol{a}_t = \frac{15}{3} \frac{\boldsymbol{\phi}_t}{\mathrm{tr}(\boldsymbol{\phi}_n)} \tag{4.14}$$

with $\mathrm{tr}(\cdot)$ being the trace operator. Equation (4.12) implies $\mathrm{tr}(\boldsymbol{\phi}_t) = 0$ given the normality of $\boldsymbol{t}$ and $\boldsymbol{n}$.

The tensor's deviatoric invariant is used to quantify the degree of anisotropy:

$$a_{[\,]} = \mathrm{sign}(S_{[\,]}) \sqrt{\frac{3}{2} \boldsymbol{a}_{[\,]} : \boldsymbol{a}_{[\,]}} \tag{4.15}$$

where the subscript $[\,]$ stands for c, n, or t, corresponding to the three aforementioned anisotropy tensors, respectively. $S_{[\,]}$ is a normalized first joint invariant between two tensors (Li and Dafalias, 2012; Guo and Zhao, 2013) defined by

$$S_{[\,]} = \frac{\boldsymbol{a}_{[\,]} : \mathbf{s}}{\sqrt{\boldsymbol{a}_{[\,]} : \boldsymbol{a}_{[\,]}} \sqrt{\mathbf{s} : \mathbf{s}}} \tag{4.16}$$

where $\mathbf{s} = \boldsymbol{\sigma} - p\boldsymbol{I}$ and the well-known deviatoric stress $q = \sqrt{(3/2)\mathbf{s} : \mathbf{s}}$. Generally $S_{[\,]}$ quantifies the level of proportionality between two tensors, with $S_{[\,]} = 1.0$ corresponding to the case where two tensors are proportional. Given these anisotropy tensors affected by $\mathbf{s}$, $S_{[\,]}$ can be approximately regarded as defining the relative orientation of the principal axes (PA) of $\boldsymbol{a}_{[\,]}$ with respect to PA of $\mathbf{s}$, i.e., level of coaxiality.

Figure 4.15 displays evolutions of $S_{[\,]}$ at the states of τ_y/p_0 reaching $\pm\mathrm{CSR}_y$ in each loading cycle for the four shear paths, i.e., C_1 and C_3 of each loading cycle, where the system forms stable load-bearing network according to the previous analysis of particle connectivity. In each loading cycle, one may expect the marked oscillations of $S_{[\,]}$, which is true for the 1-D linear, 2-D linear and figure-8 tests as presented in the zoomed-up window of each subplot but not for the circular

test. The difficulty dealing with cyclic loading is the absence of an ultimately converged state, like critical state (CS) for monotonic loading. For conventional cyclic simple shear test, the states closest to CS are C_1 and C_3, thus being extended to the other three shear paths. It is believed that q/p has its critical state values at these states after sufficient number of loading cycles.

Figure 4.15 indicates that force anisotropy tensors $\boldsymbol{a}_n$ and $\boldsymbol{a}_t$ have been almost proportional to $\mathbf{s}$ since the beginning of cyclic loading at C_1 and C_3 while it takes majority of the pre-liquefaction period to change the geometrical structure of the system so that $\boldsymbol{a}_c$ gets close to be proportional to the $\mathbf{s}$ at the selected states. In post-liquefaction period, all the anisotropy tensors become nearly proportional to $\mathbf{s}$ at selected states. During the selected loading cycle in each inset window, significant change in $S_{[\,]}$ is observed at the instance of unloading, where S_t oscillates most. In the subsequent loading, $\boldsymbol{a}_t$ and $\boldsymbol{a}_n$ adjust themselves to follow $\mathbf{s}$ more quickly than $\boldsymbol{a}_c$. It should be noted that the three anisotropy tensors from the circular shear path almost changes at the same pace to $\mathbf{s}$.

According to Rothenburg and Bathurst (1989) and Ouadfel and Rothenburg (2001), one can

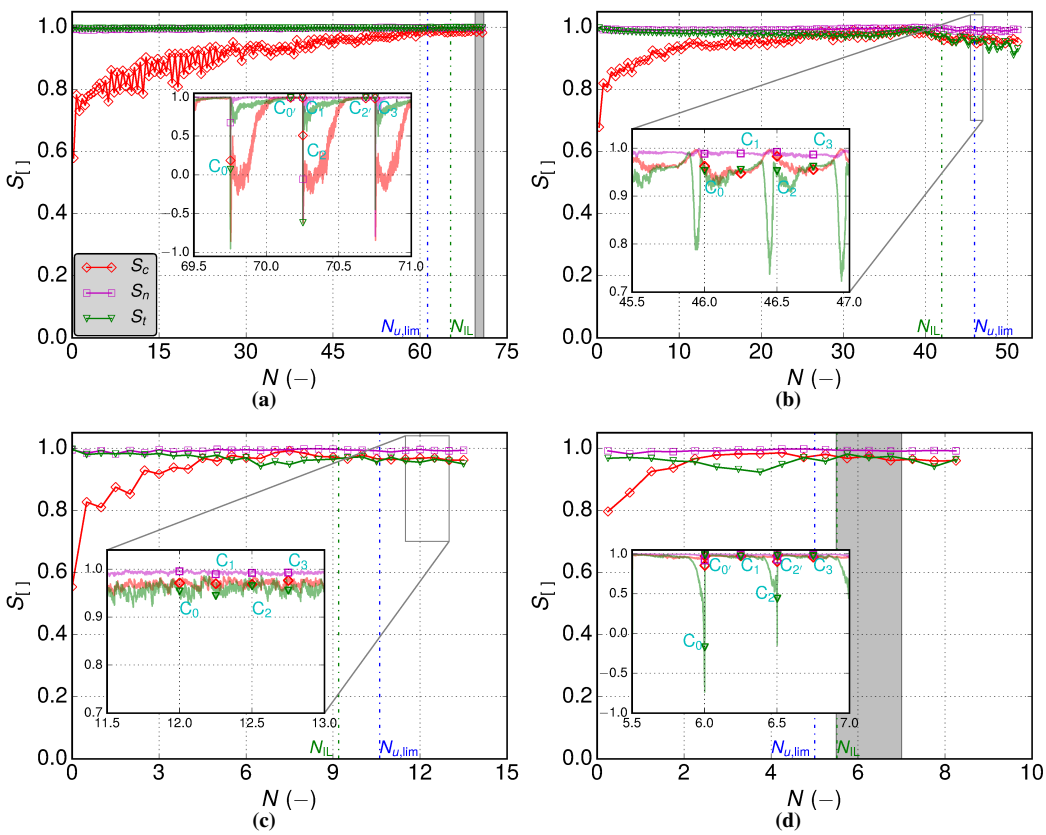

Figure 4.15: Evolution of normalized first joint invariant between fabric tensors and deviatoric stress tensor at C_1 and C_3 of each loading cycle for shear path of (a) 1-D linear; (b) 2-D linear; (c) circular; (d) figure-8.

approximate the shear strength via the aforementioned three anisotropy tensors as given below:

$$\frac{\mathbf{s}}{p} \simeq \frac{2}{5}\left(\boldsymbol{a}_c + \boldsymbol{a}_n + \frac{3}{2}\boldsymbol{a}_t\right) \tag{4.17}$$

Recall Figure 4.15 tells that these anisotropy tensors are nearly proportional at selected states after sufficient number of loading cycles, thus Equation (4.17) can be further simplified as

$$\frac{q}{p} \simeq \frac{2}{5}\left(a_c + a_n + \frac{3}{2}a_t\right) \tag{4.18}$$

Verification of Equation (4.18) for the four shear paths can be checked in Figures 4.16(a), (c), (e) and (g), where evolutions of fabric and force anisotropies at C_1 and C_3 of each loading cycle are presented, along with a zoomed-up window revealing the detailed change of anisotropies during the selected post-liquefaction loading cycle. In post-liquefaction period, saturation of the three anisotropies is finally achieved, with values increasing in the order of a_t, a_c and a_n. The oscillation of anisotropies is very similar to $S_{[\,]}$. Figures 4.16(b), (d), (f) and (h) normalized anisotropies and deviatoric stress ratio q/p by $(2/5)a_c + (2/5)a_n + (3/5)a_t$, i.e., the right hand side of Equation (4.18). Thus one can observe how each anisotropy contributes to q/p given the ratio between q/p and $(2/5)a_c + (2/5)a_n + (3/5)a_t$ being close to 1. It shows that after initial liquefaction, the weight of each anisotropy to q/p almost reaches a plateau, where the value for a_c is around 0.4, the value for a_n is around 0.5 and the value for a_t is around 0.1, irrespective of shear path type. One may attribute this universal partition to the intrinsic feature of the material and its state, which, for example, can be changed by particle shape and size polydispersity based on studies of monotonic loading (Nguyen et al., 2015; Cantor et al., 2018).

4.5 Conclusion

In this chapter, we used a 3D DEM to conduct a comprehensive series of multidirectional cyclic shear tests covering 1-D linear, 2-D linear, circular/oval, and figure-8 paths. At system level, accumulation of large shear strain is observed for all the simulated tests although mean stress does not vanish for some of them. A well-defined relationship between the limiting pore pressure ratio and the corresponding shear stress ratio was evidenced. With initial liquefaction defined by total shear strain reaching 3.0% for the first time, cyclic liquefaction resistance decreases in the order of 1-D linear, 2-D linear, circular and figure-8, for $\mathrm{AR} = \mathrm{CSR}_x/\mathrm{CSR}_y = 1$ in the two latter cases. As AR decreases with fixed value of CSR_y, both circular/oval and figure-8 paths present enhanced cyclic resistance, which is expected to approach the value of 1-D linear path as $\mathrm{AR} = 0$. As for effect of $\mathrm{SSR}_{[\,]}$, for all the shear paths, cyclic liquefaction resistance decreases first with increasing

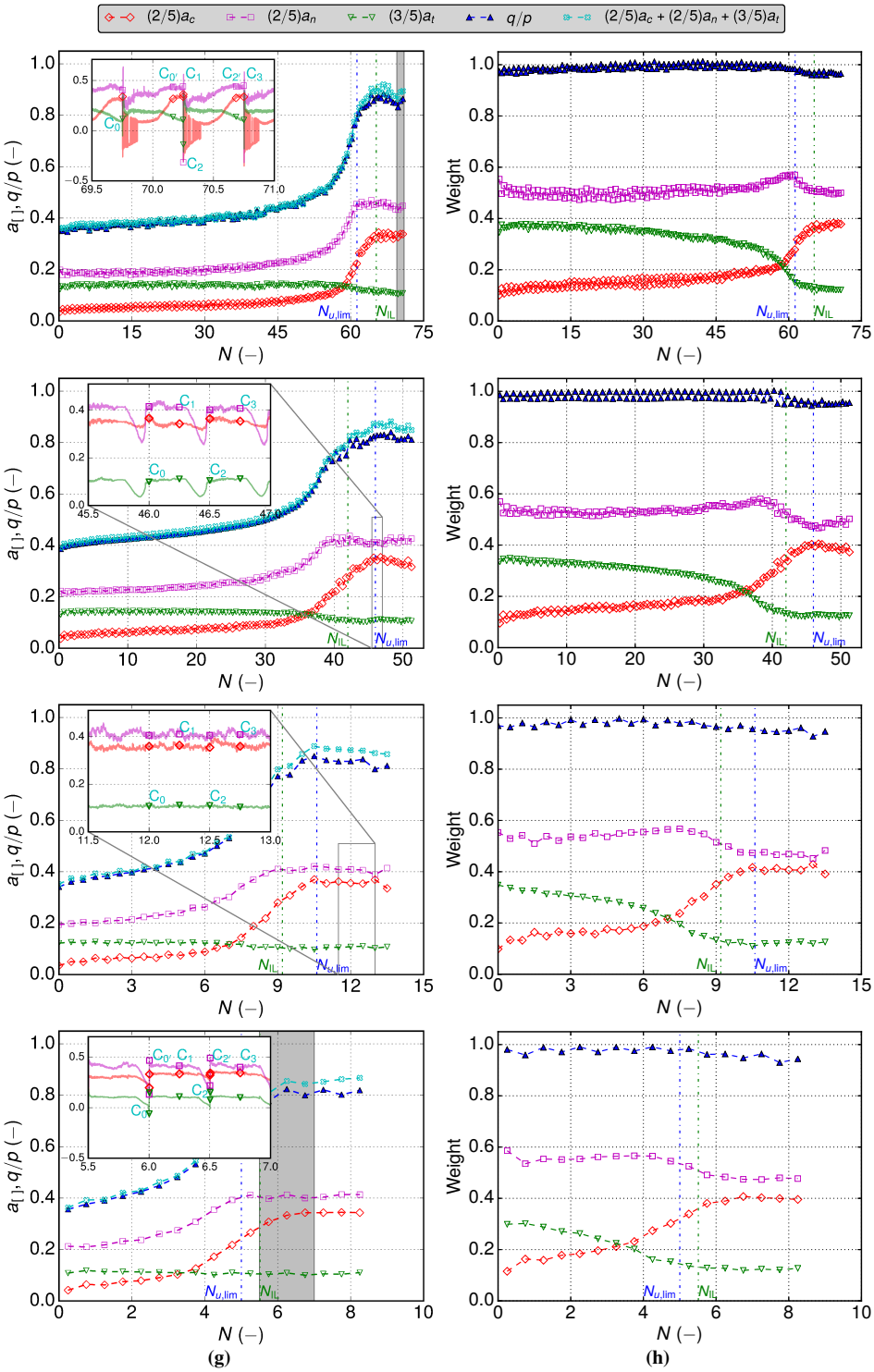

Figure 4.16: Evolution of anisotropies at C_1 and C_3 of each loading cycle and their weights contributing to deviatoric stress ratio q/p according to Equation (4.18) for shear path of (a)(b) 1-D linear; (c)(d) 2-D linear; (e)(f) circular; (g)(h) figure-8.

$SSR_{[\,]}$ and then increases later for the larger $SSR_{[\,]}$. However, a subsequent decrease in cyclic resistance is observed only for circular paths.

Micromechanical analysis was carried out on three aspects. From the view of system stability, the coordination number along with particle connectivity diagram indicates that the system becomes transiently under-constrained for 1-D linear and figure-8 shear paths, occurring at the instance of zero mean stress while the system stays over-constrained for 2-D linear and circular shear paths. The under-constrained state of the system is also characterized with a large proportion of mobilized contacts and a scattering of short and weak force chains. To understand the macro deformation mode, a particle-void fabric indicator called centroid distance D_c was adopted. A significant drop of D_c occurs near initial liquefaction, indicating noticeable redistribution of voids by destroying large voids into small ones. D_c presents a general decreasing trend in post-liquefaction period, related to accumulation of the shear strain. In 1-D linear and figure-8 tests, the change of D_c mainly happens when $r_u \geq 0.99$, corresponding to the deformation mode of cyclic mobility. In 2-D linear and circular tests, the change of D_c occurs randomly in the whole loading cycle, related to the deformation mode of residual deformation. Finally, fabric and force anisotropies were calculated to explain the source of the load-bearing network where force anisotropy tensors quickly become almost proportional to the deviatoric stress tensor while fabric anisotropy tensor needs most of pre-liquefaction period to follow the loading. The deviatoric stress ratio at the peak of applied shear stress can be well approximated by the sum of these anisotropies, and their weights in post-liquefaction period saturate, with the same values irrespective of shear path type.

The current study can be extended by incorporating aspherical particles or assemblies with different particle size distributions (PSD). It is expected that the observed mechanisms in this study in terms of macro response and microstructure of the granular system are expected to hold qualitatively even for other choices of particle shape and PSD affects, not most likely will be different quantitatively. For example, macroscopically, the values for quantifying the cyclic liquefaction resistance of samples under different shear paths may change but it is expected the decreasing order in terms of 1-D linear, 2-D linear, circular, and figure-8 remains valid. Microscopically, as the threshold for judging whether the system is under-constrained or over-constrained, i.e., the value of $z_g = 3.6$ may change; however, the presence of such a threshold is still expected. Similarly, the contribution from each anisotropy to the deviatoric stress ratio may vary but one still the stress-force-fabric relationship is still expected to remain valid by considering a contribution from the branch vector fabric. These extensions remain to be further explored further in future studies.

Chapter 5: SANISAND-MSf: a Memory Surface with Semifluidized State Enhanced Sand Plasticity Model for Undrained Cyclic Shearing

In this chapter, an advanced constitutive model is developed by incorporating a novel feature of memory surface and a simplified ingredient of semifluidized state into the reference DM04 model for more precise simulation of undrained unidirectional cyclic shear tests. This chapter is reproduced from the paper co-authored with Mahdi Taiebat and Yannis F. Dafalias, which was accepted subject to minor revisions for publication in *Géotechnique* (Yang et al., 2020a).

5.1 Introduction

During the dynamic analysis of geostructures, the phenomenon of sand liquefaction is a predominant event that must be accounted for. Hence, the underlying mechanism and patterns of liquefaction have been explored by laboratory experimentalists where regular harmonic loading is usually exerted on the soil specimen. An undrained cyclic torsional test on Ottawa-F65 sand with the relative density $D_{\mathrm{r}} = 60\%$ is presented in Figure 5.1 to illustrate the response when the sample is sheared with cyclic stress ratio (CSR) 0.20, where CSR is the ratio of the cyclic shear stress amplitude τ^{amp} and the initial mean effective stress p_0. The stress path of shear stress τ and mean effective stress p in Figure 5.1(a) and the shear stress-strain curves in Figure 5.1(b) can be decomposed into two stages based on whether the mean effective stress p reaches zero or not, named pre- and post-liquefaction stages, respectively, with the following response characteristics: (a) intense plastic volumetric contraction tendencies along with small shear strain in pre-liquefaction stage; (b) large but limited shear deformation with increasing amplitude in post-liquefaction stage where the mean effective stress almost vanishes instantaneously and repeatedly, also called cyclic mobility (Castro, 1975).

The effort to simulate numerically the foregoing two response characteristics has led to extensive exploration in developing different constitutive models in recent decades. Within the framework of bounding surface (BS) plasticity and hypoplasticity (Dafalias, 1986), Wang et al. (1990) formulated a plastic shear modulus dependence on the accumulated deviatoric plastic strain, which can effectively represent the response shown in Figure 5.1. Papadimitriou et al.

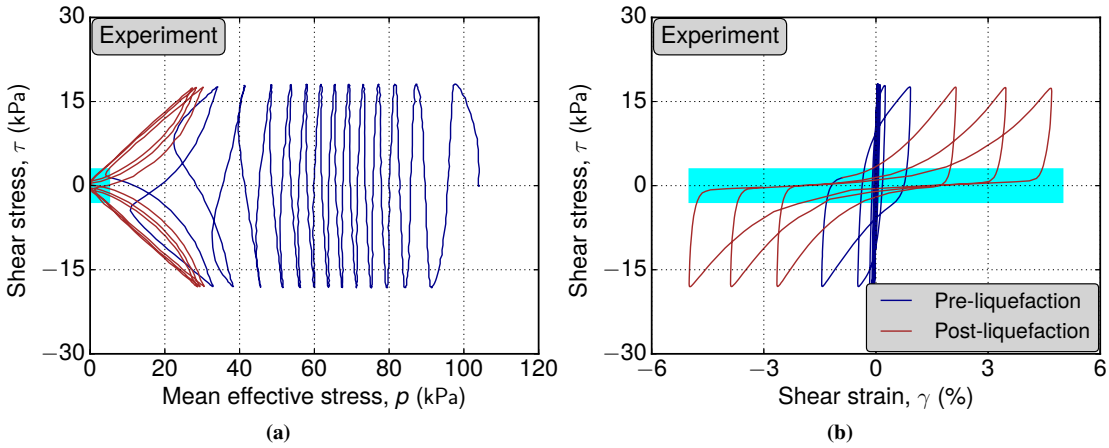

Figure 5.1: Experimental data of undrained cyclic torsional test for Ottawa-F65 sand at $D_r = 60\%$ after Ueda (2018): (a) stress path; (b) stress-strain response.

(2001), Papadimitriou and Bouckovalas (2002) and Dafalias and Manzari (2004), used a macroscopic fabric-dilatancy tensor to influence plastic modulus and dilatancy coefficient such that large contraction occurs upon loading reversal after a dilative phase that brings the mean effective stress p close to zero and enables the simulation of the typical butterfly shape as shown in Figure 5.1(a). To address bounded strain cyclic mobility, Elgamal et al. (2003) activated a constant-volume perfectly plastic phase with the stress state frozen when the loading stress path intersects the phase transformation line at low confinement, until a user-defined octahedral shear strain increment is accumulated. Khosravifar et al. (2018) updated the flow rule to address dependence on number of loading cycles, effective overburden stress and static shear stress. Boulanger and Ziotopoulou (2013) have addressed observed cyclic stiffness degradation as a function of quantities related to cumulative plastic shear strains and proposed accordingly the PM4Sand model that is based on the Dafalias and Manzari (2004) platform. Zhang and Wang (2012) and Wang et al. (2014) decomposed the dilatancy and volumetric strain rate into reversible and irreversible components, introduced the concept of volumetric strain threshold below which the soil is considered liquefied, and used cumulative irreversible volumetric strain as a model parameter. In addition, these authors were able to address the phenomenon of large but limited shear strain accumulation in the post-liquefaction stage.

These and several other similar approaches have contributed significantly to the modeling of cyclic mobility, however, they share a general shortcoming and a lack of calibration flexibility on separate pre- and post-liquefaction response simulations. The shortcoming is the use of a quantity related to cumulative plastic volumetric or shear strain in their formulation for dilatancy determination or stiffness degradation, that stays in the model after the completion of a cyclic loading process, based on the non-decreasing nature of a cumulative quantity. Yet, there is no constitutive mechanism to eliminate such influence in a subsequent drained monotonic or

undrained cyclic loading, which are thus affected unduly and irrationally by a past cyclic loading event. The lack of calibration flexibility is that while these models can fit by purpose the practically important liquefaction strength curve, i.e., CSR versus the total number of cycles N_{ini} for reaching the so-called initial liquefaction, such overall fitting does not correspond necessarily to correct fitting of the general stress-strain and undrained stress path response in the pre- and post-liquefaction stages separately. This is because there are no constitutive mechanisms for addressing the cyclic response separately for pre- and post-liquefaction stages.

The objective of this work is to present a new constitutive model for sands, by remedying two simulative inadequacies of a reference two-surface constitutive model by Dafalias and Manzari (2004), abbreviated as DM04 model, which is an extension of its precursor by Manzari and Dafalias (1997). The DM04 model is critical state compatible and is built within the framework of Bounding Surface (BS) plasticity, thus, by the very nature of BS it can address qualitatively the response under cyclic loading. However, the first simulative inadequacy is that with stiffness determined by fitting monotonic undrained loading, it overpredicts the pore water pressure and shear strain accumulation under cyclic loading in the pre-liquefaction stage. Increasing the stiffness by means of increasing the value of the plastic modulus K_{p}, will address successfully both pore water pressure and shear strain accumulation simultaneously, since both depend on plastic modulus, but at the same time it will disqualify the simulation under monotonic loading. It is therefore necessary to invent a constitutive scheme that can increase the stiffness under cyclic loading without altering the stiffness under monotonic.

This scheme introduces a new constitutive ingredient described by the concept and role of "memory surface" (MS) in stress space that stores the previously experienced maximum stress ratio while increasing the stiffness for stress states within MS without altering the stiffness for stress states on the MS during monotonic loading. Memory surfaces of various types go quite back in time as in Wang et al. (1990), Stallebrass and Taylor (1997), Maleki et al. (2009) and di Benedetto et al. (2014). The MS adopted in this study is a multifaceted modification of the original proposition by Corti et al. (2016) that was later adjusted by Liu et al. (2019) to be compatible with the DM04 model platform. The use of MS was shown to be successful in simulating plastic volumetric and deviatoric strain variations in drained cyclic shear tests but has not yet been tested extensively for simulations of multiple data under undrained conditions. It must be mentioned that the MS introduced by Corti et al. (2016), fades away during extensive dilation, usually obtained by extensive monotonic loading of dense samples, thus, returning to its original size before the cyclic loading and is ready to play again its role upon a new such loading.

The second simulative inadequacy of the reference DM04 model is that after reaching the post-liquefaction stage under undrained cyclic loading, the undrained stress path stabilizes acquiring the usual butterfly shape, and similarly the cyclic stress-strain loops stabilize at a fixed

shear strain amplitude. And while the butterfly stabilized shape is desirable for the undrained stress path because it is exactly what experimental data show, the stress-strain stabilization is against the experimental observation of increasing shear amplitude with number of post-liquefaction cycles, with an eventual saturation level. Contrary to what was done with the MS for pre-liquefaction stage, namely to increase the stiffness via the plastic modulus K_p for both deviatoric and volumetric plastic strain rates, now one must progressively decrease the stiffness only for deviatoric plastic strain rate in order to achieve the increasing shear strain amplitude, while maintaining the same stiffness for plastic volumetric strain rate in order to maintain the stabilized butterfly shaped undrained stress path. This new combination of stiffness modification protocol can be achieved by decreasing simultaneously by the same factor the plastic modulus K_p and the dilatancy D. This is because the decrease of K_p will achieve the shear strain amplitude increase while the same decrease of D will maintain fixed the value of the ratio D/K_p on which the plastic volumetric strain rate and consequently the undrained stress path depend, thus maintaining the same butterfly shape of the latter. Notice that the foregoing conclusions are valid for any plasticity model because they address the basic constitutive relations irrespective of the specific format they acquire.

The above required constitutive modification to the DM04 model was in fact addressed in Barrero et al. (2020) by a new constitutive ingredient reflecting the physical existence of a "semifluidized (Sf) state" for very low effective mean stress reached in post-liquefaction stage. It introduced a new internal degradation variable for plastic modulus and dilatancy, named Strain Liquefaction Factor (SLF), that increases towards a saturation value of unity during undrained cyclic loading, while it demises in a continuous way upon subsequent drainage. Notice that both the evolution of, and analytical effect on K_p and D by the SLF are active only for states within the semifluidized state while leaving almost intact the response outside that state. More details can be found in the foregoing reference and in a subsequent section of this work.

It is worth mentioning at the outset, that the introduction of the two new constitutive ingredients of MS and SLF, besides remedying the two simulative inadequacies of the DM04 model under undrained cyclic loading, they also address the aforementioned shortcoming and lack of calibration flexibiblity encountered in various other constitutive models. First, the fact that MS fades away upon dilation and SLF demise upon drainage, allows a new cyclic loading to start anew without unjustified effect from a previously performed cyclic loading that resulted in accumulated and permanently stored quantities such a cumulative shear strain. Second, the MS and SLF aim at improving the cyclic stress-strain response for pre- and post-liquefaction stages, respectively, without affecting each other, thus, they contain the seed for a separate rather than overall successful simulation of the CSR versus total number of cycles for reaching initial liquefaction. This does not necessarily mean that other models cannot achieve the same goal, but

here at least it is achieved by separate constitutive design for each stage.

The new model maintains of course all innate capabilities of the DM04 model to be Critical State compatible and effective in simulating the response under various pressures and densities using a unique set of model constants for monotonic loading. In fact, its simulating capability of monotonic non-proportional loading is and control of strain accumulation under cyclic triaxial loading in compression and extension, is improved by two small modifications that will be described in the next section. Its effectiveness for cyclic loading will be shown by successful simulation of two extensive experimental databases on undrained cyclic torsional and triaxial tests with different CSRs. In the process, the detailed calibration procedures for the model constants related to the new constitutive ingredients, the semifluidized state and the memory surface, will be fully explained. These two new constitutive ingredients suggest the name SANISAND-MSf for the model, because it is a member of the SANISAND family of models (Taiebat and Dafalias, 2008), with M standing for Memory surface and Sf for Semifluidized state.

In terms of basic notation, tensor-value quantities will be shown by bold face characters and the symbol : between two tensors denotes summations over the adjacent pairs of indices in reverse order of the tensors, which in the case of second-order tensors implies the trace, namely $\mathrm{tr}(\mathbf{AB}) = \mathbf{A} : \mathbf{B} = A_{ij}B_{ji}$.

5.2 Reference DM04 model

The DM04 has four conical surfaces as illustrated in Figure 5.2 in the deviatoric stress space, shown for convenience only as the π-plane for the stress ratio. These surfaces are a small yield

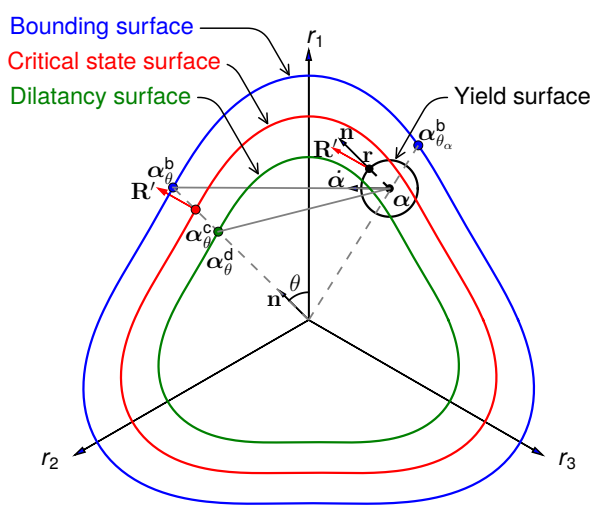

Figure 5.2: Schematic illustration of model surfaces and mapping rules on the deviatoric stress ratio π plane.

surface (YS) centred at the back-stress ratio $\boldsymbol{\alpha}$ that obeys kinematic hardening (KH), and three other origin-concentric surfaces: bounding surface (BS), critical state surface (CS), and dilatancy surface (DS). A mapping rule from the origin along the unit-norm deviatoric tensor $\mathbf{n}$, normal to the YS at the stress ratio $\mathbf{r}$, specify image points on BS and DS whose distances from the current back-stress ratio $\boldsymbol{\alpha}$ control the plastic modulus and dilatancy, respectively.

The constitutive equations of the DM04 model are presented collectively in Table 5.1, together with some modifications to be discussed in the sequel. With more details provided in Dafalias and Manzari (2004), it is only expedient to briefly outline here the symbols and basic definitions. The elastic and plastic strains are denoted by the superscripts e and p, respectively, while a superposed dot implies the rate. The $p = \mathrm{tr}(\boldsymbol{\sigma})/3$ is the mean effective stress, with $\boldsymbol{\sigma}$ being the effective stress tensor and $\mathrm{tr}(\cdot)$ the trace operator; $\mathbf{s} = \boldsymbol{\sigma} - p\mathbf{I}$ is the deviatoric stress tensor, with $\mathbf{I}$ being the second-order identity tensor, and $\mathbf{r} = \mathbf{s}/p$ is the stress ratio in Figure 5.2; $\varepsilon_{\mathrm{v}} = \mathrm{tr}(\boldsymbol{\varepsilon})$ is the volumetric strain, with $\boldsymbol{\varepsilon}$ being the strain tensor; $\mathbf{e} = \boldsymbol{\varepsilon} - \left(\varepsilon_{\mathrm{v}}/3\right)\mathbf{I}$ is the deviatoric strain tensor; L is the plastic multiplier that includes the plastic modulus K_{p} in its denominator and is enclosed into the Macaulay brackets such that $\langle L \rangle = L$ if $L \geq 0$ and $\langle L \rangle = 0$ if $L < 0$; D is the dilatancy ratio; $\mathbf{R}'$ represents the deviatoric flow rule direction normal to the CS surface at the image point $\boldsymbol{\alpha}^{\mathrm{c}}_{\theta}$, also shown transferred at the stress ratio point $\mathbf{r}$, Figure 5.2. The A_0 and h are directly related to dilatancy and plastic modulus, respectively, and their definitions are of cardinal importance for the performance of the model. The $\mathbf{z}$ is an evolving dilatancy fabric tensor whose role is to induce large contraction upon unloading after a dilative phase. The $\boldsymbol{\alpha}_{\mathrm{in}}$ is the initial value of $\boldsymbol{\alpha}$ at initialization of a new loading process and is updated when the denominator of h becomes negative as per the rules discussed by Dafalias (1986). The $g(\theta, c)$ is the interpolation function for the DS, BS and CS, with θ the Lode angle and c the ratio between triaxial extension and compression critical stress ratio values; $\psi = e - e_{\mathrm{c}}$ is the state parameter (Been and Jefferies, 1985) defined as the difference between the current void ratio e and the critical void ratio e_{c} at same p on the Critical State Line (CSL) in the $e - p$ space (Li and Wang, 1998).

Two modifications are introduced to the DM04 model. The first defines a modified flow rule along $\mathbf{R}^*$ obtained by interpolation between $\mathbf{n}$ and the unit norm $\mathbf{R}'/||\mathbf{R}'||$, with $||.||$ being the norm operator, as:

$$\mathbf{R}^* = I(x_\alpha)\mathbf{n} + [1 - I(x_\alpha)]\frac{\mathbf{R}'}{||\mathbf{R}'||} \tag{5.1}$$

with the interpolation factor $x_\alpha = \langle \alpha^{\mathrm{b}}_{\theta_\alpha} - ||\boldsymbol{\alpha}|| \rangle / \alpha^{\mathrm{b}}_{\theta_\alpha}$ measuring the relative distance of $\boldsymbol{\alpha}$ from its BS projection $\boldsymbol{\alpha}^{\mathrm{b}}_{\theta_\alpha}$ along the radius from the origin (see Figure 5.2 and Table 5.1 for the definition of the unbold $\alpha^{\mathrm{b}}_{\theta_\alpha}$); the $I(x_\alpha)$ is an interpolation function varying together with x_α from 1 to 0, as $\boldsymbol{\alpha}$ moves from the origin onto or outside the BS, and accordingly the $\mathbf{R}^*$ varies from $\mathbf{n}$ to

Table 5.1: Changes from basic to modified DM04 model equations related to flow rule and dilatancy updates.

Description	DM04 equations	Modified equations	Constants
Elastic relations	$\dot{\varepsilon}_{\mathrm{v}}^{\mathrm{e}} = \dot{p}/K;\ \ \dot{\mathbf{e}}^{\mathrm{e}} = \dot{\mathbf{s}}/(2G)$		
Plastic relations	$\dot{\varepsilon}_{\mathrm{v}}^{\mathrm{p}} = \langle L \rangle D;\ \dot{\mathbf{e}}^{\mathrm{p}} = \langle L \rangle \mathbf{R}'$	$\dot{\mathbf{e}}^{\mathrm{p}} = \langle L \rangle \mathbf{R}^*$	
Hypoelastic moduli	$G = G_0 p_{\mathrm{at}}(2.97-e)^2/(1+e)(p/p_{\mathrm{at}})^{1/2}$		G_0
	$K = 2(1+\nu)/[3(1-2\nu)G]$		ν
Yield surface	$f = \sqrt{(\mathbf{s}-p\boldsymbol{\alpha}):(\mathbf{s}-p\boldsymbol{\alpha})} - \sqrt{2/3}pm = 0$		m
Dilatancy	$D = A_0(1+\langle \mathbf{z}:\mathbf{n}\rangle)(\boldsymbol{\alpha}_\theta^{\mathrm{d}} - \boldsymbol{\alpha}):\mathbf{n}$	$D = A_0 g(\theta,c)^{-n_g}(1+\langle \mathbf{z}:\mathbf{n}\rangle)(\boldsymbol{\alpha}_\theta^{\mathrm{d}} - \boldsymbol{\alpha}):\mathbf{n}$	A_0, n_g
Deviatoric flow rule	$\mathbf{R}' = B\mathbf{n} - C[\mathbf{n}^2 - (1/3)\mathbf{I}]$	$\mathbf{R}^* = x_\alpha^2\mathbf{n} + (1-x_\alpha^2)\mathbf{R}'/\|\|\mathbf{R}'\|\|$	
	$\mathbf{n} = (\mathbf{r}-\boldsymbol{\alpha})/\|\|\mathbf{r}-\boldsymbol{\alpha}\|\|$	$x_\alpha = \langle \alpha_{\theta_\alpha}^{\mathrm{b}} - \|\|\boldsymbol{\alpha}\|\|\rangle/\alpha_{\theta_\alpha}^{\mathrm{b}}$	
	$B = 1+3(1-c)/(2c)g(\theta,c)\cos 3\theta$	$\alpha_{\theta_\alpha}^{\mathrm{b}} = \sqrt{2/3}[g(\theta_\alpha,c)M\exp(-n^{\mathrm{b}}\psi)-m]$	c
	$C = 3\sqrt{3/2}(1-c)g(\theta,c)/c$	$\cos 3\theta_\alpha = \sqrt{6}\mathrm{tr}(\mathbf{n}_\alpha^3);\ \mathbf{n}_\alpha = \boldsymbol{\alpha}/\|\|\boldsymbol{\alpha}\|\|$	
	$g(\theta,c) = 2c/[(1+c)-(1-c)\cos 3\theta]$		
Kinematic hardening	$\dot{\boldsymbol{\alpha}} = \langle L \rangle (2/3)h(\boldsymbol{\alpha}_\theta^{\mathrm{b}} - \boldsymbol{\alpha})$		
Fabric-dilatancy rate	$\dot{\mathbf{z}} = -c_z\langle -\dot{\varepsilon}_{\mathrm{v}}^{\mathrm{p}}\rangle(z_{\max}\mathbf{n}+\mathbf{z})$		c_z, $z_{\max}$
Hardening coefficient	$h = b_0/[(\boldsymbol{\alpha}-\boldsymbol{\alpha}_{\mathrm{in}}):\mathbf{n}]$		
	$b_0 = G_0 h_0(1-c_h e)(p/p_{\mathrm{at}})^{-1/2}$	$b_0 = G_0 h_0 g(\theta,c)^{-n_g}(1-c_h e)(p/p_{\mathrm{at}})^{-1/2}$	h_0, c_h
Image point on DS	$\boldsymbol{\alpha}_\theta^{\mathrm{d}} = \sqrt{2/3}[g(\theta,c)M\exp(n^{\mathrm{d}}\psi)-m]\mathbf{n}$		n^{d}, M
Image point on BS	$\boldsymbol{\alpha}_\theta^{\mathrm{b}} = \sqrt{2/3}[g(\theta,c)M\exp(-n^{\mathrm{b}}\psi)-m]\mathbf{n}$		n^{b}
Critical state line	$e_{\mathrm{c}} = e_{\mathrm{c}}^{\mathrm{ref}} - \lambda_{\mathrm{c}}(p/p_{\mathrm{at}})^{\xi}$		$e_{\mathrm{c}}^{\mathrm{ref}}$, λ_{c}, ξ

$\mathbf{R}'/||\mathbf{R}'||$. The choice $I(x_\alpha) = x_\alpha^2$ is made for simplicity here, as shown in the third column of Table 5.1, without adding a new constant (the exponent 2 is a default value). Alternative choices are possible as for example one variant of the sigmoidal function widely used in machine learning $\sigma(x_\alpha) = I(x_\alpha) = 1/\{1 + \exp[-k(x_\alpha - R_\mathrm{c})]\}$ that approaches 1 and 0 as close as desired by the specification of its two constants k and R_c. Figure 5.3 shows the simulation versus data for undrained simple shear test of Toyoura sand (data from Yoshimine et al. (1998), also appeared in Figure 12 of Dafalias and Manzari (2004)) using four different flow rules associated with $\mathbf{n}$, $\mathbf{R}'$ and two $\mathbf{R}^*$ according to Equation (5.1) with the aforementioned two interpolation functions. The

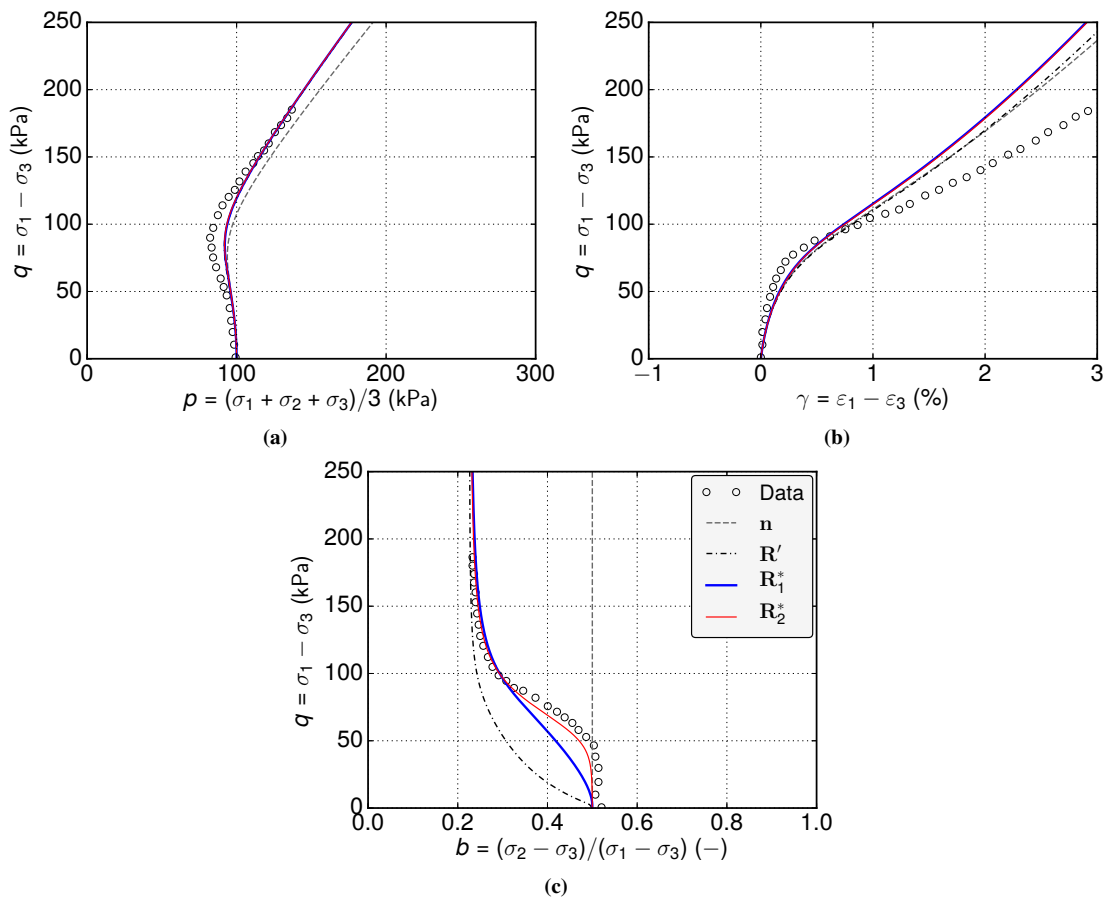

Figure 5.3: Simulation of undrained simple shear test data of Toyoura sand (Yoshimine et al., 1998) using flow rules associated with n, R′ and from Equation (5.1) $\mathbf{R}_1^*$ for $I(x_\alpha) = x_\alpha^2$ and $\mathbf{R}_2^*$ for $I(x_\alpha) = \sigma(x_\alpha)$ where $k = 15$ and $R_\mathrm{c} = 0.6$.

plots in Figure 5.3(a) and (b) do not differ significantly, but the one in Figure 5.3(c) shows the advantages of using the modified flow rule for non-proportional loading.

The second modification consists of dividing dilatancy D and plastic modulus K_p, by $g(\theta, c)^{n_g}$ with n_g a model constant, as shown in the third column of Table 5.1; the foregoing division of K_p is achieved by dividing the b_0 term of its coefficient h. Dividing both D and K_p by the same factor, maintains the same plastic volumetric strain rate and correspondingly pore water pressure rate, and

undrained stress paths, while controlling the relative magnitude of shear strain amplitude in triaxial compression and extension, thus, allowing to control by a proper choice of n_g the shifting of the stress-strain loops during cyclic triaxial loading. The use of $g(\theta, c)^{n_g}$ has a minimal effect on the stress-strain curve in extension, while compression is unaltered because $g(\theta, c)^{n_g} = 1$.

5.3 Memory surface

The memory surface (MS) by Corti et al. (2016) and its extension by Liu et al. (2019) is equipped with both isotropic and kinematic hardening (KH) in the deviatoric stress ratio space, and its role is that of an auxiliary bounding surface aimed at adding extra stiffness to the deviatoric and volumetric plastic strain rates for stress points within the MS prompted by comparison of simulations with data. It is thought that the role of the MS as a stiffening constitutive ingredient is related to micromechanical fabric characteristics adjustments due to experienced past loading range in stress space.

The formulation of memory surface developed in this study is different from that of Corti et al. (2016) and Liu et al. (2019) in regard to the following aspects:

- It is a MS for the back-stress ratio rather than stress ratio, compatible with the formulation of DM04 model, that allows the minimum of its size to be zero.
- It derives the evolution of MS in general, using BS techniques, as opposed to the assumption that the virgin loading formulation is extended to cases under general loading (Liu et al., 2019).
- It tackles the singular case where a denominator can go to zero under certain loading conditions, existing in Liu et al. (2019).
- It does not make use of MS for the determination of dilatancy D that is evaluated with the equation listed in Table 5.1 using the dilatancy fabric tensor $\mathbf{z}$, according to DM04 model. If an improvement of dilatancy is found necessary, one could make use of the dilatancy-triggering surface proposed by Woo et al. (2019) in a role similar to that of the MS while being compatible with the DM04 model platform.

The memory surface is defined analytically by:

$$f^{\mathrm{M}} = \sqrt{(\boldsymbol{\alpha}_{\theta}^{\mathrm{M}} - \boldsymbol{\alpha}^{\mathrm{M}}) : (\boldsymbol{\alpha}_{\theta}^{\mathrm{M}} - \boldsymbol{\alpha}^{\mathrm{M}})} - \sqrt{2/3} m^{\mathrm{M}} = 0 \tag{5.2}$$

where $\boldsymbol{\alpha}^{\mathrm{M}}$ is its center and m^{M} its size. As illustrated in Figure 5.4, $\boldsymbol{\alpha}_{\theta}^{\mathrm{M}}$ is the image point of $\boldsymbol{\alpha}$ on the MS obtained by projection from $\boldsymbol{\alpha}^{\mathrm{M}}$ along $\mathbf{n}$ on it, expressed analytically by:

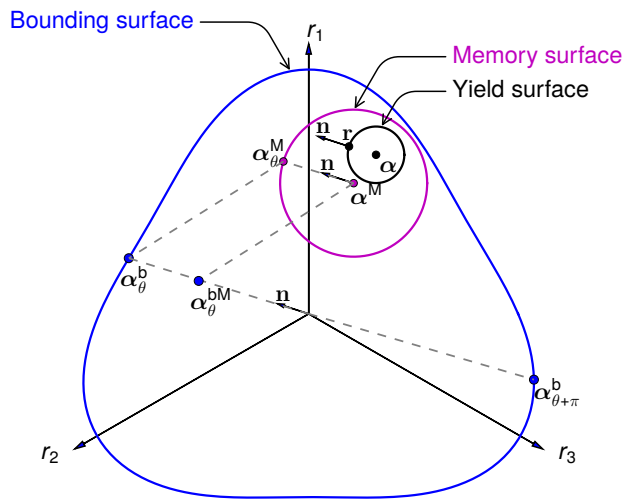

Figure 5.4: Illustration of the conceptual framework of bounding-memory surface models.

$$\boldsymbol{\alpha}_\theta^{\mathrm{M}} = \boldsymbol{\alpha}^{\mathrm{M}} + \sqrt{\frac{2}{3}} m^{\mathrm{M}} \mathbf{n} \tag{5.3}$$

where the use of the subscript θ in all the above is indicative of the corresponding Lode angle θ. The distance of $\boldsymbol{\alpha}$ from $\alpha_\theta^{\mathrm{M}}$ projected on $\mathbf{n}$, will be the key new quantity for increasing the stiffness. During the loading process one must make sure that the $\boldsymbol{\alpha}$ does not move outside the MS so that the aforementioned quantity remains positive. To this extent, one can write:

$$\begin{aligned}\dot{\boldsymbol{\alpha}} &= \dot{\boldsymbol{\alpha}}_\theta^{\mathrm{M}} + \langle L \rangle \frac{2}{3} h^* (\boldsymbol{\alpha}_\theta^{\mathrm{M}} - \boldsymbol{\alpha}) \\ &= \dot{\boldsymbol{\alpha}}^{\mathrm{M}} + \sqrt{\frac{2}{3}} \dot{m}^{\mathrm{M}} \mathbf{n} + \sqrt{\frac{2}{3}} m^{\mathrm{M}} \dot{\mathbf{n}} + \langle L \rangle \frac{2}{3} h^* (\boldsymbol{\alpha}_\theta^{\mathrm{M}} - \boldsymbol{\alpha})\end{aligned} \tag{5.4}$$

where the rate of Equation (5.3) was used in deriving Equation (5.4) which is valid for $\boldsymbol{\alpha}$ inside or on the MS. Equation (5.4) simply states that $\boldsymbol{\alpha}$ will move as much as its image point $\boldsymbol{\alpha}_\theta^{\mathrm{M}}$ plus an additional motion along $\boldsymbol{\alpha}_\theta^{\mathrm{M}} - \boldsymbol{\alpha}$ controlled by a free to choose modulus h^*, hence, guaranteeing that $\boldsymbol{\alpha}$ will never cross and move outside the MS because the additional motion will stop when $\boldsymbol{\alpha}_\theta^{\mathrm{M}} - \boldsymbol{\alpha} = \mathbf{0}$ no matter what the value of h^* is. By multiplying Equation (5.4) with $\mathbf{n}$ and taking the trace of each term one obtains:

$$\dot{\boldsymbol{\alpha}} : \mathbf{n} = \dot{\boldsymbol{\alpha}}^{\mathrm{M}} : \mathbf{n} + \sqrt{\frac{2}{3}} \dot{m}^{\mathrm{M}} + \langle L \rangle \frac{2}{3} h^* (\boldsymbol{\alpha}_\theta^{\mathrm{M}} - \boldsymbol{\alpha}) : \mathbf{n} \tag{5.5}$$

noticing that $\dot{\mathbf{n}} : \mathbf{n} = 0$ implied by $\mathbf{n} : \mathbf{n} = 1$. Equation (5.5) becomes the consistency condition for the MS when $\boldsymbol{\alpha}$ is on it, i.e., when $\boldsymbol{\alpha}_\theta^{\mathrm{M}} - \boldsymbol{\alpha} = \mathbf{0}$ as can be seen by taking the rate of f^{M} in Equation (5.2) and observing from Figure 5.4 that the normal $\mathbf{n}$ to the YS at $\mathbf{r}$, is same with the

normal $\mathbf{n}$ to the MS at $\boldsymbol{\alpha}_\theta^{\mathrm{M}}$.

5.3.1 Rate of $\boldsymbol{\alpha}^{\mathrm{M}}$

Referring to Figure 5.4 one can observe that eventually $\boldsymbol{\alpha}$ will reach the BS at its image point $\boldsymbol{\alpha}_\theta^{\mathrm{b}}$ and the MS at its image point $\boldsymbol{\alpha}_\theta^{\mathrm{M}}$, thus, $\boldsymbol{\alpha}_\theta^{\mathrm{M}}$ will reach the BS at the same point $\boldsymbol{\alpha}_\theta^{\mathrm{b}}$. Consequently the $\boldsymbol{\alpha}^{\mathrm{M}}$ will reach a point $\boldsymbol{\alpha}_\theta^{\mathrm{bM}}$, which is inwards from $\boldsymbol{\alpha}_\theta^{\mathrm{b}}$ along $\mathbf{n}$ and defined by:

$$\boldsymbol{\alpha}_\theta^{\mathrm{bM}} = \boldsymbol{\alpha}_\theta^{\mathrm{b}} - \sqrt{\frac{2}{3}} m^{\mathrm{M}} \mathbf{n} \tag{5.6}$$

Based on Equations (5.3) and (5.6) one has $\boldsymbol{\alpha}_\theta^{\mathrm{bM}} - \boldsymbol{\alpha}^{\mathrm{M}} = \boldsymbol{\alpha}_\theta^{\mathrm{b}} - \sqrt{2/3} m^{\mathrm{M}} \mathbf{n} - \boldsymbol{\alpha}^{\mathrm{M}} = \boldsymbol{\alpha}_\theta^{\mathrm{b}} - \boldsymbol{\alpha}_\theta^{\mathrm{M}}$, thus, the following rate equation of evolution can be written for $\boldsymbol{\alpha}^{\mathrm{M}}$:

$$\dot{\boldsymbol{\alpha}}^{\mathrm{M}} = \langle L \rangle \frac{2}{3} h^{\mathrm{M}} (\boldsymbol{\alpha}_\theta^{\mathrm{bM}} - \boldsymbol{\alpha}^{\mathrm{M}}) = \langle L \rangle \frac{2}{3} h^{\mathrm{M}} (\boldsymbol{\alpha}_\theta^{\mathrm{b}} - \boldsymbol{\alpha}_\theta^{\mathrm{M}}) \tag{5.7}$$

with h^{M} an appropriate modulus to be defined in the following.

5.3.2 Rate of m^{M}

The isotropic hardening/softening (IH) of the MS is given by the rate of its size m^{M}. A modification of the proposition by Liu et al. (2019) can be expressed by:

$$\dot{m}^{\mathrm{M}} = \sqrt{\frac{3}{2}} \dot{\boldsymbol{\alpha}}^{\mathrm{M}} : \mathbf{n} - \frac{m^{\mathrm{M}}}{\varsigma} \langle -\dot{\varepsilon}_{\mathrm{v}}^{\mathrm{p}} \rangle \tag{5.8}$$

Observe the deletion of the complicated term f_{shr} used in the proposition by Liu et al. (2019) in the second term of Equation (5.8), necessary to keep the MS from becoming smaller that the YS; this is because in our case the MS refers to the back-stress ratio $\boldsymbol{\alpha}$ and not to the stress ratio $\mathbf{r}$, hence, it is allowed to shrink down to zero size, i.e., $m^{\mathrm{M}} = 0$, due to dilation. The MS shrinking was an original suggestion by Corti et al. (2016) that is very important because it provides the mechanism to eliminate a previous MS upon dilation and start anew in a subsequent loading process.

The next step would be to substitute the expression of $\dot{\boldsymbol{\alpha}}$ as listed in Table 5.1, and Equations (5.7) and (5.8) into the consistency Equation (5.5) and solve for the parameter h^{M} necessary for the operation of Equation (5.7). In doing so two traps may arise. First, during dilation and softening, common to dense sands, the second term of the right hand side (RHS) of Equation (5.8) may render the size m^{M} of the MS zero, and if the first term is negative, then Equation (5.8) will yield an unacceptable negative value of m^{M}. This eventuality is possible because one may have $\boldsymbol{\alpha} = \boldsymbol{\alpha}_\theta^{\mathrm{M}}$

during monotonic loading from the origin for which all tensors are along $\mathbf{n}$, and because during softening the $\boldsymbol{\alpha}$ is outside the BS, a standard feature of the DM04 model, so will be the $\boldsymbol{\alpha}_\theta^{\mathrm{M}}$; consequently, it follows from Equation (5.7) that the $\dot{\boldsymbol{\alpha}}^{\mathrm{M}}$ which is along $\boldsymbol{\alpha}_\theta^{\mathrm{b}} - \boldsymbol{\alpha}_\theta^{\mathrm{M}}$ will be along $-\mathbf{n}$ (recall the $\boldsymbol{\alpha}_\theta^{\mathrm{M}}$ is further out than $\boldsymbol{\alpha}_\theta^{\mathrm{b}}$ along $\mathbf{n}$), hence, the first term of the RHS of Equation (5.8) will be negative, establishing the first trap. The second trap is more serious. In solving Equation (5.5) for h^{M}, after the aforementioned substitutions, the term $(\boldsymbol{\alpha}_\theta^{\mathrm{b}} - \boldsymbol{\alpha}_\theta^{\mathrm{M}}) : \mathbf{n}$ will appear in the denominator and it is possible for cases where some part of the MS has moved outside the BS, to have $(\boldsymbol{\alpha}_\theta^{\mathrm{b}} - \boldsymbol{\alpha}_\theta^{\mathrm{M}}) : \mathbf{n} = 0$ even if $\boldsymbol{\alpha}_\theta^{\mathrm{b}} \neq \boldsymbol{\alpha}_\theta^{\mathrm{M}}$. This will cause singularity and an infinite value for h^{M} that may create serious numerical problems upon implementation. Such zeroing of the corresponding quantity $(\mathbf{r}_\theta^{\mathrm{b}} - \mathbf{r}^{\mathrm{M}}) : \mathbf{n}$ may occur in the denominator of the second term of the RHS of Equation (18) in Liu et al. (2019).

In order to avoid the foregoing two traps, the following equation is proposed in lieu of Equation (5.8), using the plastic volumetric strain rate as given in Table 5.1 and Equation (5.7):

$$\dot{m}^{\mathrm{M}} = \langle L \rangle \left[\sqrt{\frac{2}{3}} c_{\mathrm{c}} h^{\mathrm{M}} \langle (\boldsymbol{\alpha}_\theta^{\mathrm{b}} - \boldsymbol{\alpha}_\theta^{\mathrm{M}}) : \mathbf{n} \rangle - \frac{m^{\mathrm{M}}}{\varsigma} |(\boldsymbol{\alpha}_\theta^{\mathrm{b}} - \boldsymbol{\alpha}_\theta^{\mathrm{M}}) : \mathbf{n}| \langle -D \rangle \right] \tag{5.9}$$

One can identify the following changes in regard to Equation (5.8). First the Macaulay brackets appear in the first term of the RHS of Equation (5.9) by applying them to $\dot{\boldsymbol{\alpha}}^{\mathrm{M}} : \mathbf{n}$ and using Equation (5.7), while treating h^{M} as positive, a hypothesis that must be confirmed at the end. Therefore, the first term will not contribute to the shrinkage of the memory surface when $(\boldsymbol{\alpha}_\theta^{\mathrm{b}} - \boldsymbol{\alpha}_\theta^{\mathrm{M}}) : \mathbf{n} < 0$ so that it excludes the aforementioned first trap of m^{M} becoming negative. Second, the quantity $|(\boldsymbol{\alpha}_\theta^{\mathrm{b}} - \boldsymbol{\alpha}_\theta^{\mathrm{M}}) : \mathbf{n}|$ is introduced in the second term of the RHS in order to address the eventuality of $(\boldsymbol{\alpha}_\theta^{\mathrm{b}} - \boldsymbol{\alpha}_\theta^{\mathrm{M}}) : \mathbf{n} = 0$ in the denominator of the solution of Equation (5.5) for h^{M}, with which it will be cancelled. Use of absolute value $|\cdot|$ is necessary in case of a MS larger than the BS where the negative value of $(\boldsymbol{\alpha}_\theta^{\mathrm{b}} - \boldsymbol{\alpha}_\theta^{\mathrm{M}}) : \mathbf{n}$ would induce increase rather than decrease of the MS size during dilation. The factor c_{c} is added to simply provide a greater flexibility in the relative contributioFiguren of IH and KH to the evolution of m^{M}. Its default value $c_{\mathrm{c}} = 1$, proposed in Corti et al. (2016), implies that the rate of IH is exactly equal to the rate of KH when $\boldsymbol{\alpha}$ is on the MS; in practical terms it means that as the $\boldsymbol{\alpha}$ moves away from the origin during virgin loading, the centre $\boldsymbol{\alpha}^{\mathrm{M}}$ of the MS is half the value of $\boldsymbol{\alpha}$ and equals m^{M}. So, the MS develops with one end on $\boldsymbol{\alpha}$ and the other fixed at the origin, as presented in Figure 5.5. If $c_{\mathrm{c}} > 1$ the KH will contribute more to IH and the stress origin will be inside the MS while if $c_{\mathrm{c}} < 1$ the KH will have a lesser contribution to IH and the origin will be left outside the MS, during virgin loading. Irrespective of the value of c_{c}, the structure of Equations (5.7) and (5.9) implies that for monotonic radial virgin loading from the origin, the current back-stress point will be simultaneously on the yield and memory surfaces; thus the value of c_{c} will affect the response only upon reverse loading after

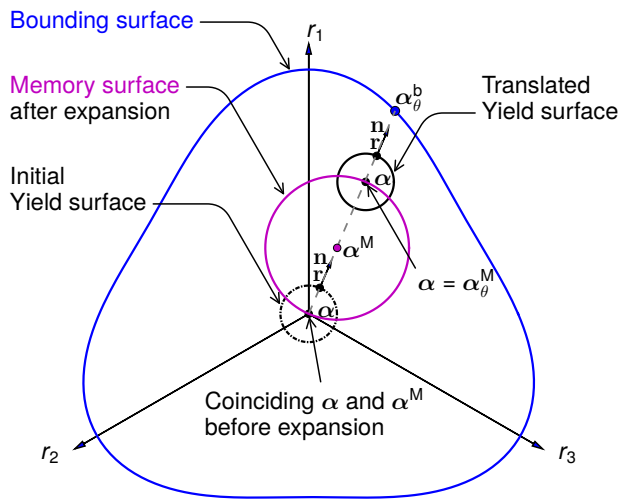

Figure 5.5: Memory surface expansion and translation during virgin loading.

monotonic, as per the foregoing description of the stress origin position relatively to the MS. The constant ς, appearing in Equation (5.9), controls the pace of MS shrinking during dilation, hence, it affects the post-liquefaction stress path. Default value of $\varsigma = 0.00001$ is found effective. Finally, the assumption $h^* = h$ in Equation (5.5) is necessary, without any significant loss of generality, for the elimination of the effect of zero denominator when $(\boldsymbol{\alpha}_\theta^{\mathrm{b}} - \boldsymbol{\alpha}_\theta^{\mathrm{M}}) : \mathbf{n} = 0$ because the choice $h^* = h$ makes the foregoing zero term appearing also in the numerator, hence, it will be cancelled.

Based on the foregoing, substitution of $\dot{\boldsymbol{\alpha}}$ from Table 1 and Equations (5.7) and (5.9) in Equation (5.5), yields for h^{M} the solution:

$$h^{\mathrm{M}} = \frac{1}{1 + c_{\mathrm{c}}\mathscr{H}[(\boldsymbol{\alpha}_\theta^{\mathrm{b}} - \boldsymbol{\alpha}_\theta^{\mathrm{M}}) : \mathbf{n}]} \left\{ h + \sqrt{\frac{3}{2}} \frac{m^{\mathrm{M}}}{\varsigma} \mathrm{sgn}[(\boldsymbol{\alpha}_\theta^{\mathrm{b}} - \boldsymbol{\alpha}_\theta^{\mathrm{M}}) : \mathbf{n}] \langle -D \rangle \right\} \tag{5.10}$$

where the Heaviside function $\mathscr{H}[x] = 1$ if $x \geq 0$ and $\mathscr{H}[x] = 0$ if $x < 0$; the sign function $\mathrm{sgn}[x] = 1$ if $x > 0$, $\mathrm{sgn}[x] = 0$ if $x = 0$ and $\mathrm{sgn}[x] = -1$ if $x < 0$. Recall that in writing Equation (5.9) it is hypothesized that $h^{\mathrm{M}} > 0$ so that it is taken outside the $\langle \cdot \rangle$ and this hypothesis must now be confirmed. Indeed when $(\boldsymbol{\alpha}_\theta^{\mathrm{b}} - \boldsymbol{\alpha}_\theta^{\mathrm{M}}) : \mathbf{n} > 0$ Equation (5.10) yields $h^{\mathrm{M}} > 0$, but when $(\boldsymbol{\alpha}_\theta^{\mathrm{b}} - \boldsymbol{\alpha}_\theta^{\mathrm{M}}) : \mathbf{n} < 0$ it is possible to have $h^{\mathrm{M}} < 0$ depending on the relative values of the first and second terms of the RHS of Equation (5.10). But in this case the first term of the RHS of Equation (5.9) goes to zero anyway irrespective of the sign of h^{M}, and any negative value of the latter has no adverse effect on the formulation for the rate of m^{M}.

The Heaviside and sign functions in Equation (5.10) are discontinuous upon change of sign of their argument. This has no effect in radial loading if the change of sign of $(\boldsymbol{\alpha}_\theta^{\mathrm{b}} - \boldsymbol{\alpha}_\theta^{\mathrm{M}}) : \mathbf{n}$ occurs when $\boldsymbol{\alpha}_\theta^{\mathrm{b}} = \boldsymbol{\alpha}_\theta^{\mathrm{M}}$ because then $\dot{\boldsymbol{\alpha}}^{\mathrm{M}} = \mathbf{0}$; but if it happens that for a continuously changing direction

$\mathbf{n}$ the sign of $(\boldsymbol{\alpha}_\theta^{\mathrm{b}} - \boldsymbol{\alpha}_\theta^{\mathrm{M}}) : \mathbf{n}$ changes without having $\boldsymbol{\alpha}_\theta^{\mathrm{b}} = \boldsymbol{\alpha}_\theta^{\mathrm{M}}$, then discontinuities on the value of h^{M} appear. However, this will show no discontinuous stress-strain response because it will only affect the rate of evolution of MS without any discontinuity of the MS itself.

5.3.3 The role of MS

With Equations (5.7), (5.9) and (5.10) the evolution of the MS is complete. Its link to the DM04 model can then be expressed by modifying the value of the hardening coefficient h, listed in Table 5.1, as follows:

$$h = \frac{b_0}{(\boldsymbol{\alpha} - \boldsymbol{\alpha}_{\mathrm{in}}) : \mathbf{n}} \exp\left[\frac{\mu_0}{||\boldsymbol{\alpha}_{\mathrm{in}}||^u + \varepsilon}\left(\frac{b^{\mathrm{M}}}{b_{\mathrm{ref}}}\right)^w\right] \tag{5.11}$$

where $b^{\mathrm{M}} = (\boldsymbol{\alpha}_\theta^{\mathrm{M}} - \boldsymbol{\alpha}) : \mathbf{n}$ and $b_{\mathrm{ref}} = (\boldsymbol{\alpha}_\theta^{\mathrm{b}} - \boldsymbol{\alpha}_{\theta+\pi}^{\mathrm{b}}) : \mathbf{n}$ (refer to Figure 5.4 for identification of the foregoing tensors), $\boldsymbol{\alpha}_{\mathrm{in}}$ is the value of $\boldsymbol{\alpha}$ at the initiation of a new loading process as explained in DM04, and μ_0, u are model constants. Default values of $w = 2$ and $\varepsilon = 0.001$ are found very effective. The exponential term in Equation (5.11) adds stiffness to the deviatoric response by increasing the value of h in analogy to the distance b^{M} of $\boldsymbol{\alpha}$ from its image $\boldsymbol{\alpha}_\theta^{\mathrm{M}}$ on the MS, projected on $\mathbf{n}$, a standard BS scheme, since the MS is in fact an auxiliary BS for stiffness control. The analytical expression of this exponential term follows an initial suggestion by Liu et al. (2019) where the factor $(p/p_{\mathrm{atm}})^{0.5}$ of this suggestion, that may adversely affect the simulation of liquefaction resistance with increasing initial p, is substituted by $(||\boldsymbol{\alpha}_{\mathrm{in}}||^u + \varepsilon)^{-1}$ that accounts for cyclic shear stress amplitude effects.

5.4 Semifluidized state

Based on the laboratory observations of undrained cyclic shear tests on sand, the concept of "semifluidized state" is introduced in Barrero et al. (2020), which refers to the state of granular material when the mean effective stress is very small, namely when $p < p_{\mathrm{th}}$ with the threshold mean effective stress p_{th} being a model constant. An internal state variable named "Strain Liquefaction Factor" (SLF) and symbolized by ℓ is introduced, whose purpose is to induce stiffness degradation within the semifluidized state. The ℓ evolves only when $p < p_{\mathrm{th}}$ according to the rate equation:

$$\dot{\ell} = \langle L \rangle [c_\ell \langle 1 - p_{\mathrm{r}} \rangle (1 - \ell)^{n_\ell}] - c_{\mathrm{r}} \ell |\dot{\varepsilon}_{\mathrm{v}}| \tag{5.12}$$

where c_ℓ is a model constant controlling the evolution rate of ℓ; n_ℓ is a model constant with the default value 8.0; the pressure ratio $p_\mathrm{r} = p/p_\mathrm{th}$ compared to 1 determines if the stress state falls into the semifluidized state, and p_th is given the default value of 10 kPa, but it can be re-adjusted if necessary for various sands. In regard to such re-adjusted values of p_th, a more thorough investigation should be undertaken in the future, possibly using the tool of Discrete Element Method. A big advantage of the present scheme is that the analytical dependence of the response on p_th, is not very sensitive to a more exact and different value of p_th. Because of $\langle 1 - p_\mathrm{r} \rangle$ the ℓ evolves from min value 0 to max value 1 only when $p_\mathrm{r} < 1$ within the semifluidized state. The last term of Equation (5.12) is zero for undrained loading where $\dot{\varepsilon}_\mathrm{v} = 0$, and leads ℓ towards zero . This last term is a very important constitutive element because it allows readjustment of ℓ to its initial zero value, and eliminates the shortcoming of various models mentioned in the Introduction associated with the use of the ever increasing cumulative plastic shear strain for stiffness degradation. The effect of this last term is not addressed in this work because no draining after undrained loading is considered. Yet, one can refer to Barrero et al. (2020) for a detailed qualitative investigation on the role of the back-to-zero last term of Equation (5.12) to the response after reaching liquefaction, followed by subsequent drainage and new cyclic loading till re-liquefaction, where the significant effect of the value of model constant c_r is illustrated. Comparison with data is a future necessary endeavor.

The role of SLF is to decrease stiffness and dilatancy by decreasing the values of h_0 and A_0 listed in Table 5.1, according to the following two equations:

$$h_0 = h_0' \left[\left(1 - \langle 1 - p_\mathrm{r} \rangle\right)^{x\ell} + f_\ell \right] \tag{5.13}$$

$$A_0 = A_0' \left[\left(1 - \langle 1 - p_\mathrm{r} \rangle\right)^{x\ell} + f_\ell \right] \tag{5.14}$$

where x and f_ℓ are model constants, the latter with the default value 0.01. The primed quantities h_0' and A_0' are in fact the quantities h_0 and A_0 of DM04 model, listed in Table 5.1. The new h_0 of Equation (5.13) will transfer via b_0 as listed in Table 5.1, the effect of ℓ on the value of h in Equation (5.11). Thus, the resulting value of h will be simultaneously affected by the roles of MS and SLF. Observe that outside the semifluidized state one has $p_\mathrm{r} = p/p_\mathrm{th} > 1$, hence, Equations (5.13) and (5.14) become $h_0 = h_0'(1 + f_\ell)$ and $A_0 = A_0'(1 + f_\ell)$, respectively, rendering h_0 and A_0 almost equal to their original primed values, given the very small default value of $f_\ell = 0.01$. Finally, it follows from Equations (5.13) and (5.14) and the equations of Table 5.1, that $h_0'/A_0' = h_0/A_0 = K_\mathrm{p}/D$, and since the plastic volumetric strain rate is proportional to D/K_p, one has that within the semifluidized state this rate is unaltered by the modifications of h_0' and A_0' to h_0 and A_0, in Equations (5.13) and (5.14), respectively. That was exactly what was intended to achieve, based on experimental data the simulation of which required a strong softening related only to

deviatoric plastic strain rate. It is worth noting that the SLF rate equation in Barrero et al. (2020), corresponding to Equation (5.12) in the present work, had an additional term $(p/p_{\mathrm{inr}})^a$ to allow for an overall fitting of the CSR-N_{ini} curve, often inaccurately balanced between pre- and post liquefaction stages, that is no longer needed given the role of the MS in pre-liquefaction model performance.

Table 5.2 presents a summary of the transition from the modified DM04 model equations, to those of the new SANISAND-MSf model, in conjunction with the newly introduced constants including those with default values.

5.5 Calibration

The new SANISAND-MSf model requires the calibration of 21 model constants, divided into three groups. The first group includes 16 constants inherited from DM04 and its modification as listed in Table 5.1; details of their calibration can be found in Taiebat et al. (2010).

The second group is related to the effect of MS on stiffness by means of h, Equation (5.11), and consists of two constants μ_0 and u. Effects of μ_0 and u on the simulated liquefaction strength curve with initial liquefaction referring to $r_u = 0.95$ are illustrated in Figures 5.6(a) and (b). It can

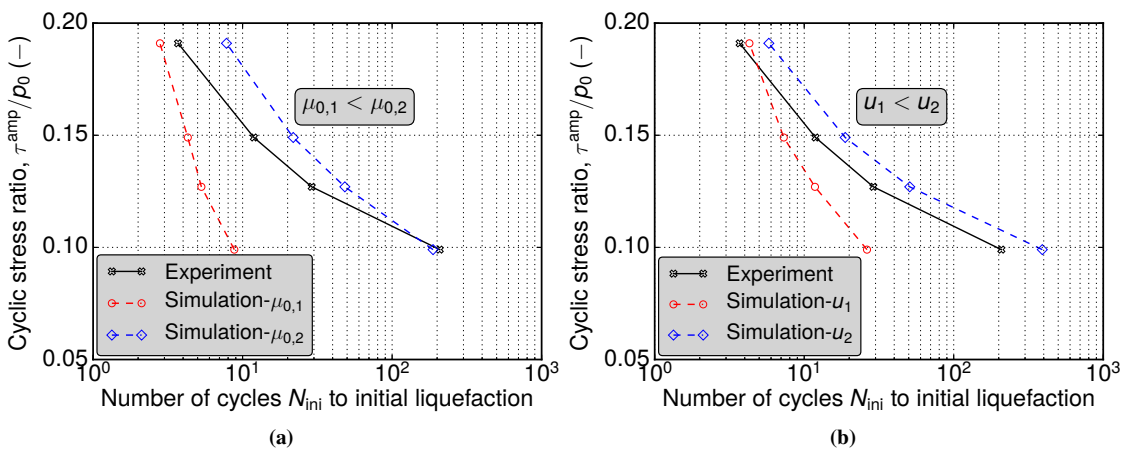

Figure 5.6: Effects of SANISAND-MSf model constants μ_0, u on the simulated liquefaction strength curve with initial liquefaction referring to $r_u = 0.95$ based on undrained cyclic torsional tests under constant CSR: (a) role of μ_0; (b) role of u.

be concluded that μ_0 mainly affects the position of liquefaction strength curve while u affects both the position and the slope.

The last group of model constants, linked to semifluidized state, is used to capture the post-liquefaction shear strain development, without any effect on pre-liquefaction. It consists of c_ℓ and c_{r}, entering Equation (5.12) and x entering Equations (5.13) and (5.14). As mentioned after Equation (5.12) the effect of c_{r} is not addressed in this work, but a parametric study is carried

Table 5.2: Changes from modified DM04 to SANISAND-MSf model equations related to memory surface and semifluidized state.

Description	DM04 modified equations	SANISAND-MSf	Constants*
Memory surface	-	$f^{\mathrm{M}} = \sqrt{(\boldsymbol{\alpha}_\theta^{\mathrm{M}} - \boldsymbol{\alpha}^{\mathrm{M}}) : (\boldsymbol{\alpha}_\theta^{\mathrm{M}} - \boldsymbol{\alpha}^{\mathrm{M}})} - \sqrt{2/3} m^{\mathrm{M}} = 0$	
Image point on MS	-	$\boldsymbol{\alpha}_\theta^{\mathrm{M}} = \boldsymbol{\alpha}^{\mathrm{M}} + \sqrt{2/3} m^{\mathrm{M}} \mathbf{n}$	
		$\dot{\boldsymbol{\alpha}}^{\mathrm{M}} = \langle L \rangle (2/3) h^{\mathrm{M}} (\boldsymbol{\alpha}_\theta^{\mathrm{b}} - \boldsymbol{\alpha}_\theta^{\mathrm{M}})$	
		$\dot{m}^{\mathrm{M}} = \langle L \rangle [\sqrt{2/3} c_{\mathrm{c}} h^{\mathrm{M}} \langle (\boldsymbol{\alpha}_\theta^{\mathrm{b}} - \boldsymbol{\alpha}_\theta^{\mathrm{M}}) : \mathbf{n} \rangle - m^{\mathrm{M}}/\varsigma \lvert (\boldsymbol{\alpha}_\theta^{\mathrm{b}} - \boldsymbol{\alpha}_\theta^{\mathrm{M}}) : \mathbf{n} \rvert \langle -D \rangle]$	$c_{\mathrm{c}} = 1$ $\varsigma = 0.00001$
		$h^{\mathrm{M}} = \{h + \sqrt{3/2}(m^{\mathrm{M}}/\varsigma) \mathrm{sgn}[(\boldsymbol{\alpha}_\theta^{\mathrm{b}} - \boldsymbol{\alpha}_\theta^{\mathrm{M}}) : \mathbf{n}] \langle -D \rangle\} / (1 + c_{\mathrm{c}} \mathscr{H}[(\boldsymbol{\alpha}_\theta^{\mathrm{b}} - \boldsymbol{\alpha}_\theta^{\mathrm{M}}) : \mathbf{n}])$	
Hardening coefficient	$h = b_0 / [(\boldsymbol{\alpha} - \boldsymbol{\alpha}_{\mathrm{in}}) : \mathbf{n}]$	$h = \{b_0 / [(\boldsymbol{\alpha} - \boldsymbol{\alpha}_{\mathrm{in}}) : \mathbf{n}]\} \times \exp[\{\mu_0 / (\lVert \boldsymbol{\alpha}_{\mathrm{in}} \rVert^u + \varepsilon)\} (b^{\mathrm{M}}/b_{\mathrm{ref}})^w]$	μ_0, u $\varepsilon = 0.01$, $w = 2$
		$b^{\mathrm{M}} = (\boldsymbol{\alpha}_\theta^{\mathrm{M}} - \boldsymbol{\alpha}) : \mathbf{n}$	
		$b_{\mathrm{ref}} = (\boldsymbol{\alpha}_\theta^{\mathrm{b}} - \boldsymbol{\alpha}_{\theta+\pi}^{\mathrm{b}}) : \mathbf{n}$	
SLF rate	-	$\dot{\ell} = \langle L \rangle [c_\ell \langle 1 - p_{\mathrm{r}} \rangle (1 - l)^{n_\ell}] - c_{\mathrm{r}} \ell \lvert \dot{\varepsilon}_{\mathrm{v}} \rvert$	c_ℓ, $n_\ell = 8$, c_{r}
		$p_{\mathrm{r}} = p / p_{\mathrm{th}}$	$p_{\mathrm{th}} = 10$ kPa
	h_0	$h_0 = h_0' [(1 - \langle 1 - p_{\mathrm{r}} \rangle)^{xl} + f_\ell]$	x, $f_\ell = 0.01$
	A_0	$A_0 = A_0' [(1 - \langle 1 - p_{\mathrm{r}} \rangle)^{xl} + f_\ell]$	

* Some constants have indicated default numerical values.

out to illustrate the effect of c_ℓ and x on the post-liquefaction shear strain development. With reference to the typical data of Toyoura sand at $D_r = 70\%$, the numerical results shown in Figure 5.7 are obtained with a shear stress amplitude of 40 kPa for three combinations of c_ℓ and x keeping the other model constants fixed. Based on the foregoing, the following calibration procedure is

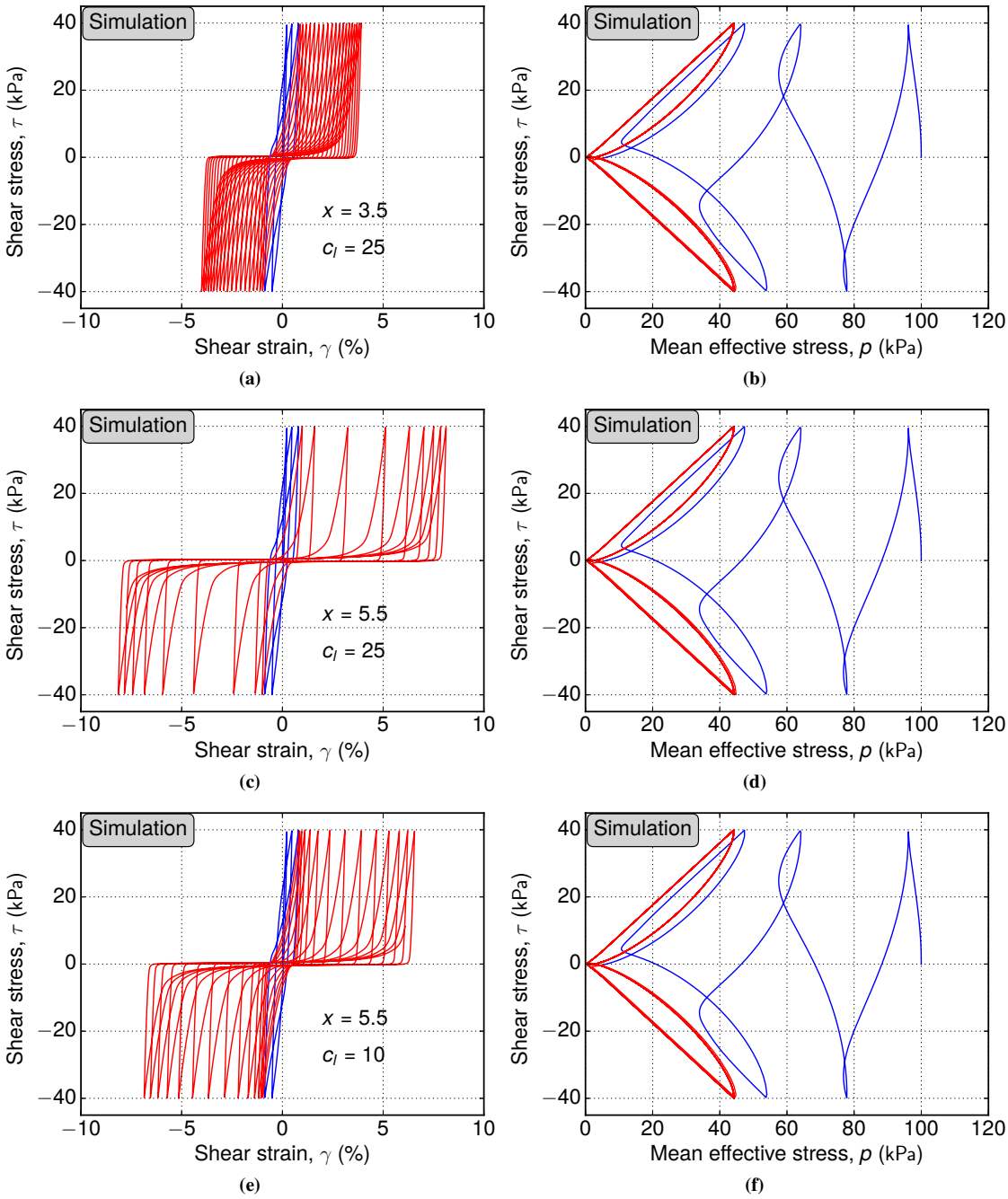

Figure 5.7: Effects of SANISAND-MSf model constants in semifluidized state on simulated stress-strain response and effective stress path: (a), (b) $x = 3.5$, $c_\ell = 25$; (c), (d) $x = 5.5$, $c_\ell = 25$; (e), (f) $x = 5.5$, $c_\ell = 10$. Blue and red lines represent pre- and post-liquefaction, respectively.

suggested: (1) keep c_ℓ, and vary x to capture the general trend of shear strain development; (2) tune c_ℓ for local revision of this general trend towards a better match for each cycle.

5.6 Model performance

5.6.1 Undrained cyclic torsional tests

The experimental data of undrained stress paths, shear strain development and pore pressure generation under undrained cyclic torsional tests on Ottawa-F65 sand from Ueda (2018) will be simulated by the SANISAND-MSf model. The samples are isotropically consolidated at around 100 kPa ending up with very similar relative densities of 50%. Four tests are carried out with CSR values of 0.19, 0.15, 0.13 and 0.10. Recall that here CSR $= \tau^{\text{amp}}/p_0$. The model constants are provided in Table 5.3 with most inherited from DM04 model, as determined in Ramirez et al. (2018), while $z_{\max}$ and c_z are tuned for better approaching the semifluidized state. The other

Table 5.3: SANISAND-MSf calibrated model constants for two types of sands

Model constant	Symbol	Ottawa-F65	Karlsruhe
Elasticity	G_0	125	100
	ν	0.05	0.05
CSL	M	1.26	1.28
	c	0.735	0.75
	$e_{\text{c}}^{\text{ref}}$	0.78	1.038
	λ_{c}	0.0287	0.056
	ξ	0.7	0.28
Yield surface	m	0.01	0.01
Dilatancy	n^{d}	2.50	1.20
	A_0'	0.626	0.56
	n_g	0.9	0.95
Kinematic	n^{b}	0.60	1.0
Hardening	h_0'	4.00	7.60
	c_h	0.968	1.015
Fabric-dilatancy	$z_{\max}$	15.0	15.0
	c_z	2000	1000
Memory surface	μ_0	4.08	7.80
	u	0.96	0.87
Semifluidized state	c_ℓ	35	25
	x	3.5	3.3
	c_{r}	0^*	0^*

* Calibration requires detailed data for multiple-liquefaction stages.

model constants related to memory surface and semifluidized state are calibrated by following the aforementioned procedures in the calibration section.

Figures 5.8–5.11 present experiments and simulations for the aforementioned four CSRs. The

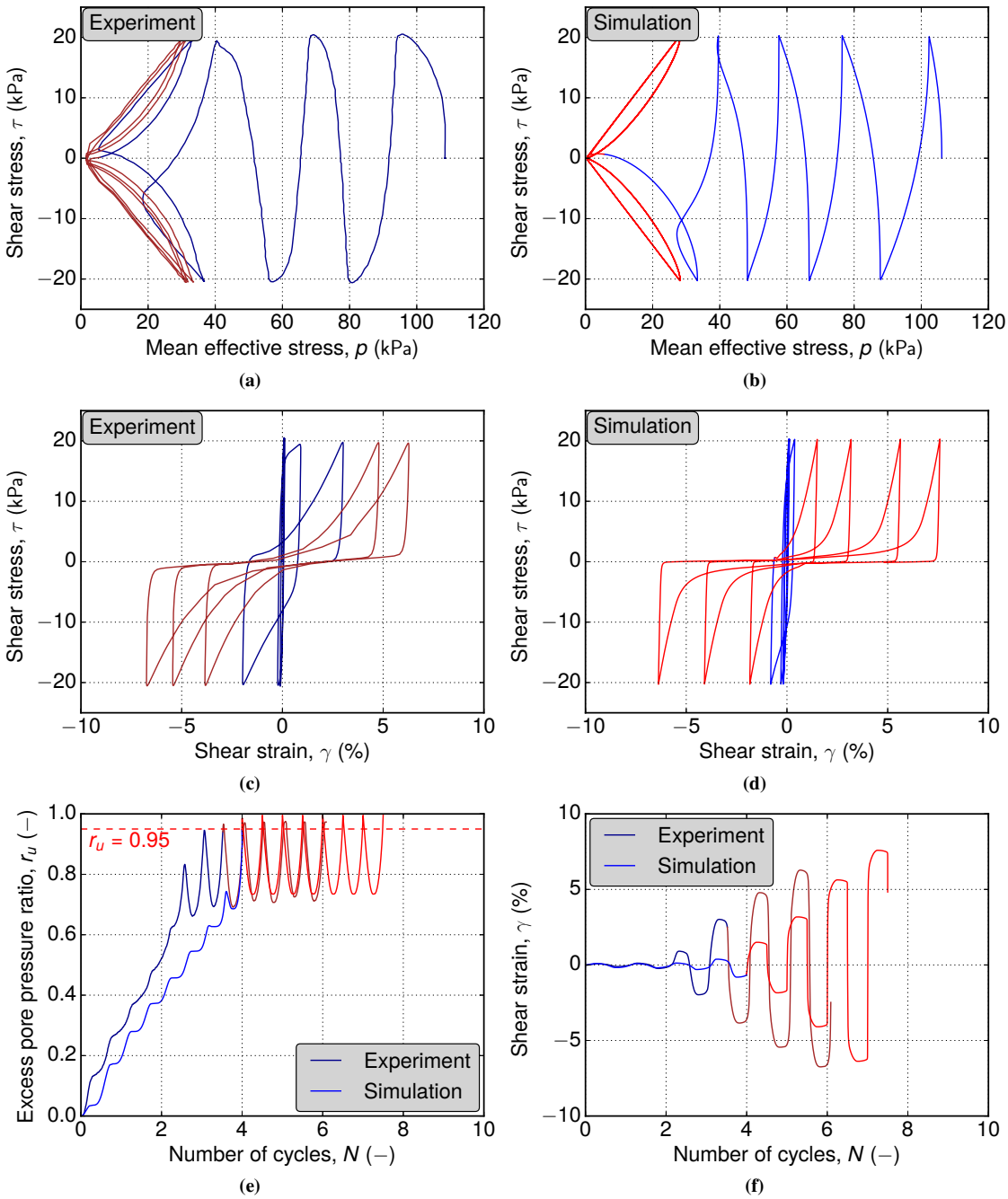

Figure 5.8: Simulations compared with experiments in undrained cyclic torsional test with CSR $= 0.19$ on isotropically consolidated sample of Ottawa-F65 sand with $D_r = 50\%$: (a), (c) experimental data from Ueda (2018); (b), (d) simulations using SANISAND-MSf; (e), (f) comparisons between experiments and simulations in terms of pore pressure generation and shear strain development.

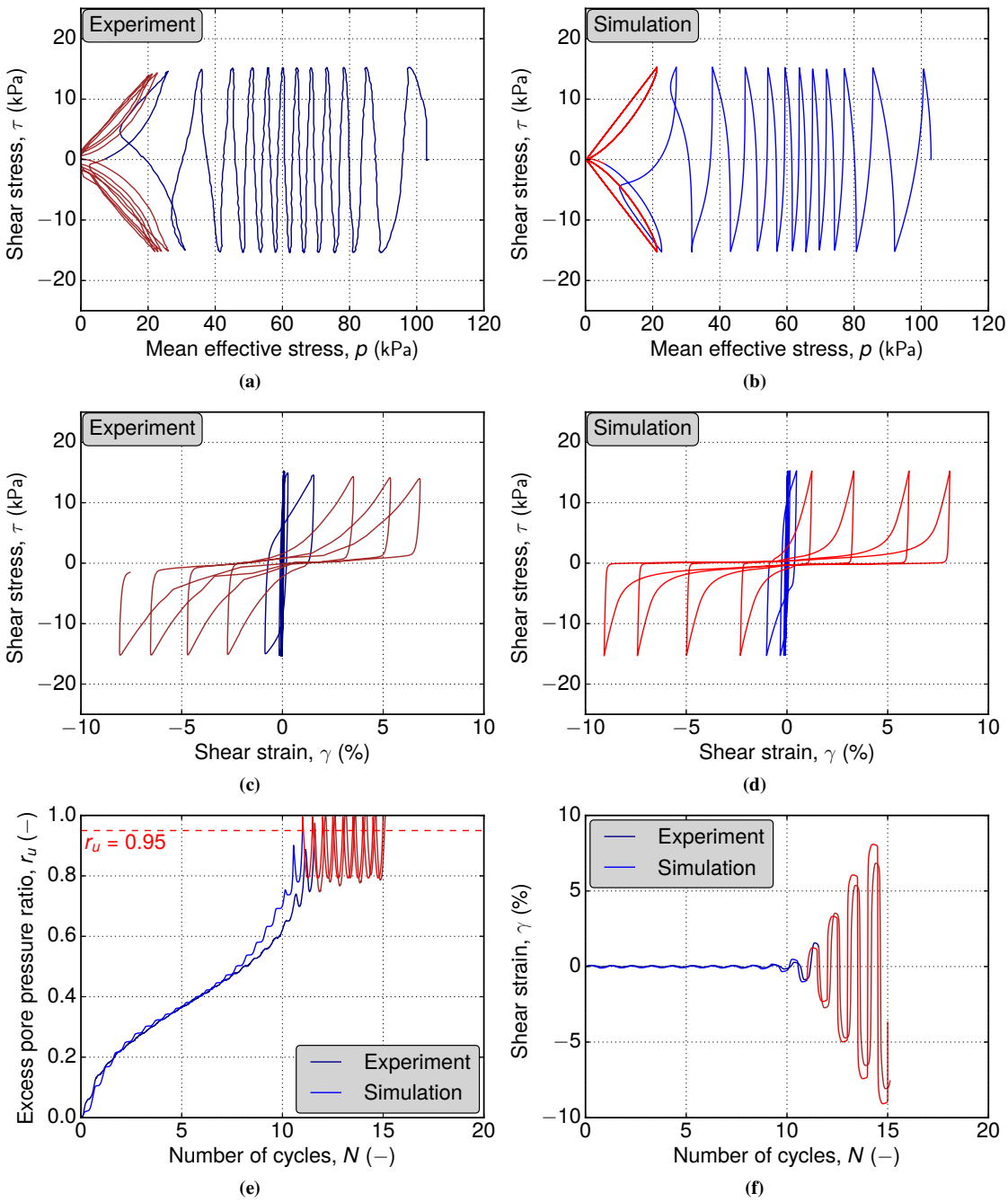

Figure 5.9: Simulations compared with experiments in undrained cyclic torsional test with CSR $= 0.15$ on isotropically consolidated sample of Ottawa-F65 sand with $D_r = 50\%$: (a), (c) experimental data from Ueda (2018); (b), (d) simulations using SANISAND-MSf; (e), (f) comparisons between experiments and simulations in terms of pore pressure generation and shear strain development.

loading process is divided into two stages, before and after the excess pore pressure ratio $r_u = 0.95$ for the first time so that the comparisons can be made separately for pre- and post-liquefaction stages, colored blue and red, respectively. Such comparisons are in general quite satisfactory as eloquently shown in the figures and one can emphasize the following few points. As the CSR

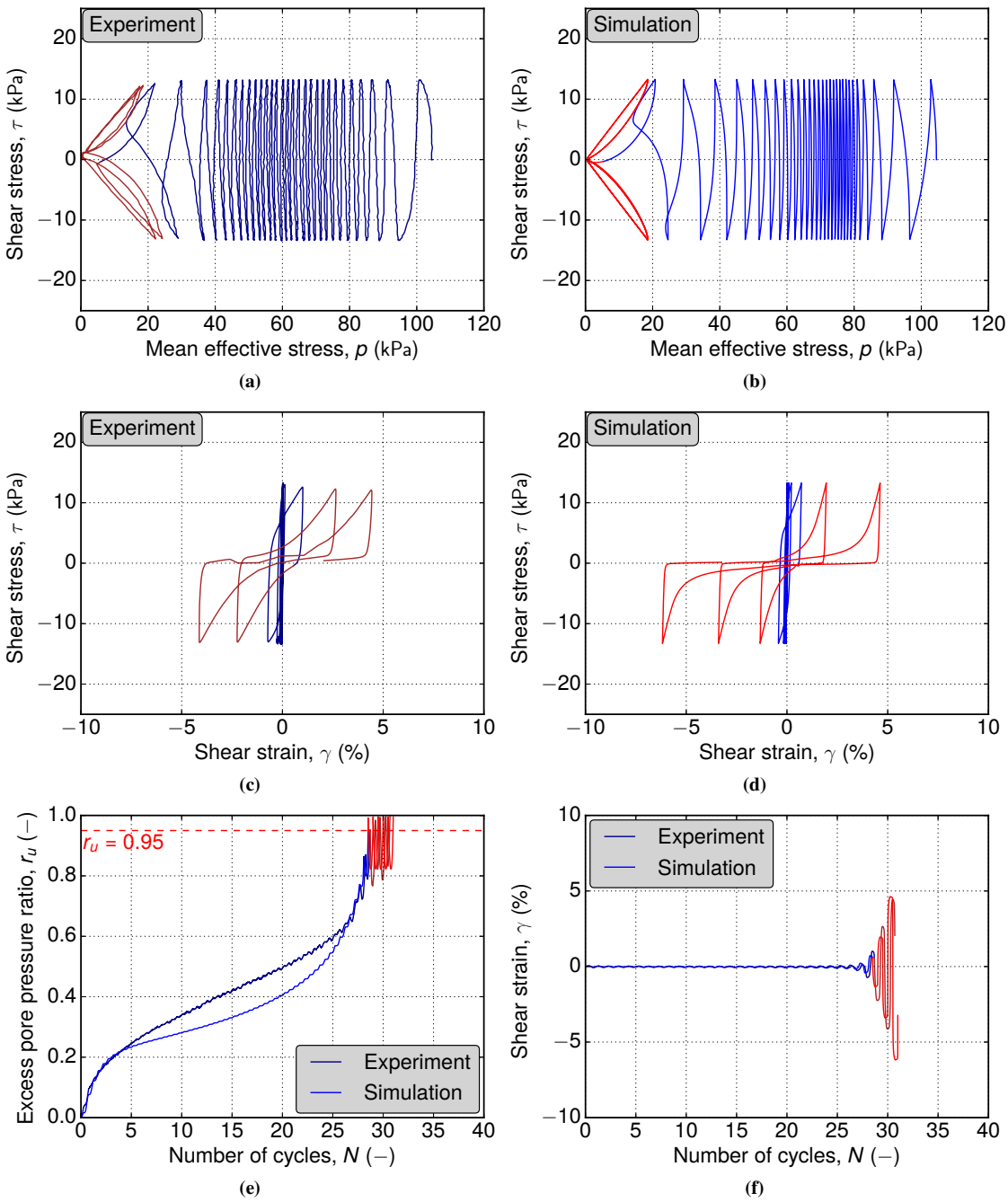

Figure 5.10: Simulations compared with experiments in undrained cyclic torsional test with CSR $= 0.13$ on isotropically consolidated sample of Ottawa-F65 sand with $D_r = 50\%$: (a), (c) experimental data from Ueda (2018); (b), (d) simulations using SANISAND-MSf; (e), (f) comparisons between experiments and simulations in terms of pore pressure generation and shear strain development.

becomes progressively smaller, the model can capture the increasing number of cycles during the pre-liquefaction stage shown by the blue curves of parts (b) as compared with the corresponding experimental curves of parts (a) of Figures 5.8–5.11. In particular Figure 5.11(b) compared with Figure 5.11(a) present successful simulations for the very low CSR $= 0.10$ that are beyond the

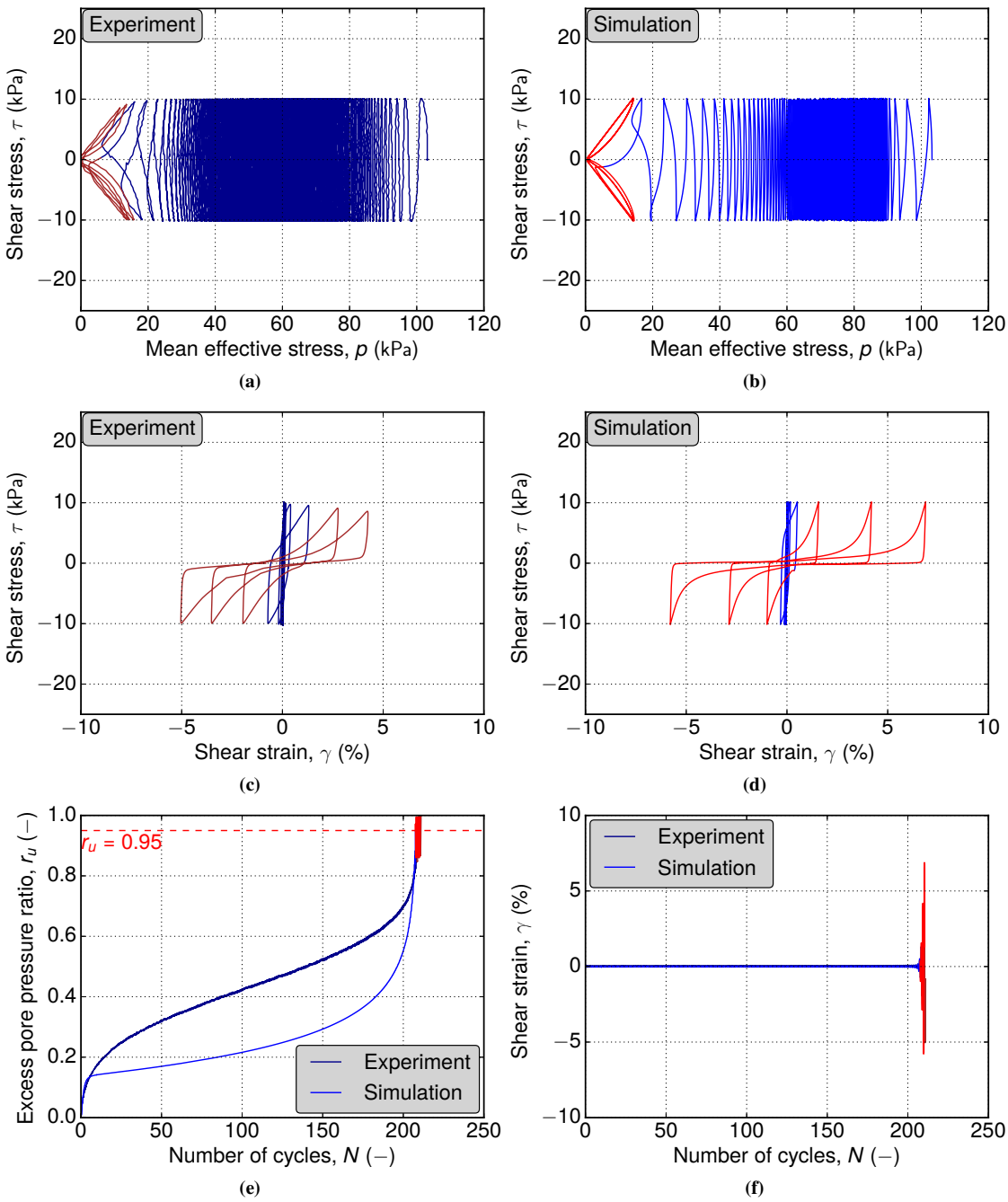

Figure 5.11: Simulations compared with experiments in undrained cyclic torsional test with CSR $= 0.10$ on isotropically consolidated sample of Ottawa-F65 sand with $D_{\mathrm{r}} = 50\%$: (a), (c) experimental data from Ueda (2018); (b), (d) simulations using SANISAND-MSf; (e), (f) comparisons between experiments and simulations in terms of pore pressure generation and shear strain development.

capabilities of most existing constitutive models, including DM04, but for SANISAND-MSf the ingredient of memory surface allows to capture over 200 cycles in the pre-liquefaction stage till reaching $r_u = 0.95$. Similarly, owing to the constitutive ingredient of the semifluidized state, the model can capture the increasing shear strain amplitude in the post-liquefaction stage shown by

the red curves of parts (d) in comparison with the experiments of parts (c) of Figures 5.8–5.11. Characteristically Figure 5.9(d) shows a slowdown of the strain strain amplitude increase, exactly as the data in Figure 5.9(c) exhibit, and this is the result of the SLF ℓ approaching its saturation value of 1. Parts (e) and (f) of Figures 5.8–5.11 illustrate the successful simulations of the previous parts from the perspective of pore water pressure and shear strain amplitude variations versus the number of cycles for the four different CSRs.

5.6.2 Undrained cyclic triaxial tests

Data of undrained cyclic triaxial loading on Karlsruhe fine sand from Wichtmann and Triantafyllidis (2016) will be simulated by the SANISAND-MSf model. The sand samples are isotropically consolidated around 100 kPa ending up with similar relative densities around $D_{\mathrm{r}} \approx 78\%$. Three experimental tests are carried out with different CSRs of 0.25, 0.20 and 0.15. Here $\mathrm{CSR} = q^{\mathrm{amp}}/(2p_0)$, i.e., the ratio of the deviatoric stress amplitude to twice the initial mean effective stress. The calibrated model constants are provided in Table 5.3 with most related to DM04 model and adopted from Liu et al. (2018), while the others are calibrated as mentioned in the calibration section.

Figures 5.12–5.14 present data and simulations for the aforementioned CSRs. The asymmetries of the undrained stress path butterfly shapes in parts (b) and stress-strain loops in parts (d) of the foregoing figures, are in agreement with the corresponding experimental data of parts (a) and (c), respectively, and result from setting the model constant $c = 0.712$, while size-wise the simulated strain is close to data thanks to the semifluidized state incorporation. For the same reason of $c = 0.712$, one has the shifting of the stress-strain loops towards extension observed experimentally in parts (c) and successfully simulated in parts (d) of Figures 5.12–5.14. Such shifting is controlled by the introduction of $g(\theta, c)^{n_g}$ in the modification of the DM04 shown in Table 5.1, and had it not been introduced, the shifting would have been unrealistically larger. Observe that shifting of the stress-strain loops in Figures 5.13(d) and 5.14(d) towards extension is slightly larger than the data, and this can be attributed to the shifting occurring in the pre-liquefaction stage, shown by the blue color loops. In conclusion, the successful simulation of undrained stress paths, and the pore pressure generation and shear strain development in both pre- and post-liquefaction stages, further confirms that SANISAND-MSf model can address the main ingredients of granular material under undrained cyclic triaxial shearing.

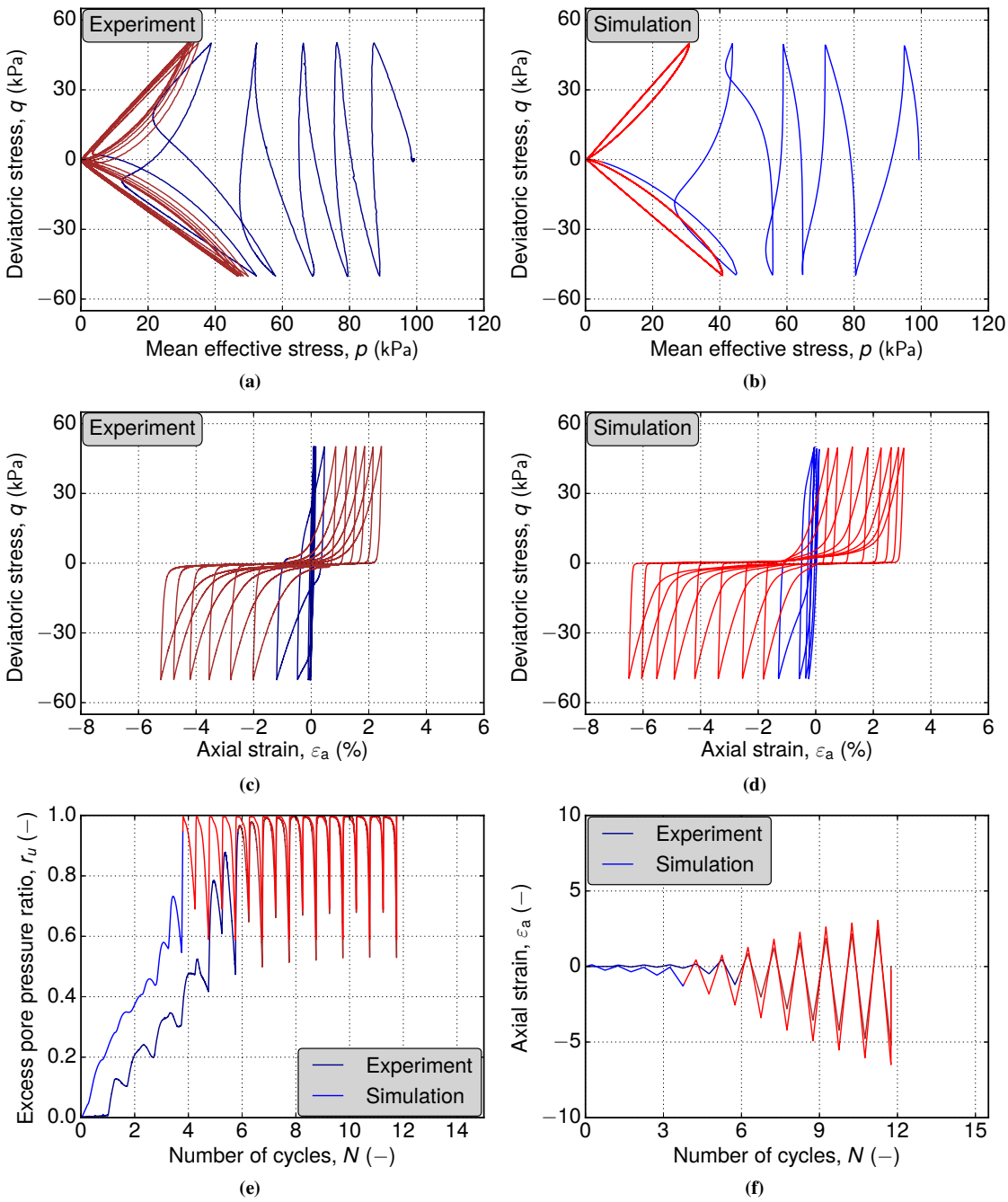

Figure 5.12: Simulations compared with experiments in undrained cyclic triaxial test with CSR $= 0.25$ on isotropically consolidated sample of Karlsruhe find sand with $D_r = 79\%$: (a), (c) experimental data from Wichtmann and Triantafyllidis (2016); (b), (d) simulations using SANISAND-MSf; (e), (f) comparisons between experiments and simulations in terms of pore pressure generation and axial strain development.

5.6.3 Liquefaction strength curve

The liquefaction strength curve, i.e., the plot of CSR versus the number of cycles to initial liquefaction, is a different perspective and a practically important measure of a simulation

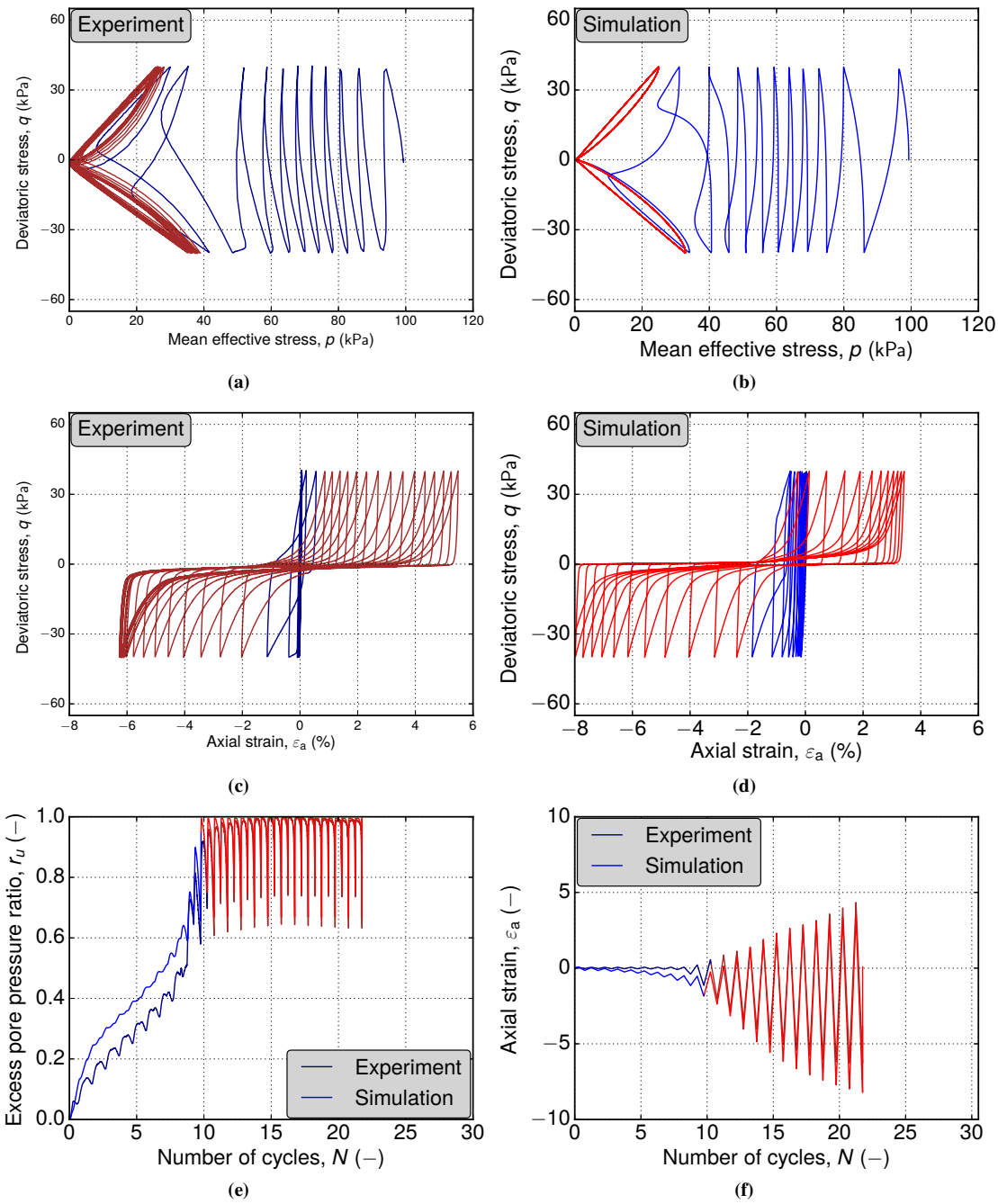

Figure 5.13: Simulations compared with experiments in undrained cyclic triaxial test with CSR $= 0.20$ on isotropically consolidated sample of Karlsruhe find sand with $D_r = 78\%$: (a), (c) experimental data from Wichtmann and Triantafyllidis (2016); (b), (d) simulations using SANISAND-MSf; (e), (f) comparisons between experiments and simulations in terms of pore pressure generation and axial strain development.

success. The foregoing data and simulations will be used to plot the corresponding strength curves, adopting four criteria for initial liquefaction, namely one r_u-based and three shear strain-based.

Figure 5.15 presents the liquefaction strength curves for the four undrained cyclic torsional tests

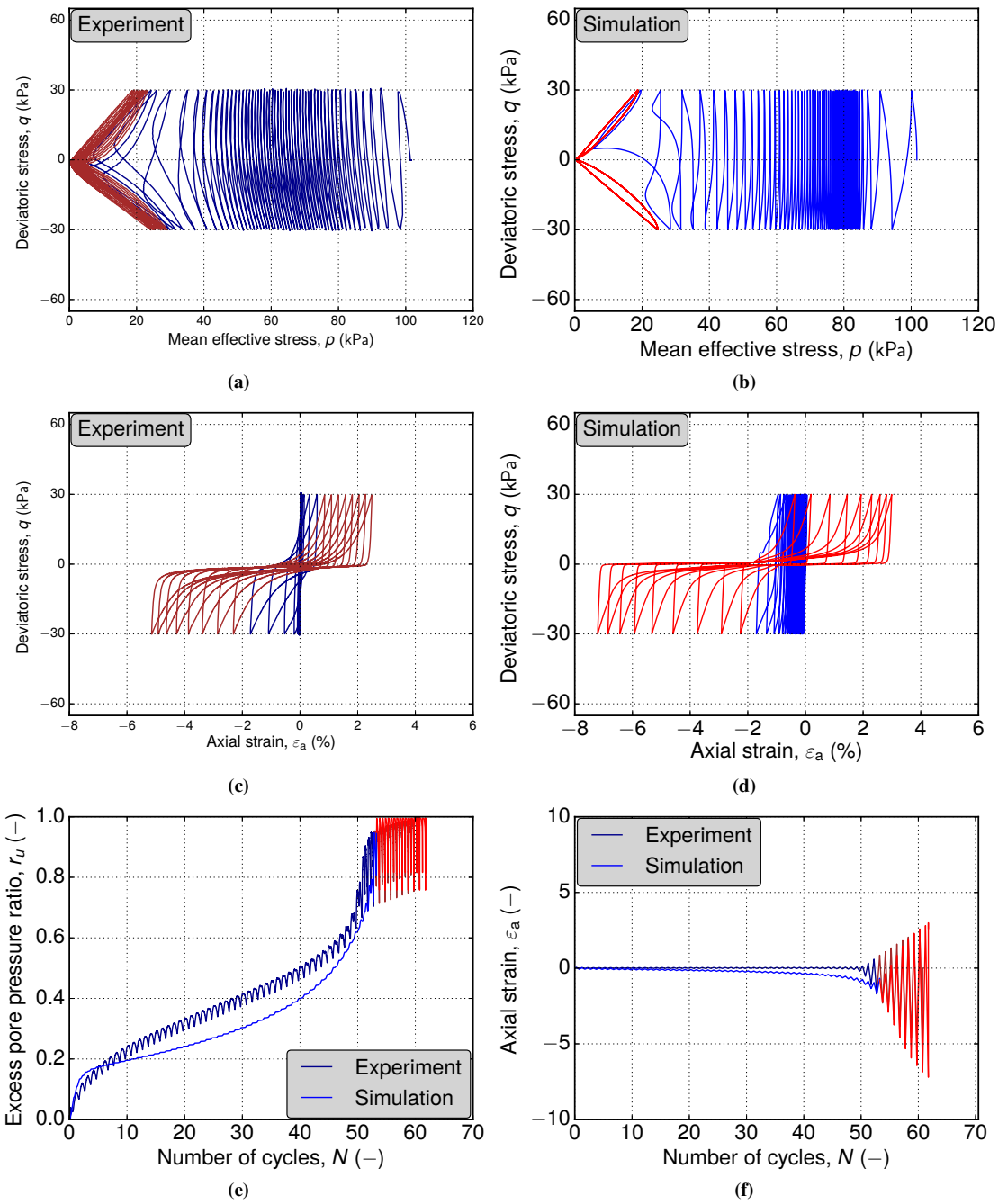

Figure 5.14: Simulations compared with experiments in undrained cyclic triaxial test with CSR $= 0.15$ on isotropically consolidated sample of Karlsruhe find sand with $D_r = 78\%$: (a), (c) experimental data from Wichtmann and Triantafyllidis (2016); (b), (d) simulations using SANISAND-MSf; (e), (f) comparisons between experiments and simulations in terms of pore pressure generation and axial strain development.

on Ottawa F65 sand with $D_r = 50\%$. The criteria for the initial liquefaction are excess pore pressure ratio $r_u = 0.95$, and three double amplitudes of shear strain, namely $\gamma^{DA} = 1.5\%$, $\gamma^{DA} = 3.0\%$ and $\gamma^{DA} = 7.5\%$. The data imply that $r_u = 0.95$ happens between $\gamma^{DA} = 3.0\%$ and $\gamma^{DA} = 7.5\%$ while the model suggests a value of around 1.5%. The model can give very precise simulation on the

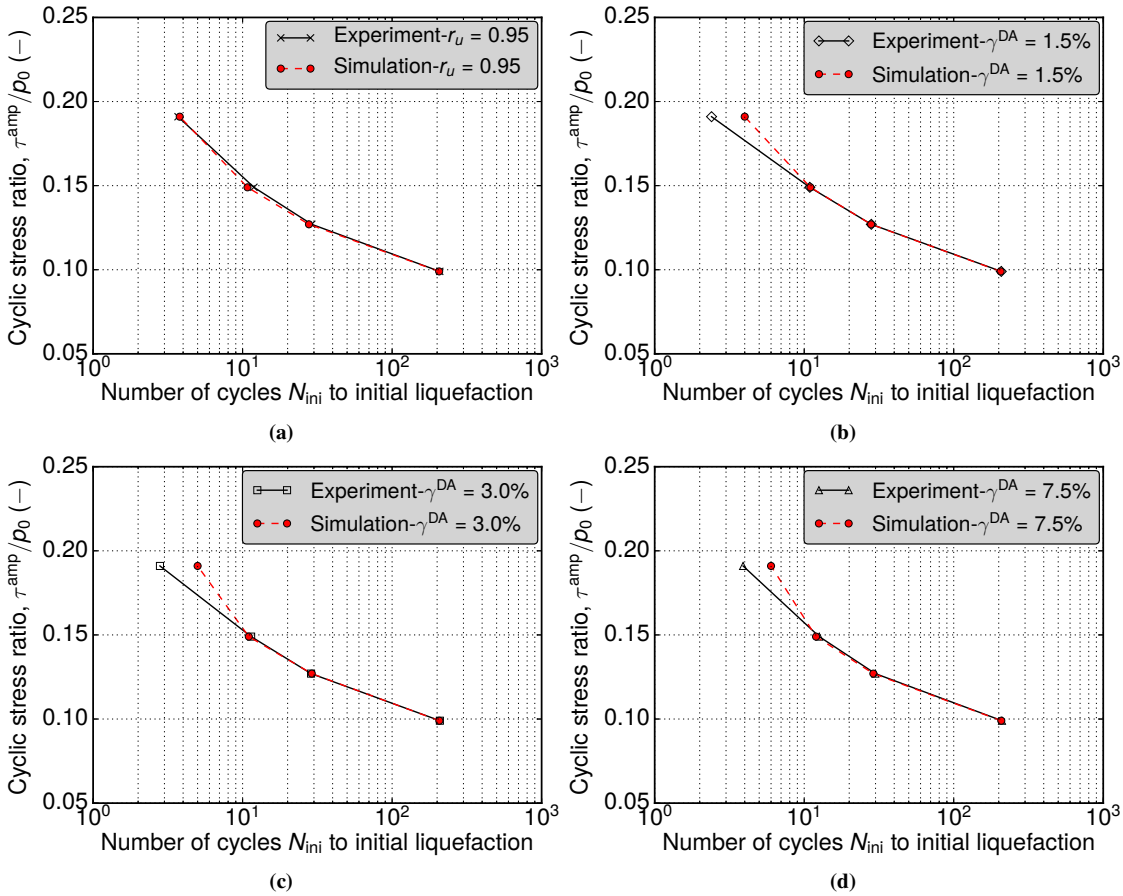

Figure 5.15: Liquefaction strength curves on Ottawa-F65 sand with $D_r = 50\%$: (a) $r_u = 0.95$; (b) $\gamma^{DA} = 1.5\%$; (c) $\gamma^{DA} = 3.0\%$; (d) $\gamma^{DA} = 7.5\%$.

number of cycles for $r_u = 0.95$ for all CSRs, as seen in Figure 5.15(a). For the three shear strain-based criteria the model slightly overpredicts the number of cycles, with small variations between higher and lower CSRs. In general, the performance is very satisfactory.

Figure 5.16 presents the liquefaction strength curve for the three undrained cyclic triaxial tests on Karlsruhe fine sand with $D_r \approx 78\%$. The four criteria for initial liquefaction are excess pore pressure ratio $r_u = 0.95$, and three double amplitudes of axial strain $\varepsilon_a^{DA} = 1.0\%$, $\varepsilon_a^{DA} = 2.5\%$ and $\varepsilon_a^{DA} = 5.0\%$. The data imply that $r_u = 0.95$ happens between $\varepsilon_a^{DA} = 2.5\%$ and $\varepsilon_a^{DA} = 5.0\%$ while the model suggests a range between $\varepsilon_a^{DA} = 1.0\%$ and $\varepsilon_a^{DA} = 2.5\%$. For all four criteria data and simulations are in good agreement on the average for all CSRs, with some small overprediction of the number of cycles for the strain-based criteria, except from the test with the lowest CSR that exhibits excellent performance shown in Figures 5.16(b), (c) and (d). The experiments from Figures 5.15 and 5.16 indicate that large deformation happens along with excess pore pressure ratio approaching 0.95, irrespective of which criterion is adopted for initial liquefaction. This message is also conveyed by the present model.

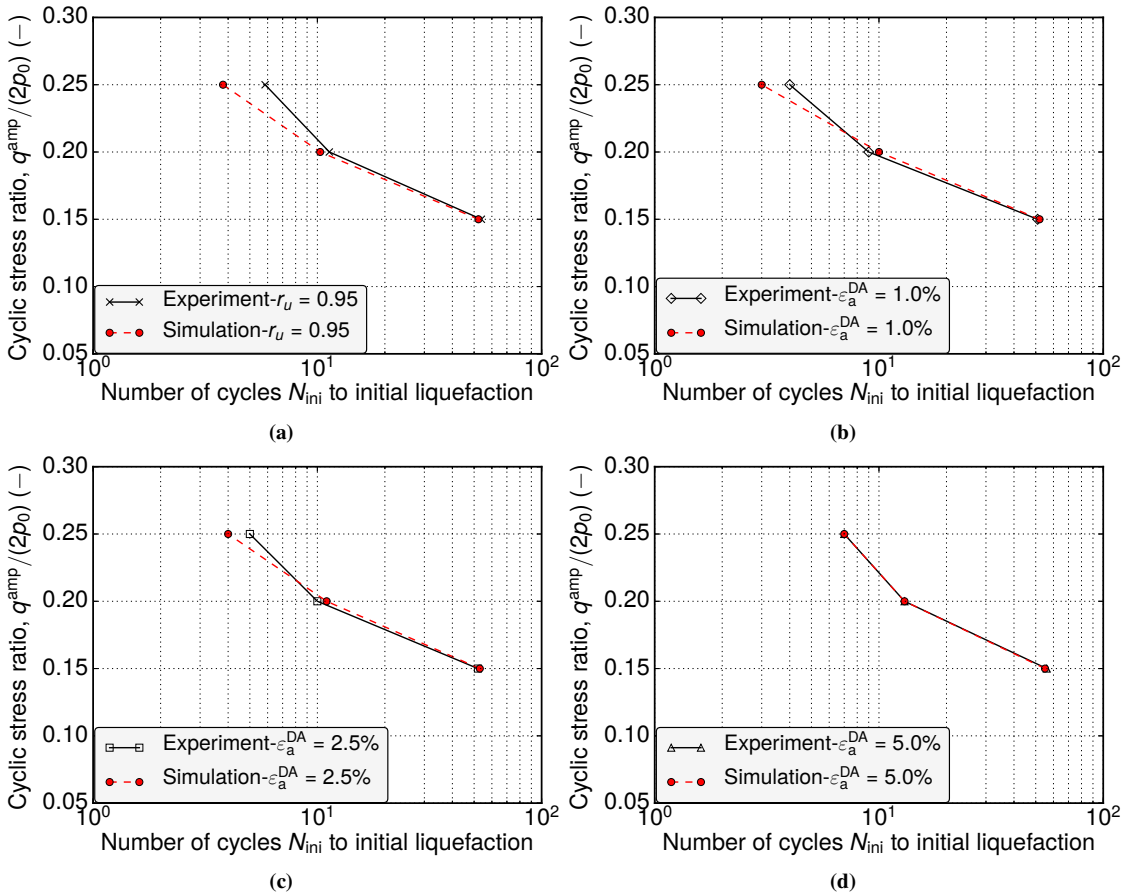

Figure 5.16: Liquefaction strength curves on Karlsruhe fine sand with $D_r \approx 78\%$: (a) $r_u = 0.95$; (b) $\varepsilon_a^{DA} = 1.0\%$; (c) $\varepsilon_a^{DA} = 2.5\%$; (d) $\varepsilon_a^{DA} = 5.0\%$.

5.6.4 Effect of initial conditions

While the foregoing addressed simulations for various values of CSR at the same initial relative density D_r and mean stress p_0, the following address simulations for different values of D_r and p_0 under the same constant CSR. Various laboratory experiments (Vaid et al., 2001; Hyodo et al., 2002; Kiyota et al., 2008; Yang and Sze, 2011; Wichtmann and Triantafyllidis, 2016) indicate that cyclic liquefaction resistance increases with increasing relative density or decreasing initial mean stress.

Figure 5.17 compares simulation and experimental plots of pore pressure generation and axial strain development versus number of cycles, for two undrained cyclic triaxial tests on isotropically consolidated samples of Karlsruhe fine sand with the same $p_0 = 100$ kPa but different relative densities subjected to a CSR of 0.15. Similarly, Figure 5.18 compares same plots of experiments and simulations of two undrained cyclic triaxial tests on isotropically consolidated samples of Karlsruhe fine sand with similar $D_r \approx 65\%$ but different initial mean stresses under a CSR of 0.125. The reasonable agreement between simulations and experimental data in Figures 5.17 and

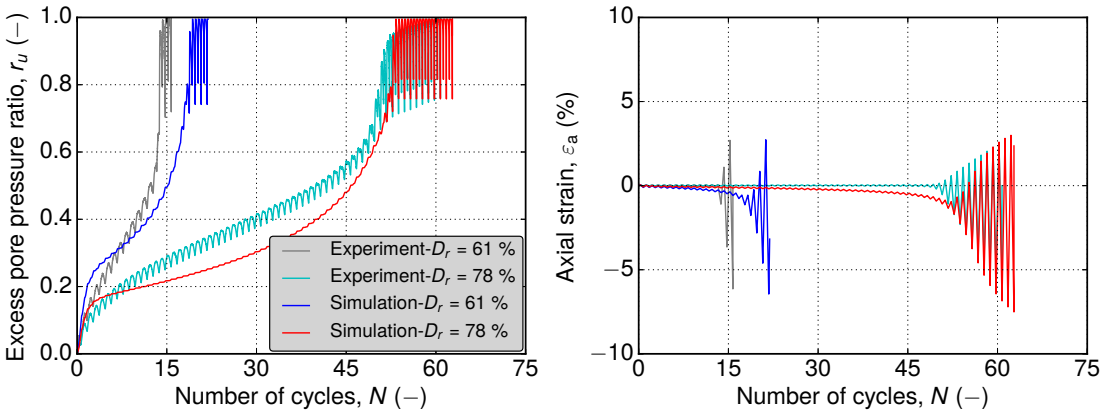

(a) (b)

Figure 5.17: SANISAND-MSf model performance in simulating effect of initial relative density D_r on isotropically consolidated samples of Karlsruhe fine sand with $p_0 = 100$ kPa and CSR $= 0.15$: (a) pore pressure generation; (b) axial strain development.

5.18, show that SANISAND-SMf is capable of capturing the effects of different initial densities and mean stresses.

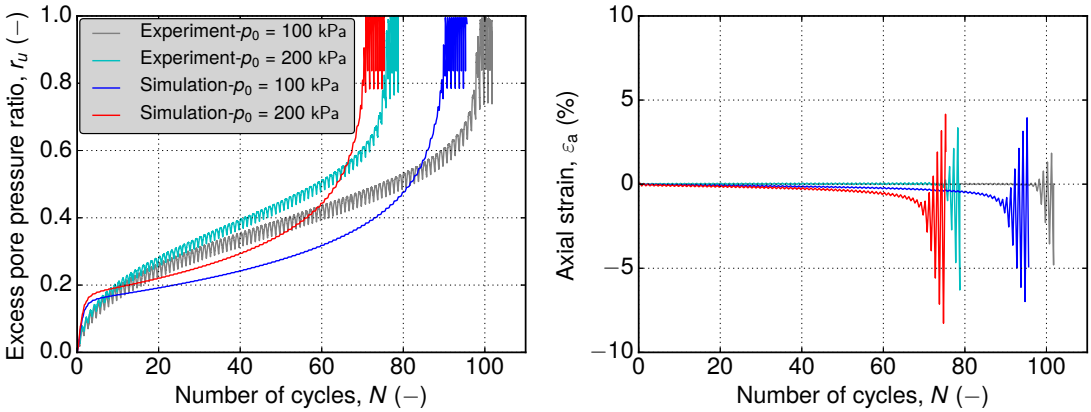

(a) (b)

Figure 5.18: SANISAND-MSf model performance in simulating effect of initial pressure p_0 on isotropically consolidated samples of Karlsruhe fine sand with $D_r \approx 65\%$ and CSR $= 0.125$: (a) pore pressure generation; (b) axial strain development.

5.7 Conclusions

The new SANISAND-MSf constitutive model for sands is formulated by introducing minor and major modifications into the DM04 model platform by Dafalias and Manzari (2004). The minor modification consists of two parts, one that improves the accuracy of the non-associative flow rule and a second that improves the cyclic shear stress-strain loops shifting under cyclic triaxial loading by introducing a simple Lode angle dependence. The major modification has also two

parts, incorporating two new constitutive ingredients. The first is a back-stress ratio-based memory surface (MS), which is a drastic modification of the original idea proposed by Corti et al. (2016) and adjusted by Liu et al. (2019) to align with the DM04 model. The role of the MS is to increase the stiffness for back-stress ratios within it, in order to better simulate the stress paths for undrained cyclic shear tests in the pre-liquefaction stage. Compared to the foregoing references, the present MS ingredient addresses several important issues, among them a size of zero initial value, greater simplicity and generality of its evolution and the avoidance of singularity occurring by possible zeroing of a denominator in the formulation. The second constitutive ingredient is the concept of semifluidized state for very low effective stresses, Barrero et al. (2020), within which strong stiffness and dilatancy degradation is described by means of an evolving state variable named Strain Liquefaction Factor (SLF), that can simulate large shear strain development in post-liquefaction stage without affecting the response in the pre-liquefaction stage. The SANISAND-MSf model is validated against two experimental databases, i.e., four undrained cyclic torsional tests and three undrained cyclic triaxial tests. The simulations of undrained stress path, stress-strain loops, excess pore pressure generation and shear strain development versus number of cycles, are successfully compared with the experimental data. Furthermore, and unlike other models, such simulation is successful separately for the pre- and post-liquefaction stages. The corresponding strength curves of CSR versus number of cycles to initial liquefaction, the latter defined in terms of both r_u-based and shear strain-based criteria, show very satisfactory comparisons with data, thus removing a simulation shortcoming of the reference base DM04 model. The constitutive ingredients of memory surface and semifluidized state have generic value and can be incorporate in other similar to DM04 model, such as the zero elastic range model developed and implemented by Dafalias and Taiebat (2016) and Petalas and Dafalias (2019), with appropriate adjustments. It is also expected that the model will perform satisfactorily under drained cyclic conditions as shown for similar formulations by Corti et al. (2016) and Liu et al. (2019), and this will be addressed in future works. Simulations under undrained cyclic loading remain though the most useful and difficult to achieve, and it is believed that the present work has contributed positively in this endeavour. With such satisfactory performance in simulating unidirectional cyclic shear tests, the next step is to conduct a systematic evaluation of SANISAND-MSf with respect to multidirectional cyclic shear tests (Yang et al., 2019), where effects of initial static bias and different cyclic shear paths are considered.

The present model is void of two common theoretical shortcomings with practical implications, encountered in other constitutive models with similar simulative capabilities. First, it does not use quantities like cumulative shear strain or cumulative fabric dependent quantity to describe stiffness degradation, which remain in the model affecting unduly subsequent loading simulations. Instead, the Strain Liquefaction Factor is introduced within the concept of semi fluidized state, that

promptly fades away upon drainage following the cyclic loading. Second, it does not introduce initial loading conditions, such as CSR or the initial value p_0 of p, into the constitutive relations; models which do, fall into the trap that any intermediate state can be virtually considered as initial loading state, by means of a stop-and-start again loading event, thus, adversely modifying the subsequent response for what is essentially the same loading process. Instead, only updatable values of internal variables at the initiation of any new plastic loading process are used, such as $\boldsymbol{\alpha}_{\text{in}}$, and it was shown that the model is capable of capturing the effect of different initial conditions on density and mean pressure.

Thermodynamic compatibility in the sense of positive dissipation (positive entropy production) is a desired feature not always addressed in inelastic constitutive modeling works, as in the present one. One way this can be achieved requires the making of sufficient but not necessary hypotheses about the structure of free energy dependence on internal variables that eventually may impose restrictions on the constant entering the evolution rate equations of such internal variables. In the case of kinematic hardening internal variables, a basic feature of the present model family, there is a standard approach that can be found in Feigenbaum and Dafalias (2008) for metals which, however, will require adjustments to accommodate the dilatancy feature for soils that does not exist in metals. An effort in this direction will be undertaken in the future.

Chapter 6: Evaluation of SANISAND-MSf in Simulating Multidirectional Cyclic Shear Tests

In this chapter, the SANISAND-MSf model developed in Chapter 5 is applied to simulate multidirectional cyclic shear tests for the evaluation. This chapter inherits the general structure from the paper co-authored with Gaziz Seidalinov and Mahdi Taiebat, which was published in *Soil Dynamics and Earthquake Engineering* (Yang et al., 2019). The main modification is replacing the original sand constitutive model DM04 (Dafalias and Manzari, 2004) with SANISAND-MSf, along with updating the corresponding simulation results.

6.1 Introduction

In recent decades, the destructive nature of earthquakes on constructed facilities has led to extensive research focused on the dynamic properties of soil. Simple shear test has been chosen as a close configuration to model the plane strain condition and the rotation of principal stress axes in soil (Boulanger et al., 1993). With or without an offset static shear stress in the same direction as the cyclic shear stress, this unidirectional shear mode can be used to replicate the response of soil subjected to one-dimensional propagation of shear waves. In the field, however, shear wave propagation is multidirectional. Even if the vertical component of the seismic loading is neglected, there exist two horizontal shear components as depicted in Figure 6.1(a), and neglecting one of them can potentially lead to underestimation of seismic demand. To mimic the response of soil element under level or sloping grounds, when subjected to multidirectional cyclic shearing, a number of more sophisticated devices for simulating the multidirectional cyclic shearing have been established, developed and refined over the years (Ishihara and Yamazaki, 1980; Boulanger et al., 1993; Kammerer et al., 2002; Matsuda et al., 2011; Sun, 2019). These apparatuses are very useful in generating a comprehensive experimental database for evaluation of various constitutive models in such complex loadings.

The soil sample in a multidirectional cyclic shear test goes through two loading stages. The first one, referred to as consolidation stage, is to reproduce the corresponding in situ state of soil consolidated under level or sloping grounds as shown in Figure 6.1(a). For modeling the initial

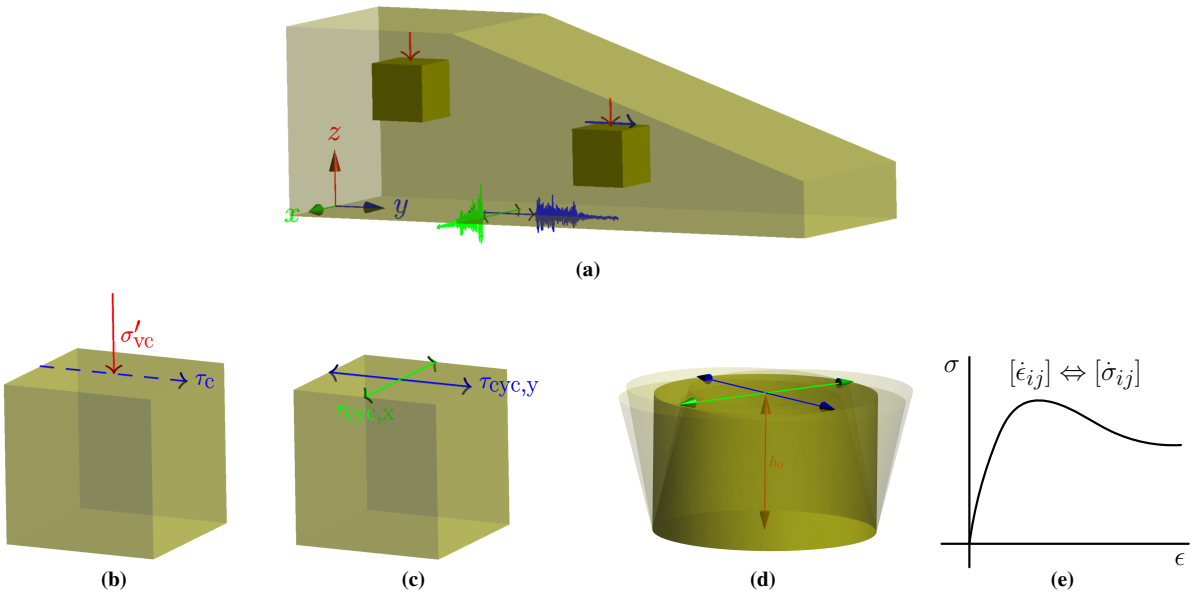

Figure 6.1: Multidirectional properties of seismic loading in real field: (a) seismic loading, (b) consolidation stage, (c) cyclic shearing stage, (d) element in experimental tests, and (e) stress-strain relationship.

condition of soil under a level ground (away from a slope), a soil element is consolidated vertically with the lateral normal strains constrained; this is typically referred to as K_0 condition. For the soil element under the sloping ground, in addition to the above K_0 consolidation, an offset consolidation shear stress τ_c perpendicular to the strike direction of the slope is also exerted on the element, as depicted in Figure 6.1(b) with blue dashed arrow; this is referred to as anisotropic consolidation and denoted as K_α condition. Here $\alpha = \tau/\sigma'_{vc}$ is the normalized magnitude of the offset consolidation shear stress, i.e., the ratio of τ and initial effective vertical stress σ'_{vc} applied on the top plane of the element. A good equivalent interpretation of the ratio α is static stress ratio (SSR) (Yang and Pan, 2017), analogous to the widely-used notation cyclic stress ratio (CSR) used to represent the normalized magnitude of cyclic shearing. It should be noted that this K_α only defines the aforementioned anisotropic consolidation condition, different from the well-known K_α correction used in liquefaction triggering analysis. A simpler case of initial condition for the first loading stage, but perhaps less realistic in the nature, is isotropic consolidation of the sample set-ups of Ishihara and Yamazaki (1980) and Ishihara and Nagase (1988). Accounting for all these possibilities in laboratory tests, there are three kinds of consolidation stages depending on whether the specimen is consolidated under isotropic, K_0 or K_α conditions, and these conditions are denoted by CI, CK_0 and CK_α, respectively. Among these stages, only CK_α would result in non-zero SSR.

The second loading stage is referred to as cyclic shearing stage. During seismic excitation on level or sloping grounds, the vertically propagating shear waves within the soil profile induce

irregular dynamic shearing in soil. This irregular shear loading may be simplified by introducing an equivalent time history of harmonic shearing, denoted by $\tau_{\mathrm{cyc}}(t)$. Similar to the irregular dynamic loading, $\tau_{\mathrm{cyc}}(t)$ can change in both magnitude and orientation. With the coordinate system shown in Figure 6.1(a), i.e., the x-axis along the strike direction of the slope, the y-axis perpendicular to that and along the slope projection on the horizontal plane, and the z-axis being vertical, the $\tau_{\mathrm{cyc}}(t)$ can be resolved into two orthogonal components, $\tau_{\mathrm{cyc},x}$ and $\tau_{\mathrm{cyc},y}$, as depicted in Figure 6.1(c). After the initial consolidation stage shown in Figure 6.1(b), the cyclic shear paths from the two orthogonal cyclic shear components are to be applied in the element test as shown in Figure 6.1(c). It should be noted that for this stage of element test, a stress controlled input is used in most of the available multidirectional cyclic shear test devices, except the ones by Matsuda et al. (2011) where the input path is strain controlled.

Majority of the laboratory element tests are performed under either drained or undrained conditions. The rapid nature of seismic excitation does not allow enough time for dissipation of pore pressure in the in situ state of soil, thereby requiring that laboratory tests be performed under undrained conditions to mimic the idealized field condition. To the authors' knowledge, almost all the multidirectional cyclic shear tests in the literature are carried out in undrained condition. Assuming a fully saturated condition and a nearly incompressible response for both water and solid grains of soil, to model the undrained condition the volume of the specimen should be kept constant during the cyclic shearing stage. With the lateral normal strains constrained, a constant volume condition can be achieved either by keeping the height of the dry specimen (h_0) constant ("constant height" test) or by closing the drainage valve of the saturated specimen ("truly undrained" test). The former manner is very common in simple shear testing where the top face of the specimen is only allowed to deform along one shear direction while the latter one is adopted in the multidirectional cyclic shearing test where the top face can move with variable shear directions as shown in Figure 6.1(d) with shadows referring to the deforming directions. More details about the equivalence of the "constant height" and "truly undrained" simple shear tests are presented in Dyvik et al. (1987). Note that the state reflected in Figure 6.1(d) should be referred to as "multidirectional cyclic shear" instead of "multidirectional cyclic simple shear" as sometimes seen in the literature, because the typical adjective "simple" implies plane strain condition, which does not apply to the multidirectional cyclic shearing (Yang et al., 2016). There are known concerns and limitations common between the simple shear and multidirectional cyclic shear tests, mainly related to the non-uniformity of stresses and strains, and equalization of pore pressures. One should keep in mind these limitations when judging the results obtained from these tests.

Given the well-established laboratory experimental database of multidirectional cyclic shear tests, this chapter is focused on evaluation of the SANISAND-MSf model in simulating these

tests. One can refer to Chapter 5 for details of this constitutive model, which is not repeated here for brevity. First, an overall experimental database of multidirectional cyclic shear tests available in the literature are summarized and presented, followed by details about the selected experiments to be simulated in this chapter. Calibration of SANISAND-MSf model is presented mainly based on cyclic simple shear tests, which enhances the capabilities of the constitutive model in capturing response of sand subjected to conventional loading conditions. The corresponding model simulations for multidirectional cyclic shear tests are presented and compared with the experimental results afterwards. Discussion about the performance of SANISAND-MSf in the so called neutral loading paths, very common in majority of elastoplasticity models, is presented at the end.

6.2 Multidirectional cyclic testing data

6.2.1 Available experimental database

Based on the offset shear applied during the consolidation stage of the multidirectional cyclic shear test in combination with the amplitudes, frequencies, and phase angle differences of the two harmonic cyclic shear components applied during the shearing stage, different types of shearing paths can be generated from this test. Eight types of such multidirectional cyclic shear tests, all available in the literature, are presented in the space of the shear components of stress or strain in Figure 6.2. In this figure, point O represents zero shear stress or strain states prior to the initial consolidation stage. Point C along the x-direction shows the state of the sample after the CI, CK_0, or CK_α consolidation stage, represented in blue; at this stage the normalized magnitude of the offset consolidation shear stress is given in terms of static stress ratio, SSR_x. Various undrained cyclic shear stress or strain paths are presented in red, for which the normalized magnitudes of the cyclic shear stresses along the x and y directions are given in terms of cyclic stress ratios, CSR_x and CSR_y. Yang et al. (2016) have elaborated how these shearing paths can be produced based on the mathematical expressions of the two shear components in the top plane of the sample. Some general information about the related available tests in the literature on clays and sands are summarized in Table 6.1.

The 1-D linear path, as shown in Figure 6.2(a), is the traditional unidirectional cyclic simple shear test), which may also include an initial offset shear stress in the same direction as the subsequent undrained cyclic shearing. This type of tests has been conducted by many researchers on different types of soil, and there is a wealth of data available, such as Boulanger et al. (1991); Kammerer et al. (2002); Sun (2019) presented in Table 6.1. When the undrained cyclic shearing is applied perpendicular to the direction of initial offset shear stress, the shearing path is denoted

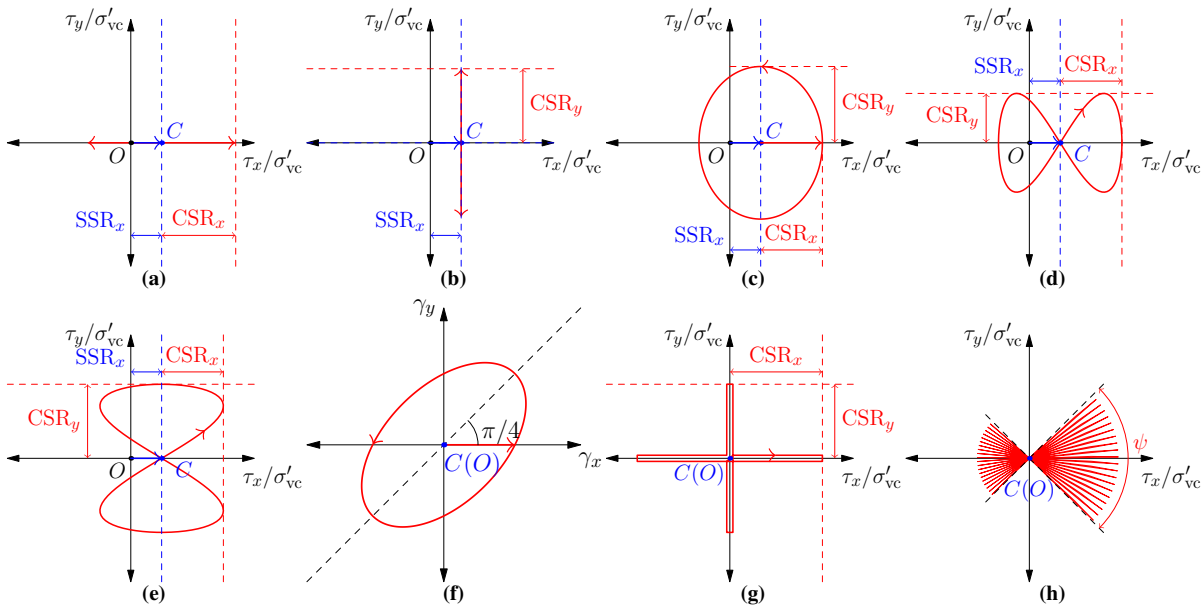

Figure 6.2: Cyclic shearing paths summarized in Yang et al. (2016) during cyclic shearing stage: (a) 1-D linear path, (b) 2-D linear path, (c) circular/oval path, (d) figure-8 type A path, (e) figure-8 type B path, (f) rotated oval path, (g) alternate path, and (h) sector path.

Table 6.1: Experimental database for multidirectional cyclic shear tests on sands.

Shearing path	Initial state	Material	Source
1-D linear path	CK_α	Sacramento River sand	Boulanger et al. (1991)
		Monterey No. 0/30 sand	Kammerer et al. (2002)
		Hostun S28 sand	Sun (2019)
2-D linear path	CK_α	Sacramento River sand	Boulanger et al. (1991)
		Monterey No. 0/30 sand	Kammerer et al. (2002)
		Hostun S28 sand	Sun (2019)
circular/oval path	CI	Fuji River sand	Ishihara and Yamazaki (1980)
	CK_0	Monterey No. 0/30 sand	Kammerer et al. (2002)
		Hostun S28 sand	Sun (2019)
	CK_α	Monterey No. 0/30 sand	Kammerer et al. (2002)
figure-8 type A path	CK_0	Monterey No. 0/30 sand	Kammerer et al. (2002)
		Hostun S28 sand	Sun (2019)
	CK_α	Monterey No. 0/30 sand	Kammerer et al. (2002)
figure-8 type B path	CK_0	Monterey No. 0/30 sand	Kammerer et al. (2002)
	CK_α	Monterey No. 0/30 sand	Kammerer et al. (2002)
rotated oval path	CK_0	Toyoura sand	Matsuda et al. (2011)
		GBFS	Matsuda et al. (2011)
alternate path	CI	Fuji River sand	Ishihara and Yamazaki (1980)
sector path	CK_0	North Sea sand	Rudolph et al. (2014)
irregular path	CI	Fuji River sand	Ishihara and Nagase (1988)

by 2-D linear path, as shown in Figure 6.2(b). This type of shearing dates back to Boulanger et al. (1991) on Sacramento River sand and later was adopted by Kammerer et al. (2002) on Monterey No. 0/30 sand and Sun (2019) on Hostun S28 sand.

Circular/oval path in Figure 6.2(c) is first reported by Ishihara and Yamazaki (1980) on Fuji River sand sample under CI condition. Later, such path was applied on Monterey No. 0/30 sand (Kammerer et al., 2002) under CK_0 and CK_α conditions, and Hostun S28 sand (Sun, 2019) under CK_0 condition. Figure-8 type A and figure-8 type-B are two non-trivial shearing paths, as shown in Figures 6.2(d) and (e), respectively. They are first reported in the experiments on Monterey No. 0/30 sand (Kammerer et al., 2002) and Sun (2019) also applied Figure-8 type A to CK_0 samples of Hostun S28 sand. Figure 6.2(f) shows another non-trivial path named rotated oval as used by Matsuda et al. (2011) on Toyoura sand GBFS. Experiments with the so-called alternate path shown in Figure 6.2(g) are reported by Ishihara and Yamazaki (1980) on Fuji River sand under CI condition. Finally Figure 6.2(h) presents a case where only the orientation of the planar shear stress magnitude continuously changes. This type of shearing has been adopted on North Sea sand (Rudolph et al., 2014) under CK_0 condition.

Aside from these, Ishihara and Nagase (1988) have reported applying the reproduced shearing paths from real earthquakes on Fuji River sand specimen under CI condition, as listed in Table 6.1. There are also some other complex paths such as half-circular/oval path and cropped figure-8 path in Kammerer et al. (2002), which for brevity are not illustrated in Figure 6.2 or listed in Table 6.1.

6.2.2 Experimental tests for this study

From the described types of shearing paths, Table 6.1 includes one relatively rich group of multidirectional cyclic shear tests on Monterey No. 0/30 sand from Kammerer et al. (2002). This group of laboratory tests appears to be suitable for the performance evaluation of various constitutive models for multidirectional cyclic shearing of sand. Particularly this database has been shared publicly by the authors where they provide all the experimental data online, from which such an evaluation study benefits extensively.

Details of all the multidirectional cyclic shear tests to be simulated in this study are listed in Table 6.2. The first seven 1-D linear tests with zero SSR_x from Wu (2002) are used for calibration of the constitutive model. The laboratory tests used for evaluation of the model consist of two 1-D linear tests with nonzero SSR_x, two 2-D linear tests, three circular/oval tests and three figure-8 tests. It should be noted that the three tests for both circular/oval and figure-8 paths have nearly zero, medium and large SSR_x, respectively while the SSR_y is relatively small. To numerically replicate the initial state of each sample, at least the initial void ratio e_{in} and the initial stress state prior to cyclic shearing stage are required for each case. All of these tests are carried out under

Table 6.2: Simulated experimental tests on Monterey No. 0/30 sand.

Test type	Test #	e_{in} $(-)$	Consolidation stage			Shearing stage	
			σ'_{vc} (kPa)	SSR_x $(-)$	SSR_y $(-)$	CSR_x $(-)$	CSR_y $(-)$
1-D linear	Ms15j*	0.699	95.00			0.195	
	Ms16j*	0.682	85.00			0.166	
	Ms19j*	0.696	80.00			0.323	
	Ms25j*	0.692	85.00			0.339	
	Ms28j*	0.692	85.00			0.247	
	Ms59j*	0.685	98.00			0.223	
	Ms79j*	0.679	79.00			0.233	
	Ms66cyck	0.617	73.24	0.290		0.510	
	Ms67cyck	0.579	77.65	0.150		0.480	
2-D linear	Ms20cyck	0.665	76.75	0.101			0.234
	Ms61cyck	0.668	82.58	0.141			0.254
Circular/oval	Ms44cyck	0.651	84.52	0.025	0.007	0.232	0.397
	Ms35cyck	0.655	87.91	0.094	0.030	0.233	0.118
	Ms59cyck	0.696	54.66	0.216	0.009	0.192	0.376
Figure-8	Ms42cyck	0.672	90.75	-0.003	0.030	0.203	0.392
	Ms38cyck	0.668	88.11	0.086	0.024	0.227	0.118
	Ms51cyck	0.668	83.49	0.225	0.000	0.439	0.220

* tests from Wu (2002) for calibration of the constitutive model.

either CK_0 or CK_α condition. In the initial consolidation stage, as the soil specimen is consolidated with lateral normal strains constrained, the initial consolidation effective vertical stress is denoted by σ'_{vc} and the normalized magnitude of initial offset shear stress along the x-direction is denoted by SSR_x. In order to simulate the experiments more accurately, in some cases a small value of SSR_y is also considered as reported in Table 6.2. For cyclic shearing stage, the quantities of CSR along the x and y directions, and the number of loading cycles are listed in the table.

6.3 Calibration of SANISAND-MSf

The SANISAND-MSf model is calibrated using experimental data of Monterey sand Wu (2002); Kammerer et al. (2002). The calibration process is briefly discussed in this section, with emphases on the parameters responsible for cyclic loading simulations.

The Monterey No. 0/30 sand database used in this study comes from a testing program at the University of California, Berkeley (Wu, 2002; Kammerer et al., 2002). To calibrate the model constants of SANISAND-MSf, both monotonic and cyclic tests are required. The above reference database however only includes unidirectional and multidirectional cyclic shear tests. Although

the Monterey No. 0/30 sand was also used as the standard laboratory testing sand at the University of Colorado, Boulder (Horita, 1985; Chen, 1988), it has been reported by Wu (2002) that this type of Monterey No. 0/30 sand at the University of Colorado is substantially different from the sand at the University of California, Berkeley. In view of unavailability of monotonic tests on Monterey No. 0/30 sand, undrained monotonic triaxial tests on Monterey No. 0 sand from Riemer (1992) are chosen for the calibration because both materials show the similarity in the respective gradation curves (Wu, 2002). In this case, most of the model constants except ones of fabric dilatancy, memory surface and semifluidized state, which are pertinent to cyclic loading simulations, are calibrated based on Monterey No. 0 sand. For calibration of the other model constants unidirectional cyclic shear tests from Wu (2002) on Monterey No. 0/30 sand are used.

The SANISAND-MSf model requires the calibration of 21 model constants, divided into three groups. The first group consists of 16 constants inherited from DM04 (Dafalias and Manzari, 2004) and details of their calibrations can be found in Taiebat et al. (2010). Based on the small strain domain of the deviatoric stress and axial strain curves provided in Riemer (1992), from several monotonic triaxial compression tests, an initial estimate is made for the the shear modulus coefficient G_0. From the critical state information of monotonic triaxial compression tests, the model constants related to the critical state line (CSL) are determined by curve fitting, and then tuned a little according to Wang and Ma (2019). Some other model parameter are typically found by a trial-and-error procedure for matching certain aspects of stress-strain response; e.g., ν, m, n^{d}, A_0', n^{b}, h_0 and c_h are determined from monotonic loading, and $z_{\max}$ and c_z from cyclic loading. In the present study, given the considerable size of experimental database, instead of using the inefficient trial-and-error procedure, an optimization algorithm suggested by Liu et al. (2016) is used for faster and better calibration of these model parameters. With the CSL parameters fixed and an initial guess on G_0, plus reasonable guesses on the initial value and bounds of the other model parameters except the ones related to cyclic test, three undrained triaxial compression tests are chosen to build the objective function. Later, c_z and $z_{\max}$ are determined by trial and error procedure on dozens of cyclic simple shear tests from Wu (2002).

The second group is related to memory surface, which controls the pace of pore pressure generation. According to the seven undrained cyclic simple shear tests in Table 6.2, one can estimate the liquefaction strength curve with initial liquefaction referring to $r_u = 0.95$. The simulated liquefaction strength curve is allowed to match the experimental one by tuning the model constants μ_0 and u, where μ_0 affects the position while u affects both the position and the slope.

The last group of model constants related to semifluidized state requires determination of x and c_ℓ for capturing post-liquefaction shear strain development. The following procedure is recommended: (1) keep c_ℓ, and vary x to capture the general trend of shear strain development;

(2) tune c_ℓ for local revision of this general trend towards a better match for each cycle.

The complete list of the calibrated model constants is given in Table 6.3. An example of the

Table 6.3: Model constants of SANISAND-MSf for Monterey No. 0/30 sand

Model constants	Symbol	Value
Elasticity	G_0	101
	ν	0.04
CSL	M	1.32
	c	0.718
	e_c^{ref}	0.900
	λ_c	0.03
	ξ	0.7
Yield surface	m	0.01
Dilatancy	n^{d}	2.0
	A_0'	0.213
	n_g	0.9
Kinematic	n^{b}	0.80
Hardening	h_0'	7.93
	c_h	1.14
Fabric-dilatancy	$z_{\max}$	25
	c_z	1000
Memory surface	μ_0	4.08
	u	2.6
Semifluidized state	c_l	20
	x	2.5

results of the calibration procedure on cyclic simple shear test is presented in Figure 6.3, including stress path, stress strain response, pore pressure generation and shear strain development. One can observe an overall satisfying comparison between experiment and simulation. In addition, Figure 6.4 displays the liquefaction strength curve with initial liquefaction defined by the first time that the double amplitude of shear strain reaches 6.0%, summarizing simulation results of all the seven undrained cyclic simple shear tests. The solid lines are fitted according to the function $\mathrm{CSR} = aN_{\mathrm{IL}}^b$ where a and b are parameters to be determined. Despite certain mismatch for some comparisons, generally, this calibration is trustworthy.

For the above mentioned cyclic loading scenarios on Monterey sand and the subsequent multidirectional simulations presented in the next section, the initial conditions considered for the numerical simulations are that of the end of the consolidation stage from the experiments. In other words, the initial consolidation stage is not simulated by SANISAND-MSf. This is partly because it is usually difficult to obtain the sample information such as the void ratio prior to the initial consolidation stage. In addition SANISAND-MSf does not consider effects from the initial

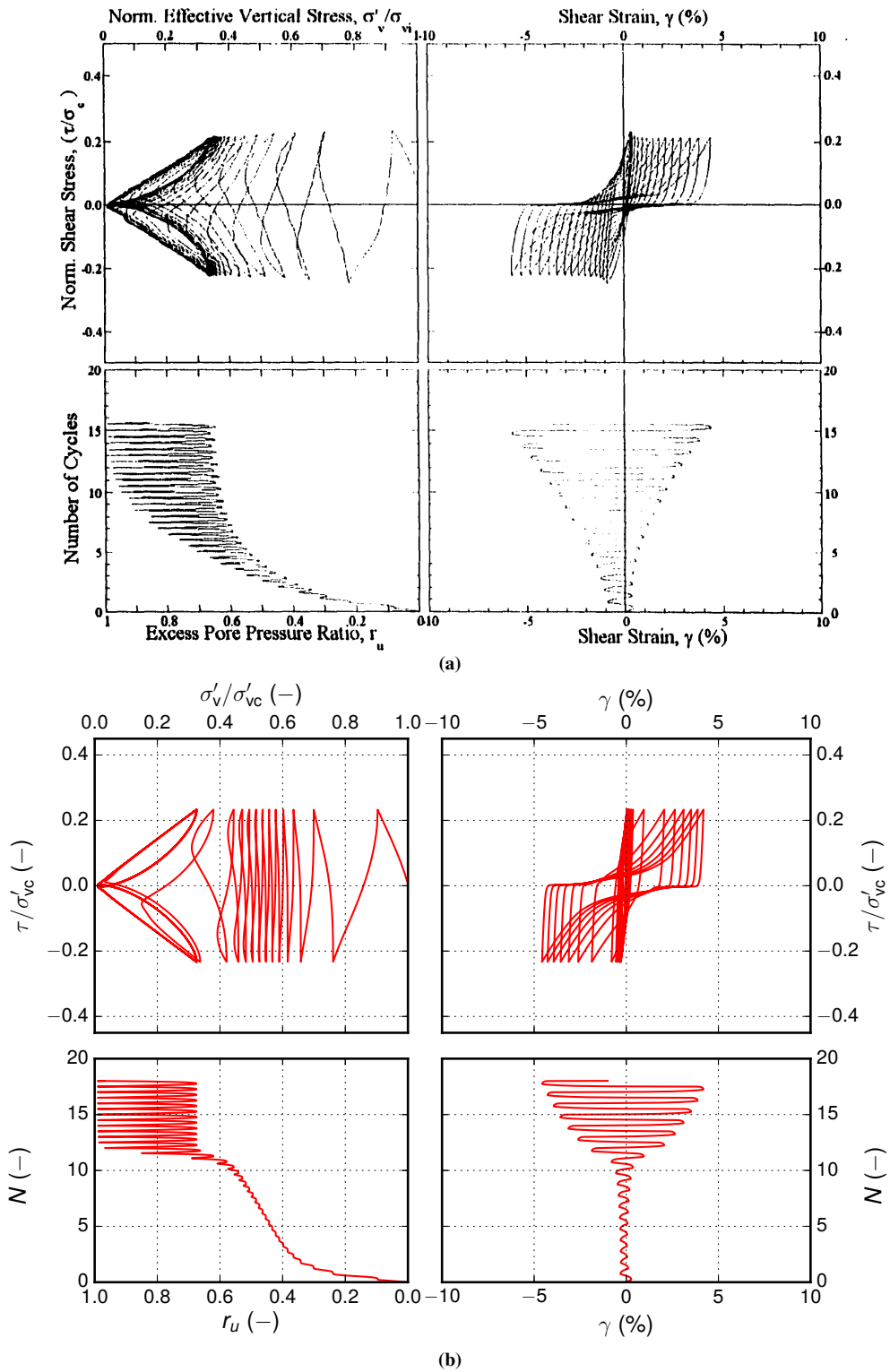

Figure 6.3: SANISAND-MSf simulation versus experiment in undrained cyclic simple shear test on CK$_0$ sample of Monterey No. 0/30 sand with $D_r = 58\%$ and $\sigma'_{vc} = 98$ kPa under a CSR of 0.223: (a) experiment from Wu (2002) and (b) simulation.

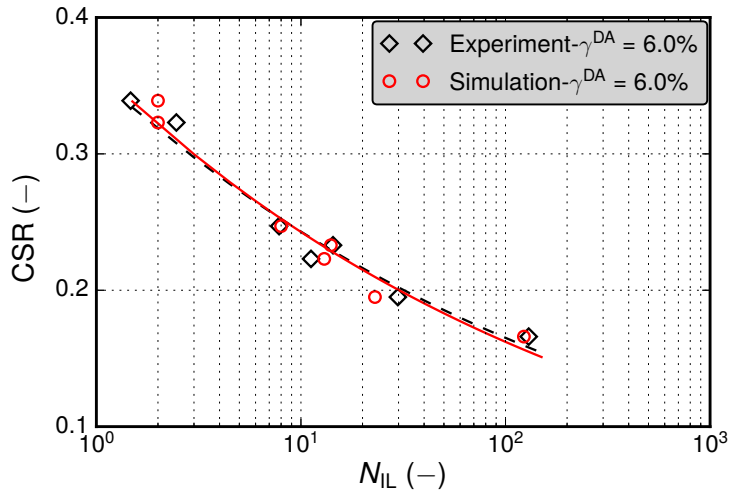

Figure 6.4: Cyclic liquefaction strength curve on CK_0 samples of Monterey No. 0/30 sand with $D_r \approx 60\%$ and $\sigma'_{vc} \approx 80$ kPa: experimental data from Wu (2002).

fabric, so there is not much point in trying to simulate the sample state during the consolidation stage. As the lateral normal stresses are not measured in the experiments, to account for the initial CK_0 and CK_α conditions an assumption is made that both initial lateral normal stresses are equal to half of the initial effective vertical stress σ'_{vc} , i.e., $K_0 = 0.5$ for both types of samples.

6.4 Simulation results for multidirectional cyclic loading

Based on the parameters calibrated in the previous section, the SANISAND-MSf model is used here for illustration of its simulative capabilities according to simulation results of ten related multidirectional cyclic shear tests. The simulated cyclic shear paths include 1-D and 2-D linear, circular/oval, and figure-8. From the large number of tests that are simulated, detailed results are presented for only selected ones. Then selected aspects are the results for all of the tests are summarized at the end.

Some of the presented results are in terms of shear strain magnitude $\gamma = \sqrt{\gamma_x^2 + \gamma_y^2}$. Of course in the 1-D linear path, it yields $\gamma = |\gamma_x|$ due to the absence of the γ_y component and instead $\gamma = \gamma_x$ is widely used by removing the operator of absolute value. In the presentation of the selected complete sets of the results two layouts are considered, each consisting of four subplots.

(i) For 1-D linear paths, normalized stress path (τ/σ'_{vc} against σ'_v/σ'_{vc}), and stress-strain path (τ/σ'_{vc} against γ) are plotted as the top two subplots of the layout. Accumulation of pore pressure ratio with number of cycles (r_u against N) and development of shear strain magnitude with number of cycles (γ against N) are plotted as the bottom two subplots of the layout.

(ii) For 2-D linear, circular/oval and figure-8 paths, normalized shear stress path (τ_y/σ'_{vc} against τ_x/σ'_{vc}), and shear strain path (γ_y against γ_x) are plotted as the top two subplots of the layout. The bottom two subplots of this layout are same as those used for 1-D and 2-D linear paths.

The layout of the summary plots consists of accumulation of pore pressure ratio with number of cycles (r_u versus N), and development of shear strains with number of cycles (γ_x and γ_y versus N).

Simulations against experiment results for Monterey No. 0/30 are provided next. The tests include two 1-D linear, two 2-D linear, three circular/oval, and three figure-8 shear paths.

6.4.1 1-D and 2-D linear stress paths

A complete set of simulation results for a 1-D linear path test Ms67cyck with initial static shear stress is presented in Figure 6.5. The model captures the contractive and dilative parts of various cycles, and with a slightly faster pace than the experiment it reaches the non-symmetric "butterfly" stress orbit where it better captures the cycles of excess pore pressure variation. In terms of shear strains development, the simulated stress-strain curve tends to shift along the initial static shear stress direction with a bit smaller amplitude of oscillation than those in the experiment. It appears that in the reverse loading cycles toward decreasing of shear stress, the model does not generate as much reversal strain as those observed in the experiment, and this is why the strain path tends toward the positive shear strain direction.

Comparison between experiments and simulation results for the two selected 1-D linear tests is summarized in Figure 6.6, including results of Ms66cyck and Ms67cyck. Simulations of pore water pressure are in acceptable agreement with the experiments in terms of both accumulation and oscillation, while simulations of shear strain γ_x overestimate the observed pace of accumulation from the experiments for the two CSRs.

A complete set of simulation results for a 2-D linear test Ms61cyck is shown in Figure 6.7. The model is successful in simulating the trend of pore pressure accumulation, despite a bit faster pace than the experiments in the beginning of the cyclic loading. Given the shear stress path shown in this figure, the simulated shear strain orbit reveals that the model behaves softer than the experiment along the initial static shear stress direction. Note that, with x and y referring to the intended slope dip and strike directions, respectively, this type of loading can be seen as a problem that an element of soil under a slope (hence under initial shearing in the slope dip direction) is subjected to an unidirectional earthquake along the slope strike direction. Similar to the experiment, the simulation indicates that accumulation of considerable shear strain should be expected along the slope dip direction, and it is insightful that the model captures this phenomenon. According to the relation of total shear strain γ and the number of cycles N, the model could not simulate the

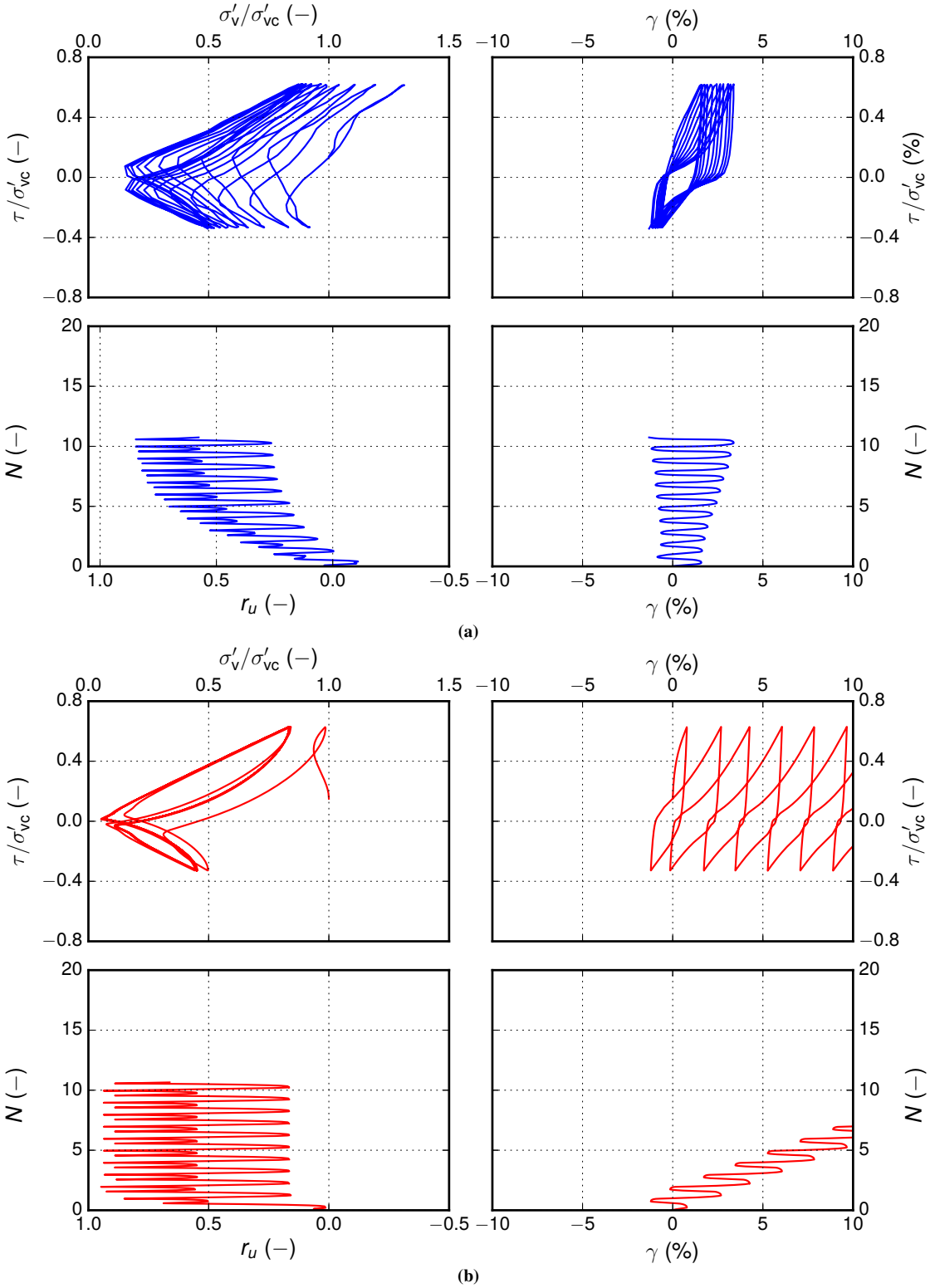

Figure 6.5: SANISAND-MSf simulation versus experiments in 1-D linear multidirectional cyclic shear test Ms67cyck on Monterey No. 0/30 sand: (a) experiment from Kammerer et al. (2002) and (b) simulation.

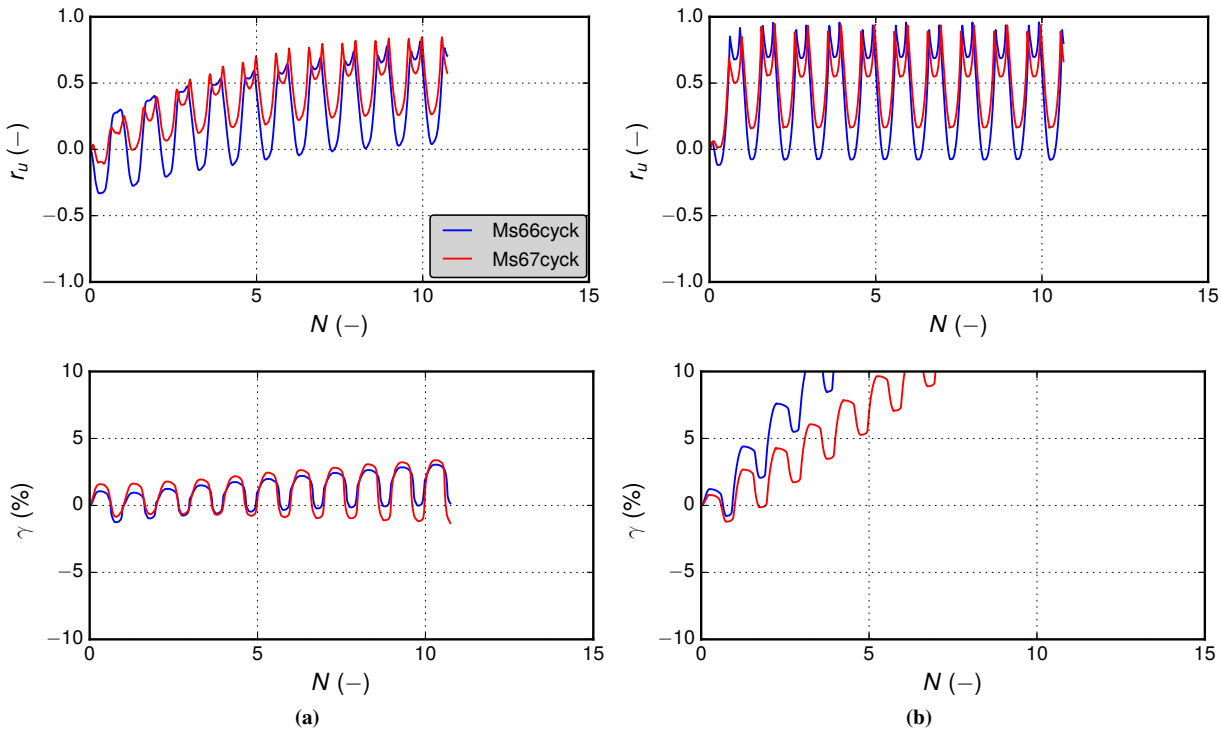

Figure 6.6: SANISAND-MSf simulations versus experiments in 1-D linear multidirectional cyclic shear tests on Monterey No. 0/30 sand: (a) experiments from Kammerer et al. (2002) and (b) simulations.

convex trend (implying a shakedown in development of γ), revealing further improvement in either calibration or modification of the constitutive model.

Comparison between experiments and simulation results for 2-D linear tests is summarized in Figure 6.8, including results of Ms20cyck and Ms61cyck. Simulations of pore pressure are in good agreement with the experiments in terms of the accumulation, but with slightly smaller oscillation magnitudes in each cycle. One may notice the simulated pace of r_u for the two tests is different from the experiments. According to Table 6.2, both tests have a similar initial void ratio but Ms61cyck has a higher SSR_x and CSR_y than Ms20cyck. Thus one may expect a faster development of r_u for Ms61cyck, not reflected by the experiments. It is likely that the simulations are more convincing. For the shear strain along the initial static shear stress direction γ_x, the average trend of the simulations is good but the model behaves softer than the experiment. In particular, after the first few cycles, the model seems to exhibit a nearly constant shear stiffness for all subsequent cycles, while in the experiment the stiffness appears to have an increasing trend with the number of cycles. From those two experiments, it is easy to assert that the mobilized maximum pore pressure ratio does not reach beyond 0.8 but the accumulated shear strain can go beyond 10%. This contradicts a very common assumption that large deformation is usually induced by liquefaction with pore pressure ratio of around 1.0.

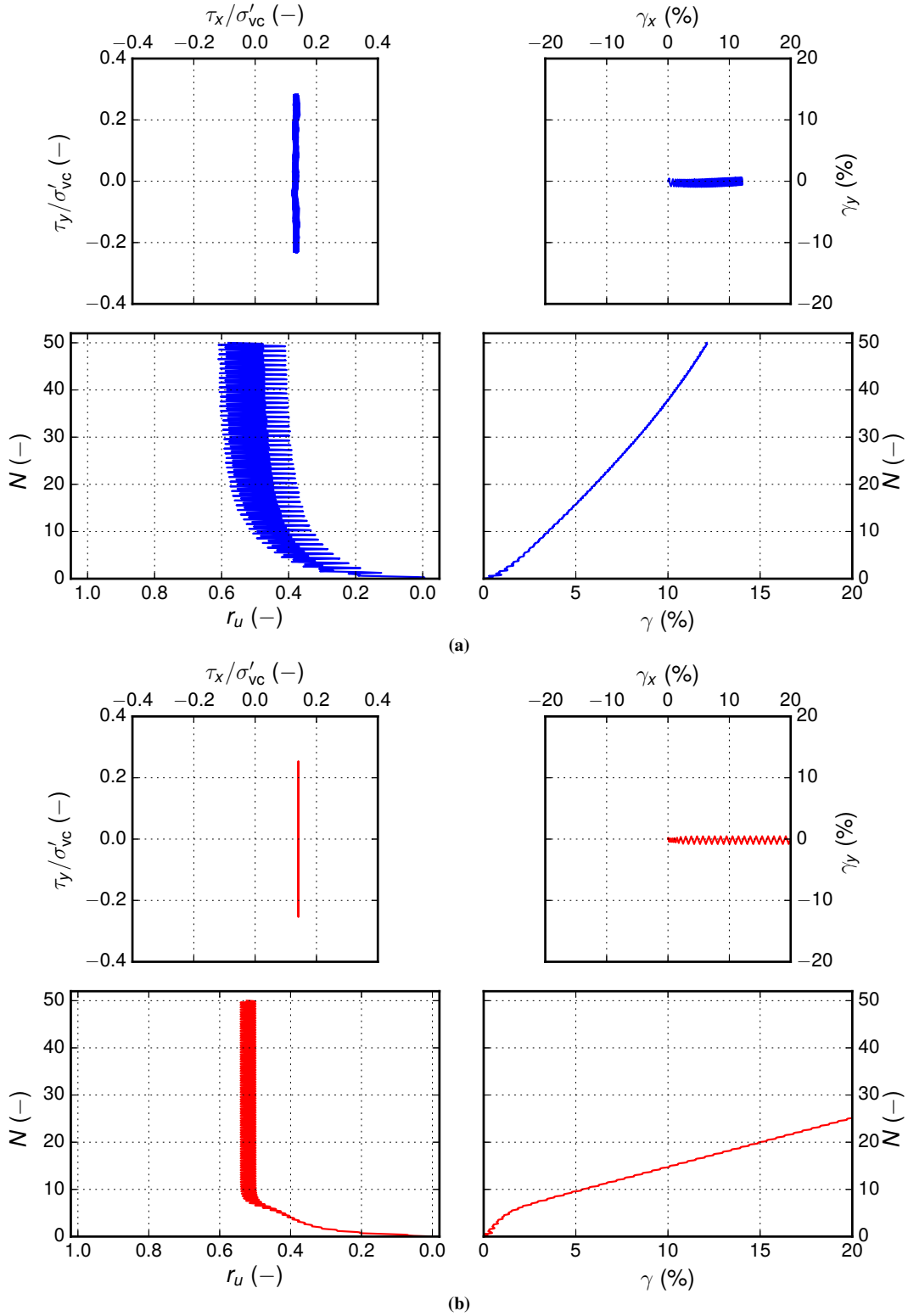

Figure 6.7: SANISAND-MSf simulation versus experiments in 2-D linear multidirectional cyclic shear test Ms61cyck on Monterey No. 0/30 sand: (a) experiment from Kammerer et al. (2002) and (b) simulation.

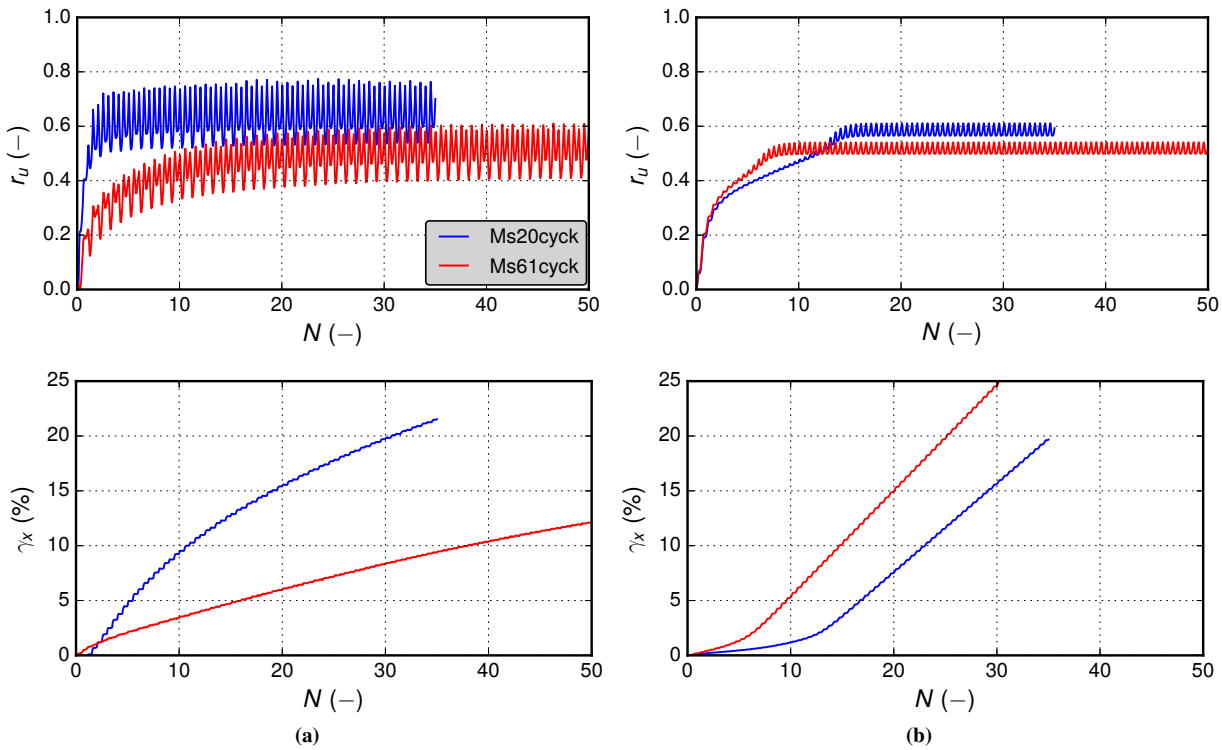

Figure 6.8: SANISAND-MSf simulations versus experiments in 2-D linear multidirectional cyclic shear tests on Monterey No. 0/30 sand: (a) experiments from Kammerer et al. (2002) and (b) simulations.

6.4.2 Circular/oval stress path

A complete set of simulation results for a circular/oval test Ms35cyck with a medium SSR_x is presented in Figure 6.9. The model still performs very well in capturing pore pressure accumulation. The simulated strain orbit of γ_y versus γ_x seems to deviate noticeably from the experiment as it only shifts along y direction rather than expands gradually. One can argue that this may share the same reason with the 1-D linear case in Figure 6.5 where the shear strain is not able to expand on both shearing directions. The constitutive ingredient of semifluidized state is helpful to increase the shear strain amplitude in Figure 6.5 at the instance of the sample falling into states of low effective stresses. However, it does not contribute to expanding the strain orbit of Figure 6.9 as the sample does not enter semifluidized state, i.e., r_u is not getting close to 1. Nevertheless, careful examination of the resultant strain shows that the model captures well the average shear strain in each cycle, implying the model deals with the effect of SSR_x properly. But the main problem here is missing the magnitude of the oscillations in each loading cycle.

Experiments and simulation results for circular/oval multidirectional cyclic shear tests are summarized in Figure 6.10, including results of Ms44cyck, Ms35cyck, and Ms59cyck. Model simulations of accumulation of pore pressure are quite similar to those observed in the experiments, with slight under-prediction of the magnitude of the oscillations. As for two shear

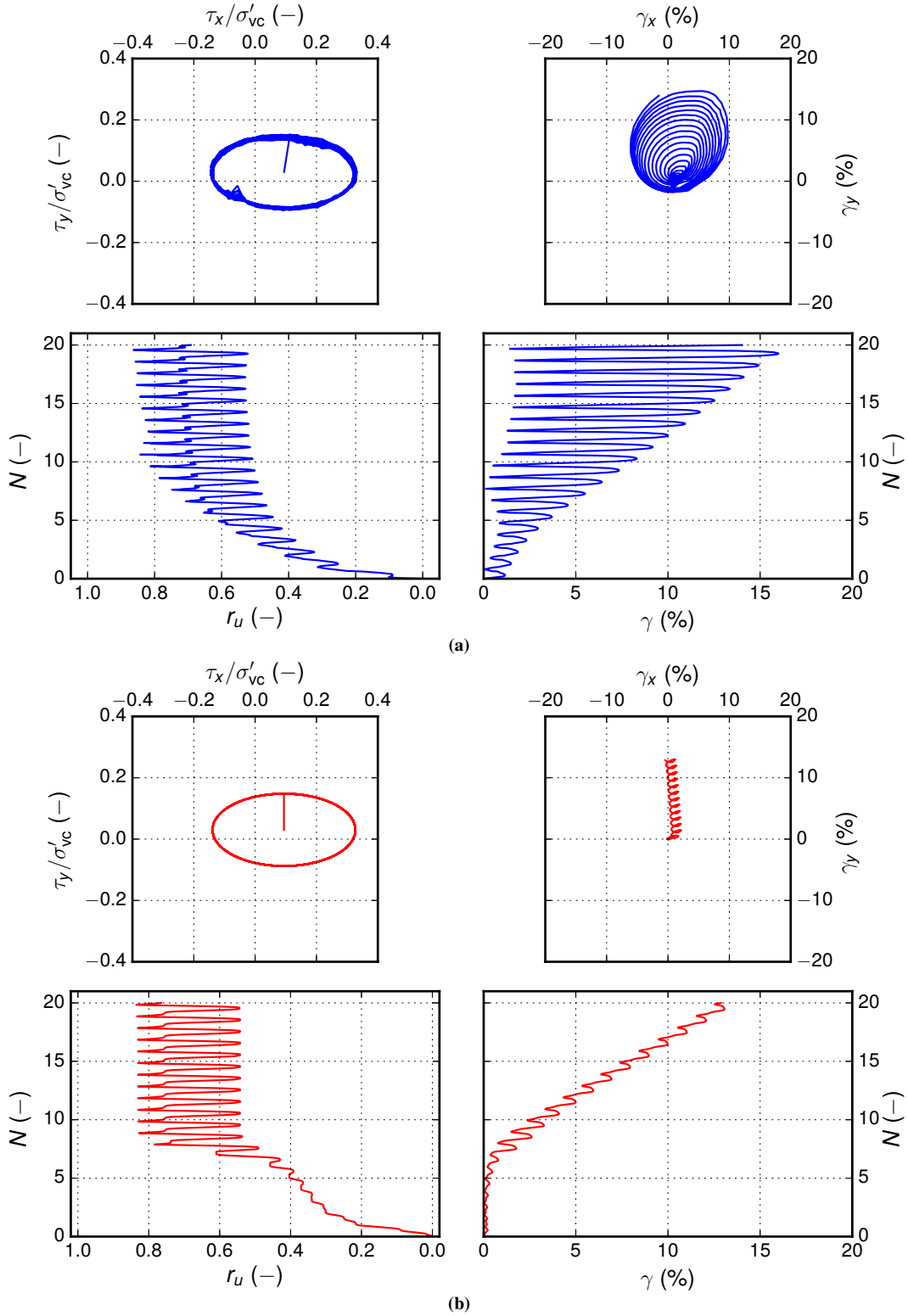

Figure 6.9: SANISAND-MSf simulation versus experiment in circular/oval multidirectional cyclic shear test Ms35cyck on Monterey No. 0/30 sand: (a) experiment from Kammerer et al. (2002) and (b) simulation.

strains of γ_x and γ_y, the model exhibits very good qualitative simulations on the development trend, but missing the amplitude of the cycles as observed and discussed before. Roughly speaking, for the element test with a small SSR, i.e., Ms44cyck, the simulated strain path tends to stay around zero while the experiment produces shear strains oscillating around 0% and increasing in magnitude up to about 10% for γ_x with the number of cycles. For the element test with a medium SSR_x, i.e., Ms35cyck, shear strains can develop and accumulate to larger values.

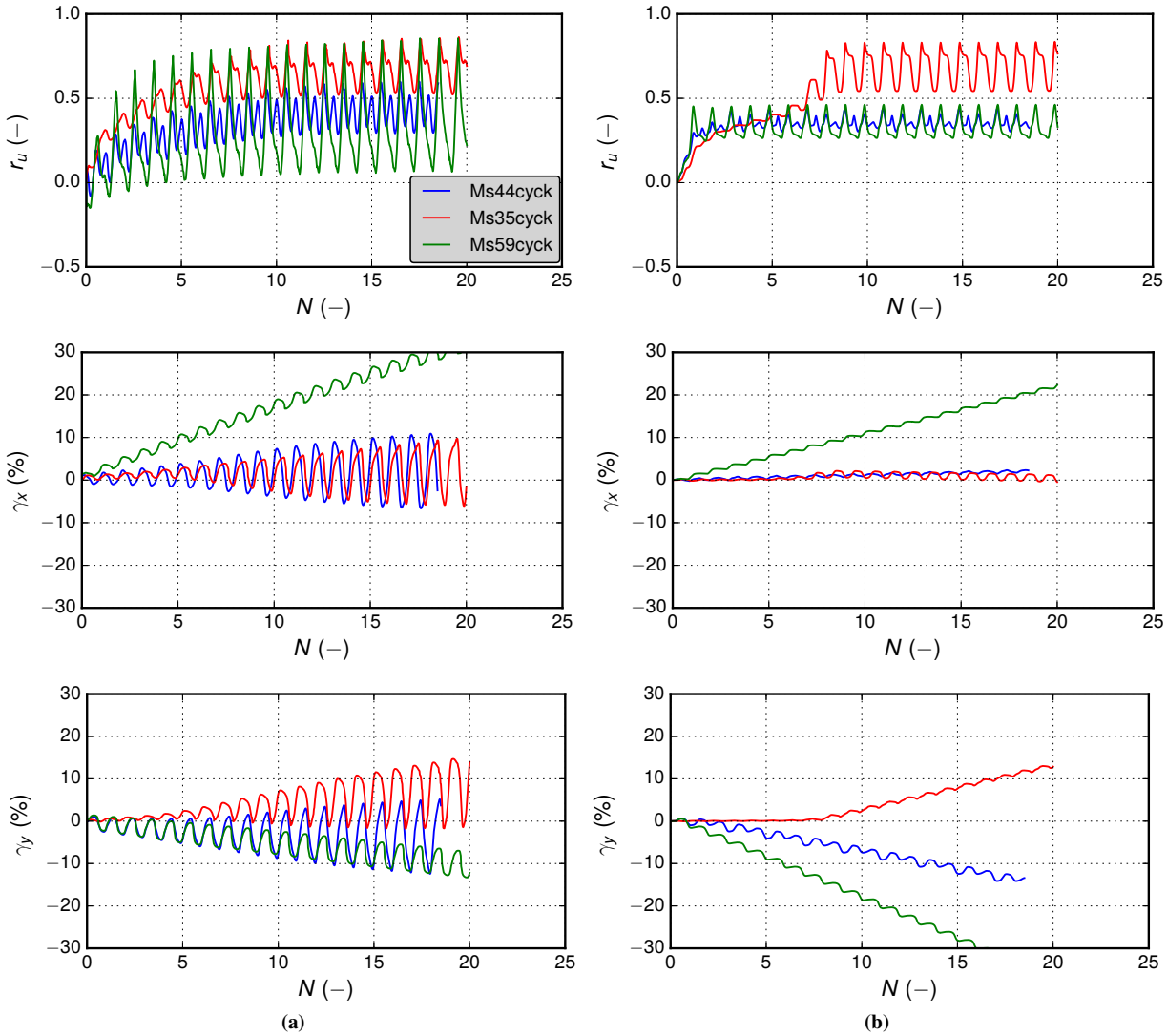

Figure 6.10: SANISAND-MSf simulations versus experiments in circular/oval multidirectional cyclic shear tests on Monterey No. 0/30 sand: (a) experiments from Kammerer et al. (2002) and (b) simulations.

6.4.3 Figure-8 stress path

A complete set of simulation results for a figure-8 test Ms42cyck with a small SSR_x is presented in Figure 6.11. The results of the model simulation with respect to the reported experiments, in terms of both pore pressure and shear strains show similar trends as those observed in the oval stress path of Figure 6.9. Although the applied shear path is close to be symmetric with respect to $\tau_x = 0$, the strain orbits of both experiment and simulation tend to evolve along the positive γ_x side. Here the simulation presents a higher development pace of γ_x and does not reflect the continuous increasing amplitude of γ_y. The general trend of the average response in terms of pore pressure is properly captured by the model, despite the faster accumulation pace in the first several cycles. In addition, the model overestimates the development pace of the resultant shear strain due to the simulated overfast γ_x, and the oscillation magnitudes in each cycle are not properly captured either.

Experiments and simulation results for figure-8 multidirectional cyclic shear test are summarized in Figure 6.12, including results of Ms42cyck, Ms38cyck, and Ms51cyck. The whole picture tells a similar story to circular/oval path in Figure 6.12. The model performs very well in simulating the average trend of the pore pressure generations. As for shear strain accumulation, the model tends to predict the general trend well despite certain mismatch. The key part is that simulations of Ms42cyck, Ms38cyck and Ms51cyck could not produce the oscillations with large amplitude. For the test with nearly zero SSR_x, i.e., Ms42cyck, the sample may fall into the semifluidized state, where considerable shear strain change corresponding to these oscillations can be simulated. However, given the level of shear strain in the experiments larger than 10%, it may be a bit demanding for the feature of semifluidized state mainly developed based on observations of cyclic simple shear tests where the deformation level is usually less than 10%. For the tests with noticeable SSR_x, the existence of SSR_x can drive the sample to deform largely, but how to capture the magnitudes well on the shear plane is still challenging.

6.4.4 Accumulated pore pressure ratio and shear strains

The SANISAND-MSf model was evaluated in modeling multidirectional cyclic shear tests on Monterey No. 0/30 sand. The shearing paths examined include 1-D and 2-D linear, circular/oval and figure-8. The total of ten experiments examined reveal a lot of information about the complexity of the material response and the capabilities and limitations of the model. A summarized comparison of the simulated and measured response for these ten tests are presented in Figure 6.13, which is conducted by selecting a state in the cyclic shearing history. Here for each case, the comparison is made at the end of the 10th cycle as shown in the legend of this figure. The results at the end of selected cycles are compared in terms of pore pressure ratio and shear strains γ_x and γ_y. The horizontal and vertical axes of each plot represent values from the

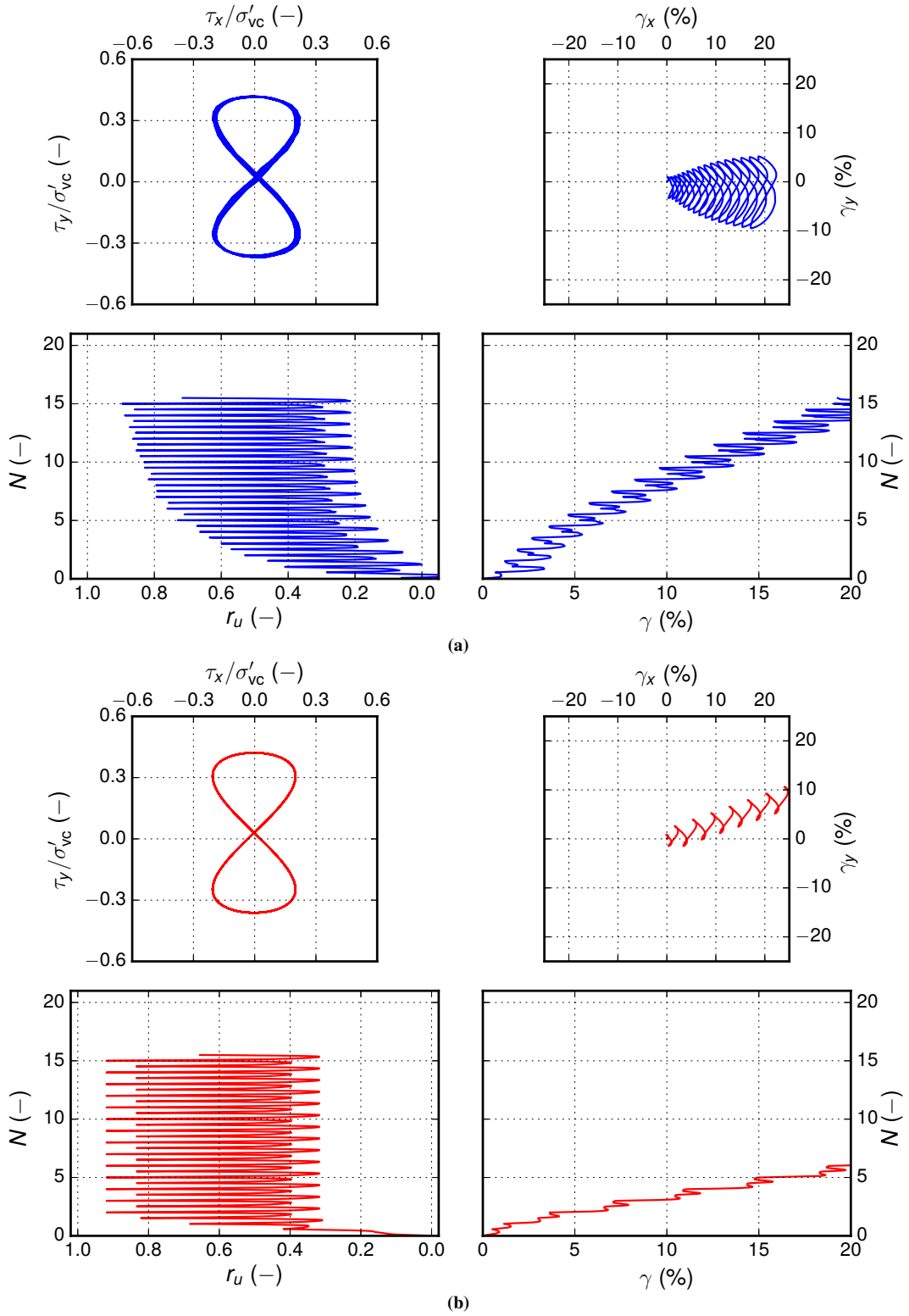

Figure 6.11: SANISAND-MSf simulation versus experiment in figure-8 multidirectional cyclic shear test Ms42cyck on Monterey No. 0/30 sand: (a) experiment from Kammerer et al. (2002) and (b) simulation.

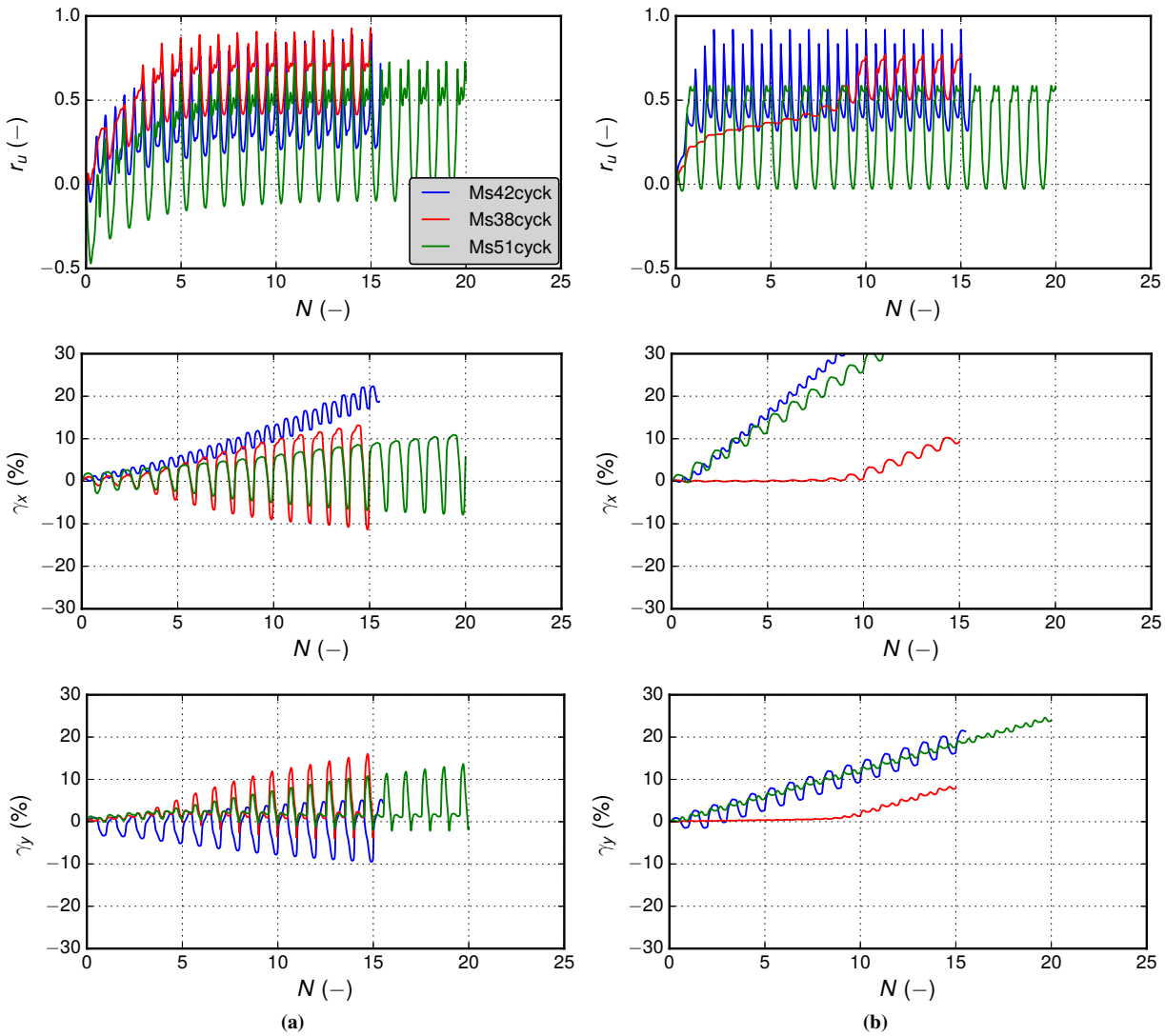

Figure 6.12: SANISAND-MSf simulations versus experiments in figure-8 multidirectional cyclic shear tests on Monterey No. 0/30 sand: (a) experiments from Kammerer et al. (2002) and (b) simulations.

experiments and simulations, respectively, with the diagonal dashed line representing the ideal situation of perfect match between the experimental and simulation results. This method of comparing the experiments as simulations at the end of selected loading cycles does not reveal many detailed aspects of the cyclic response; yet it is a way of getting an overall comparison in dealing with this extensive amount of information.

From Figure 6.13, the model simulates pore pressure ratio in good agreement with the experiments. The accumulated γ_x values are well simulated except for the 1-D linear tests Ms66cyck and Ms67cyck, figure-8 tests Ms42cyck and Ms51cyck where the model response is too soft. It should be noted that the simulated γ_x of Ms66cyck, Ms42cyck and Ms51cyck is larger than 20%, outside the scope of Figure 6.13(b) and here they are placed near the positive limit of

the simulated γ_x for illustration. The accumulated γ_y values are scattered along $1:1$ line but show the good trend except Ms42cyck. Note that almost all the related points are located in the first and third quarters of the plot, which means that simulation results share the same sign with the experiments.

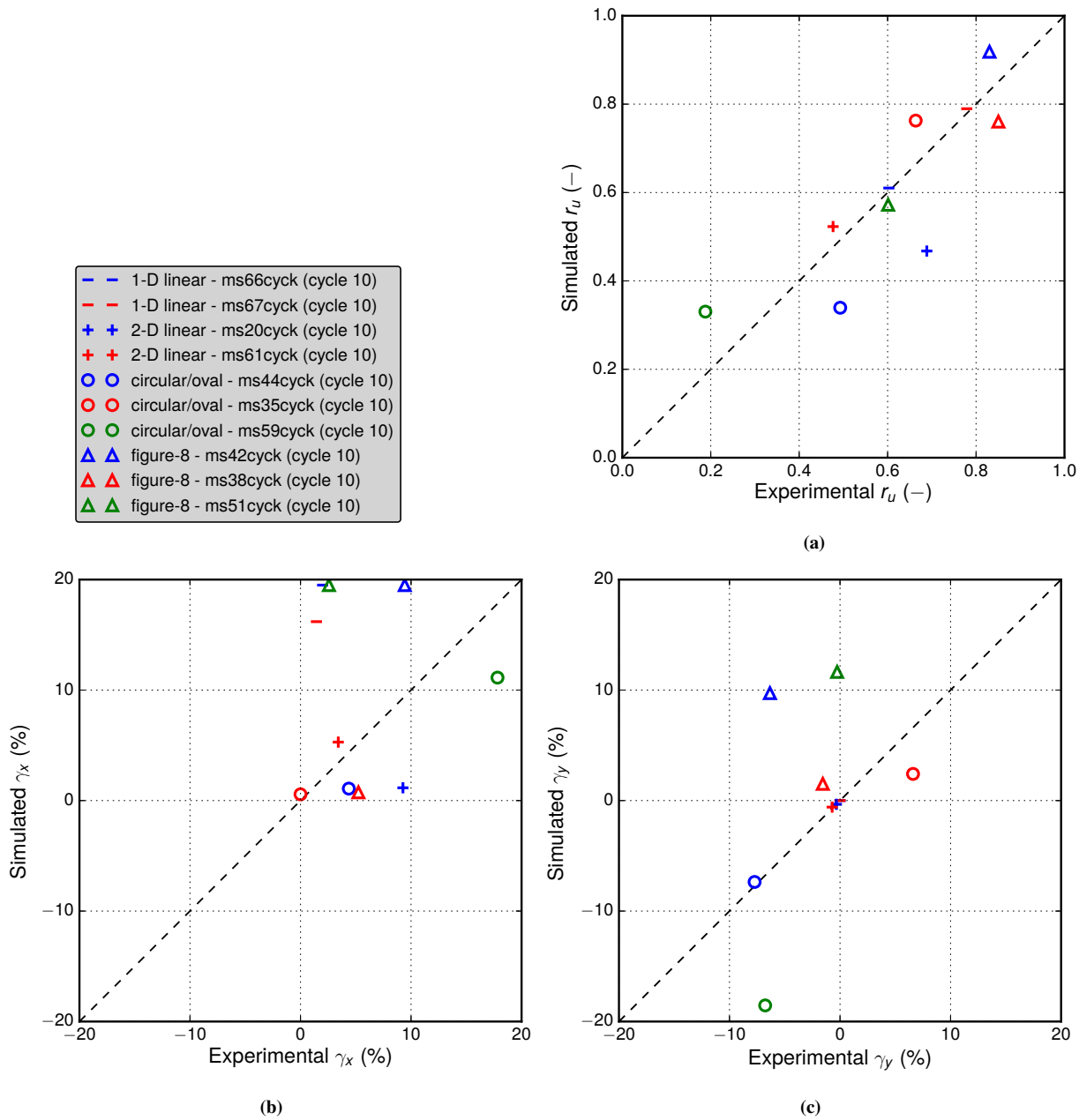

Figure 6.13: Simulations versus experiments of (a) pore pressure ratio r_u, (b) shear strain γ_x and (c) shear strain γ_y at the selected points of loading for different types of multidirectional cyclic shear tests on Monterey No. 0/30 sand (points close to $1:1$ line suggests that the corresponding simulation result is close to experiment and vice versa for the points away from $1:1$ line).

6.5 Evaluating the proximity to neutral loading

In an attempt of revealing potential shortcoming in the models, an investigation is conducted next on the proximity of SANISAND-MSf to the neutral loading when simulating these tests. Dafalias and Taiebat (Dafalias and Taiebat, 2016) recently pointed out the stress reversal surface models and the generalized plasticity models are not truly zero elastic range models, even when they are intended to be, and they produce pure elastic response for the so called neutral loading path that are normal to the "loading direction". It should be emphasized that in reality soils are not expected to exhibit purely elastic response, and the neutral loading is merely an artificial response of many constitutive models. The SANISAND-MSf model inherits the possibility of facing neutral loading condition as they fall in the category of models with stress reversal surfaces. It is therefore interesting to examine these models in the complex stress paths explored in this study.

For a plasticity model with a finite size of yield surface f, neutral loading would occur when the loading path $\dot{\boldsymbol{\sigma}}$ is tangential to the yield surface f, i.e., $(\partial f/\partial \boldsymbol{\sigma}) : \dot{\boldsymbol{\sigma}} = 0$ with $\partial f/\partial \boldsymbol{\sigma}$ being the gradient of the yield surface in the multiaxial stress space, $\dot{\boldsymbol{\sigma}}$ being the stress increment in the stress-controlled simulations, and : representing the inner product operator. For SANISAND-MSf, the neutral loading can be further simplified as the loading path $\dot{\mathbf{r}}$ being tangential to the yield surface in the stress ratio space. In other words, it takes place when $\mathbf{n} : \dot{\mathbf{r}} = 0$ with $\mathbf{n}$ being a gradient of the yield surface in the stress ratio space and $\dot{\mathbf{r}}$ being the stress ratio increment in the stress controlled simulations.

In a complex loading path, one can quantify the proximity of the model response to neutral loading by continuously examining the angle Θ between the loading direction and the stress increment. When $\Theta = 90^\circ$, the neutral loading takes place and the model produces a purely elastic response. For the multidirectional cyclic shear paths, the variation of Θ is expected to be significant. For SANISAND-MSf, Θ is the angle between $\mathbf{n}$ and $\dot{\mathbf{r}}$ given as follows:

$$\Theta = \arccos\left(\frac{\mathbf{n} : \dot{\mathbf{r}}}{\|\mathbf{n}\|\|\dot{\mathbf{r}}\|}\right) \tag{6.1}$$

where $\|\boldsymbol{x}\|$ represents the magnitude of tensor $\boldsymbol{x}$. In the formulation of SANISAND-MSf, the finite size of the yield surface allows for having $\Theta > 90^\circ$ under elastic unloading until stress reversal is detected. The variations of Θ for selected 1-D linear and 2-D linear, circular/oval, and figure-8 paths are plotted in Figure 6.14 for the first 10 cycles of the loadings. For all the applied paths except Ms51cyck, the Θ is always far away from the neutral loading.

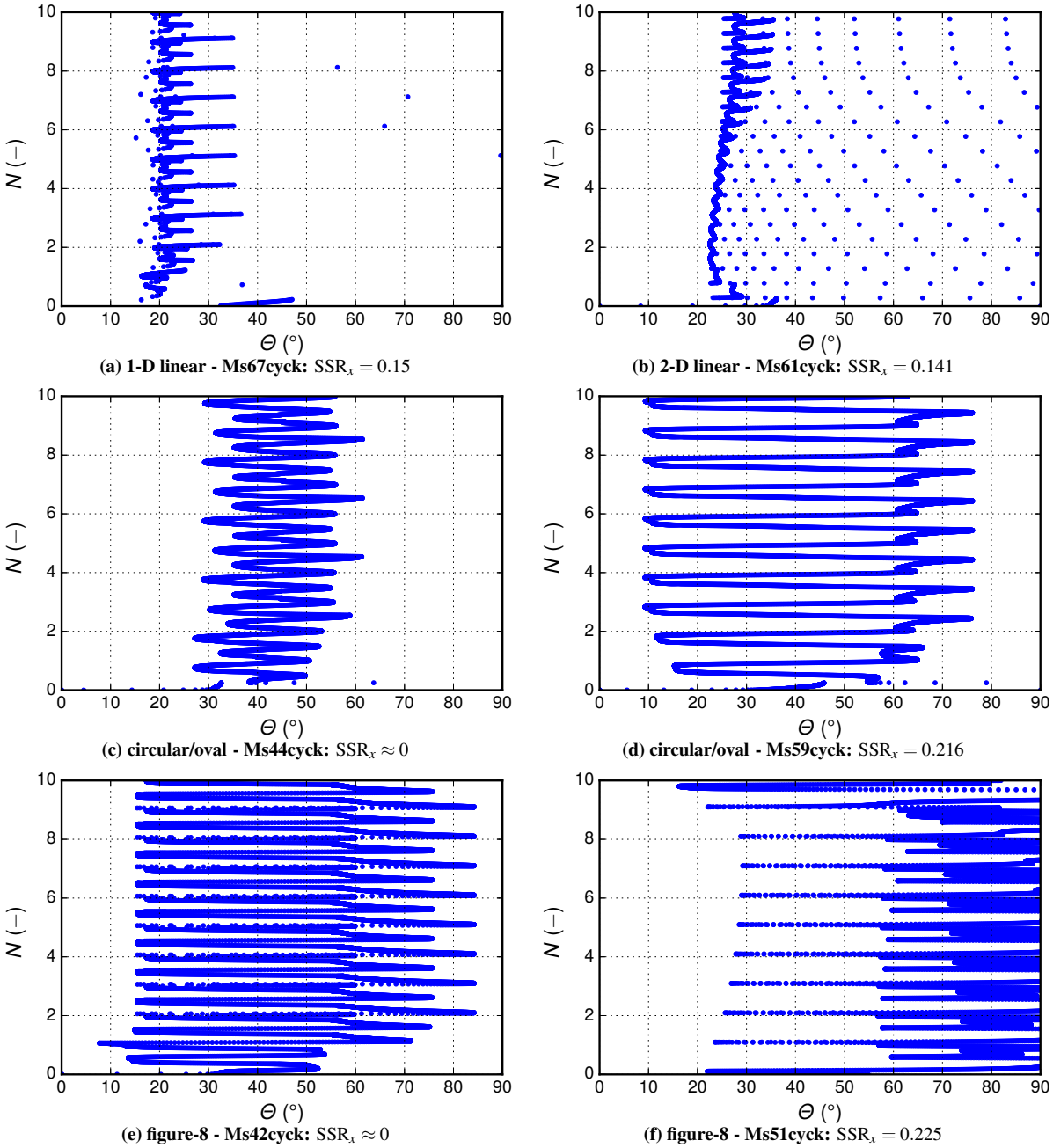

(a) 1-D linear - Ms67cyck: $\mathrm{SSR}_x = 0.15$

(b) 2-D linear - Ms61cyck: $\mathrm{SSR}_x = 0.141$

(c) circular/oval - Ms44cyck: $\mathrm{SSR}_x \approx 0$

(d) circular/oval - Ms59cyck: $\mathrm{SSR}_x = 0.216$

(e) figure-8 - Ms42cyck: $\mathrm{SSR}_x \approx 0$

(f) figure-8 - Ms51cyck: $\mathrm{SSR}_x = 0.225$

Figure 6.14: SANISAND-MSf: the angle Θ between the gradient of yield surface in the stress ratio space n and the stress ratio increment $\dot{\mathbf{r}}$ for cyclic tests simulations.

6.6 Conclusions

In this chapter, an experimental database for laboratory multidirectional cyclic shear tests of sands is established. The new model SANISAND-MSf, which has shown impressive performance in simulating unidirectional cyclic shear tests, is adopted to simulate selective multidirectional cyclic shear tests on Monterey No. 0/30 sand, including 1-D linear, 2-D linear, circular/oval and figure-8 paths. The model is calibrated based on undrained cyclic simple shear tests without initial static bias. In the simulations of multidirectional cyclic shear tests, SANISAND-MSf tends to produce better results for pore pressure accumulation (volumetric response) but does not perform well in development of shear strains (deviatoric response), which is reflected in two aspects: (1) the overall shear strain orbits do not oscillate as heavily as experiments; (2) for the tests with a higher SSR_x, the total shear strain is over-predicted.

In 1-D linear tests without initial shear stress, the first deficiency is not reflected due to semifluidized state activated when mean effective stress p drops below 10 kPa. However, this activation does not take place for the multidirectional cyclic shear tests with zero initial shear stress, i.e., circular/oval path, or the ones with large initial shear stress including 2-D linear, circular/oval and figure-8 paths. Thus, it is necessary to explore another mechanism for sand under multidirectional cyclic shearing (mainly referring to circular/oval and figure-8 paths) which allows for sufficient expansion of shear strain orbits even when the sample does not fall into semifluidized state. A possibility is to introduce an internal variable accumulating deviatoric shear strain used for decreasing the plastic modulus (Wang et al., 1990) since the start of cyclic shearing. But one should pay extra attention to introduce the healing mechanism as mentioned in Chapter 5 and balance its role with semifluidized state in unidirectional cyclic shear test.

The second deficiency is attributed to the fact that the SANISAND-MSf does not perform very well in capturing effects of a variety of initial shear stresses. The calibration was conducted only based on 1-D linear tests with $\mathrm{SSR} = 0$. In multidirectional cyclic shear tests with a medium SSR_x like Ms35cyck and Ms38cyck, the simulated total shear strain develops in good agreement with the experiments, but for the tests with the high SSR_x, SANISAND-MSf tends to over-predict the level of deformation.

These two deficiencies seem to be contradictory in terms of whether the constitutive model presents too stiff or too soft response when the sample stays outside semifluidized state. This contradiction can be argued if one considers whether the existing shear stress induces stress rotation or not. Initial shear stress does not bring stress rotation while the circular/oval and figure-8 paths do, which may imply that the SANISAND-MSf does not handle problems related to stress rotation very well. Thus, the work of Zhang and Wang (2012) and Petalas et al. (2018) motivated by stress principal axes rotation deserve extra attention.

Chapter 7: Summary, Conclusions and Future Work

7.1 Summary

This dissertation is focused on numerical modeling of the response of granular material under uni- and multidirectional cyclic shearing, with the aim of (i) exploring the physics of the granular system and (ii) developing a constitutive model for liquefaction-related problems.

Recognizing the discrete nature of soil, discrete element method (DEM) was adopted for the simulations in the first part of the thesis. A three dimensional (3D) DEM program GRFlow3D was modified to build a bi-periodic system and conduct several constant volume cyclic shear tests. The element simulation results of cyclic simple shear tests presented a promising macro-mechanical response, much like the experiments. Micro-mechanical investigations were performed with respect to contact-based quantities, including particle connectivity, force transmission, and fabric and force anisotropies. In terms of multidirectional cyclic shear test, more than fifty DEM simulations were carried out to explore effects of loading paths on the macro-mechanical response of the granular system, including limiting pore pressure ratio and strain-based liquefaction resistance. The microscopic investigation consisted of particle connectivity, particle-void fabric, and fabric and force anisotropies, corresponding to the system stability, deformation, and load-bearing network, respectively.

Given the continuum approximation of the granular system, an advanced constitutive model was developed for adequately capturing the response of sands under undrained unidirectional cyclic shearing, especially in terms of pre-liquefaction pore pressure generation and post-liquefaction shear strain development. The first aspect was achieved by formulating and incorporating a novel constitutive ingredient of memory surface into the reference model. A recently proposed concept of semifluidized state that can simulate large shear strain development in post-liquefaction stage was simplified due to the existence of memory surface. This new model called SANISAND-MSf were also validated against a series of undrained cyclic torsional and triaxial tests with different CSRs. With the achieved success in simulation of unidirectional cyclic shear tests, SANISAND-MSf was also applied to simulate a list of multidirectional cyclic shear tests on Monterey No. 0/30 sand with the loading paths of 1-D linear, 2-D linear, circular/oval and

figure-8. Comparisons between experiments and simulations were carried out and the proximity of these simulations to neutral loading was also quantified.

7.2 Conclusion

The novel contributions of the dissertation are as follows:

- **Microstructural evolution in isochoric cyclic simple shear test:** a 3D-DEM was adopted to study the cyclic response of granular assembly. The DEM simulations were able to replicate the key macroscopic response as observed in laboratory experiments. At grain scale, evolution of particle connectivity, force transmission and anisotropies of contact and force networks along the whole shearing process was explored. On the way to initial liquefaction (zero mean effective stress), particle connectivity and force transmission varied mildly and fabric anisotropy increased noticeably. Entering semifluidized state was characterized by a sudden drop of coordination number and non-rattler fraction, a significant widening of normal contact force distribution and a high percentage of mobilized contacts, and random particle collisions and short fragile force chains. The system needed to deform significantly to reconstruct the contact network, providing the geometrical basis for rebuilding the force network, thereby exiting liquefaction state. The DEM simulations suggested a critical value of geometrical coordination number 3.6 for onset and offset of liquefaction state, irrespective of the initial and loading conditions. The relationship between deviatoric stress ratio and anisotropies, known to hold in the triaxial setting, also held with reasonable accuracy in the cyclic simple test. Interestingly, fabric and force anisotropies at the peak shear stress appeared to level off after several cycles in post-liquefaction period. Their respective contributions to deviatoric stress ratio were not affected by changing initial and loading conditions.

- **Effects of shear paths on mechanical response of the granular system:** a comprehensive series of simulations covering 1-D linear, 2-D linear, circular/oval and figure-8 shear paths were generated. Macroscopically, effect of shear paths on pore pressure generation was studied, revealing a linear relationship between the limiting pore pressure ratio and the minimum resultant shear stress. Strain-based criterion liquefaction strength curve also indicated the liquefaction resistance decreased in the order of 1-D linear, 2-D linear, circular and figure-8. At the grain scale, evolution of particle connectivity indicated the system became unstable instantaneously for the selected 1-D and figure-8 paths, and stayed stable for 2-D and circular paths. A particle-void descriptor named centroid distance was also monitored to shed light on the shear strain development, from which a general

decreasing trend with shear strain accumulation was evidenced. Finally, evolution of fabric and force anisotropies at specified states of each loading cycle revealed that fabric one needed more time to follow the external shearing compared with the force ones. All these anisotropies tend to level off in post-liquefaction period and their proportions contributing to the deviatoric stress ratio were not affected by the shear paths.

- **Constitutive modeling of sands under undrained unidirectional cyclic shearing:** an advanced constitutive model called SANISAND-MSf was formulated by introducing minor and major modifications into the DM04 model platform by Dafalias and Manzari (2004). The minor modification consisted of modifying the non-associative flow rule for more accurate simulation in non-proportional loading and introducing a simple Lode angle dependence to improve the stress-strain loops shifting in undrained cyclic shear test. The major modification had two parts, incorporating two constitutive ingredients. The first was back-stress ratio-based memory surface used to increase the stiffness for back-stress ratios within it, in order to accurately capture pre-liquefaction pore pressure generation. The second one was the concept of semifluidized state for low effective stresses proposed by Barrero et al. (2020) and simplified herein due to introducing memory surface, allowing simulation of post-liquefaction shear strain development. The SANISAND-MSf model was validated against two experimental databases, undrained cyclic torsional tests and undrained cyclic triaxial tests.

- **Evaluation of the constitutive model in simulating multidirectional cyclic shearing:** by collecting the experimental database for laboratory multidirectional cyclic shear tests, the newly developed SANISAND-MSf model was applied to simulate some of them. SANISAND-MSf tended to produce good simulations for pore pressure accumulation but needed improvement in capturing the oscillations of shear strains, especially for the tests not frequently entering semifluidized state. A quantity was proposed to quantify the proximity of the simulations to neutral loading.

7.3 Recommendations for future work

A number of very interesting studies that may be explored as extension of this thesis are as follows:

- **Effect of particle shape and particle size distribution on the response of granular material under isochoric cyclic simple shearing:** the present unidirectional DEM study adopts one type of particle shape (sphere) and one type of particle size distribution (uniform). The findings of using the $z_g = 3.6$ to quantify onset of semifluidized state and

the weights of each anisotropy contributing to the deviatoric stress ratio may be influenced when other particle shapes or particle size distributions are used. In addition, one can also analyze their effects on the macroscopic response (like stress path and stress-strain) of the granular systems under the same initial and loading conditions.

- **Evaluation of SANISAND-MSf in capturing effect of static shear stress on the response of sands under undrained cyclic shearing:** this model was mainly validated against undrained cyclic shear tests without static shear stress in this dissertation. To apply it to simulate slope-related dynamic problems, evaluating its performance in capturing the effect of static shear stress on the stress path and stress-strain curve is necessary, which can be achieved by simulating a series of the corresponding laboratory element tests. If modification is needed, two directions may deserve extra attention: revisiting the expression of relating the distance of current stress state and the image on the bounding surface to the plastic modulus, and varying the formula of incorporating memory surface into plastic modulus.

- **Application of SANISAND-MSf in simulating boundary value problems related to seismic excitation of sand deposits:** given the success of SANISAND-MSf in simulating undrained cyclic simple shear tests, it is straightforward to apply it to certain boundary value problems of sand deposits under dynamic shaking. Achieving this goal requires a robust numerical implementation and integration in a continuum modeling platform that accounts for fluid-mechanical interactions. One can simulate the centrifuge experiments from the Verification of Liquefaction Analyses and Centrifuge Studies (VELACS) (Arulanandan and Scott, 1993) and the Liquefaction Experiments and Analysis Projects (LEAP) (Manzari et al., 2014) including LEAP-GWU-2015 (Kutter et al., 2018), LEAP-UCD-2017 (Kutter et al., 2020), LEAP-Aisa-2019 (Tobita et al., 2020) for the validation process. After that, statistical analyses of running a number of simulations by varying model constants may help proper use of this constitutive model.

- **Improvement of SANISAND-MSf in simulating large shear strain oscillations of multidirectional cyclic shear tests:** SANISAND-MSf has attained a considerable improvement compared to DM04 in capturing the response in cyclic shearing. However, it needs further refinement for simulating development patterns of shear strains under complex multidirectional stress paths such as circular/oval and figure-8, especially in terms of the oscillations when the sample does not fall into the semifluidized state. This is a very challenging task, not only theoretically but also given the limited experimental laboratory databases. It would be valuable to explore further the reasons for shear strain development in some of these complex stress paths, such as circular/oval, via discrete element modeling,

maybe with much attention on the effect of stress rotation or local failure. This, of course, is not a straightforward task, but if and once the mechanism is understood, it would lead to ideas for refined constitutive formulations to approximate the physics behind such mechanism.

Bibliography

Agnolin, I. and Roux, J.-N. (2007). Internal states of model isotropic granular packings. ii. compression and pressure cycles. *Physical Review E*, 76(6):061303.

Alawaji, H., Runesson, K., and Sture, S. (1992). Implicit integration in soil plasticity under mixed control for drained and undrained response. *International Journal for Numerical and Analytical Methods in Geomechanics*, 16(10):737–756.

Alonso-Marroquin, F. and Herrmann, H. J. (2004). Ratcheting of granular materials. *Physical Review Letters*, 92(5):054301.

Alonso-Marroquin, F., Luding, S., Herrmann, H. J., and Vardoulakis, I. (2005). Role of anisotropy in the elastoplastic response of a polygonal packing. *Physical Review E*, 71(5):051304.

Amirrahmat, S., Imseeh, W. H., Alshibli, K. A., Kenesei, P., Jarrar, Z. A., and Sharma, H. (2020). 3d experimental measurements of evolution of force chains in natural silica sand. *Journal of Geotechnical and Geoenvironmental Engineering*, 146(5):04020027.

Amritkar, A., Deb, S., and Tafti, D. (2014). Efficient parallel cfd-dem simulations using openmp. *Journal of Computational Physics*, 256:501–519.

Arulanandan, K. and Scott, R. F. (1993). Project VELACS—Control test results. *Journal of Geotechnical Engineering*, 119(8):1276–1292.

Asadzadeh, M. and Soroush, A. (2017). Macro- and micromechanical evaluation of cyclic simple shear test by discrete element method. *Particuology*, 31:129–139. 10.1016/j.partic.2016.05.015.

Asadzadeh, M. and Soroush, A. (2018). Evaluation of stress and strain non-uniformity during cyclic simple shear test using dem: effect of the horizontal platen asperities. *Granular Matter*, 20(3):43.

Azéma, E. and Radjaï, F. (2012). Force chains and contact network topology in sheared packings of elongated particles. *Physical Review E*, 85(3):031303.

Azéma, E., Radjaï, F., and Dubois, F. (2013). Packings of irregular polyhedral particles: strength, structure, and effects of angularity. *Physical Review E*, 87(6):062203.

Azéma, E., Radjaï, F., Peyroux, R., and Saussine, G. (2007). Force transmission in a packing of pentagonal particles. *Physical Review E*, 76(1):011301.

Bardet, J.-P. and Choucair, W. (1991). A linearized integration technique for incremental constitutive equations. *International Journal for Numerical and Analytical Methods in Geomechanics*, 15(1):1–19.

Barrero, A. R., Oquendo, W., Taiebat, M., and Lizcano, A. (2018). Cyclic shearing response of granular material in the semifluidized regime. In *Proceedings of Geotechnical Earthquake Engineering and Soil Dynamics V: Numerical Modeling and Soil Structure Interaction (GSP 292)*, pages 100–107. American Society of Civil Engineers Reston, VA, Austin, TX, USA.

Barrero, A. R., Taiebat, M., and Dafalias, Y. F. (2020). Modeling cyclic shearing of sands in semifluidized regime. *International Journal for Numerical and Analytical Methods in Geomechanics*, 44:371–388.

Been, K. and Jefferies, M. G. (1985). A state parameter for sands. *Géotechnique*, 35(2):99–112.

Bernhardt, M. L., Biscontin, G., and O'Sullivan, C. (2016). Experimental validation study of 3d direct simple shear dem simulations. *Soils and Foundations*, 56(3):336–347.

Bi, D., Zhang, J., Chakraborty, B., and Behringer, R. P. (2011). Jamming by shear. *Nature*, 480(7377):355–358.

Bjerrum, L. and Landva, A. (1966). Direct simple-shear tests on a norwegian quick clay. *Géotechnique*, 16:1–20.

Bonilla, R. R. O. (2004). *Numerical simulations of undrained granular media*. PhD thesis, University of Waterloo, University of Waterloo Waterloo, Canada.

Boulanger, R. W., Chan, C. K., Seed, H. B., Seed, R. B., and Sousa, J. B. (1993). A low-compliance bi-directional cyclic simple shear apparatus. *Geotechnical Testing Journal*, 16(1):36–45.

Boulanger, R. W. and Seed, R. B. (1995). Liquefaction of sand under bidirectional monotonic and cyclic loading. *Journal of Geotechnical Engineering*, 121(12):870–878.

Boulanger, R. W., Seed, R. B., Chan, C. K., Seed, H. B., and Sousa, J. (1991). Liquefaction behavior of saturated sands under uni-directional and bi-directional monotonic and cyclic simple shear loading. Technical Report 2, University of California, Berkeley, The address of the publisher. UCB/GT/91-08.

Boulanger, R. W. and Ziotopoulou, K. (2013). Formulation of a sand plasticity plane-strain model for earthquake engineering applications. *Soil Dynamics and Earthquake Engineering*, 53:254–267.

Cantor, D., Azéma, E., Sornay, P., and Radjaï, F. (2018). Rheology and structure of polydisperse three-dimensional packings of spheres. *Physical Review E*, 98(5):052910.

Carlton, B. D. and Kaynia, A. M. (2016). Comparison of the seismic response of offshore slopes using 1, 2, or 3 ground motion components. In *Offshore Technology Conference*, pages 1–12, Houston, TX, USA.

Castro, G. (1975). Liquefaction and cyclic mobility of saturated sands. *Journal of Geotechnical Engineering Division*, 101(GT6):551–569.

Cerna-Diaz, A., Olson, S. M., Numanoglu, O. A., Hashash, Y. M. A., Bhaumik, L., Rutherford, C. J., and Weaver, T. (2017). Free-field cyclic response of dense sands in dynamic centrifuge tests with 1D and 2D shaking. In *Geotechnical Frontiers 2017*, pages 121–130. American Society of Civil Engineers.

Chapman, B., Jost, G., and Van Der Pas, R. (2008). *Using OpenMP: portable shared memory parallel programming*. MIT press.

Chen, J.-W. (1988). *Stress path effect on static and cyclic behavior of Monterey No. 0/30 sand*. PhD thesis, University of Colorado, Boulder, CO, USA. Department of Civil, Environmental and Architectural Engineering.

Chiaro, G., Kiyota, T., and Koseki, J. (2013). Strain localization characteristics of loose saturated toyoura sand in undrained cyclic torsional shear tests with initial static shear. *Soils and Foundations*, 53(1):23–34.

Chiaro, G., Koseki, J., and Sato, T. (2012). Effects of initial static shear on liquefaction and large deformation properties of loose saturated Toyoura sand in undrained cyclic torsional shear tests. *Soils and Foundations*, 52(3):498–510.

Christoffersen, J., Mehrabadi, M. M., and Nemat-Nasser, S. (1981). A micromechanical description of granular material behavior. *Journal of Applied Mechanics*, 48(2):339–344.

Corti, R., Diambra, A., Wood, D. M., Escribano, D. E., and Nash, D. F. T. (2016). Memory surface hardening model for granular soils under repeated loading conditions. *Journal of Engineering Mechanics*, 142(12):04016102.

Cundall, P. A. and Strack, O. D. L. (1979). A discrete numerical model for granular assemblies. *Géotechnique*, 29(1):47–65.

Dabeet, A. (2014). *Discrete element modeling of direct simple shear response of granular soils and model validation using laboratory tests*. PhD thesis, University of British Columbia.

Dafalias, Y. F. (1986). Bounding surface plasticity. i: Mathematical foundation and hypoplasticity. *Journal of Engineering Mechanics*, 112(9):966–987.

Dafalias, Y. F. and Manzari, M. T. (2004). Simple plasticity sand model accounting for fabric change effects. *Journal of Engineering Mechanics*, 130(6):622–634.

Dafalias, Y. F. and Taiebat, M. (2016). SANISAND-Z: zero elastic range sand plasticity model. *Géotechnique*, 66(12):999–1013.

di Benedetto, H., Blanc, M., Tiouajni, S., and Ezaoui, A. (2014). Elastoplastic model with loading memory surfaces (lms) for monotonic and cyclic behaviour of geomaterials. *International Journal for Numerical and Analytical Methods in Geomechanics*, 38(14):1477–1502.

Dyvik, R., Lacasse, S., Berre, T., and Raadim, B. (1987). Comparison of truly undrained and constant volume direct simple shear tests. *Géotechnique*, 37(1):3–10.

EDEM (2016). *EDEM 2017 User Guide*. DEM Solutions Ltd., Edinburgh, Scotland, UK.

El Shafee, O., Abdoun, T. H., and Zeghal, M. (2017). Centrifuge modelling and analysis of site liquefaction subjected to biaxial dynamic excitations. *Géotechnique*, 67(3):260–271.

Elgamal, A., Yang, Z., Parra, E., and Ragheb, A. (2003). Modeling of cyclic mobility in saturated cohesionless soils. *International Journal of Plasticity*, 19(6):883–905.

Evans, T. M. and Zhang, L. (2019). A numerical study of particle friction and initial state effects on the liquefaction of granular assemblies. *Soil Dynamics and Earthquake Engineering*, 126:105773.

Feigenbaum, H. P. and Dafalias, Y. F. (2008). Simple model for directional distortional hardening in metal plasticity within thermodynamics. *Journal of Engineering Mechanics*, 134(9):730–738.

Fuentes, W., Wichtmann, T., Gil, M., and Lascarro, C. (2019). Isa-hypoplasticity accounting for cyclic mobility effects for liquefaction analysis. *Acta Geotechnica*, pages 1–19.

Georgiannou, V. N. and Konstadinou, M. (2014). Effects of density on cyclic behaviour of anisotropically consolidated Ottawa sand under undrained torsional loading. *Géotechnique*, 64(4):287–302.

Ghaboussi, J. and Dikmen, S. U. (1981). Liquefaction analysis for multidirectional shaking. *Journal of the Geotechnical Engineering Division*, 107(5):605–627.

Gong, G., Thornton, C., and Chan, A. H. C. (2012). DEM simulations of undrained triaxial behavior of granular material. *Journal of Engineering Mechanics*, 138(6):560–566.

Gopalakrishnan, P. and Tafti, D. (2013). Development of parallel dem for the open source code mfix. *Powder Technology*, 235:33–41.

Guo, N. and Zhao, J. (2013). The signature of shear-induced anisotropy in granular media. *Computers and Geotechnics*, 47:1–15.

Hall, S. A., Bornert, M., Desrues, J., Pannier, Y., Lenoir, N., Viggiani, G., and Bésuelle, P. (2010). Discrete and continuum analysis of localised deformation in sand using x-ray μct and volumetric digital image correlation. *Géotechnique*, 60(5):315–322.

He, X., Wu, W., and Wang, S. (2019). A constitutive model for granular materials with evolving contact structure and contact forces—part i: framework. *Granular Matter*, 21(2):16.

Hill, R. (1958). A general theory of uniqueness and stability in elastic-plastic solids. *Journal of the Mechanics and Physics of Solids*, 6(3):236–249.

Horita, M. (1985). *Modeling of cyclic behavior of saturated Monterey No. 0/30 sand*. PhD thesis, University of Colorado, Boulder, CO, USA. Department of Civil, Environmental and Architectural Engineering.

Huang, X., Hanley, K. J., Zhang, Z., Kwok, C., and Xu, M. (2019a). Jamming analysis on the behaviours of liquefied sand and virgin sand subject to monotonic undrained shearing. *Computers and Geotechnics*, 111:112–125.

Huang, X., Hanley, K. J., Zhang, Z., and Kwok, C.-y. (2019b). Structural degradation of sands during cyclic liquefaction: Insight from DEM simulations. *Computers and Geotechnics*, 114:103139.

Huang, X., Kwok, C.-y., Hanley, K. J., and Zhang, Z. (2018). Dem analysis of the onset of flow deformation of sands: linking monotonic and cyclic undrained behaviours. *Acta Geotechnica*, 13(5):1061–1074.

Hyodo, M., HYDE, A. F., Aramaki, N., and Nakata, Y. (2002). Undrained monotonic and cyclic shear behaviour of sand under low and high confining stresses. *Soils and Foundations*, 42(3):63–76.

Hyodo, M., Murata, H., Yasufuku, N., and Fujii, T. (1991). Undrained cyclic shear strength and residual shear strain of saturated sand by cyclic triaxial tests. *Soils and Foundations*, 31(3):60–76.

Iai, S., Tobita, T., Ozutsumi, O., and Ueda, K. (2011). Dilatancy of granular materials in a strain space multiple mechanism model. *International Journal for Numerical and Analytical Methods in Geomechanics*, 35(3):360–392.

Idriss, I. M. and Boulanger, R. W. (2006). Semi-empirical procedures for evaluating liquefaction potential during earthquakes. *Soil Dynamics and Earthquake Engineering*, 26(2-4):115–130.

Idriss, I. M. and Boulanger, R. W. (2008). *Soil liquefaction during earthquakes*. Earthquake Engineering Research Institute.

Ishihara, K. (1993). Liquefaction and flow failure during earthquakes. *Géotechnique*, 43(3):351–451.

Ishihara, K. and Nagase, H. (1988). Multi-directional irregular loading tests on sand. *Soil Dynamics and Earthquake Engineering*, 7(4):201–212.

Ishihara, K., Tatsuoka, F., and Yasuda, S. (1975). Undrained deformation and liquefaction of sand under cyclic stresses. *Soils and Foundations*, 15(1):29–44.

Ishihara, K., Yamazaki, A., and Haga, K. (1985). Liquefaction of K_0-consolidated sand under cyclic rotation of principal stress direction with lateral constraint. *Soils and Foundations*, 25(4):63–74.

Ishihara, K. and Yamazaki, F. (1980). Cyclic simple shear tests on saturated sand in multi-directional loading. *Soils and Foundations*, 20(1):45–59.

Itasca (2018). *FFC-Particle Flow Code, Version 6.0*. Itasca Consulting Group, Inc., Minneapolis, Minnesota.

Janda, T. and Mašín, D. (2017). General method for simulating laboratory tests with constitutive models for geomechanics. *International Journal for Numerical and Analytical Methods in Geomechanics*, 41(2):304–312.

Jefferies, M. and Been, K. (2015). *Soil liquefaction: a critical state approach*. CRC press.

Jiang, M., Zhang, A., and Li, T. (2019). Distinct element analysis of the microstructure evolution in granular soils under cyclic loading. *Granular Matter*, 21(2):39.

Kammerer, A. M., Pestana, J. M., and Seed, R. B. (2002). Undrained response of monterey 0/30 sand under multidirectional cyclic simple shear loading conditions. Geotechnical Engineering Report UCB/GT/02-01, University of California, Berkeley.

Kammerer, A. M., Pestana, J. M., and Seed, R. B. (2005). Behavior of monterey 0/30 sand under multidirectional loading conditions. In *Geomechanics: testing, modeling, and simulation*, pages 154–173. American Society of Civil Engineers.

Kanatani, K.-I. (1984). Distribution of directional data and fabric tensors. *International Journal of Engineering Science*, 22(2):149–164.

Khosravifar, A., Elgamal, A., Lu, J., and Li, J. (2018). A 3d model for earthquake-induced liquefaction triggering and post-liquefaction response. *Soil Dynamics and Earthquake Engineering*, 110:43–52.

Kiyota, T., Sato, T., Koseki, J., and Abadimarand, M. (2008). Behavior of liquefied sands under extremely large strain levels in cyclic torsional shear tests. *Soils and Foundations*, 48(5):727–739.

Kloss, C., Goniva, C., Hager, A., Amberger, S., and Pirker, S. (2012). Models, algorithms and validation for opensource DEM and CFD–DEM. *Progress in Computational Fluid Dynamics, an International Journal*, 12(2-3):140–152. http://www.cfdem.com.

Konstadinou, M. and Georgiannou, V. N. (2013). Cyclic behaviour of loose anisotropically consolidated Ottawa sand under undrained torsional loading. *Géotechnique*, 63(13):1144–1158.

Koseki, J., Yoshida, T., and Sato, T. (2005). Liquefaction properties of toyoura sand in cyclic torsional shear tests under low confining stress. *Soils and Foundations*, 45(5):103–113.

Kramer, S. L. (1996). *Geotechnical earthquake engineering*. Prentice Hall, Upper Saddle River.

Kruyt, N. P. (2010). Micromechanical study of plasticity of granular materials. *Comptes rendus mécanique*, 338(10-11):596–603.

Kuhn, M. R. (2017). *Granular geomechanics*. Elsevier.

Kuhn, M. R. and Daouadji, A. (2019). Stress fluctuations during monotonic loading of dense three-dimensional granular materials. *Granular Matter*, 21(1):10.

Kuhn, M. R., Renken, H. E., Mixsell, A. D., and Kramer, S. L. (2014). Investigation of cyclic liquefaction with discrete element simulations. *Journal of Geotechnical and Geoenvironmental Engineering*, 140(12):04014075.

Kutter, B. L., Carey, T. J., Hashimoto, T., Zeghal, M., Abdoun, T. H., Kokkali, P., Madabushi, G., Haigh, S., dArezzo, F. B., Madabushi, S., Hung, W. Y., Lee, C. J., Cheng, H. C., Iai, S., Tobita, T., Ashino, T., Ren, J., Zhou, Y. G., Chen, Y., Sun, Z. B., and Manzari, M. T. (2018). LEAP-GWU-2015 experiment specifications, results, and comparisons. *Soil Dynamics and Earthquake Engineering*, 113:616–628.

Kutter, B. L., Carey, T. J., Stone, N. annd Bonab, M. H., Manzari, M. T., Zeghal, M., Escoffier, S., Haigh, S. annd Madabhushi, G., Hung, W. Y., Kim, D. S., Kim, N. R., Okamura, M., Tobita, T., Ueda, K., and Zhou, Y. G. (2020). LEAP-UCD-2017 v. 1.01 model specifications. In Kutter, B. L. e. a., editor, *Model Tests and Numerical Simulations of Liquefaction and Lateral Spreading: LEAP-UCD-2017*, pages 41–62. Springer.

Li, X., Yu, H.-S., and Li, X.-S. (2009). Macro-micro relations in granular mechanics. *International Journal of Solids and Structures*, 46(25-26):4331–4341.

Li, X.-S. and Dafalias, Y. F. (2012). Anisotropic critical state theory: role of fabric. *Journal of Engineering Mechanics*, 138(3):263–275.

Li, X.-S. and Wang, Y. (1998). Linear representation of steady-state line for sand. *Journal of Geotechnical and Geoenvironmental Engineering*, 124(12):1215–1217.

Liu, H. Y., Abell, J. A., Diambra, A., and Pisanó, F. (2019). Modelling the cyclic ratcheting of sands through memory-enhanced bounding surface plasticity. *Géotechnique*, 69(9):783–800.

Liu, H. Y., Zygounas, F., Diambra, A., and Pisano, F. (2018). Enhanced plasticity modelling of high-cyclic ratcheting and pore pressure accumulation in sands. In *Numerical Methods in Geotechnical Engineering IX, Volume 1: Proceedings of the 9th European Conference on Numerical Methods in Geotechnical Engineering (NUMGE 2018)*, page 87. Porto, Portugal.

Liu, Y., Sun, W., and Fish, J. (2016). Determining material parameters for critical state plasticity models based on multilevel extended digital database. *Journal of Applied Mechanics*, 83(1):011003.

Luding, S. (2008). Cohesive, frictional powders: contact models for tension. *Granular Matter*, 10(4):235–246.

Majmudar, T. S. and Behringer, R. P. (2005). Contact force measurements and stress-induced anisotropy in granular materials. *Nature*, 435(7045):1079–1082.

Maleki, M., Cambou, B., and Dubujet, P. (2009). Development in modeling cyclic loading of sands based on kinematic hardening. *International Journal for Numerical and Analytical Methods in Geomechanics*, 33(14):1641–1658.

Manzari, M. T. and Dafalias, Y. F. (1997). A critical state two-surface plasticity model for sands. *Géotechnique*, 47(2):255–272.

Manzari, M. T., Kutter, B. L., Zeghal, M., Iai, S., Tobita, T., Madabhushi, S. P. G., Haigh, S. K., Mejia, L., Gutierrez, D. A., Armstrong, R. J., et al. (2014). LEAP projects: Concept and challenges. *Geotechnics for Catastrophic Flooding Events*, pages 109–116.

Martin, E. L., Thornton, C., and Utili, S. (2020). Micromechanical investigation of liquefaction of granular media by cyclic 3D DEM tests. *Géotechnique*, 70(10):906–915.

Martins, G. H. B. and Atman, A. P. F. (2017). Methods of parallel computation applied on granular simulations. *EPJ Web Conferences*, 140:15024. doi: 10.1051/epjconf/201714015024.

Matsuda, H., Hendrawan, A. P., Ishikura, R., and Kawahara, S. (2011). Effective stress change and post-earthquake settlement properties of granular materials subjected to multi-directional cyclic simple shear. *Soils and foundations*, 51(5):873–884.

Mattson, T. (2013). Introduction to OpenMP. Online course: https://www.youtube.com/playlist?list=PLLX-Q6B8xqZ8n8bwjGdzBJ25X2utwnoEG.

MiDi, G. D. R. (2004). On dense granular flows. *The European Physical Journal E*, 14(4):341–365.

Mutabaruka, P. (2013). *Numerical modeling of immersed granular media: initiation and propagation of avalanches in a fluid*. PhD thesis, Université Montpellier II-Science and Technology of Languedoc, Montpellier, France.

Mutabaruka, P., Taiebat, M., Pellenq, R. J.-M., and Radjaï, F. (2019). Effects of size polydispersity on random close-packed configurations of spherical particles. *Physical Review E*, 100(4):042906.

Ng, T.-T. and Dobry, R. (1994). Numerical simulations of monotonic and cyclic loading of granular soil. *Journal of Geotechnical Engineering*, 120(2):388–403.

Nguyen, D.-H., Azéma, E., Sornay, P., and Radjaï, F. (2015). Effects of shape and size polydispersity on strength properties of granular materials. *Physical Review E*, 91(3):032203.

Oda, M. (1982). Fabric tensor for discontinuous geological materials. *Soils and Foundations*, 22(4):96–108.

O'Sullivan, C. (2011). *Particulate discrete element modelling: a geomechanics perspective*. CRC Press.

Ouadfel, H. and Rothenburg, L. (2001). 'Stress–force–fabric' relationship for assemblies of ellipsoids. *Mechanics of Materials*, 33(4):201–221.

Papadimitriou, A. G. and Bouckovalas, G. D. (2002). Plasticity model for sand under small and large cyclic strains: a multiaxial formulation. *Soil Dynamics and Earthquake Engineering*, 22:191–204.

Papadimitriou, A. G., Bouckovalas, G. D., and Dafalias, Y. F. (2001). Plasticity model for sand under small and large cyclic strains. *Journal of Geotechnical and Geoenvironmental Engineering*, 127(11):973–983.

Petalas, A. L. and Dafalias, Y. F. (2019). Implicit integration of incrementally non-linear, zero-elastic range, bounding surface plasticity. *Computers and Geotechnics*, 12:386–402.

Petalas, A. L., Dafalias, Y. F., and Papadimitriou, A. G. (2018). Sanisand-fn: An evolving fabric-based sand model accounting for stress principal axes rotation. *International Journal for Numerical and Analytical Methods in Geomechanics*, 43(1):97–123.

Peters, J. F., Muthuswamy, M., Wibowo, J., and Tordesillas, A. (2005). Characterization of force chains in granular material. *Physical Review E*, 72(4):041307.

Poblete, M., Fuentes, W., and Triantafyllidis, T. (2016). On the simulation of multidimensional cyclic loading with intergranular strain. *Acta Geotechnica*, 11(6):1263–1285.

Potyondy, D. O. and Cundall, P. A. (2004). A bonded-particle model for rock. *International Journal of Rock Mechanics and Mining Sciences*, 41(8):1329–1364.

Pouragha, M. and Wan, R. (2016). Onset of structural evolution in granular materials as a redundancy problem. *Granular Matter*, 18(3):38.

Pyke, R. M., Seed, R. B., and Chan, C. K. (1975). Settlement of sands under multidirectional shaking. *Journal of the Geotechnical Engineering Division*, 101(4):379–398.

Radjai, F. (2015). Modeling force transmission in granular materials. *Comptes Rendus Physique*, 16:3–9.

Radjai, F., Delenne, J.-Y., Azema, É., and Roux, S. (2012). Fabric evolution and accessible geometrical states in granular materials. *Granular Matter*, 14(2):259–264.

Radjaï, F. and Dubois, F. (2011). *Discrete-element modeling of granular materials*. Wiley-Iste. ISBN: 978-1-848-21260-2, 496 pages.

Radjai, F. and Richefeu, V. (2009). Bond anisotropy and cohesion of wet granular materials. *Philosophical Transactions of the Royal Society A*, 367:5123–5138.

Radjai, F., Roux, J.-N., and Daouadji, A. (2017). Modeling granular materials: Century-long research across scales. *Journal of Engineering Mechanics*, 143:04017002.

Radjai, F. and Roux, S. (2004). Contact dynamics study of 2d granular media : Critical states and relevant internal variables. In Hinrichsen, H. and Wolf, D. E., editors, *The Physics of Granular Media*, pages 165–186, Weinheim. Wiley-VCH.

Radjaï, F., Roux, S., and Moreau, J. J. (1999). Contact forces in a granular packing. *Chaos: An Interdisciplinary Journal of Nonlinear Science*, 9(3):544–550.

Radjai, F., Troadec, H., and Roux, S. (2004). Key features of granular plasticity. In Antony, S., Hoyle, W., and Ding, Y., editors, *Granular Materials: Fundamentals and Applications*, pages 157–184, Cambridge. RS.C.

Radjai, F., Wolf, D. E., Jean, M., and Moreau, J. (1998). Bimodal character of stress transmission in granular packings. *Physical Review Letter*, 80:61–64.

Radjaï, F., Jean, M., Moreau, J.-J., and Roux, S. (1996). Force distribution in dense two-dimensional granular systems. *Physical Review Letters*, 77(2):274–277.

Ramirez, J., Barrero, A. R., Chen, L., Dashti, S., Ghofrani, A., Taiebat, M., and Arduino, P. (2018). Site response in a layered liquefiable deposit: evaluation of different numerical tools and methodologies with centrifuge experimental results. *Journal of Geotechnical and Geoenvironmental Engineering*, 144(10):04018073.

Reyes, A., Adinata, J., and Taiebat, M. (2019). Impact of bidirectional seismic shearing on the volumetric response of sand deposits. *Soil Dynamics and Earthquake Engineering*, 125:105665.

Reyes, A., Yang, M., Barrero, A. R., and Taiebat, M. (2020). Numerical modeling of soil liquefaction and lateral spreading using the SANISAND-Sf model in LEAP experiments. *Soil Dynamics and Earthquake Engineering*. In review.

Richefeu, V., El Youssoufi, M. S., Azéma, E., and Radjai, F. (2009). Force transmission in dry and wet granular media. *Powder Technology*, 190:258–263.

Riemer, M. F. (1992). *The effects of testing conditions on the constitutive behavior of loose, saturated sands under monotonic loading*. PhD thesis, University of California at Berkeley, Department of Civil and Environmental Engineering.

Rothenburg, L. and Bathurst, R. J. (1989). Analytical study of induced anisotropy in idealized granular materials. *Géotechnique*, 39(4):601–614.

Rudolph, C., Grabe, J., and Albrecht, I. (2014). Simple shear tests with a varying shearing direction during cyclic shearing. *Géotechnique Letters*, 4(2):102–107.

Satake, M. (1982). Fabric tensor in granular materials. In *Deformation and failure of granular materials(edited by Vermeer, P. A. and Lager, H. J.)*, pages 63–68. Balkema, Rotterdan.

Schwager, T. and Pöschel, T. (2007). Coefficient of restitution and linear–dashpot model revisited. *Granular Matter*, 9(6):465–469.

Seed, H. B. and Idriss, I. M. (1967). Analysis of soil liquefaction: Niigata earthquake. *Journal of the Soil Mechanics and Foundations Division*, 93(3):83–108.

Seidalinov, G. (2018). *Constitutive and numerical modeling of clay subjected to cyclic loading*. PhD thesis, University of British Columbia, Vancouver, Canada.

Seidalinov, G., Yang, M., and Taiebat, M. (2017). Multidirectional cyclic shearing of clays and sands: evaluation of two advanced plasticity models. In *3rd International Conference on Performance-based Design in Earthquake Geotechnical Engineering*, pages 1–21.

Shundyak, K., van Hecke, M., and van Saarloos, W. (2007). Force mobilization and generalized isostaticity in jammed packings of frictional grains. *Physical Review E*, 75(1):010301.

Sitharam, T. G. (2003). Discrete element modelling of cyclic behaviour of granular materials. *Geotechnical and Geological Engineering*, 21(4):297–329.

Sitharam, T. G., Vinod, J. S., and Ravishankar, B. V. (2009). Post-liquefaction undrained monotonic behaviour of sands: experiments and dem simulations. *Géotechnique*, 59(9):739–749.

Sivathayalan, S. and Ha, D. (2011). Effect of static shear stress on the cyclic resistance of sands in simple shear loading. *Canadian Geotechnical Journal*, 48(10):1471–1484.

Šmilauer, V., Catalano, E., Chareyre, B., Dorofeenko, S., Duriez, J., Gladky, A., Kozicki, J., Modenese, C., Scholtès, L., Sibille, L., et al. (2010). Yade reference documentation. *Yade Documentation*, 474(1).

Soroush, A. and Ferdowsi, B. (2011). Three dimensional discrete element modeling of granular media under cyclic constant volume loading: A micromechanical perspective. *Powder Technology*, 212(1):1–16.

Stallebrass, S. E. and Taylor, R. N. (1997). The development and evaluation of a constitutive model for the prediction of ground movements in overconsolidated clay. *Géotechnique*, 47(2):235–253.

Su, D. and Li, X.-S. (2008). Impact of multidirectional shaking on liquefaction potential of level sand deposits. *Géotechnique*, 58(4):259–267.

Sufian, A., Russell, A. R., and Whittle, A. J. (2017). Anisotropy of contact networks in granular media and its influence on mobilised internal friction. *Géotechnique*, 67(12):1067–1080.

Sufian, A., Russell, A. R., and Whittle, A. J. (2019). Evolving pore orientation, shape and size in sheared granular assemblies. *Granular Matter*, 21(1):4.

Sufian, A., Russell, A. R., Whittle, A. J., and Saadatfar, M. (2015). Pore shapes, volume distribution and orientations in monodisperse granular assemblies. *Granular Matter*, 17(6):727–742.

Sun, M. (2019). *The effects of multidirectional loading on soil liquefaction*. PhD thesis, University of Cambridge.

Taiebat, M. (2008). *Advanced elastic-plastic constitutive and numerical modeling in geomechanics*. PhD thesis, University of California, Davis, California, US.

Taiebat, M. and Dafalias, Y. F. (2008). SANISAND: Simple anisotropic sand plasticity model. *International Journal for Numerical and Analytical Methods in Geomechanics*, 32(8):915–948.

Taiebat, M., Jeremić, B., Dafalias, Y. F., Kaynia, A. M., and Cheng, Z. (2010). Propagation of seismic waves through liquefied soils. *Soil Dynamics and Earthquake Engineering*, 30(4):236–257.

Tatsuoka, F., Muramatsu, M., and Sasaki, T. (1982). Cyclic undrained stress-strain behavior of dense sands by torsional simple shear test. *Soils and Foundations*, 22(2):55–70.

Thornton, C. (2000). Numerical simulations of deviatoric shear deformation of granular media. *Géotechnique*, 50(1):43–53.

Thornton, C. (2015). *Granular dynamics, contact mechanics and particle system simulations*. Springer.

Tobita, T., Vargas, R. R., Ichii, K., Okamura, M., Sjafruddin, A. N., Takemura, J., Lyu, H., Ueda, K., Uzuoka, R., Iai, S., Boksmati, J., Fusco, A., Torres-Garcia, S., Haigh, S., Madabushi, G., Manzari, M. T., Escoffier, S., Li, Z., Kim, D. S., Manandhar, S., Hung, W. Y., Huang, J. X., Pham, T. N. P., Zeghal, M., Abdoun, T., Korre, E., Kutter, B. L., Carey, T. J., Stone, N., Zhou, Y. G., Liu, K., and Ma, Q. (2020). LEAP-ASIA-2019: validation of centrifuge experiments and generalized scaling law on liquefaction-induced lateral spreading. *Soil Dynamics and Earthquake Engineering*, (submitted).

Towhata, I. and Ishihara, K. (1985). Undrained strength of sand undergoing cyclic rotation of principal stress axes. *Soils and Foundations*, 25(2):135–147.

Tu, X. and Andrade, J. E. (2008). Criteria for static equilibrium in particulate mechanics computations. *International Journal for Numerical Methods in Engineering*, 75(13):1581–1606.

Ueda, K. (2018). Leap-asia-2018: Stress-strain response of ottawa sand in cyclic torsional shear tests. *DesignSafe-CI [publisher]*. Dataset, doi:10.17603/DS2D40H.

Vaid, Y. P. and Chern, Jing C.and Tumi, H. (1985). Confinement pressure, grain angularity and liquefaction. *Journal of Geotechnical Engineering*, 111(10):1229–1235.

Vaid, Y. P. and Chern, J.-C. (1983). Effects of static shear on resistance to liquefaction. *Soils and Foundations*, 23(1):47–60.

Vaid, Y. P. and Liam Finn, W. D. (1979). Static shear and liquefaction potential. *Journal of the Geotechnical Engineering Division*, 105(10):1233–1246.

Vaid, Y. P. and Sivathayalan, S. (1996). Static and cyclic liquefaction potential of fraser delta sand in simple shear and triaxial tests. *Canadian Geotechnical Journal*, 33(2):281–289.

Vaid, Y. P., Stedman, J. D., and Sivathayalan, S. (2001). Confining stress and static shear effects in cyclic liquefaction. *Canadian Geotechnical Journal*, 38(3):580–591.

Voivret, C., Radjaï, F., Delenne, J.-Y., and Youssoufi, M. S. E. (2007). Space-filling properties of polydisperse granular media. *Physical Review E*, 76(2):021301.

Wang, G. and Wei, J. (2016). Microstructure evolution of granular soils in cyclic mobility and post-liquefaction process. *Granular Matter*, 18(3):51.

Wang, R., Fu, P., Zhang, J.-M., and Dafalias, Y. F. (2016). DEM study of fabric features governing undrained post-liquefaction shear deformation of sand. *Acta Geotechnica*, 11(6):1321–1337.

Wang, R., Zhang, J.-M., and Wang, G. (2014). A unified plasticity model for large post-liquefaction shear deformation of sand. *Computers and Geotechnics*, 59:54–66.

Wang, Z. and Ma, F. (2019). Bounding surface plasticity model for liquefaction of sand with various densities and initial stress conditions. *Soil Dynamics and Earthquake Engineering*, 127:105843.

Wang, Z.-L., Dafalias, Y. F., and Shen, C.-K. (1990). Bounding surface hypoplasticity model for sand. *Journal of Engineering Mechanics*, 116(5):983–1001.

Wei, J. (2017). *Discrete element analysis of fabric evolution in cyclic liquefaction of granular soils*. PhD thesis, The Hong Kong University of Science and Technology, Hong Kong.

Wei, J., Huang, D., and Wang, G. (2018). Microscale descriptors for particle-void distribution and jamming transition in pre-and post-liquefaction of granular soils. *Journal of Engineering Mechanics*, 144(8):04018067.

Wei, J., Huang, D., and Wang, G. (2020). Fabric evolution of granular soils under multidirectional cyclic loading. *Acta Geotechnica*, pages 1–15.

Wei, J. and Wang, G. (2017). Discrete-element method analysis of initial fabric effects on pre-and post-liquefaction behavior of sands. *Géotechnique Letters*, 7(2):161–166.

Wichtmann, T. and Triantafyllidis, T. (2016). An experimental database for the development, calibration and verification of constitutive models for sand with focus to cyclic loading: part i—tests with monotonic loading and stress cycles. *Acta Geotechnica*, 11(4):739–761.

Wijewickreme, D., Sriskandakumar, S., and Byrne, P. (2005). Cyclic loading response of loose air-pluviated fraser river sand for validation of numerical models simulating centrifuge tests. *Canadian Geotechnical Journal*, 42(2):550–561.

Woo, S. I., Salgado, R., and Prezzi, M. (2019). Dilatancy-triggering surface for advanced constitutive modelling of sand. *Géotechnique Letters*, 9(2):136–141.

Wood, D. M. (1990). *Soil behaviour and critical state soil mechanics*. Cambridge university press.

Wu, J. (2002). *Liquefaction triggering and post-liquefaction deformation of Monterey 0/30 sand under uni-directional cyclic simple shear loading*. PhD thesis, University of California at Berkeley, Department of Civil and Environmental Engineering.

Yang, J. and Sze, H. Y. (2011). Cyclic behaviour and resistance of saturated sand under non-symmetrical loading conditions. *Géotechnique*, 61(1):59–73.

Yang, M., Seidalinov, G., and Taiebat, M. (2019). Multidirectional cyclic shearing of clays and sands: Evaluation of two bounding surface plasticity models. *Soil Dynamics and Earthquake Engineering*, 124:230–258.

Yang, M., Taiebat, M., and Dafalias, Y. F. (2020a). SANISAND-MSf: a memory surface enhanced sand plasticity model with semifluidized state for undrained cyclic shearing. *Géotechnique*. Doi: 10.1680/jgeot.19.P.363.

Yang, M., Taiebat, M., and Dafalias, Y. F. (2021). A new sand constitutive model for pre- and post-liquefaction stages. In *16th International Conference of IACMAG*, pages 1–8. Torino, Italy.

Yang, M., Taiebat, M., Mutabaruka, P., and Radjaï, F. (2018). Multidirectional cyclic shearing of granular media using discrete element simulations. In *IS-Atlanta 2018: Geo-Mechanics from Micro to Macro*, pages 1–6. Atlanta, Georgia, US.

Yang, M., Taiebat, M., Mutabaruka, P., and Radjaï, F. (2020b). Evolution of granular materials under isochoric cyclic simple shearing. Submitted.

Yang, M., Taiebat, M., Mutabaruka, P., and Radjaï, F. (2020c). Macro response and micro structure of 3D granular media subjected to multidirectional cyclic shearing. In preparation.

Yang, M., Taiebat, M., and Vaid, Y. P. (2016). Bidirectional monotonic and cyclic shear testing of soils: state of knowledge. In *69th Canadian Geotechnical Conference*, Vancouver, BC, Canada. Paper ID: 4198, 8 pages.

Yang, Z. X. and Pan, K. (2017). Flow deformation and cyclic resistance of saturated loose sand considering initial static shear effect. *Soil Dynamics and Earthquake Engineering*, 92:68–78.

Yoshimine, M., Ishihara, K., and Vargas, W. (1998). Effects of principal stress direction and intermediate principal stress on undrained shear behavior of sand. *Soils and Foundations*, 38(3):179–188.

Zeghal, M., El-Shafee, O., and Abdoun, T. (2018). Analysis of soil liquefaction using centrifuge tests of a site subjected to biaxial shaking. *Soil Dynamics and Earthquake Engineering*, 114:229–241.

Zhang, J.-M. and Wang, G. (2012). Large post-liquefaction deformation of sand, part i: physical mechanism, constitutive description and numerical algorithm. *Acta Geotechnica*, 7(2):69–113.

Zhang, L. and Evans, T. M. (2018). Boundary effects in discrete element method modeling of undrained cyclic triaxial and simple shear element tests. *Granular Matter*, 20(4):60.

Zhang, L. and Evans, T. M. (2020). Investigation of initial static shear stress effects on liquefaction resistance using discrete element method simulations. *International Journal of Geomechanics*, 20(7):04020087.

Zhang, Y., Zhou, X., and Wen, Y. (2020). Constitutive theory for sand based on the concept of critical fabric surface. *Journal of Engineering Mechanics*, 146(4):04020019.

Zhou, W., Liu, J., Ma, G., and Chang, X. (2017). Three-dimensional DEM investigation of critical state and dilatancy behaviors of granular materials. *Acta Geotechnica*, 12(3):527–540.